AIX-MARSEILLE UNIVERSITÉ

UNIVERSIDAD AUTÓNOMA DE MADRID

ECOLE DOCTORALE Physique et Sciences de la Matière / ED352

Fondation Universitaire A*MIDEX

CINaM – Centre Interdisciplinaire de Nanosciences de Marseille / UMR 7325
Departamento de Física Teórica de la Materia Condensada, Facultad de Ciencias, UAM

Thèse présentée pour obtenir le grade universitaire de docteur

Discipline: Physique et sciences de la matière
Spécialité: Matière Condensée et Nanosciences

Rajarshi SINHA ROY

Thesis: *Ab initio* Simulation of Optical Properties of Noble-Metal Clusters

Titre de la thèse: Modélisation des propriétés optiques de nanoparticules métalliques

Soutenue le 19/01/2018 devant le jury composé de:

Eleonora LUPPI	Université Pierre et Marie Curie	Rapporteur
Thomas NIEHAUS	Institut Lumière Matière, Lyon	Rapporteur
Magali BENOIT	CEMES - UPR8011 - Toulouse	Examinateur
Rubén ESTEBAN	Donostia International Physics Center	Examinateur
Matthias HILLENKAMP	Institut Lumière Matière, Lyon	Examinateur
Hans-Christian WEISSKER	CINaM, Aix-Marseille Université	Directeur de thèse
Pablo GARCÍA-GONZÁLEZ	Universidad Autónoma de Madrid	Co-directeur de thèse
Christine MOTTET	CINaM, Aix-Marseille Université	Co-directrice de thèse
Antonio Issac FERNÁNDEZ-DOMÍNGUEZ	Universidad Autónoma de Madrid	Invité

Numéro national de thèse/suffixe local: 2018AIXM0001/001ED352

Acknowledgements

This thesis is an example of people having different theoretical viewpoints working together to link two different directions of theoretical research on the topic “Optical Properties of Noble-Metal Clusters”. Therefore, foremost, I would like to express my sincere gratitude to my thesis supervisors, Hans-Christian Weissker and Pablo García-González, for conceiving this PhD project. Besides my supervisors, I thank my collaborator Antonio Issac Fernández-Domínguez who has played a key role in this project by introducing me to the classical-optics viewpoints. To all of the three I express my sincere gratitude for constantly supporting and motivating me, and also for helping me to find potential within me. I also thank Christine Mottet for being my official thesis-supervisor and helping me with all the necessary administrative tasks related to the successful completion of my thesis.

My sincere thanks go to the directors of CINaM - Centre Interdisciplinaire de Nanoscience de Marseille, Claude Henry, Frédéric Fagès, Pierre Müller, and to all the members of the research group TSN - Théorie et simulation numérique for having me amidst the research environment of CINaM and Aix-Marseille Université. At the same time, I express my thanks to the head of the Departamento de Física Teórica de la Materia Condensada, Facultad de Ciencias, Universidad Autónoma de Madrid (UAM), Alfredo Levy Yeyati for having me amidst the research environment in UAM. My sincere thanks go to the Fondation A*MIDEX, Aix-Marseille Université, for funding my PhD thesis.

I thank the technical and administrative staffs, in particular to Frédéric Augier, Francis Quintric, Béatrice Prudhon, Dominique Destre, Valérie Juvenal, Élodie Pico, and Karine Millé in CINaM, and Stefan Bilan and Laura Ramos Juanino in UAM for all the assistances.

At the end, I would like to express my thanks to my parents, to my sister Titly, and most importantly to my friends who have constantly stayed beside me during this three-year-long journey of PhD thesis.

Marseille, 23/01/2018.

Abstract

The fundamental research interest in nanometric pieces of noble metals is mainly due to the localized surface-plasmon resonance (LSPR) in the optical absorption. Different aspects related to the theoretical understanding of LSPRs in 'intermediate-size' noble-metal clusters are studied in this thesis. To gain a broader perspective both the real-time *ab initio* formalism of time–dependent density-functional theory (RT-TDDFT) and the classical electromagnetics approach are employed. A systematic and detailed comparison of these two approaches highlights and quantifies the limitations of the electromagnetics approach when applied to quantum-sized systems. The differences between collective plasmonic excitations and the excitations involving d-electrons, as well as the interplay between them are explored in the spatial behaviour of the corresponding induced densities by performing the spatially resolved Fourier transform of the time-dependent induced density obtained from a RT-TDDFT simulation using a δ-kick perturbation. In this thesis, both bare and ligand-protected noble-metal clusters were studied. In particular, motivated by recent experiments on plasmon emergence phenomena, the TDDFT study of Au-Cu nanoalloys in the size range just below 2 nm produced subtle insights into the general effects of alloying on the optical response of these systems.

Résumé

L'intérêt de la recherche fondamentale pour les morceaux nanométriques de métaux nobles est principalement dû à la résonance localisée des plasmons de surface (LSPR) dans l'absorption optique. Différents aspects, liés à la compréhension théorique de la LSPR dans le cas de clusters de métaux nobles de taille dite intermédiaire, sont étudiés dans ce manuscrit. Afin d'avoir une vision plus large nous utilisons deux approches : l'approche électromagnétique classique et le formalisme ab initio en temps réel de la théorie de la fonctionnelle de la densité dépendant du temps (RT-TDDFT). Une comparaison systématique et détaillée de ces deux approches souligne et quantifie les limitations de l'approche électromagnétique lorsqu'elle est appliquée à des systèmes de taille quantique. Les différences entre les excitations plasmoniques collectives et celles impliquant les électrons d, ainsi que leurs interactions, sont étudiées grâce au comportement spatial des densités correspondantes. Ces densités sont obtenues en appliquant une transformée de Fourier dans l'espace à la densité obtenue par les simulations DFT utilisant une perturbation delta-kick. Dans ce manuscrit, des clusters de métaux nobles nus et protégés par des ligands sont étudiés. En particulier, motivé par de récents travaux sur les phénomènes d'émergence de plasmon, l'étude par TD-DFT de nano-alliages Au-Cu de taille tout juste inférieure à 2nm à fourni de subtiles connaissances sur les effets d'alliages sur la réponse optique de tels systèmes.

Resumen

La aparición de resonancias de plasmón de superficie localizado (LSPR de sus siglas en inglés) en el espectro de absorción ha recibido gran atención en la investigación básica de las propiedades de estructuras nanométricas compuestas de metales nobles. En esta tesis estudiamos diferentes aspectos de las LSPRs en agregados de metales nobles de tamaño intermedio. En particular, para obtener una perspectiva amplia sobre la generación y propiedades de las LSPRs en estos sistemas, usaremos el formalismo ab-initio basado en la Teoría del Funcional de la Densidad en tiempo real (RT-TDDFT), pero también métodos basados en el electromagnetismo clásico. Así, compararemos de manera sistemática y detallada ambas prescripciones, resaltando y cuantificando las limitaciones del electromagnetismo clásico cuando se aplica a sistemas en los que su tamaño hace emerger fenómenos típicamente cuánticos. A su vez, estudiaremos como las diferencias entre excitaciones colectivas (plasmónicas) y aquellas que involucran a electrones d localizados, así como su interrelación, se manifiestan en la densidad de carga inducida representada espacialmente. Tal densidad de carga se obtendrá a partir de la transformada de Fourier de la densidad de carga inducida por una perturbación tipo delta de Dirac en $t = 0$. Finalmente, en esta tesis analizaremos agregados de metales nobles encapsulado por ligandos. En concreto, motivados por recientes experimentos, el estudio TDDFT de Au-Cu nanoaleaciones en el rango de tamaños del orden de 2 nm permite profundizar en los efectos debidos a la composición de la aleación en las propiedades de respuesta óptica de estos sistemas.

Aix-Marseille Université
Universidad Autónoma de Madrid

Résumé Substantiel

Ecole Doctorale Physique et sciences de la matière ED 352
Programa de Doctorado en Física de la Materia Condensada, Nanociencia y Biofísica

Thèse de doctorat sur

Modélisation des propriétés optiques de nanoparticules métalliques

Rajarshi Sinha Roy

L'intérêt de la recherche fondamentale pour les fragments nanométriques de métaux nobles est principalement dû à la résonnance localisée des plasmons de surface (localized surface-plasmon resonance, LSPR) dans l'absorption optique. Les LSPRs apparaissent dans le spectre d'absorbance optique de nanoparticules de métaux nobles comme les caractéristiques spectrales dominantes, larges et lisses, dans les domaines du visible et de l'ultraviolet. La LSPR est utilisée dans de nombreux domaines de recherche en biologie et en chimie, et est la base de certaines nouvelles technologies en optique, électronique ou médecine, pour la thérapie comme pour le diagnostic [1–6].

Les études théoriques sur les LSPRs des nanoparticules sont effectuées en utilisant différents niveaux de théorie, en fonction de la taille des nanoparticules. En particulier, la transition à partir des nanoparticules de grand taille, avec des bandes électroniques et des spectres optiques lisses, vers des clusters de petite taille et se comportant comme des molécules (dis molecule-like), avec des états électroniques discrets dans le spectres, reflète la nature quantique des clusters [7–9]. De plus, dans certains métaux nobles, Au par exemple, nous obersvons le phénomène d'émergence de LSPR dans cette gamme de taille, appelée gamme de taille intermédiaire. Ce sont ces clusters de métaux nobles de taille intermédiaire qui ont été principalement étudiés dans ce travail de thèse.

Différentes communautés, ayant différents intérêts et contextes, ont travaillé sur la réponse optique de particules de métaux nobles de taille intermédiaire. En particulier, la communauté de la plasmonique, très active, a utilisé des approches basées sur les théories électromagnétiques. Toutefois, avec la miniaturisation progressive des objets pouvant être produits, manipulés et utilisés, il est de plus en plus important d'ajouter des corrections quantiques à la description purement classique. Cependant, des études précises des limites et problèmes liés à ces méthodes ne sont que rarement disponibles.

D'un autre côté, la description quantique de clusters de métaux nobles de taille intermédiaire a été développée en utilisant principalement la théorie de la fonctionnelle de la densité (density-functional theory, DFT), à la fois statique et dépendant du temps. En pratique, les calculs de la théorie fonctionnelle de densité dépendant du temps (time– dependent DFT, TDDFT) contiennent nécessairement des approximations, notamment les différentes fonctionnelles ou kernels d'échange et corrélation. De plus, de nombreux effets sont soit complètement négligés (comme souvent la température), soit approximativement prises en compte (la structure de la surface/interface par exemple).

Cette thèse est consacrée à la LSPR, et comprend différents aspects de la recherche actuelle sur les interactions des ondes électromagnétiques avec des clusters de métaux nobles à des échelles de taille atomique.

L'étude des propriétés optiques de clusters de métaux nobles de taille intermédiaire est ici effectuée en utilisant deux méthodes : la méthode ab initio, et l'approche classique de l'électromagnétique, afin d'obtenir une plus large perspective sur l'utilisation de ces différentes méthodologies. Les calculs ab initio sont effectués en TDDFT en temps réel (real-time TDDFT, RT-TDDFT) dans le régime de réponse linéaire, alors que les calculs électromagnétiques classiques sont effectués pour différentes descriptions de la permittivité des métaux.

L'un des objectifs de cette thèse est d'explorer les avantages et les limites de la méthode optique classique pour expliquer les propriétés optiques de clusters de métaux nobles de taille intermédiaire, en comparant systématiquement cette méthode aux approches de TDDFT ab initio. Pour cela, les structures atomistiques doivent être remplacées par des géométries équivalentes dans les calculs optiques classiques. Nous avons donc développé un modèle simple et intuitif (à la fois des formes et des dimensions) afin de permettre l'équivalence entre les structures atomistiques de dimensions latérales sub-nanométriques et les géométries correspondantes pour les calculs électromagnétiques.

Pour représenter au mieux la terminaison correspendant à un seul atome des bâtonnets atomistiques, une géométrie en « cigare » est choisie pour les régions métalliques dans les calculs électromagnétiques. La densité électronique dans les cigares est définie comme étant identique à la densité des électrons s moyenne dans le système infini, et le volume du cigare est fixé de telle sorte que le nombre d'électrons à l'intérieur soit le même que le nombre d'électrons s dans les structures atomistiques. Enfin, le rapport d'aspect (RA) du cigare est également déterminé de façon identique à celui du système atomistique.

Les spectres d'absorption de différents clusters d'Au et d'Ag de tailles intermédiaires sont ainsi calculés par TDDFT ab initio et par la théorie électromagnétique. Les calculs électromagnétiques sont effectués à la fois sur les descriptions locales et non locales (modèle hydrodynamique) pour la permittivité des métaux. La comparaison des spectres d'absorption calculés avec ces deux méthodes révèle les observations intéressantes suivantes :

- Comme on le sait, pour les systèmes à RA élevé, le comportement de l'absorption de Au et Ag est similaire : apparition d'une LSPR forte et bien définie dans l'infrarouge. En effet, dans les deux cas (Ag et Au), pour un RA élevé, la LSPR apparaît bien en dessous du début de la transition interbande. La comparaison systématique montre que, pour les structures en bâtonnets d'Ag avec un RA > 5 et d'Au avec un RA $\gtrapprox 8$ (dont la réponse est dominée par la LSPR), la position spectrale de la LSPR ainsi que les forces d'absorption calculées en TDDFT et par les approches électromagnétiques sont en excellent accord, même si les systèmes possèdent une dimension latérale subnanométrique, manifestant une inhomogénéité atomistique.
- La comparaison avec les prédictions ab initio s'améliore encore lorsque la section efficace d'absorption électromagnétique est calculée en utilisant la permittivité hydrodynamique non locale du métal, sauf pour les chaînes atomiques linéaires, où les calculs optiques locaux semblent meilleurs.
- Lorsque le RA des systèmes est réduit, l'accord entre la TDDFT et les calculs électromagnétiques commence à se dégrader de manière significative. Cette dégradation semble être due au décalage vers le bleu de la LSPR avec la diminution du RA, ce qui provoque le couplage entre la LSPR et les transitions interbandes. Ce couplage est plus visible dans l'Au que dans l'Ag, en raison du plus faible seuil d'énergie des transitions interbandes dans l'Au.
- Dans les systèmes en bâtonnets, à mesure que le RA diminue, les calculs de TDDFT montrent le couplage entre la LSPR et les transitions interbandes lorsque les LSPRs sont fragmentées. Comme le début des transitions interbandes ne dépend pas de la taille des clusters [10], le couplage de la LSPR et des transitions interbandes est principalement régi par la position spectrale RA-dépendante de la LSPR. Ce couplage n'est pas capté par les calculs électromagnétiques non locaux. Par conséquent, dans les bâtonnets d'Au et d'Ag, c'est principalement la forme (c'est-à-dire le RA) qui détermine le couplage de la LSPR et des transitions interbandes, et donc l'accord entre les approches électromagnétiques non locales et la TDDFT.

En conclusion, nous avons comparé les méthodes optiques classiques, locales et non locale, et la méthode de la mécanique quantique ab initio pour calculer les positions spectrales et les forces des LSPR dans des systèmes allongés de taille quantique préservant le rapport d'aspect et le nombre d'électrons Drude (ou s). La comparaison montre une similatité remarquable entre ces deux approches lorsque la LSPR est largement découplée des transitions interbandes. C'est le cas pour les bâtonnets d'Ag de RA > 5 et les bâtonnets d'Au de RA $\gtrapprox 8$. De plus, nous pouvons conclure que c'est la forme qui détermine la qualité de cette similarité, et non la taille globale (c'est-à-dire le nombre d'atomes).

Par la suite, nous avons comparé la dépendance des LSPRs au rapport d'aspect, calculé par des approches classiques, avec les calculs ab initio correspondants dans différentes structures atomiques d'Ag et d'Au (bâtonnets, chaînes atomiques et clusters icosaédriques). Cette comparaison est particulièrement intéressante. En passant de structures minces (chaînes) à épaisses (bâtonnets) pour le même RA, l'énergie relative de la LSPR excitée selon l'axe longitudinal des systèmes augmente. Cette tendance d'augmentation de l'énergie de la LSPR lorsque la taille augmente n'est observée que dans les calculs ab initio pour les systèmes allongés, alors que les calculs optiques non locaux classiques montrent le comportement connu opposé : augmentation de l'énergie de la LSPR avec la diminution de la taille absolue du système. Ainsi, bien que l'optique classique obtienne les mêmes positions et forces spectrales des LSPRs dans des systèmes allongés de taille quantique, de subtils effets de mécanique quantique modifient le comportement classique de la LSPR en fonction de la taille du système. Dans les chaînes monoatomiques d'Ag, les LSPRs se révèlent exemptes de contamination de transition d, même pour des chaînes de 6 atomes seulement. En revanche, les spectres TDDFT pour des chaînes d'Au indiquent que les excitations collectives quasi-unidimensionnelles ne sont pas bien résolues pour des chaînes ayant un nombre d'atomes inférieur à douze. Cependant, lorsque le nombre d'atomes dans les chaînes d'Au diminue, on observe un transfert du poids spectral du pic le plus bas en énergie vers différents pics fragmentés de plasmon. Cela manifeste l'émergence d'un couplage de la LSPR avec des excitations d'électrons d; les prédictions de l'optique classique décrivent une moyenne spectrale approximative des pics fragmentés.

De plus, nous avons étudié les densités de charges induites aux fréquences de LSPR à partir des calculs classiques et de TDDFT. Cela a permis d'étendre l'étude comparative des deux approches théoriques différentes (électromagnétisme et TDDFT) au-delà des caractéristiques de champ lointain et de vérifier la validité des résultats également dans le régime de champ proche. En comparant les densités de charges induites des LSPRs intégrées selon les directions perpendiculairs à l'axe du bâtonnet et en fonction de la longueur du bâtonnet, nous avons démontré que les descriptions des charges induites aux énergies LSPR par la mécanique classique et par la mécanique entièrement quantique concordent remarquablement avec les systèmes allongés d'Ag. Ceci nous a permis de conclure que, en raison du haut caractère plasmonique des structures allongées, elles supportent des LSPRs collectives bien définies (à la fois comme modes de surface dans les bâtonnets, et comme modes collectifs quasi-unidimensionnels dans les chaînes), exempt de contamination par des excitations d'électron-trou.

Pour une structure moins allongée (plus compacte) d'Ag19, où la haute fréquence LSPR est visible dans son spectre d'absorption (3 eV), la même comparaison des densités de charges induites à la LSPR entre les approches électromagnétique et TDDFT montre que les transitions d'électrons d jouent un rôle clé dans la réponse optique. En effet, dans les clusters compacts de métaux nobles, les charges induites calculées par TDDFT se propagent significativement le long de la longueur du bâtonnet vers son plan médian. Ce résultat est en désaccord complet avec la prédiction électromagnétique, même si les spectres calculés avec les deux méthodes (TDDFT et optique non locale) présentent une ressemblance surprenante.

Suite à la divergence entre les prévisions obtenues par TDDFT et l'électromagnétisme sur les densités de charge induites à la LSPR dans un cluster compact d'Ag19, une vérification de la qualité des calculs ab initio utilisant la fonction PBE AGGA est effectuée pour des bâtonnets de différentes longueurs, en comparant avec une fonctionnelle d'échange et de corrélation hybride corrigée à longue portée, LC-M06L. Cette fonctionnelle est plus appropriée pour le traitement des excitations d'électrons d et fournit des spectres précis pour les petits clusters d'Ag. Malheureusement, son utilisation nécessite également un effort numérique beaucoup plus important, par comparaison avec les simples fonctionnelles GGA ou LDA. Cette analyse nous a permis de conclure que, pour des systèmes allongés (comme des bâtonnets d'Ag67), les spectres obtenus à partir des calculs TDDFT-PBE et ceux obtenus en utilisant LC-M06L ne sont pas différents. En revanche, pour des clusters compacts comme Ag19, ils sont complètement différents. Ainsi, pour les clusters compacts comme Ag19, les calculs TDDFT-PBE ne sont pas fiables et la correspondance spectrale entre les résultats classiques et entièrement quantiques est en partie une coïncidence. Ils ne parviennent pas à décrire les structures dans lesquelles les LSPRs et les électrons d se couplent fortement. Par conséquent, dans le traitement ab initio de ces systèmes, il est nécessaire d'avoir une meilleure description de l'échange et de la corrélation que les fonctionnelles AGGA.

La distribution spatiale du champ électrique induit, ou la densité de charge induite, fournit un aperçu plus profond d'une excitation optique donnée. Dans les approches électromagnétiques, les calculs sont généralement effectués dans le domaine fréquentiel, et le champ électrique induit (et donc la densité induite) à une énergie donnée peut être calculé. En RT-TDDFT, la réponse optique est calculée dans le domaine temporel, et la densité de charge induite correspondant à une excitation optique à une énergie donnée n'est pas facilement disponible. Cependant, la plupart des simulations RT-TDDFT utilisent une perturbation δ-kick. Celle-ci produit une densité de charge induite dépendant du temps qui est la superposition des densités induites qui correspondent à toutes les excitations qui apparaissent dans le spectre.

En effectuant la transformée de Fourier résolue spatialement de la densité induite dépendant du temps obtenue à partir d'une simulation RT-TDDFT, nous avons récupéré le profil spatial de la densité induite à n'importe quelle énergie d'intérêt donnée. Nous avons discuté des différences entre les excitations plasmoniques collectives et les excitations impliquant des électrons d, ainsi que l'interaction entre plasmon et électrons d dans le comportement spatial des modes correspondant respectivement à ces excitations.

- Une comparaison de la densité induite par laser à l'énergie LSPR avec la densité induite par un champ électrostatique montre le criblage dynamique par les électrons d. Nous sommes arrivés à la conclusion générale que pour la LSPR dipolaire, les contributions principales des modes de la densité induite viennent de la région de surface du cluster. En revanche, les électrons d répondent au champ généré par cette contribution de surface avec la même fréquence LSPR et une oscillation déphasée par $\pi/2$.
- En utilisant les densités transformées par la transformée de Fourier, nous sommes en mesure d'étudier les contributions spatiales à des caractéristiques individuelles dans le spectre d'absorption. Par exemple, dans un cluster plus complexe protégé par un ligand, $Ag_{29}P_4S_{24}C_{144}H_{108}$, la transformée de Fourier résolue spatialement de la densité induite dépendant du temps révèle que les excitations à basse énergie sont plus confinées au noyau d'Ag du composé que l'excitation forte à haute énergie, dont la contribution principale vient des anneaux benzéniques des ligands environnants.

Une autre partie du travail effectué dans cette thèse est consacrée à la compréhension de l'absorption optique dans une catégorie particulière de clusters d'Au et de Cu d'environ 1,8 nm. Des expériences récentes sur des clusters de type $Au_{144}(SR)_{60}$ ont démontré l'émergence d'un pic d'absorption à 550 nm (2,25 eV) lors de l'ajout de cuivre aux échantillons d'Au pur; dans certains cas, un seul atome de Cu semble avoir cet effett [11, 12]. Cette découverte est intéressante car, à cette taille, les clusters nus d'Au et de Cu (par exemple Au_{147}Ih) ne présentent pas de fortes spécificités d'absorption dans les spectres.

Pour tenter d'expliquer ces résultats, des calculs ab initio des nano-alliages de type $Au_{(144,145)-x}Cu_x(SR)_{60}$ ont également été réalisés par Malola et al. [13], qui affirmaient que « *Copper Induces a Core Plasmon in Intermetallic* $Au_{(144,145)-x}Cu_x(SR)_{60}$ *Nanoclusters* ». Pour mieux comprendre et vérifier cette affirmation, nous avons réalisé des calculs ab initio similaires sur ces clusters. Cette étude ab initio minutieuse et détaillée présente des idées subtiles sur les effets de l'alliage ainsi que l'émergence de LSPRs dans les clusters $Au_{(147)-x}Cu_x$ nus et les clusters d'$Au_{(144,145)-x}Cu_x(SR)_{60}$ recouverts de ligands.

Un certain nombre de situations différentes sont considérées : aussi bien la relaxation à l'état fondamental des structures (LDA & PBE), que le choix du groupement tronqué restant des ligands thiolate (R = H, & R = CH3), ou encore les différences subtiles de symétrie (ou géométrie) de l'$Au_{144}(SR)_{60}$. Nous avons montré que l'addition de cuivre n'induit pas le développement de résonance proéminente, plasmonique ou autre. Les principaux changements sont faibles et consistent principalement en (a) la suppression de l'intensité spectrale dans la gamme comprise entre 2,0 et 3,5 eV (620 à 350 nm), et (b) un décalage vers le rouge des caractéristiques spectrales les plus basses. De plus, nous avons démontré que les changements faibles mais visibles liés à l'insertion d'un unique atome de cuivre dans la lacune centrale de l'$Au_{144}(SR)_{60}$ pur sont presque entièrement dus à l'effet géométrique de l'insertion du cuivre et non à la différence chimique entre le Cu et l'Au.

Les résultats ne dépendent que très peu des détails du modèle structurel, de la nature du groupement « rest » (de repos) utilisé pour le ligand ou des approximations utilisées dans les calculs. Ceci permet de conclure de façon générale que l'alliage avec le cuivre *ne crée pas* de résonances plasmoniques dans les clusters d'or dans cette gamme de taille (autour de 1,8 nm) où les spectres ne montrent pas encore de LSPR claire. Ces résultats signifient que les expériences dans lesquelles le développement d'un pic de type LSPR a été observé ne peuvent pas être expliquées par l'hypothèse que l'insertion de cuivre modifie la réponse optique en induisant une résonance plasmonique. D'autres hypothèses devront être explorées afin d'obtenir une compréhension fondamentale des effets mis en jeu dans les expériences.

Contents

Acknowledgements **i**

Abstract | Résumé | Sumario **iii**

Résumé Substantiel **v**

1 General Introduction **1**
- 1.1 Historical Introduction . . . 1
- 1.2 Application of Surface Plasmon and Localized Surface Plasmon . . . 2
- 1.3 Bibliography and State of The Art . . . 4
  - 1.3.1 Plasmons . . . 4
  - 1.3.2 Clusters and Localized Surface Plasmons . . . 5
  - 1.3.3 Realization of LSPR In Different Size Ranges . . . 6
    - 1.3.3.a Different Sizes Manifest Different Physical Effects . . . 6
    - 1.3.3.b Description of Intermediate-size Clusters . . . 8
- 1.4 On This Thesis . . . 9
  - 1.4.1 Objectives . . . 9
  - 1.4.2 Organization of the Thesis . . . 10

2 Classical Approaches **13**
- 2.1 The Framework of Classical Electrodynamics . . . 13
  - 2.1.1 Classical Description of LSPR . . . 14
    - 2.1.1.a Spherical geometry . . . 14
    - 2.1.1.b Ellipsoidal geometry . . . 16
  - 2.1.2 Dielectric Function . . . 17
    - 2.1.2.a Lorentz–Drude model . . . 17
- 2.2 Dispersion Relations of Different Types of Electromagnetic Modes . . . 20
  - 2.2.1 Surface plasmon polariton . . . 20
    - 2.2.1.a LSPR as confined dipolar SPP . . . 22
  - 2.2.2 Bulk plasmons . . . 23
    - 2.2.2.a Transverse solution: Bulk plasmon polaritons . . . 23

2.2.2.b Longitudinal solution: Longitudinal volume plasmon 24
2.3 Nonlocal Optics 26
2.3.1 Hydrodynamic model 27
2.3.1.a Hydrodynamic equation of motion 27
2.3.1.b Electromagnetic response 28
2.3.2 Nonlocal Effects On SPP Dispersion 34
2.3.3 Local analogue model (LAM) 36

3 *Ab initio* Theoretical Framework 39

3.1 Recapitulation of DFT 39
3.1.1 Hohenberg-Kohn Theorem 40
3.1.1.a Many electron Hamiltonian 40
3.1.1.b Theorem I 41
3.1.1.c Theorem II 41
3.1.2 Kohn-Sham Scheme 42
3.1.2.a Solving Kohn–Sham equations self-consistently 47
3.1.2.b Intricacies in Kohn–Sham DFT 48
3.1.3 Approximate XC Functionals 49
3.1.3.a Orbital-dependent functionals 51
3.1.4 Pseudopotential Description 52
3.2 Time-Dependent Density-Functional Theory 55
3.2.1 Runge-Gross Theorem 55
3.2.1.a Intricacies and limitations of the Runge–Gross theorem 57
3.2.2 Time–Dependent Kohn–Sham Scheme 58
3.2.2.a Time–dependent v-representability problem 58
3.2.2.b van Leeuwen theorem 59
3.2.2.c Time–Dependent Kohn–Sham (TDKS) equations 59
3.3 Using the TDKS Equation in Practice 61
3.3.1 Adiabatic Approximation 62
3.3.2 Solving the TDKS Equations Self-consistently 63
3.4 Linear Response Theory and TDDFT 64
3.4.1 General Framework of Liner Response 64
3.4.2 Linear Response of Kohn–Sham System 66
3.4.2.a xc kernel 68
3.4.2.b Casida formalism 70
3.5 Real-Time TDDFT 71
3.5.1 Optical Absorption Spectrum 71
3.5.2 Delta Kick Perturbation 73
3.5.2.a Electric field with delta impulse in time 74

3.6 RT-TDDFT versus LR-TDDFT Casida method 77
3.7 *Ab Initio* Simulations 78

4 Results: Absorption 79
4.1 Introduction 79
4.1.1 Numerical Details 79
4.1.1.a *Ab Initio* Simulations 79
4.1.1.b Classical Simulations 80
4.2 Equivalent Geometries 80
4.3 147-atom Quasi-Spherical Clusters of Ag & Au 85
4.3.1 Electromagnetics Simulations 86
4.3.2 TDDFT Simulations Using Laser 87
4.4 Elongated Clusters of Ag & Au : Rods & Chains 90
4.4.1 Rods vs Icosahedra 90
4.4.2 Classical vs TDDFT in Rods 91
4.4.2.a Effect of AR and absolute size on spectral shifts 93
4.4.3 Classical vs TDDFT in Chains 96
4.4.3.a LSPR in Quasi-one-dimension 96
4.4.3.b Plasmon–electron-hole Coupling in Au Chains 97
4.4.4 Aspect Ratio & Absolute Size Dependence 99
4.4.4.a Blue-shift with Increasing Absolute Size at High Aspect Ratio . 100
4.4.5 GGA In Describing The *Ab Initio* Spectra For Low-AR Systems (rods) . . 102

5 Results: Induced Density 105
5.1 Introduction 105
5.2 Induced Densities at LSPR in Elongated & Compact Ag Systems 107
5.2.1 *Cross-section-integrated* Induced Density from TDDFT 107
5.2.2 *Cross-section-integrated* Induced Density from Electromagnetics 108
5.2.3 Comparison of *Cross-section-integrated* Induced Density from Electromagneticsn and TDDFT 108
5.2.3.a Ag_{19}: Consequences of XC-functional 111
5.2.3.b Ag_{19}: Effect of d-electron description 111
5.3 Induced Density at LSPR: δ-kick vs QMLE 112
5.3.1 Dynamic Screening by the d-electrons in Noble-Metal Clusters 113
5.4 Spatially Resolved Fourier Transform Of The Induced Density 114
5.4.1 Reconstruction Of Modes 115
5.4.2 Modes in an Atomic Chain: Na_{20} 116
5.4.3 Modes in Compact Icosahedral Na_{55}^{+} 117
5.4.3.a Resolution of The Mode 119

5.4.4 Modes in Ag_{37} Rod . . . 121
    5.4.4.a Modes at LSPR . . . 122
    5.4.4.b Static response of the induced density . . . 123
5.5 Absorption in Ligand-Protected $Ag_{29}P_4S_{24}C_{144}H_{108}$ . . . 124
5.5.1 Spatial Localization of Modes at Different Energies . . . 125
    5.5.1.a Low-energy Mode Confined To The Core . . . 125
    5.5.1.b Mode Spread Around The Ligands . . . 126

6 Absorption in Nano-Alloys of $\approx$1.8 nm Bimetallic Au-Cu Clusters 129
6.1 Nano-Alloys . . . 129
6.2 Thiolate Protected 144-atom Au Cluster Compound . . . 130
6.2.1 Alloying $Au_{144}(SR)_{60}$ With Copper . . . 130
6.3 Absorption spectra . . . 131
6.3.1 Different Technical Aspects . . . 131
6.3.2 Bare icosahedral 147-atom clusters . . . 133
6.3.3 Ligand-covered 144-atom clusters . . . 139
    6.3.3.a One copper atom . . . 142
6.4 Dynamical polarizability and induced density . . . 143
6.4.1 Density Dynamics: . . . 147
6.5 Conclusions . . . 147

7 General Conclusions and Perspective 149
7.1 English Version . . . 149
7.1.1 Performance of Classical Electromagnetics for Quantum Systems . . . 150
    7.1.1.a Aspect-ratio dependence of LSPR in sub-nanometric rods . . . 151
    7.1.1.b Subtle effects of size on the aspect-ratio dependence of LSPR . 152
    7.1.1.c Interplay between plasmon and d-electrons in Au-chains . . . 153
7.1.2 Near-field Characteristics of the Excitations . . . 153
    7.1.2.a Induced Charge Densities at LSPR . . . 153
    7.1.2.b Need for the better exchange-correlation functional . . . 154
7.1.3 Modes of Induced Density at Different Energies . . . 154
7.1.4 Effects Of Alloying . . . 155
7.1.5 Perspectives . . . 156
7.2 Versión en Español . . . 160
7.2.1 Aplicación del Electromagnetismo Clásico en Sistemas Cuánticos . . . 161
    7.2.1.a Dependencia de las LSPRs en la AR de barras metálicas . . . 162
    7.2.1.b Efecto sutil del tamaño en la dependencia las LSPRs en la AR . 163
    7.2.1.c Interrelación entre LSPRs y electrones d en cadenas de oro . . 163
7.2.2 Características de las Excitaciones en el Campo Cercano . . . 164

7.2.2.a Densidades de Carga Inducida por LSPRs 164
7.2.2.b Necesidad de un funcional de cambio y correlación mejorado . 164
7.2.3 Densidades de Carga Inducida a Diferentes Energías 165
7.2.4 Efectos debidos al aleado 166
7.2.5 Perspectivas 167

A Proof of Runge–Gross Theorem **171**

B Surface Plasmon Polaritons (SPP): From Maxwell's Equations **177**

C Hydrodynamic Equation of Motion **183**

D Working Principle Of LAM **187**

E Jellium Description **197**

Bibliography **199**

List of Figures **217**

List of Tables **221**

Symbols, Physical Constants, and Abbreviations **223**

Publications **225**

Chapter 1

General Introduction

Noble metals are undoubtedly an indelible part of the history of human civilization. The plethora of their contributions to the civilization ranges from their uses as ‘the’ materials for coinage, jeweleries, medallions, to their effervescent uses in nanometric pieces, in present day science, which is the context of this thesis. The physical properties of noble metal nanoparticles differ from bulk metallic properties in many respects. In this thesis, we study the optical properties in noble metal particles having nanometric and subnanometric dimensions.

1.1 Historical Introduction

Historically, noble-metal nanoparticles, mostly gold, were employed as colouring agents. An outstanding example of such colouring is the Lycurgus cup which dates from probably the 4th century AD and is shown today in the British Museum. The presence of gold and silver nanoparticles, typically of the order of 50 to 100 nm, endows the glass with a surprising dichroism: in reflection, the cup appears green, while when lighted from behind, it appears red [14]. In some of the medieval brilliantly coloured stained-glass church windows, noble metal nanoparticles are likewise at play.

Polychroism of Colloidal Gold Nanoparticles. The physics behind the colour of a substance is the absorption and re-emission of light by the material of that substance. The absorption and re-emission of light depend on its wavelength. In bulk form gold and copper have low reflectivity at short wavelengths, whereas yellow and red are preferentially reflected, making them appear in those colours. Silver has good reflectivity in the visible that does not vary with wavelength, and therefore appears very close to white. However, in nanometric clusters and nanoparticles absorption depends of several parameters, namely, size, shape, chemical composition & configuration, and the nature of the surrounding environment. Thus the same noble metal can give rise to different colours. Ranging from ruby red to blues to black and finally to clear and colorless, nanoparticles of gold in solutions may exhibit a wide range of colors. Also, gold can be colored blue, brown, and black, by creating surface oxide layers using some metal, like iron. A collection of blue gold "Hearts" is presented by jeweler Ludwig Muller of Switzerland [15]. Although these colouring effects of noble metals were known since ages the real reasons behind those were not sought for until the 19th century.

It was Michael Faraday who accidentally created a ruby red solution while mounting pieces of gold leaf onto microscope slides in his laboratory at the Royal Institution. He later determined the composition of the 'ruby' gold [16] which was sought for long time. In 1898, Richard Adolf Zsigmondy prepared the first colloidal gold in diluted solution [17]. The rigorous physical understanding of the properties of metal nanoparticles started later on in the 20th century, based on classical electrodynamics. Building on the works of L. Lorenz and J. C. M. Garnett, Gustav Mie published in 1908 his famous article [18] "*Beiträge zur Optik trüber Medien, speziell colloidaler Metallösungen*" ("Contribution to the optics of turbid media, particularly of colloidal metal solutions") in *Annalen der Physik*. Using classical electrodynamics, i.e., the solutions of Maxwell's equations, his seminal work calculates the scattering of an electromagnetic plane wave by a spherical metal particle. It became so influential that even today, the (localized) surface plasmon, the most prominent optical phenomenon observed in metallic nanoparticles, is often referred as Mie plasmon.

1.2 Application of Surface Plasmon and Localized Surface Plasmon

The panorama of the present-day use of noble-metal nanoparticles and clusters comprises the fields of medicine, biological researches, and physical-chemistry-based applications. Noble-metal nanoparticles and clusters are preferred for these applications because of their chemical inertness and the ability to support surface plasmon resonances (SPRs) in the visible, in contrast to most of the more reactive simple-metal clusters, where LSPRs occur in the near-infrared. In addition, in nanometric-size noble-metal clusters, localized surface-plasmon resonances (LSPRs) give rise to orders-of-magnitude enhancement of electromagnetic fields, concentrating energy around them into nanometric or even sub-nanometric regions. This energy can be used for thermal, catalytic and radiative applications. The heat generated by highly confined electromagnetic energy at LSPR in spherical gold nanoshells are reported to be used in cancer therapy (photothermal ablation therapy [PTA]), in order to ablate tumor cells [19]. Gold nanoparticles and clusters are equally used in several other biomolecular applications in specific fields which include bioconjugation chemistry [20], protein tagging [21], biomolecule labeling [22], inhibition of HIV fusion [23], growth inhibition of bacteria [24], etc.

Using electron beam lithography and atomic force microscopy, plasmonic arrays of large gold nanoparticles have been reported to be capable of guiding and controlling highly confined electromagnetic energy [25]. These nanometric plasmon waveguides can be used to build nanoscale optical devices of lateral sizes well below the diffraction limit [26, 27]. Noble-metal nanoparticles of varying sizes have been also reported to enhance the performances of solar cells [28–30]. A field of extraordinary activity, governed by surface-plasmon resonances, is nanoplasmonics. It's applications, nanometric antennas, apply the coupling between light and nanometric metal structures. Here, surface plasmons are of paramount importance. Connected with nanoplasmonics are the realized and envisioned metamaterials in which optical resonators are distributed in such a way as to produce a novel material with novel optical properties exciting new prospects for manipulating light [31].

In molecular level spectroscopic techniques, chemical detections can be achieved through the detailed information on the vibrational levels of the molecules, obtained from Raman signals which depend of the strength of the local electromagnetic field. Extremely precise detection of single or a few molecules can be achieved, when the field strength is million-fold enhanced by the localized SPRs in sub-nanometric regions, as done in surface enhanced Raman spectroscopy (SERS). This technology has been used in understanding the complex environment inside living cells [32], and also applied to other chemical detections [33, 34]. The LSPR frequencies of nanoparticles depend on the frequency dependent dielectric function of the noble-metal, the size and shape of the nanoparticles, and the dielectric function of the surroundings of the particles. Thus, monitoring the spectral changes, and controlling the size and shape of the nanoparticles, allow to detect the changes in the surrounding medium in biomolecular sensing and labeling [35–37].

Finally, it is well known that gold clusters and nanoparticles are catalytically active [38], unlike the rather inert bulk material. In addition to the direct catalytic effect, photocatalysis is also possible with noble metal clusters. Several mechanisms are presently discussed for this possibility [39–41]. Most of these concepts rely on the excitation of electron-hole pairs using the SPR, and their subsequent transfer to a substrate like, e.g., TiO_2 [42, 43]. Direct mechanisms, in which the excitation of an SPR aids the catalytic processes directly on the nanoparticle are likewise envisaged. In general, the photocatalytic activity is due to a highly complex combination of different mechanisms and far from being completely understood. In the study of catalytic mechanisms, and in general of the nanoparticles involved, spectroscopic measurements are a main source of information. Thus even for the nanoparticles which are not used for their optical properties, the knowledge of their optical response contributes important pieces of information to their study.

1.3 Bibliography and State of The Art

Localized surface-plasmon resonance (LSPR) in noble-metal clusters is the particular optical phenomenon that this thesis is centered around. In order to theoretically understand the effects of different physical and chemical phenomena on it, both the classical electrodynamics and the *ab initio* quantum mechanical approaches are used. The term 'plasmon' in general refers to collective oscillation of interacting mobile charges. Though our focus in this thesis is LSPRs, in order to contextualize, it is customary to briefly talk about different light-matter interactions that can excite collective oscillations in metallic systems.

1.3.1 Plasmons

Depending on different lenghth scales of the systems, and on the mode of excitations, different kind of plasmons are observed, namely, bulk plasmon polaritons, longitudinal bulk plasmons, surface plasmons, and localized surface plasmons. Collective excitation in a plasma, i.e., a system of mobile charged particles, were first investigated by Langmuir and Tonks [44–46], in strongly ionized gases at low pressure. The frequency of oscillations of the electrons in the plasma, about their equilibrium positions, were found by Langmuir to be in accordance with the 'plasma frequency' proposed by Drude in his electromagnetic theory of metals [47].

In metals, experimental observation of plasmon occurred in electron energy loss experiments, performed by Ruthemann [48] in 1942. The explanation of these experiments and many other inelastic electron scattering experiments [49, 50], came in the 1950s by the seminal works of Bohm and Pines, based on a rigorous many–body theoretical approach [51–53]. Their theory suggested that the energy losses experienced by fast electrons while passing through metals are due to the excitation of collective oscillations of the valence electrons in metals, similarly as observed in plasmas by Langmuir. They termed the basic unit of energy associated with this collective excitation as plasmon : $\hbar\omega_p = \hbar\sqrt{(4\pi n_e e^2/m_e)}$, where n_e is the density of valence electrons and m_e is the mass of an electron [54].

While investigating the impact of the boundaries in metallic thin films on the collective excitations described by Bohm & Pines, in 1957, R. H. Ritchie found that a new excitation can appear at a lower energy, corresponding to the collective oscillation at the boundary of the surface [55]. The experimental confirmation of this theoretical finding was made by J. C. Powell and J. B. Swan in characteristic electron energy-loss experiments on Al [56]. The name 'surface plasmon' was introduced by E. A, Stern and R. A. Ferrell for the quantum of these surface plasma oscillations at the interface between plasma and vacuum [57], the frequency of which they found to be $\omega_p/\sqrt{2}$, in accordance with Ritchie's frequency (in nonretarded limit).

In Ritchie's theory, the surface plasmon frequency shows a dispersive nature having a dependence on the wave vector. Following these findings, the coupling of electromagnetic radiation with the surface plasmons have been investigated particularly in metal films [58–62]. For the nonretarded surface plasmon, different theoretical approaches were used to understand the dispersion. Kanazawa was the first to obtain a quantum mechanical derivation of the dispersion relation using Bohm-Pines random-phase approximation (RPA), which simultaneously accounted for the bulk plasma oscillation [63]. Following this, in 1963, Ritchie proposed the "*hydrodynamic electron theory*" [64] based on Bloch's work [65], in order to explain plasmon dispersion in a simple manner. He demonstrated that the dispersion of plasmons (both volume and bulk) depends on the characteristic velocity (β) of propagation of the oscillations in the plasma. Comparing with the theory of Bohm and Pines, he found this velocity to be equal to $v_F\sqrt{3/5}$, where v_F is the Fermi velocity. While Ritchie's approach was semi-classical, an RPA-based fully quantum mechanical approach for getting the dispersion of surface plasmons was done by Beck [66].

1.3.2 Clusters and Localized Surface Plasmons

A cluster is an aggregate of a number of objects. In material science, clusters are nanometric or subnanometric multi-atom particles which are composed of a certain number of atoms, ranging from two to a few multiples of 10^7. Thus, a cluster is intermediate between an atom (or molecule) and the bulk [67]. Therefore, knowing the properties of clusters helps to know the transition of the atomistic properties of a material to its bulk properties with increasing size, or in other words, the gradual development of the physics from quantum mechanical regime to classical regime.

In describing the optical properties of clusters, the Mie theory appeared to be inadequate due to its inability to give physical insights into the material properties concerning the motion of the electrons inside the metal particles or of discrete eigenstates. In 1960s, while the experimental and theoretical investigations on surface and bulk plasmons in metallic thin films attracted most of the research attention in material science, the development of cluster science also began mostly towards the direction of understanding the interaction of electromagnetic fields with small metal particles beyond Mie's theory. The variation of electric polarizability and thus absorption with varying frequency of electromagnetic fields in 'minute' metallic particles was studied by Gor'kov and Éliashberg [68]. Excitation of plasma oscillation due to fast electrons passing through spherical electron gas was theoretically investigated by Fujimoto and Komaki [69]. Surface plasma resonances in spherical particles of silver and gold having sizes $\lesssim$ 100 nm were first experimentally observed by Kreibig and Zacharias in electron energy loss experiment [70],and thus localized surface-plasmon resonance (LSPR) started to gain researchers' interest. Efforts were made to modify Mie theory and also to go beyond it, by considering the effect of spatial dispersion on scattering and absorption in small metal spheres [71–78]. Many of these works considered the hydrodynamic description of conduction band electrons, and brought into notice the importance of longitudinal electric field modes in properly describing the optical properties of small metallic systems.

Cluster science started to advance remarkably after the experimental findings of Knight et al. They measured alkali metal clusters having < 100 atoms and found abundance of clusters having number of atoms (and thus, valence electrons), N = 8, 20, 40, 58, and 92, that follow spherical shell-closing [79], a purely quantum-mechanical effect. At the same time, quantum mechanical calculation of the absorption in spherical metal clusters, based on random-phase-approximation (RPA) for the density response function, was proposed by W. Ekardt using a jellium description for the valence band electrons [80]. Using RPA or time-dependent local density approximation (TDLDA), the jellium model has become significantly successful in describing collective optical responses in clusters of simple metals [81–83] and noble metals [84, 85], consisting of a few to hundreds of atoms and also was applied to systems having thousands of atoms [86] to discover electronic shell structures in them.

1.3.3 Realization of LSPR In Different Size Ranges

In present-day scenario, clusters are sub-categorized depending on their size, physical effects on them, and also on the requirements of suitable theoretical approaches in order to describe those effects properly. The specialty that physically makes the clusters behave differently than bulk is the increased surface-to-volume ratio. As we go down in size, quantum mechanical effects come into play, significantly modifying the optical responses in them.

1.3.3.a Different Sizes Manifest Different Physical Effects

Large noble-metal clusters, having sizes $\gtrsim 10nm$, can be considered as charge density distributions, optically characterized by bulk dielectric functions, and confined within abrupt boundaries which are separated from the surrounding dielectric. Localized surface-plasmon resonances (LSPR) in these large clusters are then understood as collective optical response of the charge densities, giving rise to smooth broadened peak in their absorption spectra, as can theoretically be found within the framework of classical electrodynamics [87–89]. The effects of size, shape and alloying on noble-metal clusters in this size limit are well studied and understood using different classical models, e.g., discrete-dipole approximation [90, 91], within the electromagnetics framework. The LSPR at and above this size and within the dipolar size limit shows no size-dependent shift in spectral position. However, it can shift depending on the geometrical shape. For instance, LSPR is red-shifted in an ellipsoidal geometry as compared to its appearance in a spherical geometry having the same volume. The strong red-shift with increasing aspect ratio of elongated structures is well captured by electromagnetics calculations.

Very small clusters, made up of **a few or a few tens of noble metal atoms**, are molecule-like systems and thus, have atomistic resolution which does not permit to consider them as smooth homogeneous charge distributions within well-defined abrupt classical boundaries. They can only be properly comprehended as many electron system bound by the ionic potential, thus having discrete electronic structure describable by quantum mechanics. Therefore, the absorption spectra of these small clusters consist of discrete peaks, characterizing individual transitions between different quantum-mechanical levels. Many of these peaks, or an ensemble of them, are represented as reminiscent of the LSPR [92]. Theoretically, clusters of this size range are treated using quantum-chemistry methods. *Ab initio* optical spectra of very small clusters were first calculated in the framework of configuration interaction (CI) or, in the linear response equation-of-motion coupled-cluster (EOM-CC) methods [93, 94].

Intermediate-size noble-metal clusters are the ones whose size range falls in between the size ranges of the large ones ($\gtrsim 10\ nm$) and the very small ones (having $\lesssim 50$ atoms). They are of particular interest because the optical absorption in them, on one hand can still show the reminiscence of the collective classical charge density oscillation: the signature of classical dipolar LSPR, while on the other hand, the atomic structure and quantum mechanical effects start to influence their absorption spectra. One of the interesting physical phenomena in the intermediate-size clusters having size $< 5\ nm$ is the size dependence of the LSPR frequency. In the case of noble-metal clusters in vacuum, a blue shift of the LSPR frequency is observed with decreasing size [8, 9, 95–98], whereas in alkali-metal clusters a red shift [99, 100] is observed for the same size effect. While classical local optics can still qualitatively describe the plasmon (if any) in the absorption spectra of many of the clusters (specially of the alkali metals) falling in this size range, the proper explanation of the size dependence of the surface plasmon in alkali- and noble-metal clusters (of this size-rang) is given by quantum mechanics [101]. There are primarily two quantum effects that need to be taken into account, in order to properly understand the size-dependence of LSPR. These are the *spill-out* of the electron density of the conduction s electrons, which invalidates the concept of abrupt classical boundary for the cluster surface; and second, the reduced screening of the plasmon at the surface of the noble-metal clusters, created by the d-electrons localized to the core of the clusters. The presence and the interplay of these two counteracting quantum mechanical effects produce the respective size dependence (red shift in alkali-metal clusters and blue shift in noble-metal ones), because the surface region becomes more important when the size goes down. Apart from the shift of the LSPR peak, the effect of decreasing the size also causes fragmentation of the LSPR peak [102].

The optical spectra and in particular the presence and appearance of the LSPR depend strongly on the coupling with the so-called interband transitions from the d-electrons. For compact (icosahedral/spherical) shapes, where the LSPR can occur in the visible, the coupling between LSPR and interband transitions make the absorption spectrum of a gold cluster entirely different from that of a silver cluster. This is because of the difference in the onset of the interband transitions: ∼2eV in gold and ∼4eV in silver [10]. Due to this difference the absorption spectra of silver clusters smaller than ∼150 atoms still show strong resonances in the visible, whereas, for gold clusters of the same sizes, no LSPRs are observed in the spectra [103].

The LSPR energies and, therefore, the degree of coupling with the interband transitions can be strongly influenced by the geometrical shape of the intermediate-size clusters. The strong red-shift of the LSPR energy, mentioned above for the large noble-metal clusters, also occurs at this size-range. In elongated gold clusters, this red-shift can shift the LSPR energy below the onset of the interband transitions, thus decoupling the LSPR from the interband transitions. Consequently, the response of high-aspect-ratio gold clusters becomes similar to that of the corresponding silver structures: appearance of a well-defined LSPR, almost at the same energy in the infrared [104].

1.3.3.b Description of Intermediate-size Clusters

The properties of clusters depend on their surrounding and surface/interface structure. Over the last decades, the synthesis and the characterization of very small clusters in gas phase [105–107], and on rare-gas matrices [108] have been vastly reported in the literature. In this thesis the focus is made on noble-metal clusters falling in the intermediate-size range. In addition, small and intermediate-size noble-metal clusters are often wet-chemically synthesized [109], which leads to atomically precise clusters stabilized by a shell of ligands. Recently, the geometries of many of these clusters have been determined experimentally. Also, the effects of alloying [11–13, 110, 111] on the optical properties have been studied, as well as of shape [112, 113], and of details of the ligand environment [114].

While significant advancements have been made in experimental findings [115], revealing various novel observations on the optical properties of intermediate-size noble-metal clusters [116], the complete theoretical understanding for many of those findings are yet not achieved. The reason is that the clusters belonging to this size range have not been accessible to atomistic calculations until recently. Transition-based quantum mechanical calculations (e.g., CI or EOM-CC) for these intermediate-size noble-metal clusters appear to be cumbersome and computationally expensive, if not undoable. For this size range, *ab initio* time-dependent density-functional theory (TDDFT) calculations are the methods of choice, and are employed to give the best possible explanations of the experiments [117]. In these calculations, the interaction of the electrons with the ion cores is described either using the jellium model [80, 85], pseudopotential description [118–122], or the projector augmented wave

(PAW) method [123–126]. While calculations using jellium model are employable for noble-metal clusters having a wide range of size (from 50 atoms to 5000 atoms), calculations using pseudopotential descriptions and/or the PAW method are expensive and limited to clusters having smaller size ($\approx$ upto 500 noble-metal atoms). These TDDFT calculations for obtaining the optical spectra are of two types: (i) real-time TDDFT (RT-TDDFT) calculations within the linear response regime, and (ii) transition-based linear-response TDDFT (LR-TDDFT) calculations. While LR-TDDFT is advantageous as it gives directly the nature and origin of the optical excitations in the spectrum, RT-TDDFT is preferred for being computational economic because empty states need not be calculated.

In search of theoretical frameworks that can substitute the computationally demanding *ab initio* calculations, quantum-mechanics-aided classical nonlocal optics calculations have been reported in the literature [127–129] in order to calculate the optical response of the intermediate-size clusters. In addition, nonlocal optics calculations based on a hydrodynamic description [130–132] of the s-electrons have been reported in good agreement with *ab initio* calculations, particularly in explaining experiments by taking into account quantum mechanical tunneling effects [133, 134].

1.4 On This Thesis

This thesis is a theoretical research work on understanding the optical phenomena in noble-metal clusters, having nanometric and/or sub-nanometric dimensions, using *ab initio* and classical simulations. The classical simulations are done within the electromagnetics framework in frequency domain using the finite element method. The *ab initio* simulations are performed using real-time TDDFT (RT-TDDFT) in a real space description. Following the objectives, the organization of the thesis is described in this section.

1.4.1 Objectives

- In order to understand the optical behaviour of large ($>$ 10nm in size) noble-metal cluster, elctromagnetics-based theoretical approaches are widely used. For obtaining the optical response in intermediate-size noble-metal clusters, *ab initio* TDDFT calculations are well established as the methods of choice. As stated in 1.3.3.b, electromagnetics-based classical nonlocal optics calculations are also used for intermediate-size noble-metal clusters, as have been elctromagnetics-based theoretical approaches that take into account the quantum mechanical effects phenomenologically. These calculations aim to describe the intermediate-size range normally treated using TDDFT. But they have not been sufficiently tested and verified, leaving a number of questions open, in particular the following:

  - Up to what physical extent, the occurrence of LSPRs and their dependence on shape and size, for intermediate-size noble-metal clusters, can be understood as the dipolar LSPRs described within electromagnetics?
  - What physical parameters determine and control the accuracy of this understanding?
  - The quantum mechanical effects, that arise from the atomistic inhomogeneity and *spill out* of electron density, transitions from discrete and localized d-electron states, are apparent in intermediate-size noble-metal clusters. Can the effects of these on LSPR be recovered by the nonlocal corrections to the local classical optics?

  A substantial part of this thesis is devoted to respond to these questions by comparing the performances of *ab initio* TDDFT-based and electromagnetics-based theoretical approaches.

- The near-field characteristics of the LSPR are reflected in the spatial distribution of the induced charges and fields in and around the system of interest. In RT-TDDFT calculations, the time–dependent induced density contains the contributions corresponding to all the excitations (LSPR, interband transitions, and their coupling) present in the absorption spectrum. A part of this thesis is dedicated to explore the spatial character of the modes of induced densities at different energies of interest. To this end, we perform spatially resolved time-to-frequency-domain Fourier transform of the time–dependent induced density obtained in RT-TDDFT calculations. In particular, the effect of dynamic screening of the d-electrons on the LSPR, and the coupling between LSPR and interband transitions are studied.
- Studies on the effects of alloying and ligands in bi-metallic ligand-protected clusters has brought in surprising observations, many of which is yet not theoretically understood. One of these observations is the appearance of strong plasmon-like features in the absorption spectra of $\mathrm{Au}_{(144,145)-x}\mathrm{Cu}_x(\mathrm{SR})_{60}$ alloy clusters [11, 12], despite the absence of plasmonic character in clusters of Au and Cu of the same size. A part of the thesis is devoted to obtain theoretical insights into this particular phenomenon, by performing TDDFT calculations.

1.4.2 Organization of the Thesis

The content of the thesis is organized in the following way, where the description of the theoretical methods precedes the presentation of the results. In the second chapter, a description of different types of plasmons, and the realization of LSPR in local and nonlocal optics using Maxwellian classical electrodynamics is discussed, accompanied by the specific techniques used to incorporate them in the simulations. The third chapter consists of the discussion of *ab initio* density functional-based theories, the framework of linear response theory, and the implementation of them in real-time simulations. The next three chapters present the work done and the results obtained. The fourth chapter talks about the LSPRs in intermediate-size noble-metal clusters (mainly of Ag and Au), in terms of electromagnetic absorptions, using both classical and *ab initio* simulations. The dependence of LSPR on the size and the shape of the clusters, and the manifestations of different quantum mechanical effects on LSPR are analyzed, and the results are interpreted to assess the performances of different theoretical approaches, in properly describing the optical responses in the corresponding systems. In chapter five, using both the classical and *ab initio* approaches, the near-field characteristics of the optical response in intermediate-size noble-metal clusters (of Ag and Au), at different frequencies (mainly at LSPR) are investigated by studying the spatial behaviour of the charge densities induced at corresponding frequencies. While chapters four and five are interrelated, giving a comprehensive analysis of the optical response in clusters, from classical and *ab initio* theoretical approaches, the sixth chapter is independent, in the sense that it addresses optical absorptions in a specific type of bimetallic ligand-protected clusters, $\mathrm{Au}_{(144,145)-x}\mathrm{Cu}_x(\mathrm{SR})_{60}$, and deals with the *ab initio* investigations on understanding the dubious emergence of LSPR-like features in their experimental absorption spectra. The general conclusions of the works performed in this thesis and the perspectives are discussed in the seventh chapter.

Chapter 2

Classical Approaches

In this chapter, optical response of metal clusters from classical electrodynamics point of view is discussed. The most noticeable optical character of noble metal clusters is localized surface plasmon resonances (LSPR). Realization of dipolar LSPR in classical electrodynamics and the effect of dispersive dielectric constant on it within the hydrodynamic model are discussed here.

2.1 The Framework of Classical Electrodynamics

Dipole approximation: Within the framework of classical electrodynamics optical excitations are electromagnetic waves interacting with a charge distribution. For an isolated metal clusters under plane wave illumination, the charge distribution is a localized one, within a medium having a dielectric constant. As the dimension ($d \sim 3$ nm) of this localized charge distribution is (in general) orders of magnitude smaller than the wavelength ($\lambda \sim 400 - 700$ nm) of the electromagnetic wave, the electric field practically remains constant in space over the charge distribution. Thus, the sole effect of the optical excitation is to induce an electric dipole moment ($\mathbf{p}$) across the charge distribution. All the higher order moments are negligibly small to be discarded. In passing, it is worth mentioning that, if the isolated cluster is excited differently other than using plane electromagnetic waves, for example by electron beams, higher order electric moments do contribute in the optical response, causing hybridization of multipolar plasmons [135].

Quasi-static limit: Of course, the electric field continues to oscillate in time, thus swapping its polarization between $plus$ and $minus$ with the frequency of the electromagnetic wave: $\mathbf{E}(\mathbf{r}, t) = \mathbf{E}_0(\mathbf{r})e^{-i\omega t}$. Within quasi-static approximation, it is assumed that all the temporal derivatives in the Maxwell's equations are much smaller than the spacial ones. Thus, $\mathbf{E}$ and $\mathbf{H}$ fields are decoupled, making the electrodymanics problem simpler, by allowing to deal only with the $\mathbf{E}$ field within the electrostatic framework. One can do so because of the fact that, the spatial extent of the charge distribution (representing the isolated cluster), is much smaller than the spatial extent over which the time–dependent variations of the fields take place. Within quasi-static approximation, the induced dipole moment, therefore, suffers no retardation effect and follows the same temporal dependence as of the electric field: $\mathbf{p}(\mathbf{r},t) = \mathbf{p}(\mathbf{r})e^{-i\omega t}$. Thus, as the temporal dependence does not couple with the spatial one, one can get the dynamical response ($\mathbf{p}(\mathbf{r},t)$) of the charge distribution due to the electromagnetic field, by knowing the static response:

$$\mathbf{p} = \epsilon_0\, \varepsilon_{med}\, \alpha \mathbf{E} \tag{2.1.1}$$

where, α is the static polarizibility. This is the quasi-static approximation, and the size limit upto which this approximation is valid is called the quasi-static limit. In this thesis, as we are dealing with clusters having sizes orders of magnitude smaller than the free space wavelength, λ_0, we are always within this limit.

2.1.1 Classical Description of LSPR

Localized surface plasmons are non-propagating excitation modes of nearly-free electrons in metal clusters and nanoparticles. They are characterized by strong resonance peak (LSPR) in the absorption spectrum which correspond to field amplification both inside and in the near-field zone outside the particles. The free-space propagation of the electric plane wave can be described as,

$$\mathbf{E}_0(\mathbf{r}) = \mathbf{E}_0 e^{i\mathbf{k_0}\cdot\mathbf{r}}, \tag{2.1.2}$$

which can be expanded to give,

$$\mathbf{E}_0(\mathbf{r}) = \mathbf{E}_0\left(1 - i\mathbf{k_0}\cdot\mathbf{r} + \cdots\right) = \mathbf{E}_0\left(1 - 2\pi i(\hat{\mathbf{k_0}}\cdot\hat{\mathbf{r}})\frac{r}{\lambda_0} + \cdots\right). \tag{2.1.3}$$

As, cluster dimension is much smaller than free-space wavelength, $r \ll \lambda_0$, and all the terms involving $(\mathbf{k_0}\cdot\mathbf{r})$ can be discarded. Thus, within the quasi-static limit, one can calculate the absorption cross-section of a cluster by calculating the electric fields inside and outside the cluster, assuming that, the cluster is put in a homogeneous incident electrostatic field $\mathbf{E_0}$. In doing so analytically, one often choses spherical or ellipsoidal geometry for describing the cluster. The frequency dependence is given by the dielectric function ($\varepsilon(\omega)$) which characterize the optical properties of the cluster.

2.1.1.a Spherical geometry

The metal cluster is considered to be a spherical particle of radius a with dielectric function $\varepsilon(\omega)$, and surrounded by a dielectric medium of dielectric constant ε_{med}. The system is illuminated by a electric plane wave $\mathbf{E}(t) = \hat{\mathbf{z}}E_0 e^{i\omega t}$, as shown in Fig.2.1. The field induces an

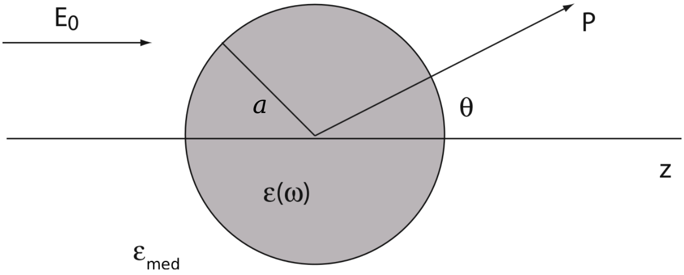

FIGURE 2.1: Courtesy: Ref. [136]. Schematic representation of electromagnetic plane-wave illumination on a system of metallic sphere (representing metallic cluster) in a dielectric medium, in quasi-static limit.

oscillating dipole moment $\mathbf{p}(t) = \mathbf{p}e^{i\omega t}$ which in turn radiates. The field at any point P due to this oscillating dipole is given by [137],

$$\mathbf{E}(\mathbf{r}) = \frac{1}{4\pi\epsilon_0\varepsilon_{med}}\left\{k^2(\hat{\mathbf{n}}\times\mathbf{p})\times\hat{\mathbf{n}}\frac{e^{ikr}}{r} + \Big[3\hat{\mathbf{n}}(\hat{\mathbf{n}}\cdot\mathbf{p})-\mathbf{p}\Big]\left(\frac{1}{r^3}-\frac{ik}{r^2}\right)\right\}, \tag{2.1.4}$$

where, $k = 2\pi/\lambda$, $\hat{\mathbf{n}}$ is the direction of the point P, and r is the distance between the center of the cluster and P. In the quasi-static limit, $kr \ll 1$, and we get,

$$\mathbf{E}^{(near)}(\mathbf{r}) = \frac{1}{4\pi\epsilon_0\varepsilon_{med}}\Big[3\hat{\mathbf{n}}(\hat{\mathbf{n}}\cdot\mathbf{p})-\mathbf{p}\Big]\frac{1}{r^3}, \tag{2.1.5}$$

where, $\mathbf{p}$ is the magnitude of the oscillating dipole moment, the expression of which in non-retarded case is given by solving the Laplace's equation for the system shown in Fig.2.1, as,

$$\mathbf{p} = 4\pi\epsilon_0\varepsilon_{med}\, a^3\, \frac{\varepsilon(\omega)-\varepsilon_{med}}{\varepsilon(\omega)+2\varepsilon_{med}} E_0\hat{\mathbf{z}} \tag{2.1.6}$$

Comparing with eq. 2.1.1, we get the expression for the static dipole polarizability as,

$$\alpha = 4\pi\, a^3\, \frac{\varepsilon(\omega)-\varepsilon_{med}}{\varepsilon(\omega)+2\varepsilon_{med}} \tag{2.1.7}$$

The cross-sections for absorption and scattering corresponding to the field (eq. 2.1.5) generated by the induced oscillating dipole, can be computed through the corresponding Poynting vector [138] as,

$$C_{scatt}(\omega) = \frac{k^4}{6\pi}\,|\alpha(\omega)|^2 = \frac{8\pi}{3}\,k^4\,a^6\left|\frac{\varepsilon(\omega)-\varepsilon_{med}}{\varepsilon(\omega)+2\varepsilon_{med}}\right|; \tag{2.1.8}$$

$$\text{and,}\quad C_{abs}(\omega) = k\,\Im\alpha(\omega) = 4\pi k a^3\,\Im\left\{\frac{\varepsilon(\omega)-\varepsilon_{med}}{\varepsilon(\omega)+2\varepsilon_{med}}\right\}. \tag{2.1.9}$$

For spherical particles having dimension $a \ll \lambda$, the absorption cross-section (which scales with a^3) overrules the scattering cross-section (which scales with a^6). The cross-section spectrum of LSPR is, therefore, given by the absorption cross-section (eq. 2.1.9). In order to obtain the spectrum, the key quantity to calculate is the dipole polarizability $\alpha(\omega)$. From the expression of absorption cross-section eq. 2.1.9, it is apparent that the maximum absorption takes place for the minimum of $\varepsilon(\omega)+2\varepsilon_{med}$. If the imaginary part of $\varepsilon(\omega)$ varies slowly with respect to frequency, then this condition for maximum absorption can be simplified to,

$$\Re\{\varepsilon(\omega)\} = -2\,\varepsilon_{med} \tag{2.1.10}$$

This is known as Fröhlich condition and the frequency at which it occurs is called the dipolar LSPR frequency.

2.1.1.b Ellipsoidal geometry

For elongated nanoparticles and clusters, a reasonably good geometrical representation is an ellipsoid. It is of particular interest for the fact that, one can have analytical expression for the absorption within quasi-static approximation. An ellipsoid is defined by its equation of plane as, $(x/a_1)^2 + (y/a_2)^2 + (z/a_3)^2 = 1$, where $a_1,\ a_2,\ a_3$, are the semiaxes as shown in Fig.2.2. The dipole polarizabilities along the principle axes $(i = 1, 2, 3)$ are given by [138],

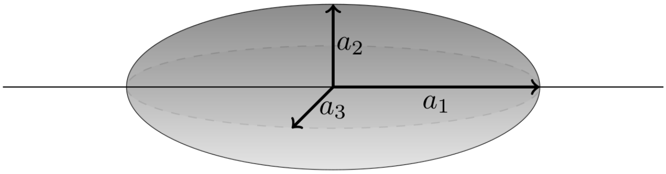

FIGURE 2.2: Schematic representation of an ellipsoid.

$$\alpha_i(\omega) = \frac{4}{3}a_1a_2a_3\,\frac{\varepsilon(\omega)-\varepsilon_{med}}{\varepsilon_{med}+L_i[\varepsilon(\omega)-\varepsilon_{med}]}, \tag{2.1.11}$$

where, L_i is a geometrical factor which satisfies $\sum_i L_i = 1$, and is calculated as,

$$L_i = \frac{a_1a_2a_3}{2}\int_0^\infty dq\,\frac{1}{(a_i^2+q)\sqrt{(q+a_1^2)(q+a_2^2)(q+a_3^2)}}. \tag{2.1.12}$$

The absorption cross-section then can be calculated using eq. 2.1.9.

The analytical expressions discussed above are strictly valid for dipolar LSPR, i.e., when the quasi-static approximation is valid. The general theory of scattering and absorption for spherical particles of larger dimension ($a \sim \lambda$ or $a > \lambda$) was developed by Mie [18] involving rigorous electrodynamic approach. Of course, for particles having sizes within quasi-static limit the Mie theory recovers the same expressions as discussed above.

2.1.2 Dielectric Function

As evident from the quasi-static expression of the dipole polarizability (eq. 2.1.7), the electromagnetic response of the system is completely described by the dielectric function, $\varepsilon(\omega)$. It is the frequency dependence of the dielectric function that characterizes the optical property of a metals, by describing the response of the conduction and valence band electrons, while interacting with an electromagnetic field. There are different models for describing the dielectric function of a metal covering different levels of physical aspects.

Drude's model. The simplest model for dielectric function came from Drude [47], from his description of electronic conduction in metal. Drude's model deals only with the nearly-free conduction-band electrons of a metal and treats them as a plasma of free, noninteracting electrons. A plasma of electrons is a gas of negatively charged particles characterized by their mass m_e and density n_e. Under the effect of an oscillating electric field, the plasma particles respond linearly with a collision frequency γ, which damps their motions. Solving the equation of motion for the noninteracting electrons particles given as,

$$m_e \frac{d^2\mathbf{X}}{dt^2} + m_e\gamma \frac{d\mathbf{X}}{dt} = -e\mathbf{E}, \tag{2.1.13}$$

and relating their displacements ($\mathbf{X}$) to the macroscopic polarization, the Drude's dielectric function is given as,

$$\varepsilon(\omega) = 1 - \frac{\omega_p^2}{\omega^2 + i\gamma\omega}, \tag{2.1.14}$$

where, $\omega_p = \dfrac{n_e e^2}{m_e \epsilon_0}$ is called the *plasma frequency* of metal. Using Drude's model, the optical properties of simple metals, like alkalies, are well explained over a wide range of frequencies.

2.1.2.a Lorentz–Drude model

The simplistic Drude's model for the free electrons is inadequate to describe properly the optical response of noble metals like gold and silver. The reason is in gold and silver, the interband transitions involving the localized d-electrons, which are close to the Fermi level, take place in the visible. A comparison of real and imaginary part of the dielectric function for gold in Drude's model and from experimental observation [139] is shown in Fig.2.3. To take into account the polarization created by the d-electrons, a dielectric constant ε_∞ is incorporated into Drude's model to give,

$$\varepsilon(\omega) = \varepsilon_\infty - \frac{\omega_p^2}{\omega^2 + i\gamma\omega}, \tag{2.1.15}$$

where, usually, $1 < \varepsilon_\infty < 10$.

In order to have a physically insightful analytical expression of the polarization created by the d-electrons in noble metals, that can account for the effects of the interband transitions involving d-electrons, the motion of the d-electrons are modeled by having a number of Lorentz-oscillators in the dynamic equation. Assuming that the binding forces between the localized d-electrons and the nucleus behave likewise as in a spring, the contribution of these forces to the equation of motion of the electronic system is described by adding a number of force terms having different characteristic force constants, i.e., different characteristic frequencies (ω_is):

$$m_e \frac{d^2\mathbf{X}}{dt^2} + m_e\gamma\frac{d\mathbf{X}}{dt} + \sum_{i=1}^{k} m_e\omega_i^2\mathbf{X} = -e\mathbf{E}. \tag{2.1.16}$$

Solving this equation of motion, and relating the displacement ($\mathbf{X}$) to the macroscopic polarization, the contribution from the ith Lorentz oscillator to the dielectric function appears to be,

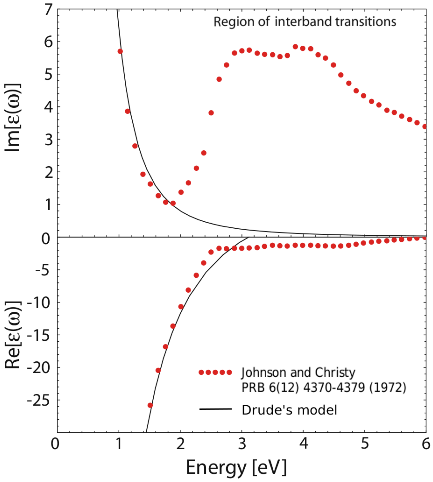

FIGURE 2.3: Courtesy: Ref. [136]. Comparions of Drude's dielectric function and experimental observation of Johnson and Christy [139], for gold.

$$\varepsilon_{i,Lor-osc}(\omega) = \frac{f_i\omega_p^2}{\omega_i^2 - (\omega^2 + i\gamma_i\omega)}, \tag{2.1.17}$$

where, ω_i and γ_i characterize the resonant behaviour of the ith Lorentz oscillator, which must be taken into account for optical excitation at ω_i. The resulting frequency dependent, analytic form of the Lorentz-Drude dielectric function is thus given by consider the contributions of all the Lorentz oscillators:

$$\varepsilon(\omega) = 1 - \frac{\omega_p^2}{\omega^2 + i\gamma\omega} + \sum_{i=1}^{k} \frac{f_i\omega_p^2}{(\omega_i^2 - \omega^2) - i\gamma_i\omega}. \tag{2.1.18}$$

There are also other models [140, 141] and extensions to the Lorentz-Drude model, in order to better describe the electromagnetic response of the noble metals. In this thesis, we have used a fitted [140] Lorentz-Drude dielectric function for gold and silver. The fitting give accurate description of the bulk optical properties of gold and silver upto 5 eV, when compared with experimental results of Johnson and Christy [139] .

Remark:

It is instructive to observe that, the absorption given by eq. 2.1.9 with the dielectric function for a noble metal, given by eq. 2.1.18, does not show any size dependence, except accounting for the strength of the absorption. All the spherical particles of the same noble metal, that fall in the quasi-static size limit, give the same frequency dependence in the strength/volume-normalized absorption spectrum. However, if the geometrical shape is changed, keeping the volume unaltered, the corresponding effect on absorption is obtained. Thus, the aspect-ratio dependence of the LSPR within quasi-static size limit is qualitatively well described using the model dielectric functions (eqs.2.1.14 & 2.1.18) discussed here. For the description of size-dependence of LSPR, one needs to consider spatially dispersive dielectric function, discussed later in this chapter. The detailed discussion on the absolute size dependence of LSPR is done in Chapter 4.

2.2 Dispersion Relations of Different Types of Electromagnetic Modes

In order to better understand the optical properties of metal clusters, a brief description of different electromagnetic excitations in different length-scales of a metallic system is given in this section. This concerns with three fundamental, yet physically different types of oscillating modes of conduction band electrons in metal. They are:

- Surface plasmon polaritons (SPPs);
- Modes associated with localized surface plasmon resonances (LSPRs); and
- Bulk plasmons or bulk plasmon polaritons

2.2.1 Surface plasmon polariton

In the previous section, the classical point of view of LSPR in metal cluster is discussed as dipolar resonant modes that appear in the absorption spectrum. While doing so, the optical characteristics of the cluster is treated as that of the bulk metal, through the dielectric function. As the dielectric function does not take into account any spatial dispersion, the LSPR as discussed in the previous section is strictly a surface mode. For this reason, they can also be realized as confined surface mode of electromagnetic surface waves, known as the surface plasmon polaritons.

Surface plasmon polaritons (SPPs) are electromagnetic surface waves, evanescent in the direction perpendicular to the surface, arising due to the coupling of the electromagnetic field with the conduction band electrons of the metal (or conductor). It exists and propagates with a propagation constant $k = 2\pi/\lambda_{SPP}$ at the interface of a dielectric and a metal (or conductor), as shown in Fig.2.4. The physical prop-

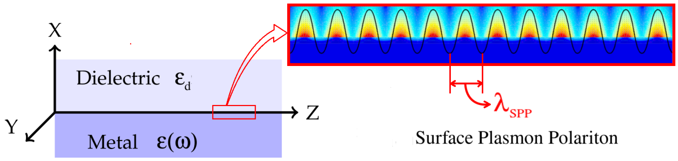

FIGURE 2.4: Schematic representation of surface plasmon polariton at the metal-dielectric interface.

erties of SPPs are understood by solving Maxwell's equation for electric field having transverse magnetic (TM) polarization, at a flat metal–dielectric interface as shown in Fig.2.4. The solution is shown in Appendix-B. The SPPs exist when the positive evanescent decay factors, κ and the dielectric functions in the corresponding media (ε_d for the dielectric and $\varepsilon(\omega)$ for the metal) fulfill the following relation,

$$\frac{\varepsilon_d}{\kappa_1} + \frac{\varepsilon(\omega)}{\kappa_2} = 0. \tag{2.2.1}$$

As κ_i is positive, this relation tells that the dielectric functions of the two media have to be of opposite signs, suggesting, one of them ought to be metal. The wave vector k, of SPP is related to the frequency ω of optical excitation, through the dispersion relation given by,

$$k = \frac{\omega}{c_0}\sqrt{\frac{\varepsilon_d\,\varepsilon(\omega)}{\varepsilon_d + \varepsilon(\omega)}} \tag{2.2.2}$$

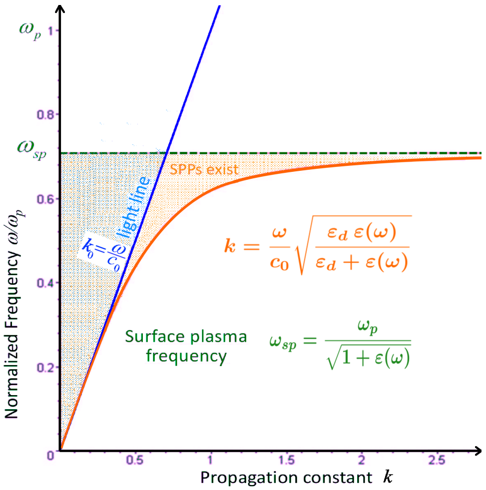

FIGURE 2.5: The dispersion relation for surface plasmo polariton (SPP).

This is shown in Fig.2.5 as the orange curve. As $k \longrightarrow \infty$, the curve asymptotically reaches a frequency called the surface-plasmon frequency ω_{sp}. The expression given by 2.2.2, for the dispersion relation of SPP is obtained from the full electrodynamic derivation. In the limit of large k, one gets the quasi-static dispersion relation for SPP as,

$$\varepsilon(\omega) = -\varepsilon_d \tag{2.2.3}$$

Considering the dielectric function of the metal to be that for an undamped plasma of noninteracting electrons, given by, $\varepsilon(\omega) = 1 - \frac{\omega_p^2}{\omega^2}$, the expression for the surface-plasmon frequency, in quasi-static limit, is obtained as,

$$\omega_{sp} = \frac{\omega_p}{\sqrt{1+\varepsilon_d}}. \tag{2.2.4}$$

2.2.1.a LSPR as confined dipolar SPP

In classical optics, the dipolar LSPR is viewed as a confined dipolar mode of SPP. In dielectric-surrounded metal nanoparticle having size comparable to the SPP wave length, $\lambda_{_{SPP}} = 2\pi/k_{_{SPP}}$ (as shown in Fig.2.4), the SPP can get confined at the particle surface, such that the surface can accommodate integral numbers of λ_{SPP}. The situation is depicted in Fig.2.6. Of course, an extra constrain on the λ_{SPP} appears in order to fit the SPP around the particle surface. And the occurrence of surface confined SPPs also depends on the geometry of the surface and the mode of excitation. However, when the particle size becomes such small that only one SPP wavelength can exist around its surface, it leads to the situation of classical dipolar LSPR. In this case the SPP oscillates, just like the oscillating dipolar LSPR, changing its polarization with the frequency ω given by the SPP dispersion relation (eq. 2.2.2). Thus the dipolar LSPR in metal clusters qualitatively follows the same trend of dispersion relation as that of the SPP. This explains the dependence of LSPR

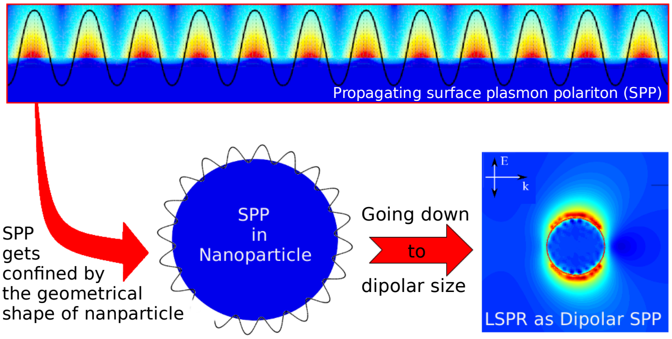

FIGURE 2.6: Schematic representation depicting realization of LSPR as confined dipolar SPP.

on the geometry, or specifically, on the aspect ratio of the cluster. This aspect will be discussed in details in chapter 4.

2.2.2 Bulk plasmons

While SPPs exist at metal–dielectric interfaces, there are other electromagnetic modes that can exist in the metal bulk. These bulk electromagnetic modes can be investigated by solving Maxwell's equations. Starting from Maxwell's equations, one can derive the electrodynamic wave equation in its general form as,

$$\nabla(\nabla \cdot \mathbf{E}) - \nabla^2 \mathbf{E} = \frac{\varepsilon}{c_0^2}\frac{\partial^2 \mathbf{E}}{\partial t^2}. \tag{2.2.5}$$

Considering plane wave form for the electric field, $\mathbf{E} = \mathbf{E_0} e^{i(\mathbf{k}\cdot\mathbf{r}-\omega t)}$, the equation transforms as,

$$\mathbf{k}(\mathbf{k} \cdot \mathbf{E}) - k^2 \mathbf{E} = -\varepsilon(\omega)\frac{\omega^2}{c_0^2}\mathbf{E}, \tag{2.2.6}$$

where, the metal dielectric function $\varepsilon(\omega)$ is only frequency dependent.

2.2.2.a Transverse solution: Bulk plasmon polaritons

The solution for a transverse electric field is obtained from eq. 2.2.6 by having $\mathbf{k} \cdot \mathbf{E} = 0$. This gives the corresponding dispersion relation for the transverse electromagnetic modes as,

$$k^2 = \varepsilon(\omega)\frac{\omega^2}{c_0^2}. \tag{2.2.7}$$

The transverse electromagnetic modes, that satisfies this dispersion relation are propagating bulk modes called as bulk plasmon polaritons. Considering the metal to behave like an undamped plasma, having a dielecric function of the form $\varepsilon(\omega) = 1 - \frac{\omega_p^2}{\omega^2}$, the dispersion relation for the bulk plasmon polaritons takes the form,

$$\omega^2 = \omega_p^2 + c_0^2 k^2. \tag{2.2.8}$$

This relation is shown in Fig.2.7 as the black curve.

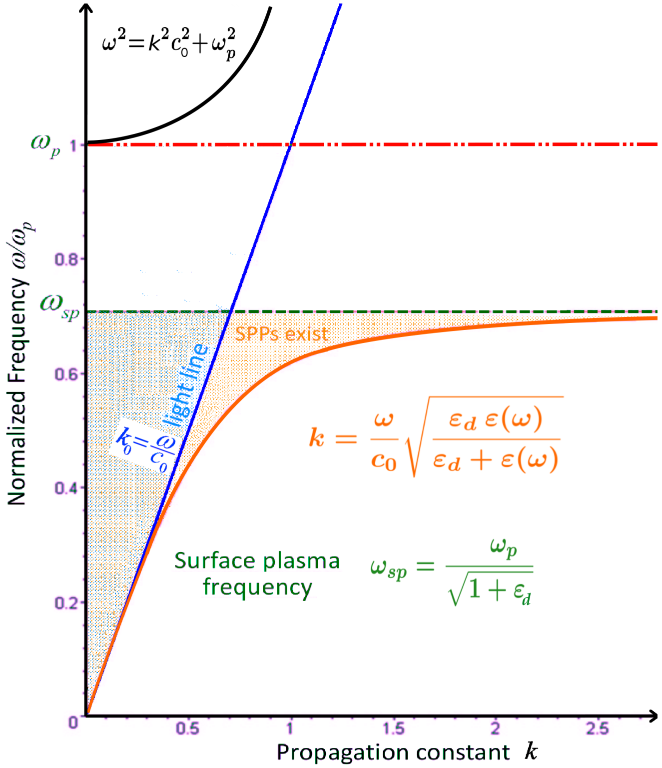

FIGURE 2.7: The dispersion relation for the bulk plasmons polaritons, longitudinal volume plasmons and SPPs.

2.2.2.b Longitudinal solution: Longitudinal volume plasmon

In order to have a solution of eq. 2.2.6 for an electric field $\mathbf{E}$, that propagates longitudinally, such that $\mathbf{k} \parallel \mathbf{E}$, we must have,

$$\mathbf{k}(\mathbf{k} \cdot \mathbf{E}) = k^2 \mathbf{E} \tag{2.2.9}$$

The equation 2.2.6 than gives,

$$\varepsilon(\omega)\,\frac{\omega^2}{c_0^2}\,\mathbf{E} = 0. \tag{2.2.10}$$

For non-vanishing $\mathbf{E}$, we then must have,

$$\varepsilon(\omega) = 0 \tag{2.2.11}$$

This is the condition for the occurrence of electromagnetic modes in bulk having longitudinal electric field. Thus the modes are called longitudinal bulk modes or ‘longitudinal volume plasmons’. Again, considering the metal dielectric function to have the form for an undamped plasma, one gets the dispersion relation for longitudinal bulk plasmons as,

$$\varepsilon(\omega) = 1 - \frac{\omega_p^2}{\omega^2} = 0, \qquad \Longrightarrow \qquad \omega = \omega_p. \tag{2.2.12}$$

For a spatially non-dispersive (homogeneous) plasma the longitudinal volume plasmons exist at $\omega = \omega_p$, the *plasma frequency*. The red dashed line in Fig.2.7 represent this mode.

2.3 Nonlocal Optics

As stated before in eq. 2.1.1, in classical optics, the optical response in a system is described by the macroscopic polarization $\mathbf{P}(\mathbf{r}) = \epsilon_0 \chi \mathbf{E}(\mathbf{r})$, where, χ is the electric susceptibility. The susceptibility, and hence the dielectric function ($\varepsilon = 1 + \chi$), is intrinsically related to the electron-density distribution, and accounts for the response in the system. The theoretical framework of local optics, described in the previous section (through the Drude and Lorentz-Drude model), when applied to metal clusters, considers the dielectric function to be isotropic and homogeneous, i.e., χ is described to be spatially local. Therefore, the metal-dielectric interface is described to be optically abrupt. However, when the cluster size becomes very small ($\lesssim 5nm$), due to atomistic resolution the electron-electron interaction becomes important. At this size limit, thus, one can no longer use local optics descriptions and the effects of the spatial nonlocality in the electronic response has to be considered. Nonlocal optics leads to $\mathbf{P}(\mathbf{r})$ depending on $\mathbf{E}(\mathbf{r}')$, where $\mathbf{r}' \neq \mathbf{r}$. The polarization at a given point depends on the excitation within a volume surrounding this point. This is due to electron-electron interactions. Consequently, the electron-density distribution can no longer considered to be abrupt. The surface to volume ratio for this size range becomes important and needs to be taken into account properly, by the proper description of the smooth variation of the electron-density across the metal-dielectric boundary. The density-density response function becomes nonlocal in space : $\chi = \chi(\mathbf{r}, \mathbf{r}')$, consequently making the dielectric function spatially dispersive: $\varepsilon(\mathbf{k}, \omega)$.

The ideal approach to describe the nonlocal optical response is, of course, to use *ab initio* quantum mechanical, or density functional theories for optical excitations. The density functional framework is discussed in details in chapter 3. Though *ab initio* theories can give proper nonlocal response, in practice, the use of it is limited to systems comprising of small numbers of atoms ($\sim 3000\ electrons$), or for larger sizes, to the use of simple models, like jellium. However, within the framework of classical optics, the effect of spatial nonlocality on optical response of the loosely bound, conduction band electrons in a metal, can be described by the hydrodynamic model [64, 73–75, 142–146].

2.3.1 Hydrodynamic model

The model describes the spatial nonlocal effect on the macroscopic optical response of the conduction band electrons, by the introduction of an electron pressure term in the free electron (plasma) model as described by Drude. The electron pressure term accounts for the Pauli exclusion principle as understood within the Thomas–Fermi theory.

2.3.1.a Hydrodynamic equation of motion

The equation of motion for the conduction band electrons in the hydrodynamic description is given as,

$$m_e \frac{d^2\mathbf{X}}{dt^2} + m_e\gamma\frac{d\mathbf{X}}{dt} + \frac{\nabla p}{n_e} = -e\mathbf{E}, \tag{2.3.1}$$

$$(neglecting\ the\ magnetic\ component\ of\ the\ force)$$

where, m_e is the effective mass of a conduction band electron, n_e is the density o conduction band electrons; and p is the electron pressure. The electron pressure originates from the quantum mechanical fact that electrons are fermions. Due to the fermionic interaction they follow Pauli exclusion principle, and occupy different quantum states. As a consequence, they can not be compressed infinitely (as was possible in Drude's model of noninteracting plasma of electrons). They occupy a spatial region that is larger that a sphere having Thomas-Fermi wavelength.

Relating n_e to the current density $\mathbf{J}$, through the continuity equation, and then relating $\mathbf{J}$ to the macroscpic polarization through,

$$\mathbf{J} = \frac{d\mathbf{P}}{dt}, \tag{2.3.2}$$

the eq. 2.3.1 becomes,

$$\frac{d^2\mathbf{P}}{dt^2} + \gamma\frac{d\mathbf{P}}{dt} - \frac{e}{m_e}\nabla p = \frac{n_e e^2}{m_e}\mathbf{E}. \tag{2.3.3}$$

The last term in the L.H.S. can be expressed in terms of electron density using the expression of electron pressure p in Thomas–Fermi model:

$$p(\mathbf{r},t) = \zeta \Big[n_e(\mathbf{r},t) \Big]^{5/3}, \quad where, \quad \zeta = \frac{h^2(3\pi^2)^{2/3}}{5m_e}. \tag{2.3.4}$$

With this expression of pressure in eq. 2.3.3, we get the hydrodynamic equation of motion for the conduction band electrons as,

$$-\beta^2\, \nabla(\nabla\cdot\mathbf{P}) \;+\; \frac{d^2\mathbf{P}}{dt^2} + \gamma\frac{d\mathbf{P}}{dt} \;=\; \epsilon_0\, \omega_p^2\, \mathbf{E}, \tag{2.3.5}$$

where, $\omega_p = \sqrt{n_e e^2/(\epsilon_0 m_e)}$ is the plasma frequency, and β is called the hydrodynamic *nonlocal parameter* which is of the order of the Fermi velocity (v_F). A detailed derivation of the hydrodynamic equation of motion is done in Appendix C.

2.3.1.b Electromagnetic response

The response of the electromagnetic field on the conduction band electrons is obtained by solving the Maxwell's equations. The Maxwell's equations combines to give the electromagnetic wave equation as,

$$\nabla\times\nabla\times\mathbf{E} = -\frac{\partial}{\partial t}(\nabla\times\mathbf{B}) = -\frac{\partial}{\partial t}\left(\frac{1}{c_0^2}\frac{\partial\mathbf{E}}{\partial t} + \mu\mathbf{J}\right)$$

$$or, \quad \nabla(\nabla\cdot\mathbf{E}) - \nabla^2\mathbf{E} + \frac{1}{c_0^2}\frac{\partial^2\mathbf{E}}{\partial t^2} = -\mu_0\frac{\partial^2\mathbf{P}}{\partial t^2}, \tag{2.3.6}$$

where, the metal is assumed to be non-magnetic, $\mu = \mu_0$, and eq. 2.3.2 is used.

In order to obtain the spatial nonlocal response, on the electrons described in the hydrodynamic model, one needs to solve eq. 2.3.6 simultaneously with eq. 2.3.5. Considering plane wave propagation for the electric field and hence for the polarization:

$$\mathbf{E}(\mathbf{r},t) = \mathbf{E}e^{i(\mathbf{k}\cdot\mathbf{r}-\omega t)}, \quad \mathbf{P}(\mathbf{r},t) = \mathbf{P}e^{i(\mathbf{k}\cdot\mathbf{r}-\omega t)}; \tag{2.3.7}$$

the equations 2.3.6 and 2.3.5 can respectively be written as,

$$\mathbf{k}(\mathbf{k}\cdot\mathbf{E}) - k^2\mathbf{E} + \frac{\omega^2}{c_0^2} = \omega^2\mu_0\mathbf{P} \tag{2.3.8}$$

$$\text{and,}\quad \beta^2\mathbf{k}(\mathbf{k}\cdot\mathbf{P}) - (\omega^2 + i\gamma\omega)\mathbf{P} = \epsilon_0\omega_p^2\mathbf{E}. \tag{2.3.9}$$

Transverse Bulk Plasmon:

The usual transverse solution for the wave equation (2.3.8) is obtained by having the electric field perpendicular to the direction of wave propagation: $\mathbf{k} = \mathbf{k}_\perp$, such that, $\mathbf{k}_\perp \cdot \mathbf{E} = 0$. The wave equation then gives the dispersion relation for the transverse modes:

$$\begin{aligned}
\left(-k_\perp^2 + \frac{\omega^2}{c_0^2}\right)\mathbf{E} &= -\omega^2\mu_0\epsilon_0\chi_T(\omega)\mathbf{E} \\
\implies k_\perp^2 - \frac{\omega^2}{c_0^2} &= \frac{\omega^2}{c_0^2}\chi_T(\omega) \\
\implies k_\perp^2 &= \frac{\omega^2}{c_0^2}(1 + \chi_T(\omega)) = \frac{\omega^2}{c_0^2}\varepsilon_T(\omega) \qquad (2.3.10)
\end{aligned}$$

This is the same dispersion relation as shown in Fig,2.7 for the transverse bulk plasmon polaritons in black.

As, the electric field is transverse, so is the polarization. Thus, having $\mathbf{k}_\perp \cdot \mathbf{P} = 0$ in eq. 2.3.9 we get,

$$-(\omega^2 + i\gamma\omega)\epsilon_0\chi_T(\omega)\mathbf{E} = \epsilon_0\omega_p^2\mathbf{E} \tag{2.3.11}$$

which gives,

$$\chi_T(\omega) = -\frac{\omega_p^2}{\omega^2 + i\gamma\omega} \tag{2.3.12}$$

leading to the corresponding transverse component of the dielectric function as,

$$\varepsilon_T(\omega) = 1 + \chi_T(\omega) = 1 - \frac{\omega_p^2}{\omega^2 + i\gamma\omega}. \tag{2.3.13}$$

Thus, for the transverse electromagnetic modes, the dielectric function remains same as in the local optics description given by Drude's model. The spatial nonlocality has no effect on the transverse bulk plasmon polaritons.

Longitudinal Bulk Plasmon:

For longitudinal solution of the wave equation (2.3.8), the propagation vector and the electric field are parallel: $\mathbf{k}_{||} \parallel \mathbf{E}$. In the previous section, it is discussed that, having this condition in the wave equation leads to the dispersion relation for the longitudinal modes as, $\varepsilon_{_L}(\omega) = 0$

As, the polarization corresponding to the longitudinal mode should also be longitudinal, in eq. 2.3.9 we have, $\mathbf{k}_{||}(\mathbf{k}_{||} \cdot \mathbf{P}) = |\mathbf{k}_{||}|^{\mathbf{2}}\mathbf{P}$; and the eq. 2.3.9 takes the form,

$$\left[\beta^2|k_{||}|^2 - (\omega^2 + i\gamma\omega)\right]\epsilon_0\chi_{_L}\mathbf{E} = \epsilon_0\omega_p^2\mathbf{E} \tag{2.3.14}$$

to give the longitudinal susceptibility as,

$$\chi_{_L} = \frac{-\omega_p^2}{(\omega^2 + i\gamma\omega) - \beta^2|k_{||}|^2} \tag{2.3.15}$$

Thus the dielectric function corresponding to the longitudinal modes are given as,

$$\varepsilon_{_L}(\mathbf{k}, \omega) = 1 - \frac{\omega_p^2}{(\omega^2 + i\gamma\omega) - \beta^2|k_{||}|^2} \tag{2.3.16}$$

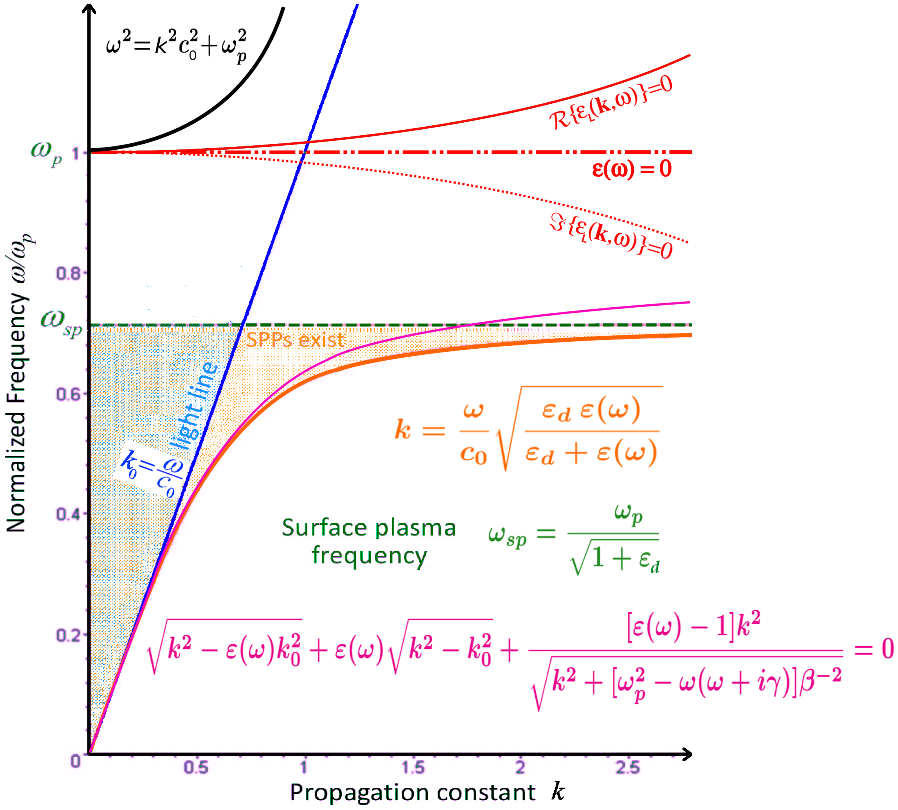

FIGURE 2.8: The solid red line corrspond to the real part while the dotted red line shows the imaginary part of the dispersion relation for the longitudinal volume plasmons. The pink curve shows the modified dispersion relation for the SPP with $\varepsilon_d = 1$, due the incorporation of spatial nonlocality. The other curves are the same as explained in Fig.2.7

The dispersion relation for the longitudinal models is then given by,

$$\varepsilon_L(\mathbf{k},\omega) = 1 - \frac{\omega_p^2}{(\omega^2 + i\gamma\omega) - \beta^2|k_{||}|^2} = 0 \tag{2.3.17}$$

For, negligible damping ($\gamma \to 0$), the dispersion relation becomes,

$$\omega^2 = \omega_p^2 + \beta^2|k_{||}|^2. \tag{2.3.18}$$

The real and imaginary part of the dispersion relation of the longitudinal (spatially dispersive) bulk modes are shown in the Fig.2.8 as solid and dotted red curves respectively. From this figure (2.8), it becomes clear that in order to account for spatial nonlocal effects one has to consider both the transverse and longitudinal dielectric functions. The hydrodynamic form of the dielectric tensor of the conduction band electron gas is then given by,

$$\varepsilon_{ij} = \begin{pmatrix} \varepsilon_{_T}(\omega) & 0 & 0 \\ 0 & \varepsilon_{_T}(\omega) & 0 \\ 0 & 0 & \varepsilon_{_L}(\mathbf{k},\omega) \end{pmatrix}; \tag{2.3.19}$$

where, the direction of the wave propagation is assumed to be along $\hat{z}$-direction.

Bound charges (localized d-electrons):

In the hydrodynamic description of metal, only the conduction band electrons of the system are treated as an interacting gas. However, as discussed in section 2.1.2.a, dielectric function of a metallic system and specifically of a noble metal has reasonable contributions in the visible frequencies from the localized electrons of system's interior. Within the hydrodynamic description the polarization corresponding to the localized electrons are treated to be local in space. Thus it contributes to the dielectric function similarly as in local optics description. In the Lorentz–Drude model the hydrodynamic form for the transverse and longitudinal dielectric functions are

$$\varepsilon_{_T}(\omega) = 1 + \sum_{i=1}^{k} \frac{f_i\omega_p^2}{(\omega_i^2-\omega^2)-i\gamma_i\omega} - \frac{\omega_p^2}{\omega^2+i\gamma\omega} \tag{2.3.20}$$

$$\varepsilon_{_L}(\mathbf{k},\omega) = 1 + \sum_{i=1}^{k} \frac{f_i\omega_p^2}{(\omega_i^2-\omega^2)-i\gamma_i\omega} - \frac{\omega_p^2}{(\omega^2+i\gamma\omega)-\beta^2|k_{\parallel}|^2} \tag{2.3.21}$$

Extra boundary conditions:

Nonlocal optics deals with the introduction of spatially dispersive longitudinal electromagnetic modes inside the metal, which are left out in local optics, because of the lack of spatial dispersion in the permittivity of metal. Thus in local optics the longitudinal modes cannot couple to the transverse ones, and the two sufficient boundary conditions are: the continuity of the tangential components of the electric fields $\mathbf{E}$, and of the magnetic field strengths $\mathbf{H}$ at the interface of two media. To describe the dispersive longitudinal fields inside the metal and more importantly at the metal-dielectric interface, the usual boundary conditions (which correspond to transverse wave propagation only) are insufficient and a third additional boundary condition (ABC) is required [147, 148], allowing the coupling of transverse and longitudinal waves. This third ABC is usually taken to be *the continuity of the normal component of the electric fields* $\mathbf{E}$*, at the interface of two media, and corresponds to* $v_\perp = 0$ *at the interface* [149, 150]. From the perspective of electrodynamics, this ABC is intuitive, because it yields a continuous description of the magnitudes of the electric fields across the boundary. However, the fact that $v_\perp$ vanishes at the interface, yields a discontinuity in the normal component of the current ($\mathbf{J}_\perp$) corresponding to the polarization of conduction electrons. In this thesis we have considered this ABC for all the nonlocal calculations performed using hydrodynamic description. There are, however, other choices of ABC [149], depending on the description of the static electron density profile at the boundaries.

Nonlocal effect at the metal boundary:

In the local optics description of a metallic system, surrounded by a dielectric, under the influence of an external electromagnetic field, the free charges that induce the macroscopic polarization are driven to an infinitesimally thin layer at the metal-dielectric interface. At the dipolar size limit, it is this induced charge distribution that characterize the dipolar LSPR by giving rise to electric field enhancement of several orders of magnitude, at LSPR frequency. However, at this size limit, the optically abrupt description of the metal-dielectric interface is no more valid as the induced charges spread across the interface. Nonlocal hydrodynamic description of the metal accounts for this spreading inherently through the repulsive interaction incorporated in the electron pressure. Thus, in the nonlocal description, the field enhancement is also reduced due to the spreading out of the induced charges.

A measure of the spreading of the induced charges across the metal dielectric interface is given by the inverse of the wave vector (normal to the interface), which gives the exponential decaying of the longitudinal component of the electric field parallel to the interface. It is shown later in the next section in eq. 2.3.28. This wave vector is given as $\sqrt{k^2 + q_{_L}^2}$, which is approximately equal to $q_{_L}$ as $k \ll q_{_L}$. The expression for $q_{_L}$ is obtained as $k_{||}$ from the expression of $\varepsilon_{_L}$ in eq. 2.3.21 as,

$$q_{_L} = \frac{1}{\beta}\sqrt{\frac{\omega_p^2}{\varepsilon_\infty(\omega) - \varepsilon_{_L}(\mathbf{k}, \omega)} - (\omega^2 + i\gamma\omega)}, \tag{2.3.22}$$

where, $\varepsilon_\infty(\omega)$ (including Lorentzians) is the dielectric function describing the background polarization caused by the bound charges.

2.3.2 Nonlocal Effects On SPP Dispersion

The longitudinal and the transverse modes described within the hydrodynamic description of the nonlocal optical response, remain decoupled in an isotropic homogeneous medium. But, in the presence of an interface they can get coupled by means of the electromagnetic boundary conditions. This coupling of longitudinal and transverse modes modifies the local-optics dispersion relation of the surface plasmon polaritons (SPPs). The magenta curve in the Fig.2.8 demonstrate this modification by differing from the orange curve, which correspond to the dispersion of SPP in local optics. In order to understand the coupling of longitudinal and transverse mode, we need to solve the Maxwell's equations for a transverse magnetic (TM) wave (which give rise to SPPs), at a metal dielectric interface, as shown in Fig. 2.9. In the figure, the region $z > 0$ correspond to the dielectric having dielectric constant $\varepsilon_d = 1$; the region $z < 0$ correspond to metal where the dielectric function is described by both the transverse component $\varepsilon_{_T}(\omega)$, and the wave vector dependent longitudinal component $\varepsilon_{_L}(\mathbf{k},\omega)$.

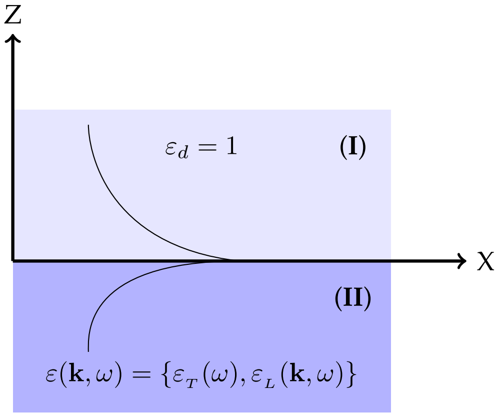

FIGURE 2.9: Schematic representation of SPP in a metal-dielectric interface, and the corresponding evanescent electric fields describing the SPP.

The TM modes are given by,

$$E_x = -i\frac{1}{\omega\varepsilon_0\varepsilon}\frac{\partial H_y}{\partial z}, \tag{2.3.23a}$$

$$E_z = -\frac{k}{\omega\varepsilon_0\varepsilon}H_y, \tag{2.3.23b}$$

and, the solution of the wave equation for the TM modes,

$$\frac{\partial^2 H_y}{\partial z^2} + (\varepsilon k_0^2 - k^2)H_y = 0, \qquad \text{where, } k_0 = \frac{\omega}{c} \tag{2.3.23c}$$

Having the solutions of the eqs. 2.3.23 in the dielectric **(I)** and metallic **(II)** regions, and the electric field components in the metallic region **(II)** together, the fields in the two sides of the interface can be presented as follows.

In region **(I)**:

$$H_y^{\mathbf{I}} = A_T\ e^{-z\sqrt{k^2-k_0^2}}\ e^{ikx}, \qquad \text{as, } \varepsilon_{\mathrm{d}} = 1 \tag{2.3.24}$$

$$E_x^{\mathbf{I}} = i\frac{\sqrt{k^2-k_0^2}}{k_0}\ A_T\ e^{-z\sqrt{k^2-k_0^2}}\ e^{ikx}, \tag{2.3.25}$$

$$E_z^{\mathbf{I}} = -\frac{k}{k_0}\ A_T\ e^{-z\sqrt{k^2-k_0^2}}\ e^{ikx}; \tag{2.3.26}$$

In region **(II)**:

$$H_y^{\mathbf{II}} = B_T\ e^{-zk_z}\ e^{ikx}, \qquad \text{where, } k_z = \sqrt{k^2 - \varepsilon_T(\omega)k_0^2}; \tag{2.3.27}$$

$$E_x^{\mathbf{II}} = \left[-i\frac{k_z}{\varepsilon_T(\omega)k_0}\ B_T e^{-zk_z} - ik_0\frac{B_L\ e^{z\sqrt{k^2+q_L^2}}}{\sqrt{k^2+q_L^2}} \right] e^{ikx} \tag{2.3.28}$$

$$E_z^{\mathbf{II}} = \left[-\frac{k}{\varepsilon_T(\omega)k_0}\ B_T\ e^{-zk_z} - \frac{k_0}{k}B_L\ e^{z\sqrt{k^2+q_L^2}} \right] e^{ikx}. \tag{2.3.29}$$

where, q_L is defined in eq. 2.3.22.

Imposing the boundary conditions as the continuity of the fields H_y, E_x, and E_z, at the interface $z = 0$, we get,

$$\begin{bmatrix} 1 & -1 & 0 \\ \dfrac{i\sqrt{k^2-k_0^2}}{k_0} & \dfrac{ik_z}{\varepsilon_T(\omega)k_0} & \dfrac{ik_0}{\sqrt{k^2+q_L^2}} \\ -\dfrac{k}{k_0} & \dfrac{k}{\varepsilon_T(\omega)k_0} & \dfrac{k_0}{k} \end{bmatrix} \begin{bmatrix} A_T \\ B_T \\ B_L \end{bmatrix} = 0 \tag{2.3.30}$$

The dispersion relation of the SPPs is then given by the nontrivial solution of eq. 2.3.30 as,

$$\begin{vmatrix} 1 & -1 & 0 \\ \dfrac{i\sqrt{k^2-k_0^2}}{k_0} & \dfrac{ik_z}{\varepsilon_T(\omega)k_0} & \dfrac{ik_0}{\sqrt{k^2+q_L^2}} \\ -\dfrac{k}{k_0} & \dfrac{k}{\varepsilon_T(\omega)k_0} & \dfrac{k_0}{k} \end{vmatrix} = 0, \tag{2.3.31}$$

which simplifies to,

$$k_z + \varepsilon_T(\omega)\sqrt{k^2-k_0^2} + \frac{[\varepsilon(\omega)-1]\,k^2}{\sqrt{k^2+q_L^2}} = 0 \tag{2.3.32}$$

$$\boxed{\sqrt{k^2-\varepsilon_T(\omega)k_0^2} + \varepsilon_T(\omega)\sqrt{k^2-k_0^2} + \frac{[\varepsilon_T(\omega)-1]k^2}{\sqrt{k^2+\dfrac{1}{\beta^2}\left[\dfrac{\omega_p^2}{\varepsilon_\infty(\omega)-\varepsilon_L(\omega)} - \omega(\omega+i\gamma)\right]}} = 0} \tag{2.3.33}$$

Considering only the first two terms of in L.H.S. of the eq. 2.3.33, and neglecting the third one (i.e., neglecting spatial nonlocality by having $\beta = 0$), the equation reduces to the local-optics description of the dispersion relation (eq. 2.2.2) of SSPs, for $\varepsilon_d = 1$. It is the third term in the L.H.S. of eq. 2.3.33 that accounts for the coupling of the longitudinal and transverse mode, and modifies the local-optics dispersion relation as shown by the pink curve in Fig. 2.8.

2.3.3 Local analogue model (LAM)

The numerical implementation of the hydrodynamic model requires to be done in three dimension due to the **k**-dependence of $\varepsilon_l(\mathbf{k},\omega)$. However, in this thesis, we have used a *local analogue model* (LAM) [146] for the hydrodynamic description, in order to implement it in two dimension, which is computationally more economic. Within the nonlocal hydrodynamic description, the effect of the longitudinal component of the electric field is to spread the surface charge distribution across the metal boundary. In the LAM, this nonlocal spread is describing the metal-dielectric interface through a fictitious thin layer having a thickness $\triangle d$, and a dielectric function given by,

$$\varepsilon_{Layer}(\omega) = \frac{\varepsilon_d\,\triangle d\,\varepsilon(\omega)\,q_L}{\varepsilon(\omega)-\varepsilon_d}. \tag{2.3.34}$$

where, ε_d is the dielectric constant of the background dielectric. The validity of LAM implementation to produce the same results as in the full three-dimensional implementation of the hydrodynamic model is based on the following philosophy. Mimicking the spatial nonlocality only through the transverse modes (as in local optics), and by playing with the width ($\triangle d$), and the dielectric function ($\varepsilon_{_{Layer}}$) of an intermediate layer between the metal and the surrounding dielectric, one obtains the same reflection and transmission coefficients as obtained by treating the nonlocal character of the metal-dielectric interface (through the three-dimensional implementation of the hydrodynamical model). It is worth mentioning here, that the consideration of the intermediate layer has nothing to do with accounting for the quantum mechanical *spill-out* of the ground-state electron density. The sole motive of LAM implementation is to get rid of the cumbersome three-dimensional implementation of the hydrodynamic model. Thus, the electromagnetic fields, in the LAM implementation, are purely transverse, and the dielectric function of the bulk metal is given by $\varepsilon(\omega) = \varepsilon_{_T}(\omega)$. A detailed discussion on the working principles of the LAM and its implementation for the case of nanoparticles is done in Appendix D.

In passing it is worth mentioning the merits and limitations of LAM. LAM can be implemented to replace the cumbersome numerical implementation of any nonlocal model [127, 151, 152] which reflects the nonlocal spatial dependence of the permittivity. As, mentioned earlier, in this thesis, we have employed LAM to replace the nonlocal model which is based on the hydrodynamic description of the electrons' motion. What limits LAM in comparison with the full three dimensional implementation of a nonlocal model is the fact that LAM implementation is possible only considering plane wave illumination. The reason behind this is an approximation used in LAM implementation which works only for the case of plane wave illumination. In the case of plane wave illumination, the longitudinal plasmon wave-vector ($q_{_L}$) normal to the metal-dielectric interface is much larger than the wave-vector (k) parallel to the interface. The latter is comparable with the free-space wave-vector of light, i.e., $k \sim k_0$, whereas, $q_{_L} \gg k_0$. For this reason, $\sqrt{k^2 + q_{_L}^2}$ can be approximated to $q_{_L}$ as we do in LAM implementation. However, for other optical excitations, e.g., microscopic emitters or electron-beams, the wave-vector ($k_{_{in}}$) associated with the incident electric field can considerably modify/enhance the wave-vector (k) parallel to the interface, making the approximation $\sqrt{k^2 + q_{_L}^2} \approx q_{_L}$ erroneous. Therefore, in these cases, the LAM implementation for the nonlocal model will not be valid and the spatial (nonlocal) dependence of the metal permittivity should be calculated properly considering the influence of k_{in} on k. So, in a few words, as far as the nonlocal effects on the dipolar LSPR under plane wave illumination is concerned, LAM gives exact results as can be found using full three dimensional implementation of any nonlocal model (in the case of this thesis, the hydrodynamic one); but never beyond that.

Chapter 3

Ab initio Theoretical Framework

In this chapter, both the formalism of ground-state Density-Functional Theory (DFT) and of Time-Dependent Density-Functional Theory (TDDFT) will be presented. Using TDDFT, the calculation of the optical absorption spectra in linear response theory (LR-TDDFT) and within the framework of real-time propagation (RT-TDDFT) will be discussed in the context of its application to metallic clusters. Following this, the advantages of both the methods (RT- & LR-TDDFT) will be discussed as well. Before going to the details of TDDFT and also in order to contextualize, a brief recapitulation of the Density-Functional Theory (DFT) is done. After theoretical principles, different ways of describing the system of interest will be discussed.

3.1 Recapitulation of DFT

The central idea of DFT is that any property of a system of many interacting electrons (or in general, interacting *fermions*) can be viewed as a functional of the ground state density $n_0(\mathbf{r})$. DFT allows to get rid of the complexity of solving the Schrödinger equation for the interacting many–particle system by solving self–consistently one–electron Schrödinger–like equations representing an equivalent non-interacting auxiliary (fictitious) system, known as Kohn-Sham system, that gives exactly the same ground state density, $n_0(\mathbf{r})$, as for the interacting system.

3.1.1 Hohenberg-Kohn Theorem

The formulation of DFT as an exact theory of any system of interacting electrons under the action of an external potential $V_{ext}(\mathbf{r})$ is based on the two theorems proposed and proved by Pierre Hohenberg and Walter Kohn [153].

3.1.1.a Many electron Hamiltonian

The total Hamiltonian of the many electron system in the external field generated by the ions is given as

$$\hat{\mathcal{H}}_{Tot} = \hat{\mathcal{T}}_{ion} + \hat{\mathcal{T}}_{e} + \hat{\mathcal{V}}_{e-ion} + \hat{\mathcal{W}}_{ion-ion} + \hat{\mathcal{W}}_{e-e} \tag{3.1.1}$$

where the operator $\hat{\mathcal{T}}$ represents kinetic energy, operator $\hat{\mathcal{V}}$ represents potential energy, and operator $\hat{\mathcal{W}}$ represents the contribution to the energy from interaction. The subscripts correspond to the objects the operators represent. As the mass of the nucleus is more than three orders of magnitude larger than that of the electrons around it, we can apply the Born–Oppenheimer (B-O) approximation. Within this approximation, the motion of the ionic system and that of the electronic system are decoupled, making it possible to solve the electronic problem for fixed ion coordinates. Therefore, the contribution of the ion-ion interaction $\hat{\mathcal{W}}_{ion-ion}$ to $\hat{\mathcal{H}}_{Tot}$ is nothing more than an additive constant and can be discarded. Thus the Hamiltonian of the electronic system that concerns us is,

$$\hat{\mathcal{H}} = \hat{\mathcal{T}} + \hat{\mathcal{V}}_{ext} + \hat{\mathcal{W}} \tag{3.1.2}$$

where, the kinetic energy operator is

$$\hat{\mathcal{T}} = \hat{\mathcal{T}}_{e} = -\frac{1}{2}\sum_{j} \nabla_j^2, \tag{3.1.3}$$

the potential operator is

$$\hat{\mathcal{V}}_{ext} = \hat{\mathcal{V}}_{e-ion} = \sum_{j} v_{ext}(\mathbf{r_j}), \tag{3.1.4}$$

representing the potential created by the ions which are external to the system of electrons. The operator describing the e-e interaction is

$$\hat{\mathcal{W}} = \hat{\mathcal{W}}_{e-e} = \frac{1}{2} \sum_{\substack{j,k \\ j \neq k}} \frac{1}{|\mathbf{r_j} - \mathbf{r_k}|}. \tag{3.1.5}$$

For such a system of N interacting electrons, the ground state wave function is

$$\Psi = \Psi(\mathbf{r_1}, \mathbf{r_2}, ..., \mathbf{r_j}, ..., \mathbf{r_N}), \tag{3.1.6}$$

which is antisymmetric with respect to permutation, and the ground state electron density is

$$n_0(\mathbf{r}) = \int \sum_{j=1}^{N} \delta(\mathbf{r} - \mathbf{r_j}) \; |\Psi(\mathbf{r_1}, \mathbf{r_2}, ..., \mathbf{r_j}, ..., \mathbf{r_N})|^2 \; d\mathbf{r_1} ... d\mathbf{r_N} \tag{3.1.7}$$

3.1.1.b Theorem I

theorem states:
For any system of interacting particles in an external potential $V_{ext}(\mathbf{r})$, the potential is determined uniquely up to an additive constant by the ground state density $n_0(\mathbf{r})$ of the system. In other words, because the $V_{ext}(\mathbf{r})$ defines our system, this means that $n_0(\mathbf{r})$ contains in principle all the information about the system.

It can be easily proven by *reductio ad absurdum*: the counterfactual assumption that different potentials might correspond to the same density is easily shown to lead to a contradiction.

Theorem I has an important consequence. Since the external potential of an N-electron system is determined by its ground-state density, the corresponding ground state can be expressed as a density functional $|\Psi_0[n]\rangle$. This means *that* all the *ground-state* properties can be written as functionals of the ground-state density.

3.1.1.c Theorem II

theorem states:
For any N-electron system under the action of a given external potential $v_{\text{ext}}(\mathbf{r})$, there

exists a density functional $E_{\mathrm{HK}}[n(\mathbf{r})]$ *such that:* ***i)*** *The ground-state energy* E_0 *of the system is the minimum value of* $E_{\mathrm{HK}}[n(\mathbf{r})]$*, minimized with respect to all the* N*-particle ground-state densities* $n(\mathbf{r})$*;* ***ii)*** *the minimizing density is the ground-state density* $n_0(\mathbf{r})$.

Let $|\Psi_0[n]\rangle$ be the N-electron ground state corresponding to $n(\mathbf{r})$. The $E_{\mathrm{HK}}[n]$ functional is expressed as

$$E_{HK}[n] = \langle\Psi[n]|\hat{\mathcal{T}} + \hat{\mathcal{V}}_{ext} + \hat{\mathcal{W}}|\Psi[n]\rangle = F_{HK}[n] + \int d^3r \; V_{ext}(\mathbf{r}) \; n(\mathbf{r}) \tag{3.1.8}$$

where,

$$F_{HK}[n] = \langle\Psi_0[n]|\hat{\mathcal{T}}|\Psi_0[n]\rangle + \langle\Psi_0[n]|\hat{\mathcal{W}}|\Psi_0[n]\rangle = T[n] + W[n], \tag{3.1.9}$$

therefore, by its constructions $F_{HK}[n]$ is *universal* as kinetic energy ($T[n]$) and interaction energy ($W[n]$) are functionals of only n. Here *universal* refers to be independent of the system, the different elements that consist the system, and the external potential.

Now we consider a ground state $\Psi^{(1)}$ having density $n^{(1)}$, of a system corresponding to external potential $V_{ext}^{(1)}$. Following, eq.3.1.8, the energy is

$$E^{(1)} = \langle\Psi^{(1)}|\hat{\mathcal{H}}^{(1)}|\Psi^{(1)}\rangle = E_{HK}[n^{(1)}] \tag{3.1.10}$$

For the same system, now we take a different density $n^{(2)}$ corresponding to a different state $\Psi^{(2)}$. Clearly, as $\Psi^{(2)}$ is different from $\Psi^{(1)}$, we have,

$$E^{(1)} = \langle\Psi^{(1)}|\hat{\mathcal{H}}^{(1)}|\Psi^{(1)}\rangle < \langle\Psi^{(2)}|\hat{\mathcal{H}}^{(1)}|\Psi^{(2)}\rangle = E^{(2)}. \tag{3.1.11}$$

This means the correct ground state energy evaluated as $E_0 = E_{HK}[n]$ is the lowest if and only if $n = n_0$.

3.1.2 Kohn-Sham Scheme

Although Hohenberg-Kohn (HK) theorems I and II tell us that in principle we could restrict ourselves to a treatment of the density, this does not provide a practical scheme for getting the density of a many–body system's ground state. It was Walter

Kohn and Lu Jeu Sham came up with an *ansatz* [154] in order to facilitate. It assumes that,

- the ground state density of an interacting many-electron system can be represented by the ground state density of a fictitious non-interacting many-electron system, usually referred as to Kohn–Sham system; and
- the Hamiltonian of the Kohn–Sham system is chosen to be expressible in terms of single–particle Hamiltonians having a kinetic energy term and an effective potential:
$$\hat{H}_s = \hat{T} + \hat{V}_s = \sum_{j=1}^{N} \hat{h}_s = \sum_{j=1}^{N} \Big(-\frac{\nabla_j^2}{2} + v_s(\mathbf{r}) \Big). \tag{3.1.12}$$

As Hohenberg-Kohn theorem applies for the Kohn-Sham system, i.e., as there is a one–to–one correspondence between $v_s(\mathbf{r})$ and $n_{0,s}(\mathbf{r})$, the ground state density of the Kohn-Sham system, we can now write the total energy corresponding to this Hamiltonian as a density functional following eq.3.1.8,

$$E_s[n] = T_s[n] + \int d^3r\ n(\mathbf{r})\ v_s(\mathbf{r}) \tag{3.1.13}$$

where, in this case, the HK functional $F_{\text{HK}}[n]$ is substituted by the universal functional $T_{\text{s}}[n]$ which is equal to the expectation energy of the kinetic energy of a *non-interacting* N-electron ground state with density $n_0(\mathbf{r})$.

The ground state energy of this system is to be found by minimizing $E_s[n]$ with respect to n, subject to the constraint that the total number of electrons $N = \int n(\mathbf{r}')\, d\mathbf{r}'$ remains unaltered. While doing so, what one needs is to have some correspondences between the actual many body system and the Kohn–Sham system, i.e., between $E_{HK}[n]$ and $E_s[n]$, such that after the minimization $E_s[n_0]$ becomes more tractable than $E_{HK}[n_0]$. This is done by a clever way of adding and subtracting the concerning terms at play. From eq.3.1.8 & eq.3.1.9, we recall,

$$E[n] = E_{HK}[n] = F[n] + \int d^3r\ V_{ext}(\mathbf{r})\ n(\mathbf{r})$$

$$E[n] = F[n] - T_s[n] + T_s[n] - \frac{1}{2}\int\int d^3r\, d^3r'\, \frac{n(\mathbf{r})\ n(\mathbf{r}')}{|\mathbf{r}-\mathbf{r}'|}$$
$$+ \frac{1}{2}\int\int d^3r\, d^3r'\, \frac{n(\mathbf{r})\ n(\mathbf{r}')}{|\mathbf{r}-\mathbf{r}'|} + \int d^3r\, V_{ext}(\mathbf{r})\, n(\mathbf{r}) \tag{3.1.14}$$

$$= \left[F[n] - T_s[n] - \frac{1}{2}\int\int d^3r\, d^3r'\, \frac{n(\mathbf{r})\ n(\mathbf{r}')}{|\mathbf{r}-\mathbf{r}'|}\right]$$
$$+ T_s[n] + \frac{1}{2}\int\int d^3r\, d^3r'\, \frac{n(\mathbf{r})\ n(\mathbf{r}')}{|\mathbf{r}-\mathbf{r}'|} + \int d^3r\, V_{ext}(\mathbf{r}) \tag{3.1.15}$$

$$= \left[T[n] - T_s[n] + W[n] - \frac{1}{2}\int\int d^3r\, d\mathbf{r}'\, \frac{n(\mathbf{r})\ n(\mathbf{r}')}{|\mathbf{r}-\mathbf{r}'|}\right]$$
$$+ T_s[n] + \frac{1}{2}\int\int d^3r\, d^3r'\, \frac{n(\mathbf{r})\ n(\mathbf{r}')}{|\mathbf{r}-\mathbf{r}'|} + \int d^3r\, V_{ext}(\mathbf{r}) \tag{3.1.16}$$

$$E[n] = E_{XC}[n] + T_s[n] + E_H[n] + \int d^3r\, V_{ext}(\mathbf{r}) \tag{3.1.17}$$

where $T_s[n]$ is the non-interacting kinetic energy, the last term is due to the external potential, and

$$E_H[n] = \frac{1}{2}\int\int d^3r\, d^3r'\, \frac{n(\mathbf{r})\ n(\mathbf{r}')}{|\mathbf{r}-\mathbf{r}'|} \tag{3.1.18}$$

is the classical Coulomb energy, generally referred to as Hartree energy. All that rests goes into $E_{XC}[n]$ called exchange–correlation (XC) functional, *defined as*,

$$E_{XC}[n] = \left[T[n] - T_s[n] + W[n] - \frac{1}{2}\int\int d^3r\, d^3r'\, \frac{n(\mathbf{r})\ n(\mathbf{r}')}{|\mathbf{r}-\mathbf{r}'|}\right]. \tag{3.1.19}$$

For a particular many–electron system, the form of $E_{XC}[n]$ is not exactly known. Therefore the accuracy of the Density–Functional–Theory methods relies on the quality the $E_{XC}[n]$. For most of the realistic situations of describing a many–electron system, certain levels of approximations (namely, Local Density Approximation, Generalized Gradient Approximation, etc.) are employed.

Now, according to Kohn–Sham *ansatz*, $E_s[n_0] = E_{HK}[n_0]$. And Hohenberg–Kohn theorem says that to get $E[n_0]$, one needs to minimize $E[n]$ with respect to n with the constraint of keeping the total number of electron unchanged. This can be do using Rayleigh–Ritz principle:

$$\begin{aligned} \delta E[n] &= 0 \\ or, \int \frac{\delta E[n]}{\delta n(\mathbf{r})} \delta n(\mathbf{r})\ d^3r &= 0 \end{aligned} \tag{3.1.20}$$

is to be solved subject to

$$\frac{\delta N}{\delta n(\mathbf{r})} = 0, \text{ where, } N = \int d^3r'\ n(\mathbf{r}'). \tag{3.1.21}$$

Using a Lagrange multiplier λ, eq. 3.1.20 & eq. 3.1.21 can be merged to get the Euler equation:

$$\int \delta n(\mathbf{r}) \left[\frac{\delta E[n]}{\delta n(\mathbf{r})} - \lambda\right] d^3r = 0 \tag{3.1.22}$$

$$\implies \qquad \frac{\delta E[n]}{\delta n(\mathbf{r})} = \lambda. \tag{3.1.23}$$

For the non-interacting Kohn–Sham system eq.3.1.23 reads as,

$$\frac{\delta T_s[n]}{\delta n(\mathbf{r})} + v_s[n](\mathbf{r}) = \lambda \tag{3.1.24}$$

(remark: In contrast to eq.3.1.13, here we write $v_s[n](\mathbf{r})$ not $v_s(\mathbf{r})$) For the interacting system following eq.3.1.2, the eq.3.1.23 becomes:

$$v_{xc}[n] + \frac{\delta T_s[n]}{\delta n(\mathbf{r})} + \int d^3r' \frac{n(\mathbf{r}')}{|\mathbf{r}-\mathbf{r}'|} + V_{ext}(\mathbf{r}) = \lambda \tag{3.1.25}$$

where the exchange-correlation (xc) potential is defined as,

$$v_{xc}[n] = \frac{\delta E_{XC}[n]}{\delta n(\mathbf{r})} \tag{3.1.26}$$

Now comparing eq.3.1.24 & eq.3.1.25 we get the expression for the Kohn–Sham potential as

$$v_s[n](\mathbf{r}) = v_{xc}[n] + v_H[n] + V_{ext}(\mathbf{r}), \tag{3.1.27}$$

where

$$v_H[n] = \int d^3r' \frac{n(\mathbf{r}')}{|\mathbf{r}-\mathbf{r}'|} \tag{3.1.28}$$

is the Hartree potential. Thus, the correspondence between the non-interacting *fictitious* Kohn–Sham system and the actual interacting many–electron system is established. The following step is to solve for the Kohn–Sham Hamiltonian $\hat{H}_s$. The advantage we have now is that as $\hat{H}_s$ is the Hamiltonian of a non-interacting system, the total wave function of the Kohn–Sham system can be written as a Slater determinant:

$$\Psi_{KS} = \begin{vmatrix} \varphi_1(\mathbf{r_1}) & \varphi_2(\mathbf{r_1}) & \dots & \varphi_N(\mathbf{r_1}) \\ \varphi_1(\mathbf{r_2}) & \varphi_2(\mathbf{r_2}) & \dots & \varphi_N(\mathbf{r_2}) \\ \vdots & \vdots & \ddots & \vdots \\ \varphi_1(\mathbf{r_N}) & \varphi_2(\mathbf{r_N}) & \dots & \varphi_N(\mathbf{r_N}) \end{vmatrix} \tag{3.1.29}$$

where $\varphi_j(\mathbf{r})$s are the N lowest normalized single–particle orbitals which satisfy single–particle Schrödinger equations

$$\hat{h}_s\varphi_j(\mathbf{r}) = -\left(\frac{\nabla^2}{2} + v_s[n](\mathbf{r})\right)\varphi_j(\mathbf{r}) = \varepsilon_j\varphi_j(\mathbf{r}) \tag{3.1.30}$$

known as Kohn–Sham equations. The ground state density for the Kohn–Sham system (and therefore also for the actual interacting many electron system) then is

$$n_0(\mathbf{r}) = \sum_{j=1}^{N} |\varphi_j(\mathbf{r})|^2. \tag{3.1.31}$$

We note in eq.3.1.30 that as the Hamiltonian is a functional of the density, the Kohn–Sham orbitals are also functionals of the density, $\varphi_j[n](\mathbf{r})$. Moreover, in eq.3.1.31, these orbitals are needed to calculate the ground state density. Therefore, the only way of solving the Kohn–Sham equations is to do it in an iterative self–consistent manner.

Once the solutions of the Kohn–Sham equations are obtained, we have access to the ground state density $n_0(\mathbf{r})$ and the eigen–solutions $\varphi_j[n_0](\mathbf{r})$. Then we can calculate the non-interacting kinetic energy functional as,

$$T_s[n_0] = \sum_{j=1}^{N} \int d^3r\, \varphi_j^*(\mathbf{r}) \left(-\frac{\nabla^2}{2}\right) \varphi_j(\mathbf{r}) = \sum_{j=1}^{N} \varepsilon_j - \int d^3r\, n_0(\mathbf{r})\, v_s[n_0](\mathbf{r}) \tag{3.1.32}$$

following eq.3.1.30. Putting this expression of $T_s[n_0]$ into eq.3.1.2 and using eq.3.1.27, we get a convenient expression of the ground state energy as,

$$E_0[n_0] = \sum_{j=1}^{N} \varepsilon_j - \frac{1}{2}\int d^3r \int d^3r' \frac{n_0(\mathbf{r})\, n_0(\mathbf{r}')}{|\mathbf{r}-\mathbf{r}'|} - \int d^3r\, n_0(\mathbf{r}) v_{xc}[n_0](\mathbf{r}) \; + E_{XC}[n_0] \tag{3.1.33}$$

3.1.2.a Solving Kohn–Sham equations self-consistently

The Kohn–Sham equations are solved self-consistently. We begin with searching for the ground state density $n_0(\mathbf{r})$ of the many–body system by solving the time–independent Kohn–Sham equation 3.1.30. The iterative self-consistent scheme for getting the $n_0(\mathbf{r})$ is shown in Fig.3.1. The Kohn–Sham orbitals are in general described in terms of some basis, for example, plane-wave (widely used for periodic systems), atomic orbitals, Gaussian basis, etc.

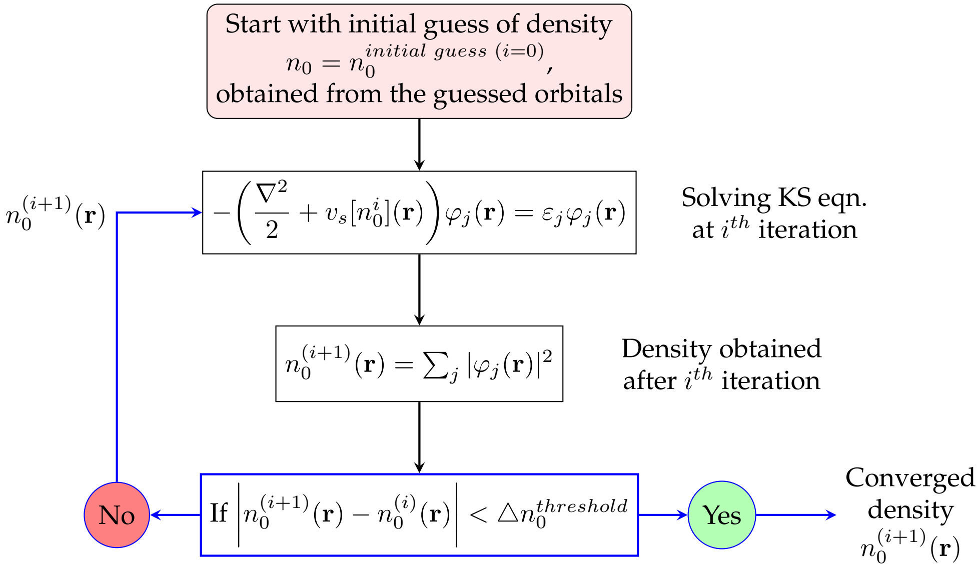

FIGURE 3.1: Schematic representation of solving self-consistently the Kohn–sham equation in order to get the converged ground state density

3.1.2.b Intricacies in Kohn–Sham DFT

There are certain subtleties while interpreting the outcomes of the Kohn–Sham scheme. These subtleties needs to be well understood and have to be properly taken care of.

- **Kohn–Sham orbitals**. In the Kohn–Sham scheme, although the exact ground state density, $n_0(\mathbf{r})$, of the interacting many–electron system is obtained from the occupied Kohn–Sham orbitals (φ_j) (3.1.31), the orbitals do not represent the actual interacting many–electron system, i.e.,

$$\Psi(\mathbf{r_1},\mathbf{r_1},...,\mathbf{r_N}) \neq \Psi_{KS}(\mathbf{r_1},\mathbf{r_1},...,\mathbf{r_N}) \tag{3.1.34}$$

- **Kohn–Sham eigen–values**. Similarly, the eigen–energies (ε_j) of the Kohn–Sham orbitals (φ_j) (3.1.30) do also not represent the quantum mechanical energy levels of the many–electron system, even though they (ε_j belonging to occupied φ_j) appear in the expression of the total energy of the many–electron ground state.
  - In general, the Kohn–Sham excitation energies ($\varepsilon_{mn} = \varepsilon_m^{unocc} - \varepsilon_n^{occ}$) are different from the excitation energies of the interacting many–electron system.
  - However, for a finite N–electron system, the highest occupied eigen–value (ε_N) equals to minus the exact ionization potential of the system [155, 156]. This is because, for a bound (finite) system, the density in long–range behaves asymptotically and is decided by the highest occupied state. Therefore, as the density is exact in Kohn–Sham DFT, so must be the eigen–value (ε_N) of the highest occupied state.

- **Kohn–Sham spin DFT**. In many cases, the practical use of the Kohn-Sham scheme is done without considering spin. In this thesis, all the calculations that will be presented are spin-unpolarized. However, the Kohn–Sham equations are also used in their spin-resolved form. The spin-dependent ground state density becomes,

$$n_0(\mathbf{r}) = n_{0\uparrow}(\mathbf{r}) + n_{0\downarrow}(\mathbf{r}) = \sum_{\sigma=\uparrow,\downarrow} \sum_{j=1}^{N_\sigma} = |\varphi_{j\sigma}(\mathbf{r})|^2, \quad \text{where } N = \sum_{\uparrow,\downarrow} N_\sigma, \tag{3.1.35}$$

the Kohn–Sham equation becomes,

$$-\left(\frac{\nabla^2}{2}+v_{s\sigma}[n_\uparrow,n_\downarrow](\mathbf{r})\right)\varphi_j(\mathbf{r})=\varepsilon_{j\sigma}\varphi_{j\sigma}(\mathbf{r}), \tag{3.1.36}$$

where the Kohn–Sham potential is defined as,

$$v_{s\sigma}[n_\uparrow,n_\downarrow](\mathbf{r})=v_{xc\sigma}[n_\uparrow,n_\downarrow]+\int d^3r'\,\frac{n(\mathbf{r}')}{|\mathbf{r}-\mathbf{r}'|}+V_{ext_\sigma}(\mathbf{r}), \tag{3.1.37}$$

and the xc energy and potential are defined in terms of individual spin-density functionals:

$$v_{xc\sigma}[n_\uparrow,n_\downarrow]=\frac{\delta E_{XC}[n_\uparrow,n_\downarrow]}{\delta n_\sigma(\mathbf{r})}. \tag{3.1.38}$$

Apart from handling magnetization and “open–shell” systems; the spin- dependent Kohn–Sham formalism allows dependence of E_{XC} on spin-up and spin-down densities which is better suited for the construction of approximations.

- **Role of XC functional: Self–interaction**. From the expression of $E_{XC}[n]$ we see that it basically contains the kinetic energy difference between the interacting and the non-interacting systems having the same density $n(\mathbf{r})$ and all the quantum effects on e-e interactions. In the Kohn–Sham scheme, the term $v_H[n]$ in $v_s[n]$ (or in $v_{s\sigma}[n_\uparrow,n_\downarrow]$), as is evident from its expression (3.1.28), includes the self–interaction of the electrons. One role of $E_{XC}[n]$ is that the contribution of the interaction of an electron with itself be excluded, because in the e-e interaction term $\hat{\mathcal{W}}$ in the many–electron Hamiltonian $\hat{\mathcal{H}}$ it is already taken care of, and therefore it is an exact condition to be fulfilled in the Kohn–Sham scheme. However, in most of the widely used approximate forms of the XC functionals, this condition is only partially fulfilled.

3.1.3 Approximate XC Functionals

Local-Density Approximation. The first approximation for the XC functional was given by Kohn and Sham [154] and is known as local-density approximation (LDA). Within this approximation one calculates the $E_{XC}[n]$ of an inhomogeneous system as the space–integral of the xc *energy density* $\epsilon_{xc}(\bar{n})$, of an homogeneous system with the same density:

$$E_{XC}^{LDA}[n] = \int d^3r \; \epsilon_{xc}(\bar{n})|_{\bar{n}=n(\mathbf{r})}. \tag{3.1.39}$$

The concept of 'local' becomes clear as for a particular space point $\mathbf{r}$ one takes the value of $\bar{n}$ to be $n(\mathbf{r})$. This approximation is exact for a homogeneous electron liquid and also holds as a sufficiently suitable and numerically economic approximation for the systems where the electron–density variations are slow, for example simple metals. Using LDA, many energetic and structural properties of a large range of materials are surprisingly well described [157]. Total atomic and molecular ground state energies are found to be close to experimental ones. Lattice constants in solids and molecular equilibrium distances are predicted well with good accuracy.

Generalized Gradient Approximation. The obvious step towards the improvement of approximate XC functionals is to take into account fast variation of the density. Recognizing the local Fermi wave–vector $k_F(\mathbf{r})$ as a length scale for density variation, in LDA the performance of $v_{xc}^{LDA}(\mathbf{r})$ depends on:

$$\frac{|\nabla n(\mathbf{r})|}{k_F(\mathbf{r}) \; n(\mathbf{r})} << 1 \tag{3.1.40}$$

Therefore, the natural idea of improving LDA was to expand the density functional in orders of $\left(\frac{|\nabla n(\mathbf{r})|}{k_F \; n(\mathbf{r})}\right)$. This scheme is known as gradient expansion approximation (GEA) [158]. However, in Generalized Gradient Approximation (GGA) one looks for an xc *energy density* ϵ_{xc}^{GGA} which depends on $n(\mathbf{r})$ and at the same time on $\nabla n(\mathbf{r})$. Thus, the GGA XC energy is

$$E_{XC}^{GGA}[n] = \int d^3r \; \epsilon_{xc}^{GGA}(n(\mathbf{r}), \nabla n(\mathbf{r})). \tag{3.1.41}$$

Unlike in LDA, in GGA there is no systematic unique way to get an expression for $\epsilon_{xc}^{GGA}(n(\mathbf{r}), \nabla n(\mathbf{r}))$. Over the years, hundreds of GGA functionals have been constructed. Some of them which are often found in literature are:

- **PBE**. One of the most successful GGA has been constructed by Perdew, Burke & Ernzerhof [159, 160]. In PBE, the XC energy functional consists of separate exchange and correlation parts.

- **BLYP**. Like PBE, BLYP also consists of separate exchange and correlation parts.

The exchange functional (known as B88) was proposed by Becke [161] empirically in terms of parameters fitted to atomic Hartee–exchange energies.The correlation energy functional was proposed for closed–shell systems by Lee, Yang and Parr [162].

- **LB94 Potential**. Apart from constructing the GGA XC functionals, there are some works done to get the GGA–exchange–correlation potential (v_{xc}^{GGA}) directly. The idea behind this approach is to get the correct asymptotic behavior of the v_{xc}^{GGA}. A well known example of such potential is the LB94 potential [163].

GGA is also not free of the problem of asymptotic behavior of the v_{xc}. Yet, the LDA functional and the functionals obtained in GGA are the ones which are widely used in DFT. However, different approximations of XC functional are found to be suitable for the description of different properties of matter. Therefore, the choice of an approximate density functional is based on experience and comparisons with benchmark results. In this thesis, LDA and PBE–GGA functionals are used for all the calculations that will be discussed in the coming chapters.

3.1.3.a Orbital-dependent functionals

For the sake of completeness, it is worth mentioning the further developments in order to have more accurate XC functionals than GGA, even though this does not directly concern the works performed in this thesis. In an increasing order of accuracy, complexity and computational cost, the developments beyond GGA goes as follows.

- **Meta–GGA Functionals**. The meta–GGA functionals are constructed using spin densities, their 1st and 2nd order gradients, and the kinetic energy densities ($\tau_\uparrow, \tau_\downarrow$) of the Kohn–Sham orbitals:

$$E_{XC}^{MGGA} = \int d^3r \; \epsilon_{xc}^{MGGA}(n_\uparrow, n_\downarrow, \nabla n_\uparrow, \nabla n_\downarrow, \nabla^2 n_\uparrow, \nabla^2 n_\downarrow, \tau_\uparrow, \tau_\downarrow) \tag{3.1.42}$$

  The meta–GGA functionals are partially free of self–interactions. An example of meta–GGA functional is PKZB [164].

- **Hybrid Functionals**. This type of functionals is made by mixing the exact exchange energy functional with LDA and/or GGA functionals:

$$E_{XC}^{hybrid} = aE_x^{exact} + (1-a)E_x^{GGA} + E_c^{GGA} \tag{3.1.43}$$

The exact exchange energy functional is obtained by Hartree–Fock calculation. Among hybrid functionals, the most popular is B3LYP [165]. This functional is constructed as,

$$E_{XC}^{B3LYP} = aE_x^{exact} + (1-a)E_x^{LDA} + bE_x^{B88} + cE_c^{LYP} + (1-c)E_c^{LDA} \quad (3.1.44)$$

where the parameters have values as, $a = 0.2$, $b = 0.72$, and $c = 0.81$. B3LYP describes the geometrical and energetic properties of molecules but it underperforms for systems having homogeneous electron densities [166]. Apart from the simple hybrid functionals there are also *range–separated hybrid* functionals [167] which are made by separating the Coulomb interaction in short–range and long–range parts, like the M06L [168, 169] used in this thesis for comparioson.

- Attempts have also been made to make the approximate XC functionals to be free of self–interactions [170]. In the literature the resulting functionals are known as *self–interaction corrected* (SIC) functionals. These functionals are dependent on densities of individual orbitals instead of total density and thus are less tractable.

All these sophisticated functionals (meta-GGA, Hybrid, SIC) *depend explicitly on the KS orbitals*.

3.1.4 Pseudopotential Description

Depending on the physical properties intended to study, there are different ways of describing a system of interest within the DFT framework, described throughout this chapter. For the study of plasmonic behaviour, the jellium description (mentioned in Appendix E) has been of enormous success. A better description of the constituents of system (solid, cluster, or molecule) is given by the use of pseudopotentials, which are used in this thesis. Among the other descriptions of a system, there are ultra-soft pseudopotentials [171] which are numerically less demanding, projector augmented wave (PAW) method [172, 173] which are more accurate, and also descriptions based on using orbitals. Here, a brief synopsis of the pseudopotential description is given in the following.

The pseudopotential method for the description of a chemical species is one of the widely used *ab initio* description based on *frozen-core approximation*. The strongly

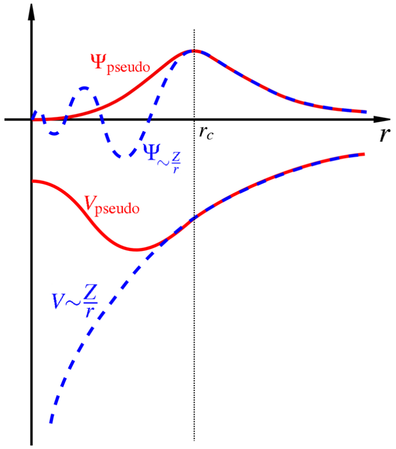

FIGURE 3.2: Schematic representation of pseudopotential (Courtesy: Wikipedia).

bound “deep” electrons of an atom do not participate in chemical bonding and are not important for the optical properties. Therefore we consider them as unchanging, which is the *frozen-core approximation*. As, the chemical properties and the low-energy part of the absorption spectra of a material are primary governed by the valence electrons, the idea of pseudopotential method [174, 175] is to describe only them.

In the *frozen-core approximation*, the valence electrons experience a resulting potential created by the strongly-bound core electrons and the nucleus together. Though the core electrons partially screen the charge of the nucleus, the resulting ion potential still has a Coulomb singularity at the nucleus, as shown by the blue dashed line representing the r^{-1} behaviour of the resulting Coulomb potential, in Fig.3.2. This makes the single-particle valence wave functions strongly oscillate in the core region. To describe this strong oscillation, in real space grids one needs much finer mesh for the core part. In basis set representation, the description would demand larger basis sets. In both way, it becomes numerically expensive if not difficult.

The idea of having pseudopotential is solely in order to get rid of the fluctuations of the valence orbitals around the core. This is done as follows. A cutoff radius, r_c, centering the nucleus is defined such that, all the fluctuation stays within the sphere of this radius (Fig.3.2). Then, the strongly oscillating valence wavefuction is replaced by a *pseudo-wavefunction* (Ψ_{pseudo}) which behaves “smoothly” within the cutoff radius, and outside the cutoff radius, remains behaving exactly same as the real valence wavefuction. The ionic potential that gives rise to this *pseudo-wavefunction* is the pseudopotential (V_{pseudo}) (Fig.3.2). While generating a pseudopotential care should be taken that,

- the Kohn-Sham orbitals outside r_c and the Kohn-Sham eigen-values remain unchanged: this is what make a pseudopotential norm-conserving;
- the total charge inside the sphere of radius r_c remains unchanged;
- the scattering properties remain unchanged.

For noble metals, the pseudopotentials describe the 11 valence electrons consisting of one s-electron and 10 d-electrons. There are several methods to construct a pseudopotentials from an all-electron calculation of the isolated atom. In this thesis norm-conserving pseudopotential of Troullier-Martins (T-M) [176] type are used.

3.2 Time-Dependent Density-Functional Theory

The Density-functional theory (DFT) is an exact theory for describing the ground state of a many-body system, but not the excited ones. Moreover, in DFT the energies of the quantum-mechanical (Kohn-Sham) states of the system have no clear physical significance, except for the highest occupied state, as mentioned in the previous section. This is the reason that the DFT-calculated band gaps in some semiconductors are incorrect, for instance, in Ge, the DFT-LDA gap is not only underestimated but even zero. To properly calculate the excited states of any system one needs to incorporate the dynamic behaviour of the system, i.e., the time-dependence should necessarily be accounted for.

In order to have a time–dependent density–functional theory (TDDFT) such that the complications of solving the time–dependent Schrödinger equation for an interacting many–electron system can be avoided by solving time–dependent single–particle equations (like the Kohn–Sham equations in DFT), we first need to establish one-to-one correspondence between the time–dependent external potential and the time–dependent density. This was done by Erich Runge and E. K. U. Gross [177]. theorem they proposed and proved for time–dependent scalar potentials is discussed below.

3.2.1 Runge-Gross Theorem

The Hamiltonian of N interacting particles in an explicitly time–dependent external *scalar* potential $v(\mathbf{r}, t)$ is given by

$$\hat{\mathcal{H}}(t) = \hat{\mathcal{T}} + \hat{\mathcal{V}}(t) + \hat{\mathcal{W}} \tag{3.2.1}$$

where the kinetic energy operator ($\hat{\mathcal{T}}$) and the interaction operator ($\hat{\mathcal{W}}$) remain the same as in the static case (3.1.3,3.1.5), and the time–dependent external potential operator is given by

$$\hat{\mathcal{V}}(t) = \sum_{j=1}^{N} v(\mathbf{r_j}, t). \tag{3.2.2}$$

To get the dynamics of the system, one needs to solve the time–dependent Schrödinger equation:

$$i\frac{\partial}{\partial t}\Psi(t) = \hat{\mathcal{H}}\Psi(t) \tag{3.2.3}$$

where, $\Psi(t) = \Psi(\mathbf{r_1}, ..., \mathbf{r_N}, t)$. From $\Psi(t)$ one can then get the density at a given time t.

Therefore, if we have a *fixed* initial state ($\Psi(t_0)$), solving 3.2.3 we'll have a relation F, mapping the external potential $v(\mathbf{r}, t)$ onto the time–dependent wave functions:

$$F : v(\mathbf{r}, t) \longrightarrow \Psi(t) \tag{3.2.4}$$

Now, densities are calculated as $n(\mathbf{r}, t) = \langle\Psi(t)|\hat{n}(\mathbf{r})|\Psi(t)\rangle$, where $\hat{n}(\mathbf{r})$ is the density operator, suggesting a relation D as $D : \Psi(t) \longrightarrow n(\mathbf{r}, t)$. Thus we can define another relation G, mapping the time–dependent potential onto the time–dependent density:

$$G : v(\mathbf{r}, t) \longrightarrow n(\mathbf{r}, t) \tag{3.2.5}$$

If this relation G is bijective, i.e. if there is a one-to-one correspondence between $v(\mathbf{r}, t)$ and $n(\mathbf{r}, t)$, then we can have a time–dependent version of the Hohenberg–Kohn theorem. But is it possible? The Runge–Gross theorem [177] is concerned with this question, which is answered *affirmatively* for scalar potentials meeting the following conditions.

- At $t = t_0$, from when the external potential began to be time-dependent, the initial state $\Psi(t_0) = \Psi_0$ should be the same for all the time–dependent external potentials, i.e., the time–dependent external potential starts to act upon the same initial state.

- If we consider two time–dependent potentials $v(\mathbf{r}, t)$ and $v'(\mathbf{r}, t)$ differing by a time–dependent additive term such that $v'(\mathbf{r}, t) = v(\mathbf{r}, t) + C(t)$, the corresponding wave functions will differ only by a phase factor $e^{-i\alpha(t)}$ (where, $C(t) = \dot{\alpha}(t)$), thus giving the same density: $n(\mathbf{r}, t) = n'(\mathbf{r}, t)$. Therefore,

  $$v(\mathbf{r}, t_0) - v'(\mathbf{r}, t_0) \neq C(t),$$

  i.e. the densities should differ by more than a time–dependent additive term.

- The potential should be Taylor expansible with respect to t around t_0 and the difference between $v(\mathbf{r}, t)$ and $v'(\mathbf{r}, t)$ should appear at some ***non-zero*** k^{th}

order (i.e. $k \geq 0$) of the expansion such that:

$$\frac{\partial^k}{\partial t^k}\Big[v(\mathbf{r},t) - v'(\mathbf{r},t)\Big]_{t=t_0} \neq constant \tag{3.2.6}$$

With these constraints on the potential, the Runge–Gross theorem [177] states: *$G : v(\mathbf{r},t) \longrightarrow n(\mathbf{r},t)$ is invertible up to an additive merely time–dependent function in the potential*. The proof is shown in Appendix-A. The consequences of the Runge–Gross theorem follows as:

- For a given initial state (Ψ_0), the time–dependent density is a unique functional of the time–dependent potential: $v(\mathbf{r},t) \longleftrightarrow n(\mathbf{r},t)$, provided the density satisfies the conditions discussed above.
- As the relation is bijective, we also have : $v(\mathbf{r},t) = v[n,\Psi_0](\mathbf{r},t)$, which means,

$$\Longrightarrow \quad \hat{\mathcal{H}}(t) = \hat{\mathcal{H}}[n,\Psi_0](\mathbf{r},t) \qquad \Longrightarrow \quad \Psi(t) = \Psi[n,\Psi_0](\mathbf{r},t) \tag{3.2.7}$$

This allows us to access the expectation values of any physical observable, as they will also be functional of the time–dependent density (for a fixed initial state):

$$O(t) = \langle \Psi[n,\Psi_0](\mathbf{r},t) \mid \hat{O}(t) \mid \Psi[n,\Psi_0](\mathbf{r},t)\rangle = O[n,\Psi_0](t). \tag{3.2.8}$$

3.2.1.a Intricacies and limitations of the Runge–Gross theorem

- The condition that $v(\mathbf{r},t)$ be Taylor expansible around t_0 is crucial for the validity of theorem. Therefore, many potentials which are not Taylor expansible are not tractable.
- Within the Runge–Gross theorem, the time–dependent wave functions are always determined as a functional of the time–dependent density up to a phase factor $e^{-i\alpha(t)}$, as we always get the same density for potentials differing merely by an additive time–dependent term. For this reason, the evaluation of the expectation values of the observables which contain derivatives and/or integral operators on t, is not as straight forward as shown in eq.3.2.8.
- Runge–Gross theorem can deal only with scalar potentials. However, time–dependent current-DFT (TDCDFT) is developed [178, 179] to treat vector potentials.

- The proof of Runge–Gross theorem requires the density at a surface around the system under consideration to vanish, so that the surface integral vanishes too. This requirement makes theorem valid for only *finite systems*.

3.2.2 Time–Dependent Kohn–Sham Scheme

After establishing the one-to-one correspondence between the time–dependent potential and the time–dependent density, the next step towards the formulation of TDDFT is to replace the interacting many–body system by an auxiliary non-interacting system (like in DFT), in order to have a time–dependent version of the Kohn–Sham equation. There is a problem in doing so.

3.2.2.a Time–dependent v-representability problem

Following Hohenberg–Kohn theorems, the functional $E[n]$ is defined only for those functions $n(\mathbf{r})$ that are actual ground-state densities belonging to some external potential v. Such functions $n(\mathbf{r})$ are called v-representable. In DFT the ground state density $n(\mathbf{r})$ of the many-electron interacting system can be obtained as a ground state density of a noninteracting system, where, for both the interacting and noninteracting (Kohn-Sham) systems the external potential is same. This is a consequence of $n(\mathbf{r})$ being v-representable in DFT. Now, in TDDFT the one-to-one correspondence between the time–dependent potential and the time–dependent density, involves an *initial state* (not necessarily the ground state). The *initial state* of the interacting system need not be the same as that of the noninteracting one. This fact questions the v-representability of the time–dependent density. The question is represented in Fig. 3.3

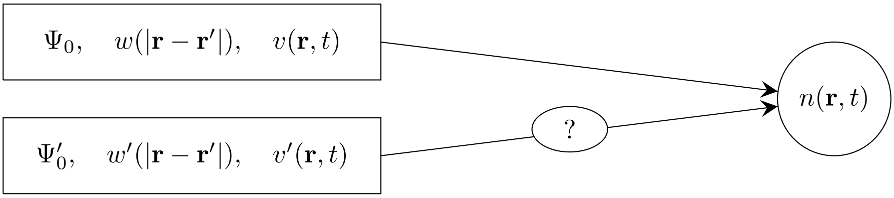

FIGURE 3.3: Schematic representation of the question answered by the van-Leeuwen theorem.

If we start from a different Hamiltonian, having a different external time–dependent potential ($v'(\mathbf{r},t)$), a different initial state (Ψ'_0), and a different interaction potential ($w'(|\mathbf{r}-\mathbf{r}'|)$) (which for the case of a non-interacting Kohn–Sham-like system is zero), is it always possible to have the same density $n(\mathbf{r},t)$ as that of the actual interacting many–body system, with the condition that the density $n(\mathbf{r},t)$ is *uniquely* determined by the potential $v'(\mathbf{r},t)$?

3.2.2.b van Leeuwen theorem

The question was affirmatively answered by van Leeuwen [180] provided some initial conditions are fulfilled. The conditions required are:

- The initial states Ψ_0 and Ψ'_0 should yield the same density at the initial time $t=t_0$,
$$n(\mathbf{r},t_0)=n(\mathbf{r},t_0); \tag{3.2.9}$$
- Also, the time derivatives of the densities at $t=t_0$ should be the same:
$$\frac{\partial}{\partial t}n(\mathbf{r},t)\bigg|_{t=t_0}=\frac{\partial}{\partial t}n'(\mathbf{r},t)\bigg|_{t=t_0}. \tag{3.2.10}$$
Recognizing, the momentum as $\mathbf{P}(t)=\int d^3r\ \mathbf{j}(\mathbf{r},t)=\int d^3r\ \mathbf{r}\ \frac{\partial}{\partial t}n(\mathbf{r},t)$, this conditions implies that the initial momenta of the two systems should be same.

Having these two initial conditions satisfied, the van Leeuwen theorem [180] ensures that, *for a time-dependent density $n(\mathbf{r},t)$ associated with a many-body system with a given particle–particle interaction $w(|\mathbf{r}-\mathbf{r}'|)$, external potential $v(\mathbf{r},t)$, and initial state Ψ_0 , there exists a different many-body system featuring an interaction $w'(|\mathbf{r}-\mathbf{r}'|)$ and a unique external potential $v'(\mathbf{r},t)$ [up to a purely time-dependent $C(t)$] which reproduces the same time–dependent density* [181]. The proof of theorem can in found in reference [180, 181].

3.2.2.c Time–Dependent Kohn–Sham (TDKS) equations

Having established the one-to-one correspondence between time–dependent density and time–dependent potential; and the question of time–dependent v-representability of the time–dependent density answered; one can chose a noninteracting ($w'=0$) Kohn–Sham system, with time–dependent potential $v_s[n](\mathbf{r},t)$, initial wavefunction

Φ_0, and in order to get the same $n(\mathbf{r},t)$ as the one corresponding to the interacting system. In general, this potential is a functional of density (n), of the initial states of the interacting system, and of the noninteracting Kohn–Sham system: $v_s[n,\Psi_0,\Phi_0](\mathbf{r},t)$.

In this noninteracting system, if Φ_0 is the ground state of the system, then following the Hohenber–Kohn theorem, along with the actual ground state (Ψ_0), it is also a functional of ground state density $n_0(\mathbf{r})$. The Φ_0 can be expressed as a single Slater determinant made up of single–particle Kohn–Sham orbitals $\varphi_j^0(\mathbf{r})$, like in eq.3.1.29, which follow the static Kohn–Sham equation 3.1.30, and also gives the ground state density as in eq.3.1.31, which is also the initial density. However, the time–dependent density $n(\mathbf{r},t)$ in this noninteracting system is given by,

$$n(\mathbf{r},t)=\sum_{j=1}^{N}|\varphi_j(\mathbf{r},t)|^2, \tag{3.2.11}$$

where each of the single–particle orbitals $\varphi_j(\mathbf{r},t)$ follows the time–dependent Schrödinger–like equations called time–dependent Kohn–Sham (TDKS) equations,

$$\left[-\frac{\nabla}{2}+v_s[n](\mathbf{r},t)\right]\varphi_j(\mathbf{r},t)=i\frac{\partial}{\partial t}\varphi_j(\mathbf{r},t), \tag{3.2.12}$$

with the initial condition,

$$\varphi_j(\mathbf{r},t_0)=\varphi_j^0(\mathbf{r}). \tag{3.2.13}$$

In eq.3.2.12, the effective Kohn–Sham potential is defined as,

$$v_s[n](\mathbf{r},t)=v(\mathbf{r},t)+v_H(\mathbf{r},t)+v_{xc}[n](\mathbf{r},t), \tag{3.2.14}$$

where the time–dependent Hartree potential is

$$v_H[n]=\int d^3r'\,\frac{n(\mathbf{r}',t)}{|\mathbf{r}-\mathbf{r}'|}. \tag{3.2.15}$$

The equation 3.2.14 also defines the time–dependent xc potential $v_{xc}[n](\mathbf{r},t)$.

There is an alternative manner to come to the TDKS, by variational principle involving the action functional, similarly as done in DFT by minimizing the total energy. Following, eq.3.2.8, one can determine the action as a functional of the time–dependent density up to some additive constant as,

$$A[n] = B[n] - \int_{t_0}^{t_1} dt \int d^3r \; v(\mathbf{r}, t) \; n(\mathbf{r}, t) \tag{3.2.16}$$

where $B[n]$ is independent of the potential $v(\mathbf{r}, t)$, and it's expression for the time–dependent Kohn–Sham system defines the exchange–correlation action functional:

$$\begin{aligned} B[n] = \int_{t_0}^{t_1} dt \; \langle \varphi_j[n](t)| \, i\frac{\partial}{\partial t} - \frac{\nabla^2}{2} \, |\varphi_j[n](t)\rangle \\ - \frac{1}{2}\int_{t_0}^{t_1} dt \int d^3r \int d^3r' \frac{n(\mathbf{r}, t) n(\mathbf{r}', t)}{|\mathbf{r} - \mathbf{r}'|} - A_{xc}[n]. \end{aligned} \tag{3.2.17}$$

The role of $A_{xc}[n]$ in TDDFT is analogous to that of $E_{xc}[n]$ in DFT. Minimizing the action functional with respect to the time–dependent density, under the constraint $n(\mathbf{r}, t) = \sum_j |\varphi_j(\mathbf{r}, t)|^2$, one gets the TDKS equations (3.2.12) and an expression for the time–dependent exchange–correlation potential as

$$v_{xc}(\mathbf{r}, t) = \frac{\delta A_{xc}[n]}{\delta n(\mathbf{r}, t)}. \tag{3.2.18}$$

3.3 Using the TDKS Equation in Practice

The TDKS equation is the working formula we use for solving many types of problems can be addressed within the framework of TDDFT. In this thesis, the problem of calculating optical absorption spectrum of clusters is discussed. Absorption is calculated by calculating the response of a system due to an external potential. Formulation of this problem within the framework of TDDFT is described as follows.

Potential and Initial State. We deal with a time–dependent problem where at $t = t_0$, a system in its ground state begins to evolve under the influence of an explicitly time–dependent potential. Therefore, we can write the potential as,

$$v(\mathbf{r}, t) = v_0(\mathbf{r}) + v_1(\mathbf{r}, t) \; \theta(t - t_0) \tag{3.3.1}$$

where $\theta(t - t_0)$ is the step function which is 1 for $t \geq t_0$ and 0 otherwise. Thus, the initial state is the ground state Ψ_0. Following Kohn–Sham DFT, the initial density

$n_0(\mathbf{r})$ (which is the ground state density) can be obtained from the Kohn–Sham orbitals (3.1.31). We notice that this way we satisfy the van Leeuwen condition 3.2.9, and thus, the Kohn–Sham orbitals φ_j^0 of the ground state give the initial state of the noninteracting time–dependent Kohn–Sham system which would give the same time–dependent density $n(\mathbf{r}, t)$ as the actual interacting system.
Here, we recall static DFT, that in order to get $n_0(\mathbf{r})$ one needs to solve Kohn–Sham equations 3.1.30 and some approximation has to be made for the xc potential ($v_{xc}[n_0](\mathbf{r})$), as discussed in the previous section.

3.3.1 Adiabatic Approximation

The time–dependent Kohn–Sham potential ($v_s[n](\mathbf{r}, t)$) in eq.3.2.14 is a functional of the time–dependent density $n(\mathbf{r}, t)$. In principle, and more precisely, $v_s[n](\mathbf{r}, t)$ is a *causal* and memory dependent functional of $n(\mathbf{r}, t)$, i.e., it depends on the entire history of the $n(\mathbf{r}, t)$. The detailed discussion on this topic is beyond the scope of this thesis and can be found in Ref. [181]. From the expression of the $v_s[n](\mathbf{r}, t)$ (3.2.14), we note that this memory dependence is entirely borne by the time–dependent xc potential $v_{xc}[n](\mathbf{r}, t)$, which makes it much more complex than the xc potential, $v_{xc}[n_0](\mathbf{r})$, in static DFT. In practice, therefore, on top of the approximations for $v_{xc}[n_0](\mathbf{r})$, one needs to make further approximation for $v_{xc}[n](\mathbf{r}, t)$ in order to make it tractable. To this end, the adiabatic approximation can be used, where we just neglect the memory dependence of the $v_{xc}[n](\mathbf{r}, t)$.

Under adiabatic approximation, the time–dependent xc potential is evaluated in the same manner as for the case of static DFT, but using the instantaneous time–dependent density instead of the ground state density:

$$v_{xc}^{Adia}(\mathbf{r}, t) = v_{xc}^0[n_0](\mathbf{r})\bigg|_{n_0(\mathbf{r})\rightarrow n(\mathbf{r},t)} \tag{3.3.2}$$

where $v_{xc}^0[n_0](\mathbf{r})$ is also approximated (by LDA, GGA, etc.) as its exact form is not known.

Here the physical meaning of “adiabatic” is that the system (here, the time–dependent Kohn–Sham system) remains in its instantaneous eigenstate (ground state) because the acting perturbation/potential (in this case the $v_s[n](\mathbf{r}, t)$), whose functional dependence is primarily characterized by $v_{xc}[n](\mathbf{r}, t)$ is slow enough. Under adiabatic approximation, the action functional is evaluated as

$$A_{xc}^{Adia}[n] = \int_{t_0}^{t_1} dt\ E_{XC}[n_0]\Big|_{n_0(\mathbf{r})\to n(\mathbf{r},t)} \tag{3.3.3}$$

where $E_{XC}[n(\mathbf{r},t)]$ is the XC functional in static DFT evaluated using $n(\mathbf{r},t)$ instead of n_0, at a time t. And thus, following the expression of $v_{xc}[n](\mathbf{r},t)$ in eq.3.2.18, one gets back to the adiabatically approximated expression of the time–dependent xc potential in eq.3.3.2.

The most common and widely used time–dependent xc potential are the adiabatic local–density approximation (ALDA) and the adiabatic generalized gradient approximation (AGGA), where local–density approximation and generalized gradient approximation are used respectively for the $v_{xc}^0[n_0](\mathbf{r})$ in eq.3.3.2. For all the calculations that will be presented in this thesis, these two types of time–dependent xc potentials are used.

The adiabatic approximation is justified only in the limit of infinitely slow electron dynamics, close to the instantaneous ground state. It is applicable to describe only that part of the excitation spectrum which correspond to single-particle excitations, and not the double- or multi-particle ones.

3.3.2 Solving the TDKS Equations Self-consistently

After discussing the details of the TDKS equation, here a brief description of solving it self-consistently is given. As mentioned earlier, in this thesis we deal with problems where the initial state is the ground state. In the TDKS scheme one needs to find the correct time evolution of the Kohn–Sham orbitals which represent (in our case) the ground state. This is done in a self-consistent manner involving the time propagation scheme:

1. The ground-state density $n_0(\mathbf{r})$ of a system and the Kohn–Sham orbitals are obtained by solving Kohn–Sham equations through an iterative self-consistent scheme as shown in Fig.3.1.
2. In the next step we need to do is to guess a time–dependent density $n(\mathbf{r},t)$ for all time t in $[t_0, t]$, except for t_0, because $n(\mathbf{r},t_0) = n_0(\mathbf{r})$ (already calculated in first step).

3. Using the density of the previous step ($n^i(\mathbf{r},t)$), the time–dependent Kohn–Sham potential is evaluated: $v_s[n^{(i)}](\mathbf{r},t)$; and propagating TDKS equation a new set of orbitals $\varphi_j^{(i+1)}(\mathbf{r},t)$ is obtained for all times t in $[t_0,t]$.

4. Using the new set of time–dependent orbitals, the new density $n^{(i+1)}(\mathbf{r},t)$ is evaluated for all times t in $[t_0,t]$. If the difference between $n^{(i+1)}(\mathbf{r},t)$ and $n^i(\mathbf{r},t)$ is greater than some given threshold value, steps 2 and 3 are repeated iteratively; otherwise the converged time–dependent density is obtained as $n^{(i+1)}(\mathbf{r},t)$.

Though the recipe of getting the time–dependent density seems to be similar to the one for the static case (Fig.3.1), it is cumbersome for the fact that one needs to do a starting guess of the density for all times between t_0 and t_1. To get rid of it, numerically the self-consistent scheme is done in small steps of time rather than over the entire time interval. The entire time interval of evolution is discretized in small steps $\triangle t$, and one calculates the propagation of the system from t to $t+\triangle t$. One example of widely used algorithm for the numerical self-consistent propagation of the TDKS equation is the Crank–Nicholson algorithm.

3.4 Linear Response Theory and TDDFT

In this section, the *ab initio* calculation of optical spectra in the framework of linear-response will be discussed. In literature, the acronym of the topic is LR-TDDFT ('LR' for *linear response*). Linear response theory is used for studying the response of a system under weak perturbations, or, more precisely, when the relation between the response of the system and the perturbation is linear.

3.4.1 General Framework of Liner Response

As shown in eq.3.3.1, the external potential has a static part and a time–dependent perturbation. The corresponding Hamiltonian, therefore, can be written as,

$$\hat{\mathcal{H}}(t)=\hat{\mathcal{H}}_0+\hat{\mathcal{H}}_1(t), \tag{3.4.1}$$

where $\hat{\mathcal{H}}_1(t)$ contains the perturbing potential (which, in the case of eq.3.3.1 is $v_1(\mathbf{r},t)\ \theta(t-t_0)$). Here we assume that out perturbing Hamiltonian has a general form,

$$\hat{\mathcal{H}}_1(t) = F(t)\ \hat{\beta} \tag{3.4.2}$$

where, $F(t)$ is an external field that couples with an observable represented by the operator $\hat{\beta}$.

Quantum mechanically, the response associated to an observable due to a perturbation is the difference in the expectation value of that observable with respect to its unperturbed expectation value:

$$\alpha(t) - \alpha_0 = \langle \Psi(t) | \hat{\alpha} | \Psi(t) \rangle - \langle \Psi_0 | \hat{\alpha} | \Psi_0 \rangle \tag{3.4.3}$$

In general, the response can be expanded in powers of the perturbation:

$$\alpha(t) - \alpha_0 = \alpha_1(t) + \alpha_2(t) + \alpha_3(t) + \cdots \tag{3.4.4}$$

where, $\alpha_1(t)$ is the linear response, $\alpha_2(t)$ is the quadratic response, and so on.

The time–dependent perturbation in eq. 3.4.2 is nothing more than a time–dependent field, $F(t)$, coupled to an observable. Noting that the unperturbed Hamiltonian $\hat{\mathcal{H}}_0$ is independent of time, the linear response for this kind of perturbation is given by,

$$\alpha_1(t) = \int_{-\infty}^{\infty} \chi_{\alpha\beta}(t - t')\ F(t') \tag{3.4.5}$$

where (in the interaction picture representation)

$$\chi_{\alpha\beta}(t - t') = -i\theta(t - t')\ \ \langle \Psi_0 | [\hat{\alpha}(t - t'), \hat{\beta}] | \Psi_0 \rangle \tag{3.4.6}$$

is the linear response function for the observable α due to the perturbation through the observable β. $\theta(t - t')$ is the step function as used in eq.3.3.1. In the frequency domain, the equation reads

$$\alpha_1(\omega) = \chi_{\alpha\beta}(\omega)\ F(\omega), \tag{3.4.7}$$

where

$$\chi_{\alpha\beta}(\omega) = -i \int_{-\infty}^{\infty} \theta(\tau)\ \ \langle \Psi_0 | [\hat{\alpha}(\tau), \hat{\beta}] | \Psi_0 \rangle\, e^{i\omega\tau}. \tag{3.4.8}$$

The linear response function, $\chi_{\alpha\beta}(\omega)$, contains all the information of the response due to a perturbation in the linear regime, and therefore is the central feature of theory.

In passing, it is worth to mention that one can derive from eq.3.4.7 the so-called Lehmann representation,

$$\chi_{\alpha\beta}(\omega) = \lim_{\eta\to 0^+} \sum_{n=1}^{\infty} \left\{ \frac{\langle\Psi_0|\hat{\alpha}|\Psi_n\rangle\,\langle\Psi_n|\hat{\beta}|\Psi_0\rangle}{\omega - \Omega_n + i\eta} - \frac{\langle\Psi_0|\hat{\beta}|\Psi_n\rangle\,\langle\Psi_n|\hat{\alpha}|\Psi_0\rangle}{\omega - \Omega_n - i\eta} \right\} \tag{3.4.9}$$

where Ψ_n $(n = 0, 1, 2, \cdots, \infty)$ are the eigenfunctions of the unperturbed Hamiltonian $\hat{\mathcal{H}}_0$, with eigen-energies $E_0 = E_{GS}, E_1, E_2, \cdots, E_\infty$; η comes from the integral representation of $\theta(\tau)$; and $\Omega_n = E_n - E_0$. The poles of a linear-response operator in the Lehmann representation occur at the exact excitation energies of the system.

3.4.2 Linear Response of Kohn–Sham System

Within the framework of linear response theory, TDDFT allows us to evaluate the response function of a many-body interacting system in terms of the response function of the corresponding Kohn–Sham system. For the many-body interacting system, from eq. 3.2.1 and eq. 3.4.2 we can write,

$$\hat{\mathcal{H}}_1(t) = F(t)\,\hat{\beta} = \hat{\mathcal{V}}^{(1)} = \int d^3r'\; v_1(\mathbf{r}, t)\;\hat{n}(\mathbf{r}') \tag{3.4.10}$$

where $v_1(\mathbf{r}, t)$ is defined in eq. 3.3.1. Therefore, following eq.3.4.5, and having understood $\hat{\beta} = \hat{n}(\mathbf{r}')$ and $\hat{\alpha} = \hat{n}(\mathbf{r})$, the density-density response due to the perturbation $v_1(\mathbf{r}, t)$ in first order is given by

$$n_1(\mathbf{r}, t) = \int dt' \int d^3r\; \chi(\mathbf{r}, \mathbf{r}', t, t')\; v_1(\mathbf{r}', t') \tag{3.4.11}$$

where, $\chi(\mathbf{r}, \mathbf{r}', t, t')$ is the response function, given as

$$\chi(\mathbf{r}, \mathbf{r}', t, t') = \left.\frac{\delta n[v](\mathbf{r}, t)}{\delta v(\mathbf{r}', t')}\right|_{v[n_0](\mathbf{r}) \equiv v_0(\mathbf{r})}. \tag{3.4.12}$$

In the corresponding time–dependent Kohn–Sham system, we deal with the effective potential (3.2.14), which is the functional of the total time–dependent density. As the total time–dependent density can be expressed up to the first-order response as

$n(\mathbf{r},t) = n_0 + n_1(\mathbf{r},t)$, the Kohn–Sham potential is rewritten up to the first order expansion as

$$v_s[n](\mathbf{r},t) = v_s[n_0](\mathbf{r},t) + v_{s1}[n_1](\mathbf{r},t), \tag{3.4.13}$$

where $v_{s1}[n_1](\mathbf{r},t)$ is the linearized effective potential, given as

$$v_{s1}[n_1](\mathbf{r},t) = v_1(\mathbf{r},t) + \int d^3r' \frac{n_1(\mathbf{r}',t)}{|\mathbf{r}-\mathbf{r}'|} + v_{xc1}(\mathbf{r},t). \tag{3.4.14}$$

As the time–dependent density corresponding to the external potential can be reproduced in the noninteracting Kohn–Sham system, so can be the linear response to the density from the linearized effective potential. Therefore, following eq.3.4.11,

$$\begin{aligned} n_1(\mathbf{r},t) &= \int dt' \int d^3r' \; \chi_s(\mathbf{r},\mathbf{r}',t,t') \; v_{s1}(\mathbf{r}',t') \\ &= \int dt' \int d^3r' \; \chi_s(\mathbf{r},\mathbf{r}',t,t') \left[v_1(\mathbf{r}',t') + \int d^3x \frac{n_1(\mathbf{x},t)}{|\mathbf{r}'-\mathbf{x}|} + v_{xc1}(\mathbf{r}',t') \right] \end{aligned} \tag{3.4.15}$$

In this expression, the integrand of the last term on the R.H.S., $v_{xc1}(\mathbf{r}',t')$, is of utmost interest. It is called the linearized xc potential, and its explicit expression comes from the functional Taylor expansion as

$$v_{xc1}(\mathbf{r},t) = \int d\tau \int d^3x \; f_{xc}(\mathbf{r},\mathbf{x},t,\tau) \; n_1(\mathbf{x},\tau), \tag{3.4.16}$$

where

$$f_{xc}(\mathbf{r},\mathbf{x},t,\tau) = \left. \frac{\delta v_{xc}[n](\mathbf{r},t)}{\delta n(\mathbf{x},\tau)} \right|_{n_0(\mathbf{r})} \tag{3.4.17}$$

is called the time–dependent xc kernel.

With the expression of $v_{xc1}(\mathbf{r},t)$ in eq.3.4.16, the expression of $n_1(\mathbf{r},t)$ (3.4.15) becomes,

$$\begin{aligned} n_1(\mathbf{r},t) = \int dt' \int d^3r' \; \chi_s(\mathbf{r},\mathbf{r}',t,t') \Bigg[& v_1(\mathbf{r}',t') + \int d^3x \frac{n_1(\mathbf{x},t)}{|\mathbf{r}'-\mathbf{x}|} \\ & + \int d\tau \int d^3x \; f_{xc}(\mathbf{r}',\mathbf{x},t',\tau) \; n_1(\mathbf{x},\tau) \Bigg] \end{aligned} \tag{3.4.18}$$

Now, as both the interacting and noninteracting (Kohn–Sham) systems give the same linear response to the density $n_1(\mathbf{r},t)$, comparing $n_1(\mathbf{r},t)$ in eq.3.4.11 with $n_1(\mathbf{r},t)$ in eq.3.4.18 we get,

$$\begin{aligned}\chi(\mathbf{r},\mathbf{r}',t,t') = \chi_s(\mathbf{r},\mathbf{r}',t,t') \\ + \int d\tau \int d^3x \int d\tau' \int d^3x'\ \chi_s(\mathbf{r},\mathbf{x},t,\tau)\Bigg\{\frac{\delta(\tau-\tau')}{|\mathbf{x}-\mathbf{x}'|} \\ + f_{xc}(\mathbf{x},\mathbf{x}',\tau,\tau')\Bigg\}\chi(\mathbf{x}',\mathbf{r}',\tau',t'),\end{aligned} \tag{3.4.19}$$

a Dyson-like equation that relates the interacting and noninteracting density–density response functions. Though it is not shown explicitly, in the expression (3.4.19) of $\chi(\mathbf{r},\mathbf{r}',t,t')$, all the quantities are functionals of the ground state density except the Hartree term (as it always has a simple explicit functional form). As mentioned earlier, the density–density response function is the key quantity in linear response; and eq.3.4.19 is the central equation of LR-TDDFT. In frequency domain it reads as,

$$\chi(\mathbf{r},\mathbf{r}',\omega) = \chi_s(\mathbf{r},\mathbf{r}',\omega) + \int d^3x \int d^3x'\ \chi_s(\mathbf{r},\mathbf{x},\omega)\ f_{Hxc}(\mathbf{x},\mathbf{x}',\omega)\ \chi(\mathbf{x}',\mathbf{r}',\omega), \tag{3.4.20}$$

where,

$$f_{Hxc}(\mathbf{x},\mathbf{x}',\omega) = \frac{1}{|\mathbf{x}-\mathbf{x}'|} + f_{xc}(\mathbf{x},\mathbf{x}',\omega) \tag{3.4.21}$$

is called the frequency dependent Hartree-exchange-correlation kernel.

3.4.2.a xc kernel

In TDDFT linear response, $\chi(\mathbf{r},\mathbf{r}',\omega)$ contains all the information of the electronic excitations. It has poles at excitation frequencies, i.e., it diverges for all values of ω that equal to the electronic transition frequencies. $\chi_s(\mathbf{r},\mathbf{r}',\omega)$ also has such poles which correspond to single-particle excitations of the Kohn–Sham system. In Lehmann representation it is expressed as,

$$\chi_s(\mathbf{r},\mathbf{r}',\omega) = 2\lim_{\eta\to 0^+}\sum_{j=1}^{\infty}\sum_{k=1}^{\infty}\left\{\frac{\varphi_j^0(\mathbf{r})\varphi_k^{0*}(\mathbf{r})\varphi_j^{0*}(\mathbf{r}')\varphi_k^0(\mathbf{r}')}{\omega-\Omega_{jk}+\eta} - \frac{\varphi_j^0(\mathbf{r})\varphi_k^{0*}(\mathbf{r})\varphi_j^{0*}(\mathbf{r}')\varphi_k^0(\mathbf{r}')}{\omega-\Omega_{jk}-\eta}\right\}, \tag{3.4.22}$$

where, $\Omega_{jk} = E_k^{(unocc)} - E_j^{(occ)}$; E_n being the eigenenergy of KS orbital φ_n^0. So, χ_s is available in the ground state Kohn–Sham scheme.

In absence of f_{Hxc}, $\chi = \chi_s$. Therefore, within the framework of linear response, the role of the kernel f_{Hxc} is to take into account all the effects of many-body interactions. It shifts (or, rearranges) the transitions of the Kohn–Sham system such that they move towards the actual transitions. Also, it renormalizes the strength of the poles of χ and gives correct oscillator strengths in the optical absorption spectrum. As an example, for an elongated system of 37 gold atoms, the effect of f_{Hxc} on the absorption spectrum is shown in Fig.3.4. Thus, in order to properly describe the excitations of an interacting many-body system the most concerned quantity is f_{Hxc}, and requires to be addressed properly.

In practice, of course approximations are needed for the kernel f_{xc}, because it is derived from E_{XC} and/or v_{xc} whose exact forms are not known. The kernel is non-local both in time and space. The approximation for the spatial non-locality is done by considering adiabatically approximated expression(s) of the time–dependent xc

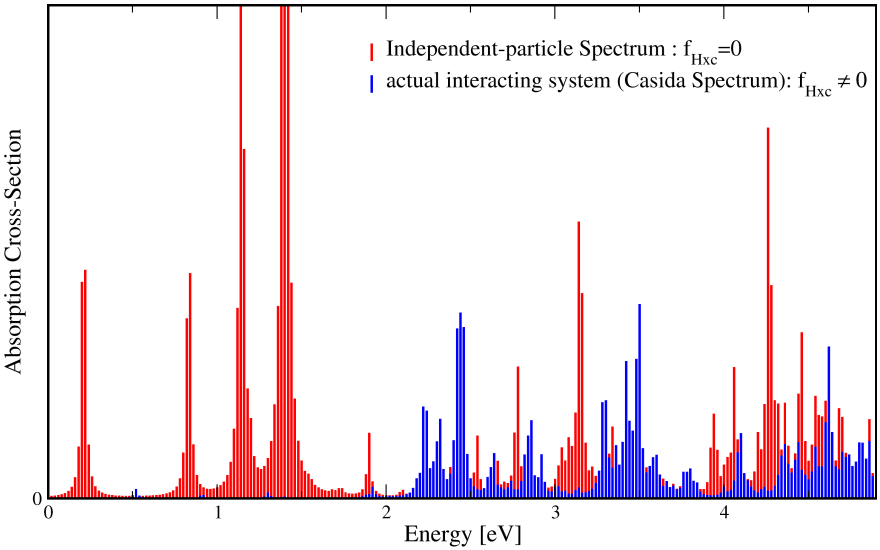

FIGURE 3.4: Optical absorption spectra for Au$_{37}$ gold rod. The red spectrum correspond to the excitation in the independent particle system, where in the Kohn–Sham potential the Hartee and xc contribution is zero. The blue spectrum correspond to the excitation of actual interacting many-electron system represented by the total Kohn–Sham pootential.

potential, $v_{xc}[n](\mathbf{r},t)$. The simplest approximation for the temporal non-locality is done by simply ignoring it as,

$$f_{xc}^{adia}[n](\mathbf{r},\mathbf{r}',t-t') = \left.\frac{\delta v_{xc}[n](\mathbf{r},t)}{\delta n(\mathbf{r}',t')}\right|_{n_0(\mathbf{r})} \delta(t-t); \tag{3.4.23}$$

i.e., we make it completely local in time.

3.4.2.b Casida formalism

In order to get the absorption cross-section due to the linear response of the many-body system, one needs to find out the poles of the density-density response function $\chi(\mathbf{r},\mathbf{r}',\omega)$. The frequency dependence of the kernel makes this job cumbersome. Mark E. Casida showed that for a frequency dependent kernel $f_{Hxc}(\omega)$, one can find the poles of $\chi(\mathbf{r},\mathbf{r}',\omega)$ by solving an equivalent eigenvalue problem [182] given as,

$$\sum_{q'} R_{qq'}\mathbf{F}_q' = \Omega_q^2 \mathbf{F}_q, \tag{3.4.24}$$

known as Casida equation, where the indices q and q' denote transitions from an occupied state to an unoccupied one, and the matrix element of $R_{qq'}$, is given by,

$$R_{qq'} = \omega_q^4 \delta_{qq'} + 4\sqrt{\omega_q \omega_q'}\, K_{qq'}, \tag{3.4.25}$$

where $\delta_{qq'}$ is the Kronecker-Delta, and the matrix elements of $K_{qq'}$ are given as,

$$K_{qq'} = \int d^3r \int d^3r'\ \xi^*(\mathbf{r})\ f_{Hxc}(\mathbf{r},\mathbf{r}',\omega)\ \xi(\mathbf{r}'), \tag{3.4.26}$$

where, $\xi(\mathbf{r}) = \varphi_{i(occ)}^{0*}(\mathbf{r})\varphi_{a(unocc)}^{0}(\mathbf{r}')$ and,

$$f_{Hxc}(\mathbf{r},\mathbf{r}',\omega) = \frac{1}{|\mathbf{r}-\mathbf{r}'|} + f_{xc}(\mathbf{r},\mathbf{r}',\omega) \tag{3.4.27}$$

By solving the Casida equation (3.4.24) one gets the excitation energies Ω_q, and the oscillator strengths for the excitations are extracted from the eigenvectors $\mathbf{F}_q$ [182]. Moreover, as the density response is given by the response function (3.4.11), in principle the spatial profiles of the eigenmodes of the density response ($n_1(\mathbf{r},\Omega_q)$) for a corresponding eigenenergies Ω_q can also be obtained. These, eigenmodes can be visualized through the transition densities which are of particular interest, because they represent unique spatial distribution of the charge-density fluctuations associated with the corresponding excitation.

3.5 Real-Time TDDFT

In the linear response TDDFT (LR-TDDFT), the linearized density response, $n_1(\mathbf{r}, t)$, relates the density–density response functions of the interacting and noninteracting (Kohn–Sham) systems. The response functions are functionals of the ground state density. The interacting response function $\chi(\mathbf{r}, \mathbf{r}', \omega)$ contains all the required information regarding the linear response spectrum. In order to get the spectrum, therefore, what one needs is to solve eq.3.4.20 in frequency domain, with proper description of the frequency dependent Hartree-xc kernel f_{Hxc}. This can be done using the prescription given by Casida [182]. Thus in LR-TDDFT one does not explicitly need $n_1(\mathbf{r}, t)$ to get the spectrum. In fact a density response due to a particular transition frequency Ω_n can be reconstructed from the transition density for that frequency as

$$n_1^{(\Omega_n)}(\mathbf{r}, t) = n_1(\mathbf{r}, \Omega_n)e^{-i\Omega_n t}. \tag{3.5.1}$$

However, within the framework of TDDFT, there exists another alternative way to calculate the optical absorption spectrum directly from $n_1(\mathbf{r}, t)$. The method is known as Real-Time TDDFT (RT-TDDFT) or also *time-evolution formalism*.

3.5.1 Optical Absorption Spectrum

In RT-TDDFT, one uses the time–dependent density, $n(\mathbf{r}, t)$, which is obtained from the time evolved Kohn–Sham states which in turn are obtained by solving the TDKS. The difference between the time–dependent and the initial (i.e. ground state) densities can then be written as,

$$\delta n(\mathbf{r}, t) = n(\mathbf{r}, t) - n_0(\mathbf{r}) = n_1(\mathbf{r}, t) + n_2(\mathbf{r}, t) + \cdots + \infty. \tag{3.5.2}$$

In the linear regime, i.e., if the relation between the perturbing potential $v_1(\mathbf{r}, t)$ and the $\delta n(\mathbf{r}, t)$ is linear, all the higher order terms other than the first one, $n_1(\mathbf{r}, t)$, can be neglected in the eq.3.5.2:

$$\delta n(\mathbf{r}, t) = n_1(\mathbf{r}, t). \tag{3.5.3}$$

In linear response RT-TDDFT, the linearized density response, $n_1(\mathbf{r}, t)$, is the central ingredient required to get the optical linear response spectra. However, in general, RT-TDDFT applies for higher order density responses too. In principle, one can obtain higher-order response spectrum by considering higher order terms in the expression of $\delta n(\mathbf{r}, t)$. In this thesis we restrict the calculation to the linear regime by using sufficiently weak perturbation.

In order to calculate the linear response photoabsorption spectrum, we begin with the induced electric dipole polarization:

$$\mathbf{p}(t) = \int dt' \, \bar{\alpha}(t - t') \, \mathbf{E}(t') \tag{3.5.4}$$

where $\bar{\alpha}$ is the dynamic polarizability tensor,

$$\bar{\alpha} = \begin{pmatrix} \alpha_{xx} & \alpha_{xy} & \alpha_{xz} \\ \alpha_{yx} & \alpha_{yy} & \alpha_{yz} \\ \alpha_{zx} & \alpha_{zy} & \alpha_{zz} \end{pmatrix}, \tag{3.5.5}$$

where the $\mu\nu$ element $\alpha_{\mu\nu}$ describes the μ-component of the dynamic polarizabilities due to the ν-component of the response $n_1(\mathbf{r}, t)$; $\mu, \nu \in \{x, y, z\}$. $\mathbf{E}(t)$ is the externally applied time–dependent electric field, and is related to the perturbing potential as

$$\mathbf{E}(t) = -\nabla v_1(\mathbf{r}, t). \tag{3.5.6}$$

In general, $\mathbf{E}(t)$ is a function of both space and time, but within dipole approximation, it is homogeneous in space. The dipole approximation is applicable to any system whose dimension along the direction of the perturbing field are much smaller the wavelength of the field. In this thesis, for all the systems studied, this dimension is $< 3nm$, whereas, the range of the optical wavelength (visible: $390nm - 700nm$) is two orders of magnitude longer. Therefore the dipole approximation is perfectly applicable

We consider a monochromatic homogeneous electric field polarized along the z-direction,

$$\mathbf{E}(t) = \hat{\mathbf{z}} \, \mathscr{E} \, sin(\omega t), \tag{3.5.7}$$

where, $\mathscr{E}$ is the amplitude of the electric field. Thus the perturbing potential is,

$$v_1(\mathbf{r}, t) = \mathscr{E}\ z\ sin(\omega t). \tag{3.5.8}$$

The z-component of the dipole polarizability is then obtained from the linearized density response as

$$p_z(t) = -\int d^3r\ z\ n_1(\mathbf{r}, t). \tag{3.5.9}$$

Performing Fourier transform, we get the expression in the frequency domain as

$$p_z(\omega) = -\int d^3r\ z\ n_1(\mathbf{r}, \omega). \tag{3.5.10}$$

The zz-element of the dynamic polarizability is then given by

$$\alpha_{zz}(\omega) = -\frac{2}{\mathscr{E}}\int d^3r\ z\ n_1(\mathbf{r}, \omega). \tag{3.5.11}$$

The corresponding photoabsorption cross-section is directly obtained from the imaginary part of α_{zz} as

$$\sigma_{zz}(\omega) = \frac{4\pi\omega}{c}\ \Im\alpha_{zz}(\omega). \tag{3.5.12}$$

The optical absorption cross-section satisfies the sum rule given by

$$\int_0^\infty d\omega\ \frac{\sigma_{zz}}{\omega^2} = \frac{2\pi^2}{c}\alpha_{zz}(0), \tag{3.5.13}$$

where $\alpha_{zz}(0)$ is the static dipole polarizability.

3.5.2 Delta Kick Perturbation

The RT-TDDFT method to obtain the absorption cross-section discussed before gives the cross-section for an excitation given by a monochromatic electric field. Therefore, in the cross-section spectrum, one would get only the response of the excitation that represents the pole of $\chi(\mathbf{r}, \mathbf{r}', \omega)$ for $\omega = \omega_{mono}$; i.e. a Dirac-delta function at ω_{mono} signifying the excitation of the corresponding eigenmode. And that only if the pole exists for the frequency ω_{mono}. All the other poles will not appear in the spectrum. In RT-TDDFT, therefore, in order to get the whole spectrum of the absorption cross-section, there are two choices.

- The first choice is to evaluate $n_1^{(\omega_i)}$ for each of the perturbing monochromatic electric field that has frequency ω_i, within a particular frequency range of interest. Then one can calculate the absorption cross-section, $\sigma(\omega_i)$, from each $n_1^{(\omega_i)}$ and finally put all of them together to get the spectrum of the chosen frequency range.
- The second choice is to find out a linearized density response $n_1^{(all)}$, that contains the linear response due to a perturbation that represents all possible excitations in the system; and then calculate the absorption cross-section from $n_1^{(all)}$.

The first choice is of course discarded due to the fact that it would require to perform the same time evolution calculation for a large number of perturbations by monochromatic field of different frequencies, which is cumbersome. Therefore, we are left with the second choice only, for which we need to find a perturbation abrupt in time, like a *hammer* hitting a bell. The *hammer* perturbation in TDDFT is employed either by using a uniform static electric field which is switched off at the initial time of perturbation: $\mathbf{E}^{step}(t) = \hat{\mathbf{n}}\ E_0\ \theta(t_0 - t)$; or by using a delta impulse in time. In this thesis the later has been used.

3.5.2.a Electric field with delta impulse in time

The electric field has the temporal shape of a delta function at $t = 0$, the beginning of the time evolution:

$$\mathbf{E}^{\text{delta}}(t) = \hat{\mathbf{n}}\ E_n^{\text{delta}}(t) = \hat{\mathbf{n}}\ \mathcal{I}\ \delta(t) \tag{3.5.14}$$

where $\hat{\mathbf{n}}$ denotes the polarization of the electric field. The dynamic dipole polarizability in frequency domain is expressed as,

$$\alpha_{\mu\nu}(\omega) = \frac{p_\mu(\omega)}{E_\nu(\omega)} \tag{3.5.15}$$

Having $E_\nu(\omega) = E_n^{\text{delta}}$, $\hat{\mathbf{n}} = \hat{\mathbf{z}}$, and $\mu = \nu = z$, we can get the component of the dynamic dipole polarizability along the direction (z-direction) of the perturbing impulsive electric field as

$$\alpha_{zz}^{\text{delta}}(\omega) = \frac{1}{\mathcal{I}}\, p_z^{\text{delta}}(\omega) \tag{3.5.16}$$

$$= \frac{1}{\mathcal{I}} \int dt\; e^{i\omega t}\; p_z^{\text{delta}}(t) \qquad \text{(by Fourier transform)} \tag{3.5.17}$$

$$= \frac{1}{\mathcal{I}} \int dt\; e^{i\omega t}\left(- \int d^3r\; z\; n_1^{\text{delta}}(\mathbf{r}, t)\right) \qquad \text{(from eq.3.5.9)}$$

$$= -\frac{1}{\mathcal{I}} \int d^3r\; z\; n_1^{\text{delta}}(\mathbf{r}, \omega). \tag{3.5.18}$$

Getting the cross-section $\sigma_{zz}(\omega)$ is then straightforward using eq.3.5.12. In Fig.3.5, the steps of the real time TDDFT scheme is shown for a 37-atom silver rod. The numerical implementation of the perturbation due impulsive electric field is tricky due to the fact that, in practice, the TDKS equations are solved in finite time steps.

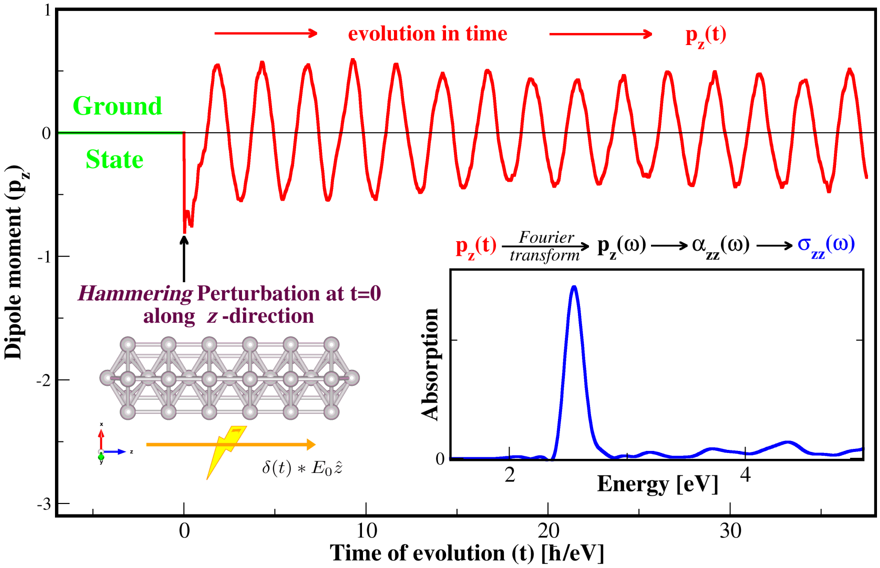

FIGURE 3.5: Schematic presentation of the RT-TDDFT in obtaining the spectrum for Ag_{37} rod using pseudopotential for describing the species. The red curve shows the oscillation of the z-component of dipole momen. The *hammering* delta-kick is the only perturbation made at $t = 0$ along z-direction. The dipole moment is obtained in frequency domain by Fourier transform and then the absorption cross-section is computed. The imaginary part of the cross-section is shown in blue.

This difficulty was overcome by a much more convenient form of the δ-kick excitation proposed by Yabana *et al.* [183, 184]. We start with a ground state at time $t_0 = 0^-$, i.e., infinitesimally before the beginning ($t = 0$) of the time evolution. The Kohn-Sham orbitals at $t_0 = 0^-$ are $\varphi_j(\mathbf{r}, 0^-)$. The Kohn-Sham orbitals infinitesimally after the beginning of time evolution, at $t_0 = 0^+$ are given by

$$\varphi_j(\mathbf{r}, 0^+) = \exp\left\{ - i \int_{0^-}^{0^+} dt' \left[\hat{\mathcal{H}}_0 + \ z\, \mathcal{I}\delta(t') \right] \right\} \varphi_j(\mathbf{r}, 0^-) \tag{3.5.19}$$

where, $\hat{\mathcal{H}}_0$ is the Kohn–Sham Hamiltonian for the ground state, and $z\, \mathcal{I}\delta(t')$ is the potential of the impulsive electric field (polarized along z-direction). The expression can be simplified as

$$\begin{aligned}\varphi_j(\mathbf{r}, 0^+) &= \exp\left\{ - i\hat{\mathcal{H}}_0 \int_{0^-}^{0^+} dt' \ - \ iz\mathcal{I} \int_{0^-}^{0^+} \delta(t')dt' \right\} \varphi_j(\mathbf{r}, 0^-) \\ &= e^{-i\hat{\mathcal{H}}_0 (0^+ - 0^-)} \ e^{-i\mathcal{I}z} \ \varphi_j(\mathbf{r}, 0^-) \\ &= e^{-i\mathcal{I}z} \left(e^{-i\hat{\mathcal{H}}_0 (0^+ - 0^-)} \ \varphi_j(\mathbf{r}, 0^-) \right) \end{aligned} \tag{3.5.20}$$

As, the interval $[0^-, 0^+]$ is infinitesimally small, the expression within the bracket can be safely approximated to yield $\varphi_j(\mathbf{r}, 0)$, i.e., the Kohn–Sham orbitals of the ground state. Consequently, we can rewrite eq. 3.5.20 as

$$\varphi_j(\mathbf{r}, 0^+) = e^{-i\mathcal{I}z} \ \varphi_j(\mathbf{r}, 0) = e^{-i\mathcal{I}z} \ \varphi_j^0(\mathbf{r}). \tag{3.5.21}$$

From this expression we can readily see that the expectation value of the momentum operator ($-i\partial/\partial z$) for any orbital $\varphi_j(\mathbf{r}, 0^+)$ is $\mathcal{I}$. Thus, the effect of the impulsive electric field perturbation is to give all the ground state Kohn–Sham orbitals a certain (the same) momentum, the magnitude of which is given by the amplitude of the impulse. As this perturbation does nothing more than multiply the initial ground state Kohn–Sham orbitals by the same phase factor, it has no effect on the initial density $v_0(\mathbf{r})$.

In this process of '*hammering*' by an impulsive electric field, in principle all the dipole-active eigenmodes of the system under consideration are excited. Therefore the absorption cross-section shows all the poles of the density-density linear response function, $\chi(\mathbf{r}, \mathbf{r}', \omega)$, provided that the strength of the '*hammering*' is as low as to remain in the linear regime, but strong enough that the response does not get drowned in numerical noise.

3.6 RT-TDDFT versus LR-TDDFT Casida method

As far as calculation of the excitation properties of metal clusters are concerned, both the Delta-kick RT-TDDFT and Casida LR-TDDFT approaches are found to be widely used in the literature. The section is closed here with a brief discussion of the pros and cons of their usage.

- The RT-TDDFT method is suitable for obtaining a spectrum over a large range of energy, while the LR-TDDFT Casida approach is preferred for calculation of well separated excitation energies. Thus, the Casida approach is more suitable for molecules or very small clusters.

- RT-TDDFT is advantageous when implemented on a real-space grid, whereas for LR-TDDFT the calculations are generally done by employing basis sets, like Gaussian basis sets for example.

- The convergence of a calculation using LR-TDDFT Casida approach depends on the size of the chosen basis. For excitations at higher energies one needs to consider larger basis, which makes the convergence of the calculation, if possible, inconveniently long to deal with. On the other hand in real-space RT-TDDFT, we do not need to calculate the empty states. The spacing and the time-step used for time evolution control the convergence. This gives real-space RT-TDDFT some degrees of advantage on handling bigger systems (5000 electrons).

- The scaling with respect to number of electron in real-space RT-TDDFT is lower than in LR-TDDFT Casida approach. However, in RT-TDDFT the time-step used for time evolution requires to be very small. For smaller spacing we need shorter time-step.

- In RT-TDDFT the information regarding the excited states is not readily accessible as the excited states are taken care of only through the time-evolution of the occupied states. They are not needed explicitly in RT-TDDFT and so we do not have them. However, projection of time-evolved wave functions on the ground state ones would be possible [185]. On the other hand, in LR-TDDFT a properly converged calculation gives all the necessary information regarding the excited states and transitions.

3.7 *Ab Initio* Simulations

All the *ab initio* simulations for obtaining the optical absorption spectra, presented in this thesis are real-space RT-TDDFT simulations performed in the real-space code `octopus` [186]. To describe the constituent species of the systems, Norm-conserving Troullier–Martins pseudopotentials [176] have been used that include the respective 5d electrons in the valence (11 valence electrons for each noble-metal atom). Relativistic effects are included as scalar relativistic correction in the radial part of the pseudopotentials. The spacing of the real-space grid was 0.20 Å for Au, 0.18 Å for Ag, and 0.16 Å for Cu. The calculation domain was made up of spheres centered around each atom with a minimum radius of 5 Å. In this way, spectra are well converged up to energies of 5.5–6.0 eV. The response for a perturbation is calculated in a particular direction. After a ground-state calculation, optical absorption spectra are calculated using the time-evolution formalism in the standard way as introduced by Yabana et al. [183, 184] where at t=0 a perturbation of the form of a δ-kick in time is applied. As explained in this chapter, technically this δ-kick corresponds to the fact that the wave functions are multiplied by a phase factor e^{ikz} that imposes a coherent velocity field and causes a dipole moment to develop as the system evolves freely. The absorption spectrum is obtained as the Fourier transform of the time-dependent dipole moment as discussed in this chapter. The total energy is used to monitor the stability of the propagation. The time step for the propagation was set to be equal to or less than 0.00197 fs. For most of the spectra presented in this thesis the total propagation time is chosen to be 25 fs which correspond to a broadening of 0.18 eV in the absorption spectra. The propagation was carried out by means of the Approximated Enforced Time-Reversal Symmetry propagator [187] as implemented in the `octopus` code.

Chapter 4

Results: Absorption

4.1 Introduction

In this chapter, we present and discuss results obtained for the absorption spectra of different 'intermediate-size' noble-metal clusters. We have mainly looked into the optical response of model noble-metal nanoparticles (Au and Ag) having the largest dimensions in the range of 0.6nm to 7nm with different aspect ratios (ARs). Absorption in these systems is studied using two distinct approaches: classical electromagnetics and *ab initio* Time-Dependent Density Functional Theory (TDDFT). In particular, the study consists in exploring the performances of these two approaches in exploring different physical effects on the localized surface-plasmon resonance (LSPR) in the aforementioned atomistic systems. These effects are the dependence of LSPR on the AR and the absolute size of the systems, and also on the materials (chemical species) that the systems are made up of.

4.1.1 Numerical Details

4.1.1.a *Ab Initio* Simulations

For the *ab initio* approach, we treated clusters with a particular aspect ratio (AR) comprising countable (3 to 167) noble-metal atoms and employed TDDFT to get their response to different optical excitation. There are three different kinds of geometries taken: (i) single- & double-layer rods having 5-fold symmetry along their axes, (ii) icosahedral clusters, and (iii) atomic chains. The atomic species in these clusters are described using norm-conserving Troullier-Martins [176] pseudopotentials. The DFT and TDDFT calculations are done using GGA and AGGA functionals, with the GGA of Perdew-Bruke-Ernzerhof (PBE) [159, 160]. The spectra are calculated using the δ-kick perturbation according to Yabana & Bertsch [183, 184] and Fourier transform of the time–dependent dipole moment. The simulations are performed using real-space code `octopus` [186]

4.1.1.b Classical Simulations

On the other hand, for the classical simulations, both in the framework of local and nonlocal (hydrodynamic) optics, we have used bulk fitted dielectric functions to describe the clusters' optical properties. In order to ensure direct comparability with the TDDFT calculations using the atomistic description of the clusters, we define equivalent geometries such that:

- they have the same aspect ratio as their atomistic counterparts, and
- also have the same number of valence-band electrons (s-electrons) as present in their atomistic counterparts.

The detailed description of the equivalent geometries corresponding to atomistic structures is given in the next section.

The classical optics calculations, both the local ones and nonlocal ones (using LAM), are performed numerically in frequency domain, using the *finite element method* (FEM) in the commercially available code COMSOL (version 3.5a). The calculations are done using cylindrical symmetry along the direction of the incident electric field, in order to solve the three-dimensional problem in two dimensions, thus making it numerically economic by reducing the degrees of freedom. The dielectric-surrounded metal cluster is described by a two-dimensional geometry put in a two-dimensional box describing the dielectric. Maxwell's equations for transverse ($\vec{E} \perp \vec{k}$) modes are solved in this box with proper boundary conditions to obtain the electric fields. Knowing the fields, the absorption cross-section is obtained from equations 2.1.5, 2.1.6 & 2.1.9.

4.2 Equivalent Geometries

In this section, we describe the construction of equivalent geometries corresponding to different atomistic systems: Spheres, Spheroids, "Cigars".

Rods. In the TDDFT calculations, we consider model pentagonal subnanometric rods of Au and Ag. These rods are formed as structured atomic layers around atomic chains. The single-layer rods are derived from the 13-atom decahedral cluster by stacking rings of 5 atoms each plus a central atom along the rotational axis. Thus, a single-layer rod can be seen as an atomic chain with one atomic layer having a pentagonal symmetry. For the case of double-layer rods, one more pentagonal layer of atoms are added as shown later in Fig. 4.10. The termination at the ends of these model systems is "soft". The modelling of the equivalent geometries for the single-layer pentagonal rods is discussed here which can be generalized as well for the double-layer ones. To properly model this geometry we proceed in three steps. First, we define L as the distance between the ionic positions of the ending atoms of the nanorod (see Fig. 4.1). That is,

$$L = \frac{N-1}{6} d_0 \ , \tag{4.2.1}$$

where N is the number of atoms (equal to the number of conduction s electrons) and $d_0 = 2.885 \ \text{Å} \simeq 5.454 \ \mathrm{a_B}$.

In the second step, we define the volume of the equivalent jellium-like structure. To do so, we consider that the averaged s-electron density equals the bulk one, given by

$$\bar{n} = \frac{3}{4\pi r_\mathrm{s}^3} \ ,$$

where the Wigner radius of Ag is $r_\mathrm{s} \simeq 3.02 \ \mathrm{b}$ (very close to the Au Wigner radius) and that the number of conduction electrons is fixed and equal to N.

If we approximate the structure as a cylinder of radius r_0, we simply have

$$N = \left(\pi r_0^2 L\right) \bar{n} \Rightarrow r_0 = 2\sqrt{\frac{2r_\mathrm{s}^3}{d_0} \frac{N}{N-1}} = r_\infty \sqrt{\frac{N}{N-1}} \ , \tag{4.2.2}$$

where $r_\infty \simeq 6.356 \ \mathrm{b}$. This way we set the lateral dimension, r_0, of the rod. The red box in Fig. 4.1 is the sideview of such a cylinder.

Finally, in order to incorporate the soft termination of the nanorod we deform the

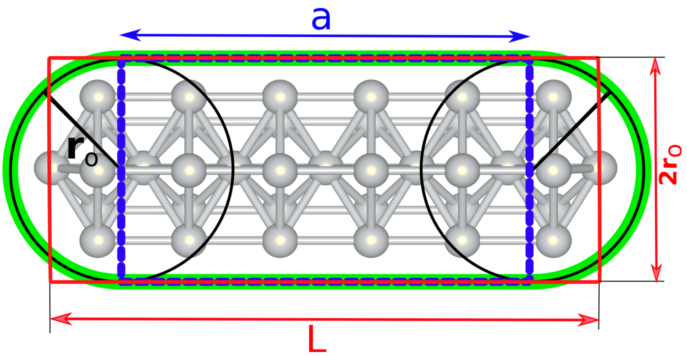

FIGURE 4.1: Constructing equivalent optimal geometries corresponding to model pentagonal sub-nanometric rod.

above-constructed cylinder and consider a more realistic geometry, namely, a sub-nanometric “cigar”. In Fig. 4.1 the longitudinal cross-section of such a cigar-shaped geometry is shown by the green enclosing curve. It is defined as a cylinder of radius r_0 and length a, terminated by two hemispheres of radius r_0, which has the same volume as the previously created cylinder in eq.B.0.5. Therefore for the cigar,

$$N = \left(\frac{4}{3}\pi r_0^3 + \pi r_0^2 a\right)\bar{n} \Rightarrow a = L - \frac{4}{3}r_0 = \frac{N-1}{6}d_0 - \frac{4r_\infty}{3}\sqrt{\frac{N}{N-1}}\,, \tag{4.2.3}$$

and we define the effective aspect ratio of this cigar shaped geometry as

$$\mathrm{AR} = \frac{a+2r_0}{2r_0} = \frac{1}{3} + \frac{L}{2r_0} = \frac{1}{3} + \frac{d_0}{12r_\infty}\sqrt{\frac{(N-1)^3}{N}}\,. \tag{4.2.4}$$

The corresponding values of the parameters L, r_0, a, and $\mathcal{R}$ are given in Table 4.1 and Table 4.2 for selected rods.

N	L ($\mathrm{a_B}$)	r_0 ($\mathrm{a_B}$)	a ($\mathrm{a_B}$)	AR
19	16.362	6.530	7.655	1.586
37	32.724	6.444	24.132	2.873
67	59.994	6.404	51.455	5.018
103	92.718	6.387	84.202	7.592
145	130.896	6.378	122.392	10.595

TABLE 4.1: Geometrical parameters of equivalent compact structures (cylinder and cigar-shape) for Ag/Au **single layer pentagonal rods** (in both cases, the bulk Wigner radius is r_{s}= 3.02 b)

N	L ($\mathrm{a_B}$)	r_0 ($\mathrm{a_B}$)	a ($\mathrm{a_B}$)	AR
87	32.724	9.8811	19.549	1.989
167	59.994	10.113	48.4863	3.298

TABLE 4.2: Geometrical parameters of equivalent compact structures (cylinder and cigar-shape) for Ag **double-layer pentagonal rods**

Atomic chains. The situation is different in atomic chains. In this case, the system is practically one-dimensional. We consider a chain of N atoms, separated by the atom-atom distance $d_0 \simeq 5.454\ \mathrm{a_B}$.

For the case of an atomic chain, while creating the equivalent cylindrical geometry following the prescription for rods, we consider $L = Nd_0$. Therefore, the optimal cylindrical geometry will be defined by

$$\pi r_0^2 L = N \frac{4\pi}{3} r_{\mathrm{s}}^3 \Rightarrow r_0 = \sqrt{\frac{4}{3} \frac{r_{\mathrm{s}}^3}{d_0}} \simeq 2.595\ \mathrm{a_B}\ . \tag{4.2.5}$$

Having the lateral dimension r_0, we construct the cigar-shaped geometry for the chain in such a way that the volume of the cigar and the cylinder is same, i.e.,

$$\pi r_0^2 a + \frac{4\pi}{3} r_0^3 = N \frac{4\pi}{3} r_{\mathrm{s}}^3 \Rightarrow a = Nd_0 - \frac{4r_0}{3}\ . \tag{4.2.6}$$

Having a and r_0, the corresponding aspect ratio will be

$$\mathrm{AR} = \frac{a + 2r_0}{2r_0}\ . \tag{4.2.7}$$

The corresponding values of the parameters L, r_0, a, and AR are given in Table 4.3 for selected chains.

N	L ($\mathrm{a_B}$)	r_0 ($\mathrm{a_B}$)	a ($\mathrm{a_B}$)	$a + 2r_0$ ($\mathrm{a_B}$)	AR
3	16.374	2.595	12.914	18.814	3.448
4	21.832	2.595	18.347	23.541	4.5.5
6	32.724	2.595	29.264	34.454	6.6385
8	43.632	2.595	40.172	45.362	8.74
10	54.54	2.595	51.08	56.27	10.842
12	65.448	2.595	61.988	67.178	12.944
18	98.172	2.595	94.712	99.902	19.249
24	130.90	2.595	127.44	132.63	25.554

TABLE 4.3: Geometrical parameters of equivalent compact structures (cylinder and cigar-shape) for Ag/Au **chains** (in both cases, the bulk Wigner radius is $r_{\mathrm{s}}= 3.02$ b)

Icosahedral clusters. For the sake of simplicity, the equivalent geometry corresponding to an icosahedral cluster is taken to be a sphere. Thus, for icosahedral clusters, the aspect ratio is one. The equivalent sphere is constructed by defining its volume (V) through the Wigner radius, and the number of s-electrons in the cluster. Defining the volume this way, the number of s-electrons can be found as,

$$N = \bar{n}V = \frac{3}{4\pi r_{\mathrm{s}}^3} \times \frac{4\pi a^3}{3}, \tag{4.2.8}$$

where a is the radius of the equivalent sphere, which can be evaluated as,

$$a = (N r_{\mathrm{s}}^3)^{1/3}. \tag{4.2.9}$$

The corresponding values of a for icosahedral clusters are given in Table 4.4.

N	a (b)	$\mathcal{R}$
55	11.485	1.00
147	15.938	1.00

TABLE 4.4: Radii of equivalent spheres for **icosaderoal clusters of Au/Ag** (in both cases, the bulk Wigner radius is $r_{\mathrm{s}}= 3.02$ b).

4.3 147-atom Quasi-Spherical Clusters of Ag & Au

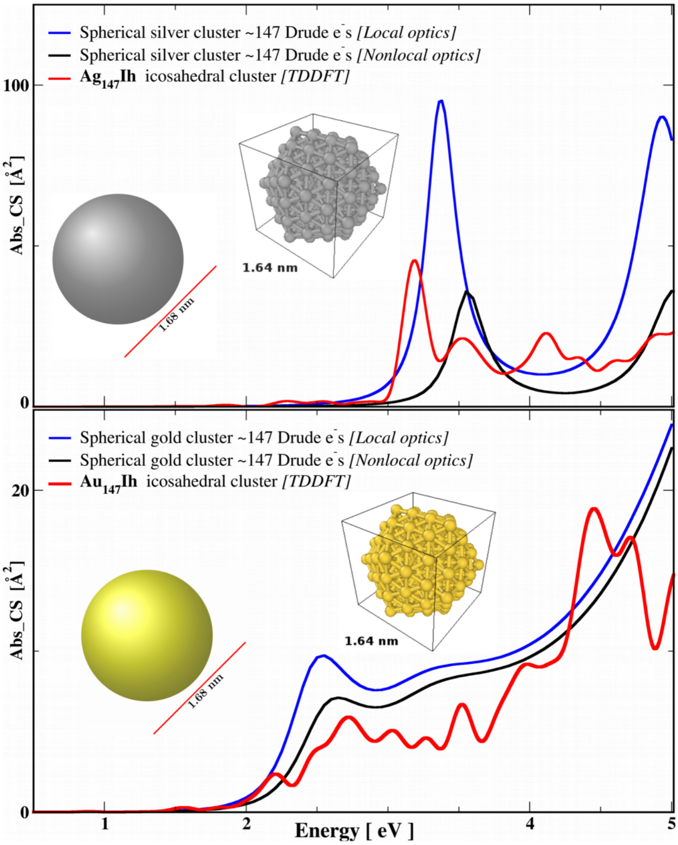

FIGURE 4.2: Optical absorption cross section, in Å^2 for Ag$_{147}$Ih (upper panel) and Au$_{147}$Ih clusters (lower panel). In red the spectra calculated in *ab initio* TDDFT and in blue and black the spectra calculated in local and nonlocal classical optics are shown.

In noble-metal clusters of 'intermediate size' (as described in chapter 1), the absorption is different for the different noble metals. The 147-atom icosahedral (Ih) cluster is an example in this size range. The absorption spectra for spherical and quasi-spherical clusters of this calculated in classical and *ab initio* theories are shown in Fig. 4.2. While the *ab initio* spectra are obtained with precise atomic structures using RT-TDDFT delta-kick simulations, (discussed in details in chapter 3), exciting along a particular direction (i.e., using a particular direction for the delta-kick), the classical calculations are done in both local and nonlocal optics by solving Maxwell's equations in a spherical geometry representing the clusters. The icosahedral symmetry make the optical response isotropic, Thus, the directionality of the δ-kick does not alter the absorption, as far as the spectral position and strength of the LSPR are concerned.

Difference between Ag & Au: Interband transitions. The red spectrum of the upper panel in Fig. 4.2 shows that Ag_{147}Ih has a well defined LSPR-like feature at 3.22 eV. In Au_{147}Ih there is no strong plasmonic peak in the absorption spectrum, the spectrum rather is fragmented in different peaks, the strengths of which are more than 5-times smaller than in the case of Ag_{147}Ih. The different optical behaviors of Au and Ag, can be traced back to the influence on the optical properties due to the different positions of the electronic states involving the d-electrons. In Ag, the d-states are situated at roughly 4 eV below the Fermi surface, whereas in Au, at roughly 2 eV [10, 188]. This means that in Ag_{147}Ih, the LSPR is only weakly coupled to the interband transitions from the d band, whereas in Au_{147}Ih the coupling is strong.

4.3.1 Electromagnetics Simulations

In classical optics, the LSPRs appear naturally as self-sustained solutions of Maxwell's equations, as discussed in chapter 2. In Fig. 4.2, the blue and black curves correspond to the spectra obtained in local and nonlocal optics, respectively. While classical local optics is known to provide the required accuracy in describing the absorption spectra of many *large* noble-metal clusters, the spectra obtained in both the local and the nonlocal optics calculations using spherical geometries equivalent and corresponding to 147-atom-Ih clusters of Au and Ag do not agree with the *ab initio* spectra. Within the framework of local optics, the existence of abrupt metal-dielectric boundaries is assumed, and the electromagnetic response of metallic regions (within the spherical geometry) is described in terms of their macroscopic, spatially non-dispersive, dielectric functions, $\varepsilon(\omega)$.

As discussed in chapter 2, in the limit of small sizes and/or sub-nanometric radii of curvature, the spatially non-local nature of the electromagnetic response becomes crucial [8, 189]. It is taken care of by the use of spatially dispersive dielectric functions (2.3.19) having transverse ($\varepsilon_T(\omega)$) and longitudinal ($\varepsilon_L(\mathbf{k},\omega)$) components, within the hydrodynamical model for electron motion as discussed in chapter 2. As a consequence, the induced charges across metal-dielectric boundaries are smeared out over a finite width. They spread *inward* from the abrupt bulk surface (which is defined as the geometrical boundary of the sphere) [190]. Compared to local classical predictions, this nonlocal correction leads to the blue-shifts of LSPR frequencies and to the decrease in the spectral strength. But, as evident from Fig. 4.2, the simplistic nonlocal corrections can not give spectra which are close to the *ab initio* ones for the case of 147-atom-Ih clusters. Clearly, the quantum-mechanical size-confinement effect starts to manifest and we are beyond the range of applicability of classical optics methods.

4.3.2 TDDFT Simulations Using Laser

In order to better understand the nature of the individual peaks in the spectrum of Au_{147}Ih, we performed TDDFT simulations using quasi-monochromatic laser excitations (QMLE) with different energies of the laser corresponding to different peaks in the spectrum.

The time dependence of the spatially homogeneous electric field describing the quasi-monochromatic laser used can be expressed as,

$$\mathbf{E}(t) = \begin{cases} E_0 \ \hat{\mathbf{n}} \ sin(\omega t) \ cos\left(\dfrac{t}{T} - \dfrac{\pi}{2}\right), & \text{for } (0 \leq t \leq T) \\ 0, \quad \text{otherwise,} \end{cases} \tag{4.3.1}$$

where $E_0 = 10^{-2}$ eV/Å is the amplitude and ω is the frequency of the laser pulse; and T is half the time period of the envelope of the laser pulse. For all the simulations, T is taken to be $(10 * 2\pi/\omega)$, so that the pulse contains 10 oscillations with the laser frequency. This means that in frequency domain, the laser pulse will have a full-width at half-maximum (FWHM) of $\triangle\omega = \omega/20$. The laser is switched off at $t = T$, and thereafter the system evolves freely without any external perturbation, for a time T or more.

The time dependences of the dipole moments obtained from QMLE simulations for Au_{147}Ih at different energies are compared in Fig. 4.3 with the same obtained for Ag_{147}Ih at the LSPR energy. In all the three cases of Au_{147}Ih, the dipole moment follows the profile of the lasers before they are switched off $(0 \leq t \leq T)$. In Au_{147}Ih for different energies the amplitude of the dipole moments do not change significantly from one case to another. For the case of Ag_{147}Ih at LSPR energy, the dipole moment does not exactly follow the profile of the laser. Not only does the amplitude of the dipole moment become stronger for the case of Ag_{147}Ih than for the case of Au_{147}Ih, but also, unlike in Au_{147}Ih, it does not tend to die out with the end of the laser pulse. Rather, at the end of the laser pulse (near $t \sim T$), a phase shift of a quarter of the period is noticed.

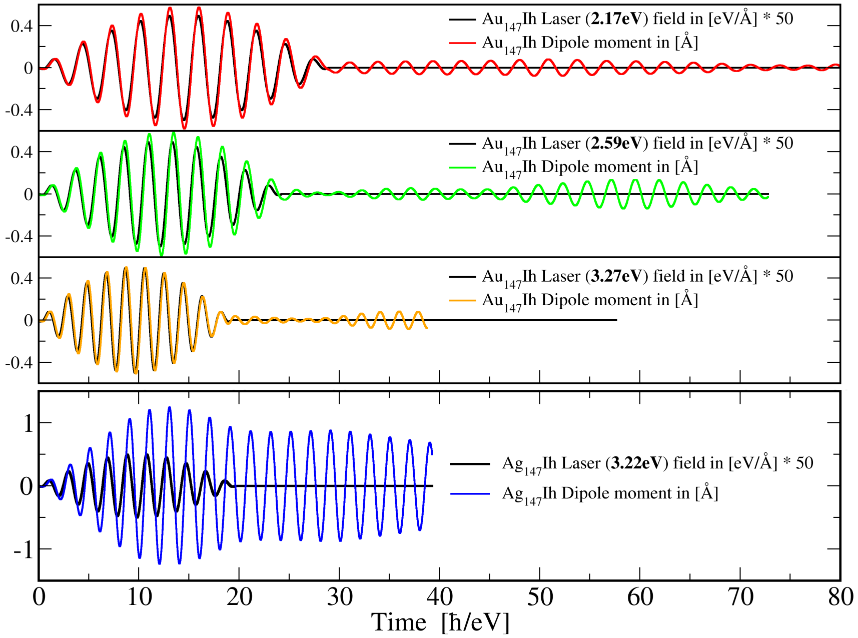

FIGURE 4.3: Time dependence of the electric fields of laser excitations at different energies (in black) and the corresponding time evolution of the dipole moments (in different colours) for Ag/Au_{147}Ih clusters. The upper three panels correspond to laser excitations in Au_{147}Ih, and the lower panel corresponds to the same in Ag_{147}Ih.

The differences in behaviours of the laser-driven dipole moment in the 147-atom icosahedral clusters Ag and Au can be understood in close correspondence with the physics of a driven oscillator. The time–dependent dipole moment is calculated from the time–dependent changes in the driven electron density with respect to its value in equilibrium (i.e., in ground state). The fact that the time–dependent dipole moment in Au_{147}Ih at different energies oscillates following the phase and the time-dependence of the amplitude of the laser suggests that in all these energies the oscillation of the electron density is not in resonance with the driving force, the laser field. By contrast, in Ag_{147}Ih at LSPR, the amplitude of the driven dipole moment keeps on increasing with the increase in the amplitude of the driving laser field and unlike in Au_{147}Ih, when the amplitude of the laser starts to fall off, the driven dipole moment tends to maintain its acquired amplitude. This tendency is reflected at the end of the laser pulse, where the driven dipole moment is noticed to oscillate out of phase with the driving laser field. This particular phase shift between the driving force and the driven oscillator and the tendency of the oscillator to keep the maximum energy (i.e., amplitude) acquired in course of being driven are the signature of resonance.

The comparison of the self-sustained evolution of the dipole moments after the switching-off of the laser, in both the systems, is of particular interest. For the cases of QMLE simulations of Au_{147}Ih at different energies, these evolutions show very weak oscillations of the dipole moments. For the case of QMLE simulations of Ag_{147}Ih at LSPR energy, the dipole moment appears to oscillate with the amplitude gained at the end of the laser pulse. This oscillation also confirms the fact that the system is in resonance with the driving force.

In all the four cases shown in Fig. 4.3, the self-sustained evolution of the dipole moments show the formation 'beat' patterns. 'Beats' are formed when more that one oscillating modes having very close frequencies of oscillation superpose. Thus, in Fig. 4.3 the presence of the 'beats' announces that energetically closely spaced modes of the electron-density oscillations are excited by the corresponding laser fields. This is due to the fact that, as the laser pulses have certain energetic width, it is possible to excite some other modes situated very close to the desired frequency (ω) in the spectrum. Thus, the resulting dipole moment is nothing but a superposition of different modes.

4.4 Elongated Clusters of Ag & Au : Rods & Chains

In the preceding section we have discussed the typical behaviour of the optical response that starts to appear in ‘intermediate-size’ noble-metal clusters of different chemical species. In this section, we’ll discuss the dependence of the optical response on the AR of ‘intermediate-size’ noble-metal clusters and also the performance of classical and *ab initio* methods to describe this dependence properly. The AR dependence of the LSPR using classical optics is well known for larger noble-metal nanoparticles [87] which we have already discussed in chaper 2. In this section, we’ll explore the validity of those known results and thus, of the classical methods in the ‘intermediate’ size range. In particular, the dependence of the LSPR energy and the coupling between LSPR and d-electron excitations (“interband transitions”) on the AR will be discussed in model pentagonal rods and atomic chains of Ag and Au. The longest rod (with highest AR) is made up of N=145 atoms while the shortest one (with lowest AR) has N = 19. The construction of these rods are discusses in the previous section. Optical absorption in most of these pentagonal rods has been studied before [191,192]. In the present work, they are employed as well-controlled model structures that enable the systematic comparison of different methodologies (classical and *ab initio*) on nanoclusters of varying LSPR energy and material and, consequently, a varying degree of coupling between the LSPR and interband transitions. The structures are the same for both Au and Ag and, to allow for a proper discussion of the dependence of the optical absorption on AR, they are not relaxed. The atom-atom distance along the rod axis is set to d_0=2.88 Å. The other class of systems here considered are single atom-chains of Au and Ag having a number of atoms between 3 and 24, with the same inter-atomic distance d_0 as in the rods. The absorption spectra are calculated for the excitations by electric fields polarized along the longitudinal axis (x-direction).

4.4.1 Rods vs Icosahedra

Fig. 4.4 shows a direct comparison between *ab initio* and local and nonlocal optics absorption spectra for Ag and Au rods. A comparison of the spectra in the uppermost panels in Fig. 4.4 with the spectra for the Ih clusters in Fig. 4.2, is of particular interest. The rods and the Ih clusters have almost same number of atoms (and thus s-electrons).

The comparison reveals that for the rods, where the AR is high ($>$10), the behaviour of the absorption in Au and Ag is similar. In fact, from Fig. 4.4, this observation remains valid at AR$\sim$8 too. However, having approximately the same number of electrons, in Ih clusters the absorption is entirely different in the two materials. The reason for this different behaviour with respect to AR is traced back to the following facts.

- As the red-shifted LSPR in the rods appear well below the onset of the inter-band transitions involving d-electrons, it corresponds primarily to the response of the s-electrons, which behave similarly in both Au and Ag. Thus, the absorptions in both Au and Ag 145-atom rods are dominated by the LSPR, and are similar.

- In rods, as the excitation is along their length, the s-electrons are guided by the length while responding to the excitation. This phenomenon favors the collective oscillation of the s-electrons in rods more than in the Ih clusters which are way more compact (AR$\simeq$1) than the rods.

- The more the collective oscillation of the s-electrons is favored, the lower is the required energy to achieve resonance. Thus the LSPRs in the 145-atom rods appear in the IR, strongly red-shifted compared to their energies in the 147-atom Ih clusters. Understanding the LSPR as localized dipolar mode of surface plasmon polaritons (SPPs), this red-shift can be understood from the dispersion relation of SPPs (2.2.2), as shown by the orange curve in Fig. 2.5. The wavelength of the dipolar SPP ($\lambda_{_{SPP}}$) is twice the dimension of the cluster along which it is excited. Thus, $\lambda_{_{SPP}}$ is larger in the 145-atom rods than in the 147-atom Ih clusters and, consequently, the corresponding wave vector ($k_{_{SPP}}$) is smaller. Following the dispersion curve, therefore, the dipolar SPP occurs at a lower energy in the rod than in the Ih cluster.

4.4.2 Classical vs TDDFT in Rods

Fig. 4.4 shows that there is an excellent agreement between TDDFT and local optics calculations for structures with $\mathrm{AR} > 5$ (whose response is dominated by the LSPR). As a matter of fact, it is worth mentioning here that this agreement does not arise from any fitting between the *ab initio* and the electromagnetics calculations. Only the *a priori* definition of classical geometries introduced at the beginning of this chapter is followed. The comparison against *ab initio* predictions improves even

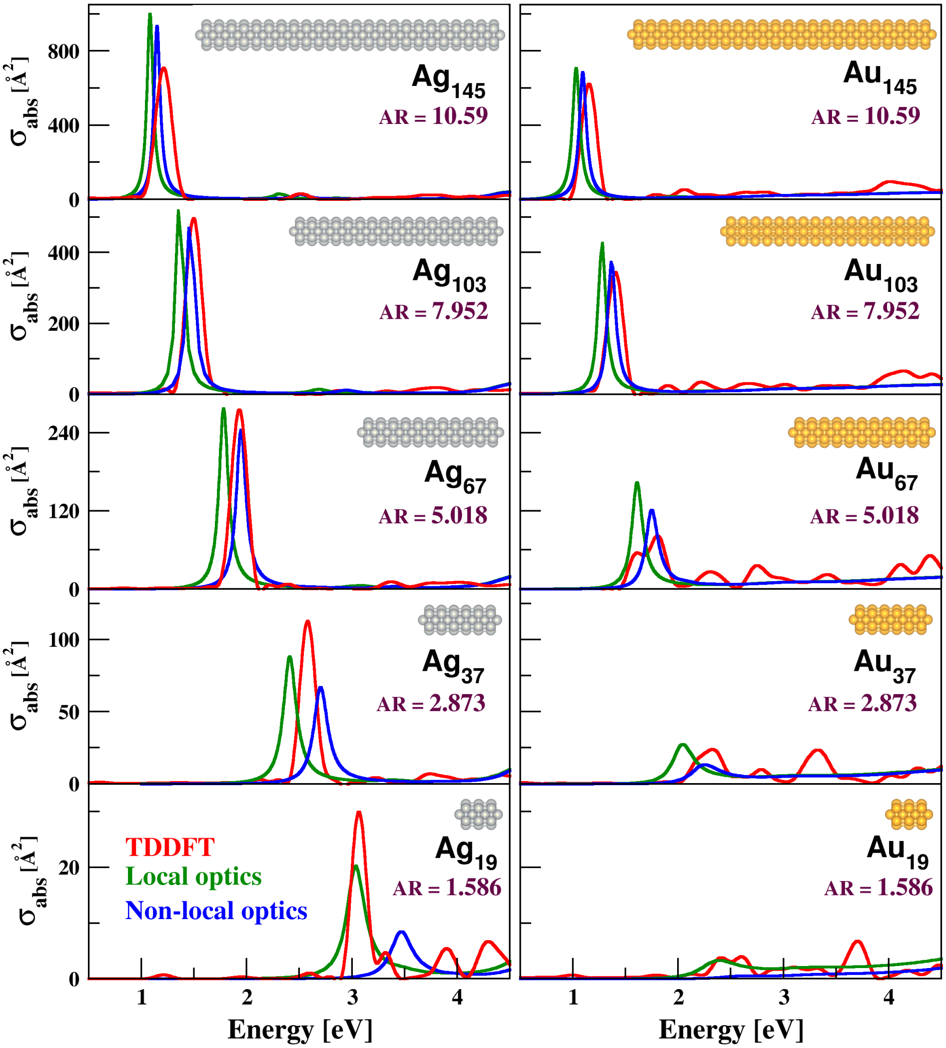

FIGURE 4.4: Optical absorption cross section, in Å^2 for silver (left column) and gold (right column) three-dimensional rods of different aspect ratio (AR) and number of atoms. The structre that coorespons to the spectra is shown in the inset.

further when the absorption cross-section is computed using the nonlocal hydrodynamic metal permittivity. This gives rise to the aforementioned nonlocal resonance blue-shift, a signature of the different LSPR dependence on absolute size in local and nonlocal optics.

However, classical optics fails to accurately describe the *ab initio* spectra for compact low-AR structures in Figure 4.4 ($N \leq 37$ atoms, AR$\lesssim 3$). This is expected, since genuine quantum effects, such as electron-density spill-out and energy level discretization due to size confinement, become more significant as the rod's length (and thus the AR) decreases. The plasmon-causing s-electrons are forced to oscillate with smaller λ_{SPP}. Thus the LSPRs get blue-shifted as the AR decreases and their coupling to the interband transitions increases.

In the case of Ag, despite relatively small spectral deviations, TDDFT and classical calculations are still in qualitative agreement even for low-AR. By contrast, for Au rods having AR$\lesssim 5$ (i.e., $N \leq 67$ atoms), classical predictions are already qualitatively different from the TDDFT spectra. In these Au systems, the classical LSPR frequencies lie at or above the onset of interband transitions (~ 2 eV) due to d-electrons. This fact prevents the formation of purely collective surface plasmon resonances in the TDDFT spectrum, which in turn is dominated by a set of multiple maxima (of similar height) originated by d-electron excitations. Identifying the lowest-frequency absorption features in the TDDFT spectra for short Au rods as LSPRs (having noticed that these are located at roughly the same position as the classical optics peaks), we can conclude that the spectral overlap with the d-excitations range gives rise to the partial damping, splitting and fragmentation of LSPRs in these systems. It is worth mentioning here that the inclusion of nonlocality in the electromagnetics calculations does not reproduce any of these purely quantum physical features. It only improves the comparison against *ab initio* results at higher AR by correcting classical optics LSPR frequencies, otherwise too red-shifted due to the abrupt character of induced local charges.

4.4.2.a Effect of AR and absolute size on spectral shifts

While presenting the spectra calculated using classical electromagnetics, we have discussed two different kinds of spectral shifts. On the one hand, we have discussed the well-known spectral shift due to the change in the AR keeping the volume (i.e.,

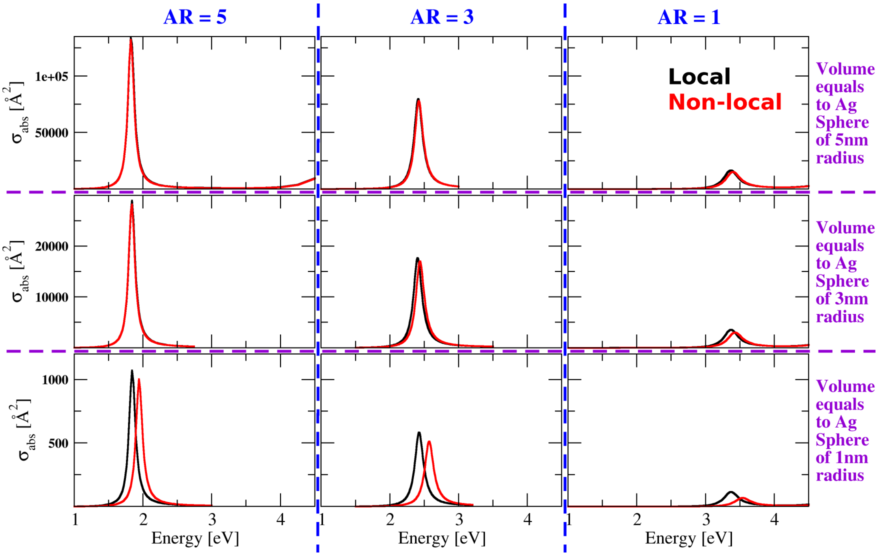

FIGURE 4.5: Dependence of nonlocal blue-shift on aspect ratio and absolute size in classical optics. The black curves correspond to the local optics spectra, while the red ones correspond to nonlocal optics.

the number of atoms) of the cluster almost the same, on the other hand, there is the spectral blue-shift caused by the smeared-out induced charges when the optical response of a cluster is calculated using a spatially dispersive dielectric function. The latter is termed as the nonlocal blue-shift which becomes apparent as the size of the cluster is decreased and thus, explains the size-dependent blue-shift observed in noble-metals in the experiments [188]. A comprehensive analysis of the dependence of this nonlocal blue-shift on absolute size and AR of the cluster is shown in Fig. 4.5. This figure shows the absolute size dependence of the nonlocal blue-shift for Ag clusters of different AR in cigar shaped geometries. For each AR, the non-local blue-shift increases as we go down in absolute size. For a particular absolute size, the amount of non-local blue-shift remains almost constant for different AR. This figure also demonstrates that the AR plays the primary role for the blue-shift of the LSPR and is stronger than the effect of absolute size, i.e. the non-local blue-shift.

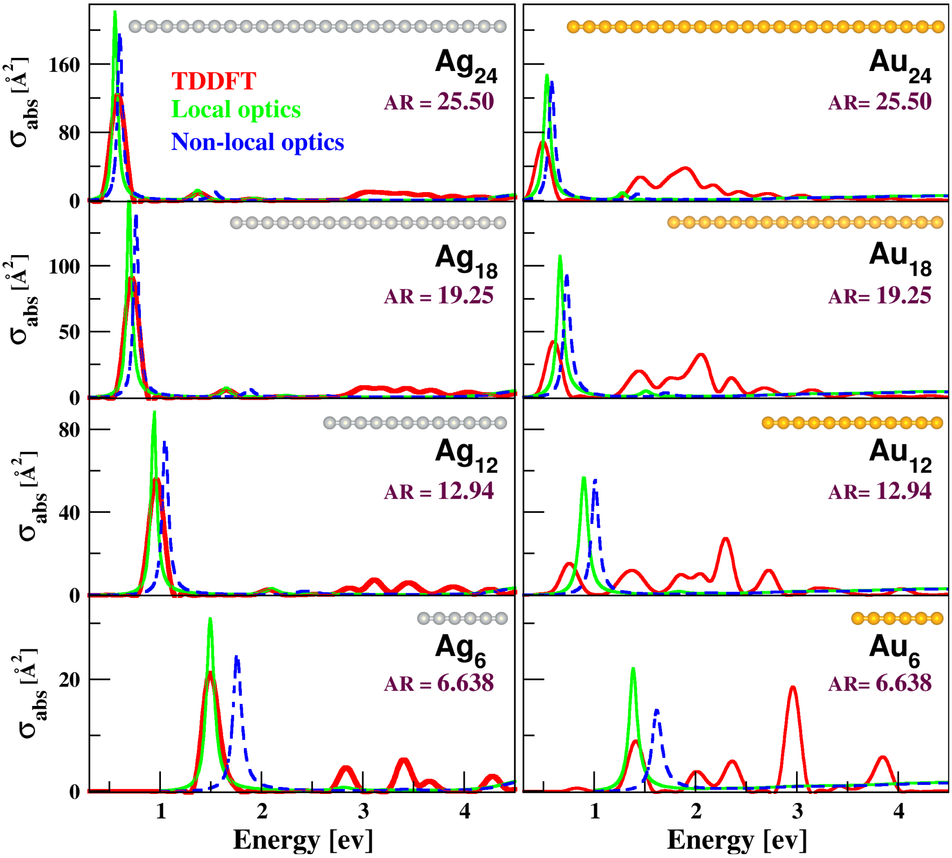

FIGURE 4.6: Optical absorption cross section, in Å^2 for quasi-one-dimensional silver (left column) and gold (right column) atomic chains of different aspect ratio (AR) and number of atoms.

4.4.3 Classical vs TDDFT in Chains

Following the performance of electromagnetics and TDDFT in describing the optical response in atomistic rods, we have performed the same study in linear atomic chains of Ag and Au. The AR-dependence of the LSPR in these atomic chains are found to be similar to that in the rods, except for the fact that the quasi-one dimensional nature of the chains makes the classical nonlocal optics predictions less accurate than the local optics ones. Figure 4.6 plots the absorption spectra for Ag and Au atomic chains of different lengths and, thus, AR. We find a strikingly good agreement between TDDFT and local optics results for Ag chains, an observation similar to previous studies on linear hydrogen atomic chains [193, 194]. As in case of the rods in Figure 4.4, for Ag atomic chains the weak spectral deviations above ~ 3 eV can be attributed to single electron-hole excitations ("interband transitions"). These spectral features are more apparent in Au chains, where the spectral weight of transitions involving d-electrons is comparable to those attributed to LSPRs. As discussed below, the predictive value of local electromagnetics calculations for high AR chains (for both Ag and Au) originates from their quasi-one-dimensional nature: electron motion in these systems is confined along the longitudinal axis. Therefore, the collective LSPR that dominates their absorption spectra cannot be regarded as a surface mode [195–198]. We note that our hydrodynamic model was constructed to account for the impact of spatial nonlocality due to the optical excitation of three-dimensional (bulk) longitudinal plasmons, described by equation 2.3.22, instead of one-dimensional ones. This explains the offset of nonlocal predictions in Figure 4.6, significantly blue-shifted with respect to local optics and *ab initio* spectra.

4.4.3.a LSPR in Quasi-one-dimension

The striking agreement between the absorption spectra for quasi-one-dimensional quantum systems and their three-dimensional local optics counterparts can be easily understood in terms of simple geometrical considerations. To a first approximation, we can take the analytical expression [138] for the lowest LSPR in ellipsoidal nanoparticles for the cigar geometries (the one used for calculating the electromagnetics spectra). In the limit of large AR, we obtain

$$\omega^2_{\mathrm{LSPR}} = \frac{4}{\pi} \frac{\rho_{\mathrm{avg}} e^2}{m_e \epsilon_0 (a + 2r_0)^2} \ln\left(2\,\mathrm{AR}\right) = \frac{n_{\mathrm{avg}} e^2}{m_e \epsilon_0 (\mathrm{AR})^2} \ln\left(2\,\mathrm{AR}\right) \tag{4.4.1}$$

where $\rho_{\mathrm{avg}} = \pi r_0^2 n_{\mathrm{avg}}$ is the number of Drude electrons per unit length, ϵ_0 is the vacuum permittivity, and m_e and e the electron mass and charge, respectively. It is worth noticing that the absence of the Lorentzian component of $\epsilon(\omega)$ in equation (4.4.1) indicates that the dynamical screening by d-electrons is ineffective for rods with large AR.

On the other hand, the plasmon dispersion relation in a homogeneous one-dimensional electron system in the long wavelength limit reads [199]

$$\omega_{\mathrm{1D}}^2(q) = -\frac{\rho_{\mathrm{avg}} e^2}{2\pi\epsilon_0 m_e} q^2 \ln\left(\frac{q\xi_0}{\pi}\right), \tag{4.4.2}$$

where, ξ_0 is the length parameter measuring the electron confinement in the transverse direction. Evaluating this expression at $q = 2\pi/\lambda_{SPP} = \dfrac{\pi}{(a+2r_0)}$ and making $\xi_0 = r_0$, we obtain the resonant frequency for the dipole collective mode sustained by the system, the *ab initio* equivalent for the classical LSPR,

$$\omega_{\mathrm{1D-dipole}}^2 = \frac{\pi}{2} \frac{\rho_{\mathrm{avg}} e^2}{m_e \epsilon_0 (a+2r_0)^2} \ln(2\,\mathrm{AR}) = \frac{\pi^2}{8} \frac{n_{\mathrm{avg}} e^2}{m_e \epsilon_0 (\mathrm{AR})^2} \ln(2\,\mathrm{AR})\,. \tag{4.4.3}$$

Equations (4.4.1) and (4.4.3) describe collective excitations of different nature, but their remarkable similarity allows us to identify both of them. This also clarifies the agreement between TDDFT and local optics spectra in Figure 4.6. It is important to note that the equations (4.4.1) and (4.4.3) yield $\omega_{\mathrm{LSPR}} < \omega_{\mathrm{1D-dipole}}$, which is also in agreement with the numerical spectra. Classical optics slightly underestimates the LSPR frequencies in the limit of very long chains (where the analytical expressions are valid), a deviation which, in principle, could be corrected through the appropriate one-dimensional nonlocal corrections.

4.4.3.b Plasmon–electron-hole Coupling in Au Chains

As mentioned above, the TDDFT spectra for Au chains in Figure 4.6 indicate that quasi-one-dimensional collective excitations are not well resolved for $N \leq 12$. In analogy with the three-dimensional case, this effect can be directly attributed to the coupling of the collective mode with single electron-hole excitations. This coupling can be observed in detail in Fig. 4.7, where we show the variation of the absorption cross section normalized to N for different Au chains. For $N = 18$, the quasi-one-dimensional LSPR is well separated from the spectral region where single-electron

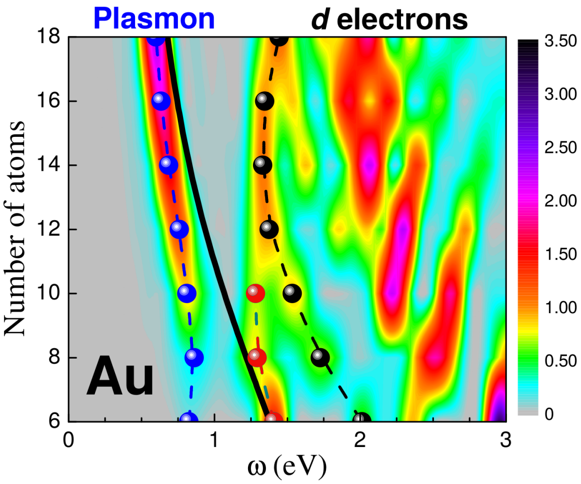

FIGURE 4.7: TDDFT absorption cross section per atom (in Å^2) versus frequency and the number of atoms in Au chains. The solid line plots the LSPR frequency under local optics descriptions. The various *ab initio* spectral maxima are given by solid circles (connected to guide the eye): collective plasmon modes in blue and single d-electron excitations in black and red.

transitions occur. As a consequence, it appears as a well defined absorption peak whose position is in good agreement with the one predicted classically. When decreasing the number of atoms, the lowest-frequency maxima lose spectral weight. For $N = 10$, this resonance is fragmented and none of the local maxima can be attributed to a collective LSPR excitation. However, Fig. 4.7 demonstrates that the classical optics description provides a rough spectral average of such fragmented peaks. Finally, for the 6-atom chain, the lowest-frequency *ab initio* maximum is very weak and the transfer of spectral weight to the electron-hole excitations region is almost complete. Interestingly, a new spectral feature emerges very close to the frequency corresponding to the classical plasmon by taking spectral weight from the original one-dimensional LSPR and the lowest-energy electron-hole excitation. Although plasmon formation in gold chains is clearly beyond the scope of any classical optics treatment, it is worth emphasizing that it seems to account rather accurately for the *spectral average* of the split quantum excitations in the *ab initio* calculations.

4.4.4 Aspect Ratio & Absolute Size Dependence

As shown in the previous section, the study combining *ab initio* method and electromagnetics modelling of Ag and Au rods indicates that, through a careful mapping between atomistic structures and classical geometries containing a bulk permittivity, LSPRs can be quantitatively described by classical optics methods as long as they are largely free of interband contamination. In order to further check this conclusion and provide a more general perspective, in Fig. 4.8 (for Au) and Fig. 4.9 (for Ag) the spectral positions of all the significant absorption maxima in Figures 4.4, 4.6 and 4.7 are plotted against the AR of the various Au and Ag systems, respectively (note the log-log scale). TDDFT results for collective LSPR-like modes are shown by stars (for Ih clusters in Fig. 4.9), solid circles (in red and gray for rods) and rhombuses (chains). In all cases, the number of atoms is indicated. Significant absorption features in Au structures originating from single electron-hole excitations are represented by empty circles (rods) and rhombuses (chains) in Fig. 4.8, and by colored empty rhombuses (chains) in Fig. 4.9. Local and nonlocal optics predictions for the corresponding cigar geometries are shown in green and blue lines, respectively. We observe that while the LSPR frequencies within the local approximation depend only on AR, they do depend on absolute size once nonlocal corrections are included. Thus, solid and dashed blue lines correspond to nonlocal resonances for rods and chains, respectively.

Figures 4.8 & 4.9 show that while the AR-dependence of LSPR frequencies obtained from local optics calculations is already in good agreement with TDDFT results, the non-local blue-shift slightly improves it for long Au and Ag rods. This suggests that, the *rods* despite having lateral sub-nanometric dimensions, preserve a quasi-bulk optical response. By contrast, in the Ag *chains* (Fig.4.9), the TDDFT resonant frequencies are better described within the local optics frame. For Au chains having N>12, the dominant resonant peaks obtained in TDDFT are also better described by local optics. For Au chains having N<12, however, the coupling with electron–hole excitations fragments the plasmon, as discussed in the previous section. In order to verify the validity of the local optics description, we evaluate the ellipsoidal LSPR dispersion of Ref. [138] for the full Drude-Lorentz permittivity as well as for a simplified Drude-only fitting. These results, plotted in magenta (full $\epsilon_{\text{bulk}}(\omega)$, i.e., Drude and Lorentz parts) and black (simplified $\epsilon_{\text{bulk}}(\omega)$, i.e., Drude part only), in Figure 4.9 upper panel (i.e., for the case of silver,) reveal that agreement with TDDFT predictions occurs if the dielectric function is mainly governed by the Drude contribution,

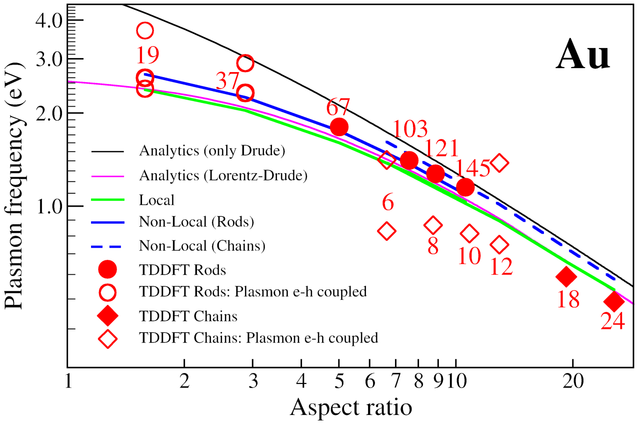

FIGURE 4.8: LSPR frequencies in Au sub-nanometric rods and atomic chains versus aspect ratio. Black (magenta) line renders analytical local optics calculations in ellipsoidal geometries with fitted Drude (Drude-Lorentz) permittivity, where analytics refers to equations 5.13b, 5.15 of Ref. [136]. Green and blue (solid corresponds to Rods and dashed corresponds to Chains) lines plot local and nonlocal classical simulations for Drude-Lorentz cigars, respectively. TDDFT LSPR frequencies for N-atom systems are shown in solid red circles (rods) and rhombuses (chains). Empty circles (rods) and rhombuses (chains) correspond to single electron-hole excitations apparent in the absorption spectra.

which is more the case in Ag than in Au.

As discussed above, in the quasi-one-dimensional chains, the nonlocal optics predictions do not agree with the TDDFT ones. Not only this failure of the nonlocal hydrodynamic model, but also the good agreement between local optics and *ab initio* predictions in Ag chains can be linked to the inherent one-dimensional nature of these systems. In the case of short Au rods and chains, the occurrence of d-electron transitions above $\sim$ 2 eV causes qualitative differences in the spectral behavior in TDDFT and in electromagnetics approaches. The discrepancy in the AR dependence between both methods is most apparent in Au chains with $N = 6 - 12$, where multiple *ab initio* single-electron peaks occur far from the LSPR band.

4.4.4.a Blue-shift with Increasing Absolute Size at High Aspect Ratio

In order to get deeper insights into the absolute size dependence of the LSPR in Ag at different AR ranges, the LSPR frequencies for 3- and 4-atom Ag chains, 55- and 147-atom Ih Ag clusters, and 87- and 167-atom double-layer Ag rods are also put

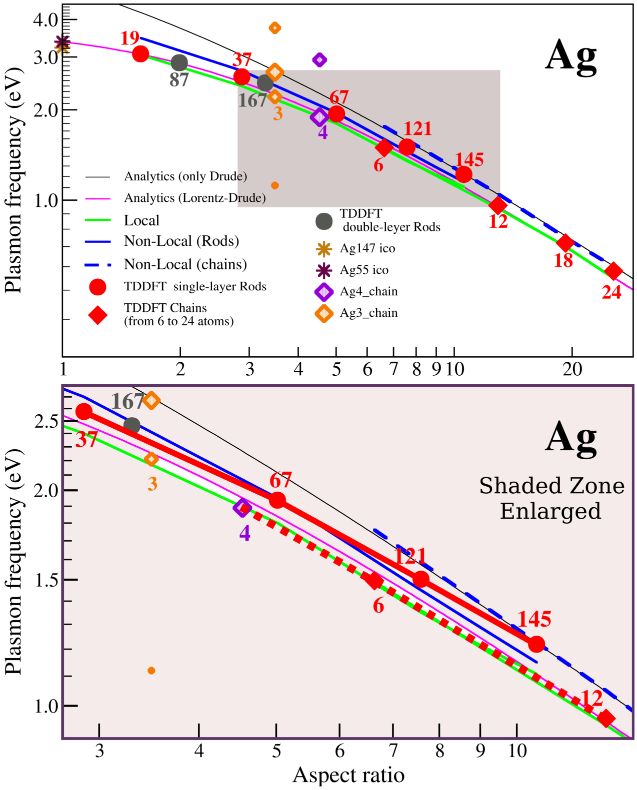

FIGURE 4.9: LSPR frequencies in different systems of Ag versus aspect ratio (upper panel), and the enlargement (lower panel) of the shaded zone of the plot. The colours of the curves and the symbols represent the same as in Fig 4.8, except otherwise stated in the legends.

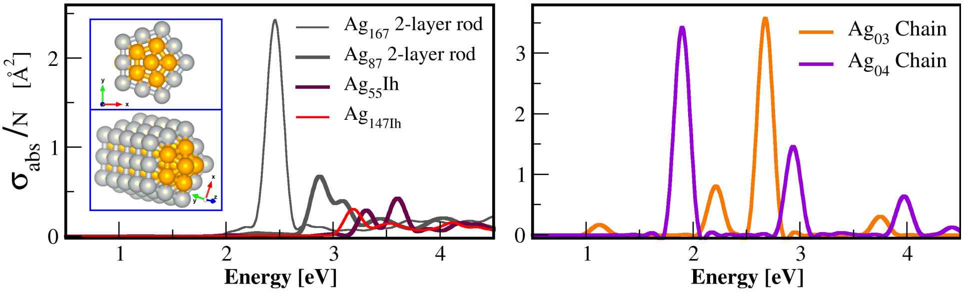

FIGURE 4.10: The absorption cross-section normalized by the number of atoms for different other systems of Ag, which were not presented earlier but shown in Fig. 4.9. Inset: two different views of the atomic structure for the double layer rods (,in this case for Ag_{87}), showing the second layer in gray to differentiate it from the core of the structure.

into Fig. 4.9. The absorption cross-section normalized by the number of atoms for these six systems is shown in Fig. 4.10. For the LSPRs in silver clusters presented in the top panel of Fig. 4.9, the circles representing the resonance energies for rods lie *above* rhombuses representing the resonance energies for chains. This observation is particularly apparent in the range of AR between 3 and 13, which is enlarged and shown in the lower panel of Fig. 4.9. This indicates that the rod LSPRs are *blue*-shifted with respect to the atomic chain ones. This indicates a blue-shift of LSPR while the size of the clusters are increased. As mentioned earlier, the nonlocal blue-shift of the LSPR is considered to give the physical explanation of the blue-shift observed in experiments when the size of the noble-metal clusters is decreased. The trend of absolute size dependence we show in the lower panel of Fig. 4.9 for the same AR is exactly the opposite to that predicted by nonlocal optics (see solid and dashed blue lines). For the moment, this opposite behaviour of the absolute size dependence in the TDDFT calculations is only a theoretical observation and requires physical understanding.

4.4.5 GGA In Describing The *Ab Initio* Spectra For Low-AR Systems (rods)

TDDFT (the theory) is in principle exact; the practical calculation are not, because we always need an approximation for the exchange-correlation functional in the calculations. As discussed in the chapter 3, in TDDFT, the time evolution of the density of the many-electron system is obtained from a fictitious non-interacting one, the time-dependent Kohn-Sham system, under the action of an effective time-dependent potential. This potential is a functional of the electron density $n(\mathbf{r}, t)$ and accounts for the non-local spatial and temporal response of the correlated many-body system [200, 201]. Therefore, TDDFT would provide all the quantum many-body corrections if it were not for the fact that we need to rely on approximate functionals/kernels for practical calculations. As long as collective excitations dominate the optical spectra, simple approximations like adiabatic generalized-gradient approximations (AGGA) suffice [202]. In all the TDDFT calculations, presented as results in this chapter, the Perdew-Burke-Ernzerhof [159, 160] (PBE) AGGA exchange-correlation functional is used. However, the AGGA exhibits problems in the descriptions of the d states, leading, in particular, to d-band energies too close to the Fermi energy, in part due to the incomplete cancellation of the electron self-interaction.

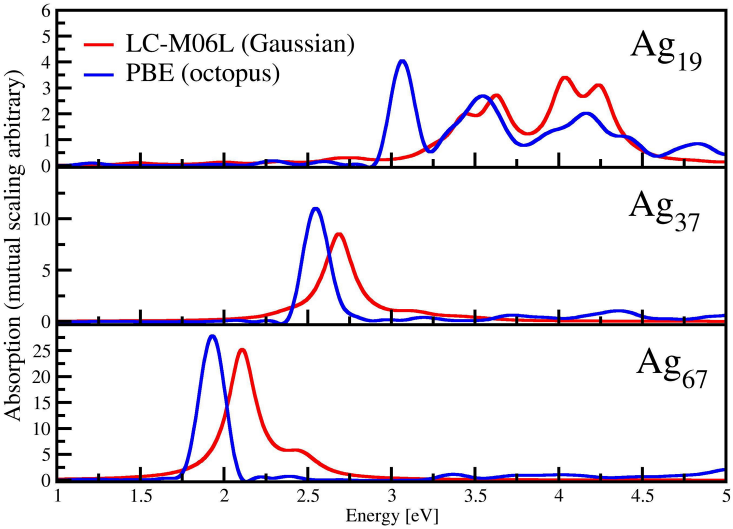

FIGURE 4.11: Comparison of spectra calculated in PBE and LC-M06L. The LC-M06L spectra are calculated by F. Rabilloud

The precise description of the delicate interplay between d-electron and collective excitations in coinage-metals requires more sophisticated functionals like the long-range-corrected ones. Therefore, as anticipated, the performance of the PBE functional requires to be assessed carefully. Fig. 4.11 shows a comparison of PBE results for selected rods with those obtained using the more sophisticated LC-M06L hybrid functional. This functional has demonstrated high accuracy for small silver clusters [203] and can therefore be considered as a benchmark. The LC-M06L functional is obtained by applying long-range corrections [168] to the meta-GGA M06L [169] functional. Here, “meta" denotes the inclusion of kinetic energy density, which depends on local derivatives of the spin orbitals. LC-M06L contains 0% Hartee-Fock exchange at short range and 100% at long range. The range separation parameter was 0.33. The LC-M06L calculations were carried out using GAUSSIAN by F. Rabilloud. The agreement is excellent for the 67- and 37-atom silver rods. There is only a small shift of about 0.2 eV which is of the order of differences which we found between two GGA calculations done using `octopus` and GAUSSIAN, respectively. In these two (Ag_{67}, and Ag_{37}) longer rods, the LSPR is the dominant excitation and well removed from the interband transitions from the d electrons. Thus, the comparison indicates that the PBE spectra are valid as long as the dominant LSPR is well decoupled from interband transitions. By contrast, the shortest rod, Ag_{19}, is very badly described by the PBE functional. For Ag_{19}, the benchmark spectrum is given by the LC-M06L calculation and not by the PBE calculation. We note that not even the character of the LC-M06L spectrum is reproduced qualitatively by the PBE calculation. This means none of the results presented in the lowest left panel of Fig 4.4 is correct.

From this particular verification of the validity of the PBE functional, an important conclusion is achieved by having a look back to the left panels in Fig. 4.4. We observe, that in all the cases, except for Ag_{19}, the LSPRs in the TDDFT spectra are recovered with moderate accuracy, by the nonlocal optics calculations, both in terms of spectral position and strength. In other words, as long as the LSPR is well separated from the region of interband transitions, the performance of the nonlocal optics is as good as that of the *ab initio* TDDFT.

Chapter 5

Results: Induced Density

5.1 Introduction

In both approaches, classical and *ab initio*, the near-field characteristics of the optical response of a cluster at a certain energy, are analyzed through the behavior of the induced density at that particular energy which is closely linked to the “fields”. While the *absorption spectrum* of a cluster gives the dependence of the optical response on different energies, the analysis of the induced density helps to understand the spatial nature of the optical response. In this thesis we are concerned with two different theoretical approaches, namely, classical electromagnetics and *ab initio* TDDFT. However, in both of these approaches, we have performed different types of simulations. In this chapter, we’ll discuss induced charge density obtained in all these different simulations. Therefore, in order to avoid any possible confusion, here we list all these different simulations where the induced densities are obtained and discussed in this chapter:

- *Ab initio* simulations:
    - **RT-TDDFT δ-kick**: As discussed in chapter 3, in this simulation, we excite all the optical modes of a system as long as we are within the linear response regime. Thus , the time–dependent induced density corresponding to this simulation consists all the excited modes and their time-dependence.
    - **RT-TDDFT QMLE**: In this simulation, we use a laser pulse which is spatially homogeneous. According to the temporal width of the pulse the lase has a finite spectral width in the frequency-domain. Thus, the time–dependent induced density corresponding to this simulation has weighted

    contribution from all the optical (laser-active) modes that fall within the aforementioned spectral width.

  - **LR-TDDFT**: In this simulation the spectrum is obtained by calculating the transitions between the occupied and unoccupied states. Thus, induced density corresponding to a particular transition can be calculated as transition densities.
  - **Electrostatic calculation**: In this simulation, a system in its ground state (calculated in DFT) is perturbed by an electrostatic field and the induced density is calculated as the difference in the electron density between the perturbed and unperturbed system.

- Classical Electromagnetics Simulations: In this simulations, the Maxwell's equations are solved to obtain the electric fields in the frequency domain.
  - **Local optics calculations**: As discussed in details in chapter 2, in this case, the dielectric function for the metal region does not have any spatial dependence.
  - **Nonlocal optics calculations**: Spatially dispersive dielectric function (as described within the hydrodynamic model) is chosen for the metal region in this simulation.

In this chapter, the spatial characteristics of the plasmonic and the non-plasmonic excitations are discussed through the analysis of induced densities. A quantitative comparison of the induced density obtained at LSPR for elongated systems, from both the classical and *ab initio* approaches, is carried out to understand the dipolar LSPR and the quantum mechanical effects. Moreover, for different 'intermediate-size' clusters, the spatial profiles of the induced density corresponding to different energies are obtained through spatially resolved Fourier transform of the time–dependent induced density obtained from the delta-kick RT-TDDFT calculation. These spatial modes at different energies are then also compared with the induced densities obtained from simulations using the quasi-monochromatic laser excitation (QMLE) at the corresponding energies.

5.2 Induced Densities at LSPR in Elongated & Compact Ag Systems

In order to compare the near-field characteristics of LSPRs in elongated systems (the spectra of which are presented in chapter 4), we evaluate the *cross-section integration* of the induced charge densities over the cross-section of some selected Ag systems and as a function of their length, within both the *ab initio* and classical optics frameworks.

5.2.1 *Cross-section-integrated* Induced Density from TDDFT

The *ab initio* induced density is obtained from TDDFT simulations by exciting the rods with a weak quasi -monochromatic laser field polarized along the rod axis (x-direction). The laser pulse has a sinusoidal envelope of finite duration, T, and its bandwidth is centered at resonance with the LSPR frequency:

$$\mathbf{E}(t) = E_0 e^{i\omega_{\mathrm{LSPR}} t} \sin\left(\omega_{\mathrm{LSPR}} t/T\right) \mathbf{e}_x. \tag{5.2.1}$$

The envelope duration was set to 10 plasmon oscillations ($T = \dfrac{20\pi}{\omega_{\mathrm{LSPR}}}$) in our calculations. The system is left to evolve freely for a sufficient amount of time after the external driving laser is switched off. The induced density corresponding to the LSPR is chosen to be the one that corresponds to a maximum of the time–dependent oscillation of the dipole moment after the switching-off of the laser. Using this induced density, the magnitude of the *cross-section-integrated* induced charge density is evaluated as,

$$S(x) = \int\int [\rho(x,y,z;\tau) - \rho_{_{GS}}(x,y,z)] dydz \tag{5.2.2}$$

where, $\rho_{_{GS}}(x,y,z)$ is the ground-state density and $\rho(x,y,z;\tau)$ is the time-dependent density at a time τ, longer than T, when the oscillation of the electron density is self-sustained, and correspond to a maximum of the time–dependent oscillation of the dipole moment, as discussed before in chapter 4.

5.2.2 *Cross-section-integrated* Induced Density from Electromagnetics

Within the *ab initio* description, the induced charges spread across the rod's volume. By contrast, in the electromagnetics picture, they are confined at the metal surface. Surface charges are located exactly at the geometric boundaries in the local optics treatment, whereas nonlocal corrections provide the charge distribution with a non-vanishing thickness. Taking this into account, we estimate the induced charges using classical electromagnetics through the discontinuity in the normal component of the electric field. Explicitly, we can write

$$S(x) = 2\pi\epsilon_0 r(x)[\mathbf{E}_{\text{out}}(x) - \mathbf{E}_{\text{in}}(x)] \cdot \mathbf{e}(x) \tag{5.2.3}$$

where, $r(x) = \sqrt{y(x)^2 + z(x)^2}$ is the radial coordinate along the metal boundary, $\mathbf{e}(x)$ is the unit vector along the surface normal, and $\mathbf{E}_{\text{out}}(x)$ and $\mathbf{E}_{\text{in}}(x)$ are the electric fields outside and inside the geometrical boundary. While in local optics, $\mathbf{E}_{\text{in}}(x)$ is evaluated at the metal-dielectric interface, in the nonlocal optics calculations, taking into account the extended character of induced surface charges, $\mathbf{E}_{\text{in}}(x)$ is evaluated exactly at a distance $1/q_{\text{L}}$ from the metal-dielectric interface.

5.2.3 Comparison of *Cross-section-integrated* Induced Density from Electromagneticsn and TDDFT

Figure 5.1 plots $S(x)$ against the length-normalized axis co-ordinate for three distinct Ag systems whose spectra (both in TDDFT-PBE and in classical optics) present a well defined LSPR: 145-atom rod (top left panel), 19-atom rod (bottom left panel) and $N = 18$ atomic chain (top right panel). In all cases, the induced density profiles obtained from TDDFT (brown), and local (violet) and non-local (green) classical optics are shown. The *cross-section-integrated* ground-state density obtained from *ab initio* calculation is shown as orange line (note the different scales of the left and right axes in all panels). To allow for a quantitative comparison between *ab initio* and electromagnetics treatments of $S(x)$, the amplitude of the driving laser in all simulations was set to 10^8 V/m (within the linear response). The insets show the laser field (blue) and the TDDFT time evolution of the induced dipole moment (red). The black arrows indicate the time τ at which the induced charges were computed. The bottom right panel shows the *ab initio* induced (brown) and ground

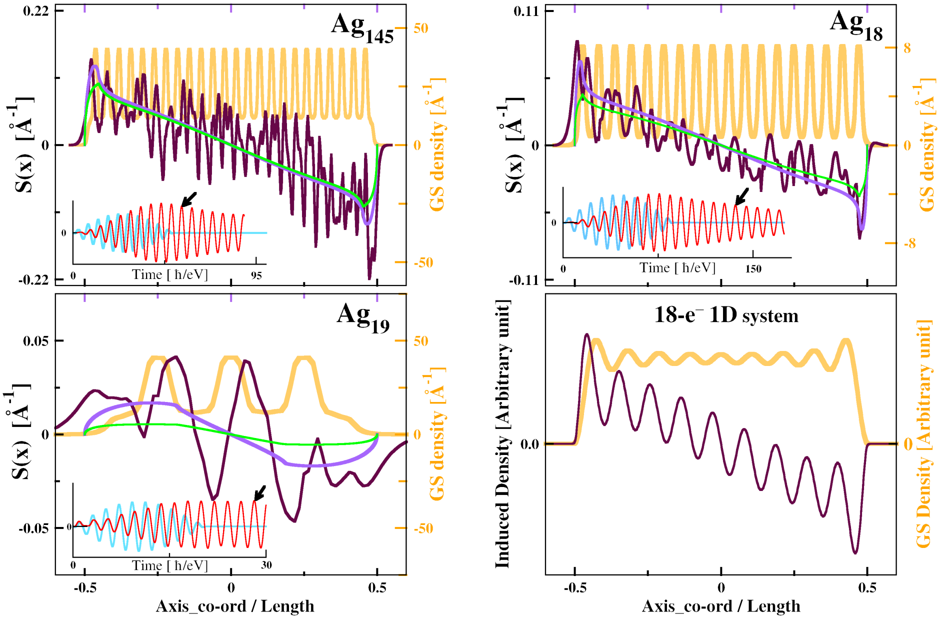

FIGURE 5.1: Induced charge density for Ag_{145} (top left), Ag_{19} (bottom left), Ag_{18} (top right), and a $N = 18$ purely one-dimensional system (bottom right). In all panels, the brown curve plots a snapshot of the TDDFT induced charge density along the normalized rod/chain length in units of electrons/Å. The orange curve renders the ground-state density profile, shown for reference. The violet and green curves in the first three panels show the induced surface charge distribution (in electrons/Å) obtained from local and non-local optics calculations, respectively. The insets show the time dependence of the driving laser (blue) and of the TDDFT induced dipole moment (red).

state (orange) density profiles for a 18-electron purely one-dimensional jellium system modelling Ag_{18}.

Figure 5.1 shows that the excellent quantitative agreement between *ab initio* and classical predictions for the absorption spectra of Ag_{145} (see Figure 4.4) and Ag_{18} (Figure 4.6) also holds in the near-field regime. Remarkably, TDDFT and electromagnetics induced charge peaks are not only located at the same position but present very similar heights. This can be interpreted as a consequence of the high plasmonic character of both structures, which support well-defined collective LSPRs free of the contamination from single electron-hole excitations. There are two relevant aspects in the *ab initio* density profiles which deserve attention.

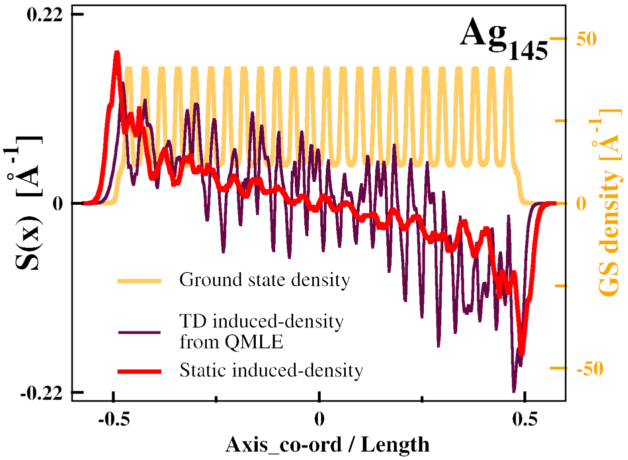

FIGURE 5.2: Induced charge density for Ag_{145}.The brown curve plots a snapshot of the TDDFT induced charge density along the normalized rod length in units of electrons/Å, obtained from a QMLE simulation with LSPR energy. The red curve shows the induced density from a electrostatic calculation. The orange curve shows the ground-state density profile, for reference.

- First, there is the inhomogeneity of $S(x)$ across the length of the structure. These regular modulations of the density are caused by the highly localized nature of the d-electrons and their contribution to the overall response of the system.

- Second, there are weak, somewhat irregular fluctuations overlaid onto those modulations. These arise from the fact that the quasi-monochromatic laser excitation has a finite energetic width and hence can excite several energetically close modes. The superposition of the different modes leads to the irregular fluctuations which modify the overall behavior of the induced density and lead to a certain asymmetry in the density profile. By comparison, a static external field would lead to a profile reflecting the perfectly symmetric geometry along the rod axis, as shown in Fig. 5.2 in red. The comparison of the induced density due to a static external field with the induced density obtained in the time–dependent calculation is discussed later in the next section in 5.4.4.b.

Both, the modulations due to the atomistic density inhomogeneity and the fluctuations due to the superposition of different modes are naturally absent in the classical induced-density profiles.

The right bottom panel of Figure 5.1 correspond to the induced density obtained using TDLDA in one-dimensional model jellium system comprising of 18 electron. It shows a perfectly symmetric and smoothly oscillating $S(x)$ (free of sharp fluctuations). Thus, it confirms our interpretation of the induced density features present in the S(x)-representation of Ag_{18}, but missing in the classical optics results.

5.2.3.a Ag_{19}: Consequences of XC-functional

In Ag_{19}, despite the correspondence in the LSPR spectral position (as can be seen in the lowest left panel in Figure 4.4), the comparison between classical and *ab initio* induced densities (shown in the left bottom panel of Figure 5.1) is rather poor. Unlike Ag_{145} and Ag_{18}, electromagnetic calculations for Ag_{19} yield a $S(x)$ profile which is not peaked at the rod ends. On the contrary, induced charges spread significantly along the nanorod length towards its middle plane. The TDDFT distribution develops several maxima along the length of the system. These are reminiscent of the sharp fluctuations in the *ab initio* $S(x)$ for Ag_{145} and Ag_{18}. This indicates that, as expected from the high LSPR frequency, apparent in its absorption spectrum (~ 3 eV), d-electron transitions play a key role in the optical response of Ag_{19}. Thus, this rod configuration presents a rather low plasmonic character, despite the fact that its TDDFT-PBE absorption spectrum is dominated by a single peak reproduced by classical optics. In fact, as mentioned before, our TDDFT calculations use the PBE AGGA functional, whose validity for the description of Ag_{19} is questionable. This appears in a refined *ab initio* study on Ag_{19}, comparing PBE with the range-separated hybrid functional LC-M06L [168, 169], which has been shown in Fig. 4.11. The LC-M06L functional is more suitable for the treatment of the d-electron excitations and yields accurate spectra for small Ag clusters [203]. From our analysis, we conclude that TDDFT-PBE calculations for Ag_{19} are not reliable, and hence, the spectral agreement between classical and fully quantum results on Ag_{19} is partially fortuitous.

5.2.3.b Ag_{19}: Effect of d-electron description

The comparison of *ab initio* and classical LSPR induced densities for Ag_{19} (see Fig. 5.1) aids to understand a common limitation of both the approaches. The breakdown of TDDFI-PBE approach occurs at the same regime where classical optics predictions are no more valid. In both the approaches the failure is due to the fact that the correct description of the d-electron excitations are missing. Thus, both of them fail to describe the structures in which LSPRs and d-electrons couple strongly. In order to properly study the optical response in these compact structures, classical electromagnetics methods are not suitable and *ab initio* TDDFT should be employed. Even in the TDDFT treatment of those systems, a description of exchange and correlation better than the AGGA functionals is required.

In contrast, if the LSPR is largely free of d-electron excitations (as it is for Ag_{145} and other long rods and atomic chains), the *ab initio* spectra obtained using PBE AGGA functionals are accurate (as can be seen in Fig. 4.11). In this situation, classical optics predicts remarkably well the TDDFT spectral position, strength and character of the induced density of the LSPR.

5.3 Induced Density at LSPR: δ-kick vs QMLE

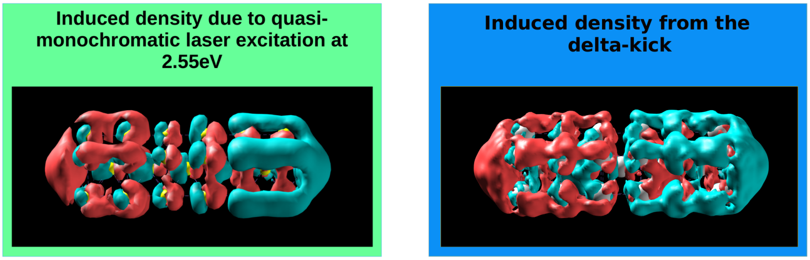

FIGURE 5.3: Induced density of Ag_{37} at LSPR: in left, from the quasi-monochromatic laser excitation (QMLE) simulation, and in right, from the delta-kick simulation. In both the cases, the induced densities correspond to maxima of the self-sustained (i.e., free of perturbing force) oscillating dipole moments in the respective simulations

When the absorption spectrum is primarily dominated by a single well-defined peak, be it an LSPR or something else, the spatial distribution of the induced density obtained from the corresponding delta-kick RT-TDDFT calculation is also dominated by the excitation mode that corresponds to the strong absorption peak. An example is the case of Ag_{37} rod when excited along its axis. This is shown in Fig. 5.3, by comparing the iso-surface of the induced density in Ag_{37} from a QMLE simulation (with laser energy equal to ω_{LSPR} =2.55eV) with the same from the delta-kick simulation.

The Fig. 5.3 also explains that, for systems having strong plasmonic character, the dominant contribution comes from the surface of the system.

5.3.1 Dynamic Screening by the d-electrons in Noble-Metal Clusters

The QMLE is analogous to driving an oscillator with a particular energy. In clusters the oscillator is the electrons. When the QMLE simulation is performed using the laser energy equal to the LSPR energy, resonance of the electron-density oscillation is observed in the time-dependence of the induced charge density. A snapshot at an extremum of this oscillation is shown in the left panel of Fig. 5.3 and for different iso-surface values in Fig. 5.4. A careful observation of the snapshot of induced densities in these figures also reveals an specific phenomenon observed in noble-metal clusters: dynamic screening by the d-electrons. The induced density at the core of the system, and around the ions, oscillates out of phase with the same at the surface region. This is because of the fact that the localized d-electrons centered around the ionic lattices respond to the field created by the de-localized s-electrons which, at LSPR, are in resonance with the laser perturbation. In a plasmonic cluster of simple-metal these opposite oscillations of the induced density around the ions would not occur, as shown in Fig. 5.5.

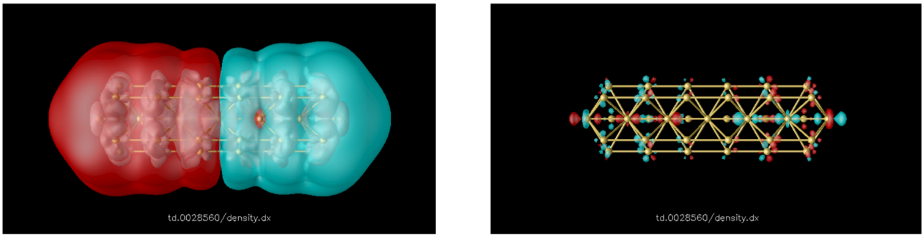

iso $=$ 1e-7 iso $=$ 3e-5

FIGURE 5.4: Different iso-surfaces of induced density of Ag$_{37}$ at LSPR (ω_{LSPR}=2.55eV) from QMLE simulation, shows that oscillation at the core is different in many sense from the dominant oscillation at the surface of the system.

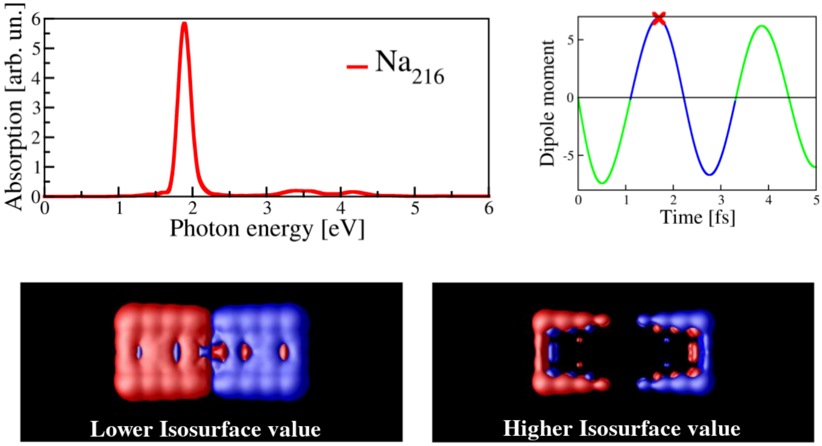

FIGURE 5.5: For comparison with the behaviour of noble-metal clusters in Fig. 5.3 & 5.4, here we show the density oscillation of a rectangular 216-atom rod of sodium, i.e., of a simple metal. The spectrum is clearly dominated by one peak (as shown in the upper-left panel), corresponding to the LSPR, and the time dependence of the dipole moment is almost perfectly sinusoidal (shown in the upper-right panel). In the lower panels, the time dependent density snapshots at a maximum of the oscillating dipole moment show that the density dynamics corresponds perfectly to the collective density oscillation. In particular, even the isosurfaces at high values of density difference do not show contributions around the atomic positions, unlike in the noble metal as shown in Fig. 5.4 for Ag_{37} at LSPR. These results are taken from Ref. [121].

5.4 Spatially Resolved Fourier Transform Of The Induced Density

As discussed in the chapter 3, using the delta-kick RT-TDDFT simulation, one excites all the possible electronic excitations depending on the direction of the delta-kick perturbation. Thus the absorption spectrum and the corresponding time–dependent induced density contain all the information of those excitations. The drawback of RT-TDDFT formalism is that, unlike the transition-based LR-TDDFT (e.g. Casida) calculations, it can't give information of the excited states. Therefore, in a delta-kick calculation, there is no direct access to the spatial distribution of the charge density, that corresponds to a particular transition. However, within the framework of RT-TDDFT simulations, it is possible to obtain the induced density corresponding to a particular transition by means of a QMLE simulation with a laser of energy equal to the energy of that transition, as shown in the previous section.

However, as the time–dependent induced density corresponding to the delta-kick RT-TDDFT simulation is the superposition of the induced densities corresponding to all the excitations that appear in the spectrum, in principle, the spatial distribution of any mode corresponding to any particular excitation can be accessed through the Fourier decomposition of the time–dependent induced density in frequency domain.

5.4.1 Reconstruction Of Modes

The delta-kick RT-TDDFT simulation uses the ground state density $\rho^{GS}(x, y, z)$, which is calculated in static DFT, as input, and gives the time- dependent density $\rho^{TD}(x, y, z, t)$. The time–dependent induced density is then simple obtained as:

$$\rho^{TD-GS}(x, y, z, t) = \rho^{TD}(x, y, z, t) - \rho^{GS}(x, y, z) \tag{5.4.1}$$

This time–dependent induced density can be expressed in a Fourier series, in terms of different Fourier components at different frequencies, as

$$\begin{aligned} \mathscr{R}(x, y, z, \omega, t) &= \mathscr{F}\big[\rho^{TD-GS}(x, y, z, t)\big] && (5.4.2) \\ &= \sum_{i=0}^{\infty} \Big(a(x, y, z, \omega_i)\ cos(\omega_i t) + b(x, y, z, \omega_i)\ sin(\omega_i t) \Big). && (5.4.3) \end{aligned}$$

So, for a particular frequency ω_i, the time–dependent spatial distribution of the corresponding mode is given as

$$\mathscr{R}(x, y, z, \omega_i,\ t) = a(x, y, z, \omega_i)\ cos(\omega_i t) + b(x, y, z, \omega_i)\ sin(\omega_i t) \tag{5.4.4}$$

where, $a(x, y, z, \omega_i)$ and $b(x, y, z, \omega_i)$ are the Fourier cosine and sine coefficients, respectively, which can be obtained through the Fourier transforms of $\rho^{TD-GS}(x, y, z, t)$ as

$$a(x, y, z, \omega_i) = \frac{1}{2\pi} \int_0^{t_\infty} cos(\omega_i t)\ \rho^{TD-GS}(x, y, z, t)\ dt, \tag{5.4.5}$$

and

$$b(x, y, z, \omega_i) = \frac{1}{2\pi} \int_0^{t_\infty} sin(\omega_i t)\ \rho^{TD-GS}(x, y, z, t)\ dt. \tag{5.4.6}$$

The square root of the sum of the squared modulus of the Fourier coefficients, for a particular frequency,

$$\mathscr{S}(x,y,z,\omega_i) = \sqrt{|a|^2(x,y,z,\omega_i) \ + \ |b|^2(x,y,z,\omega_i)}, \tag{5.4.7}$$

shows *the region in space that contribute to the induced density* that corresponds to the excitation at that frequency.

Using the ground-state and time–dependent densities obtained as output from a RT-TDDFT simulation in the code `octopus` [186, 204], we have performed the spatially resolved Fourier transform of the time-dependent induced density. Using this analysis, we have recovered the spatial profile of the induced density at any given energy (ω_i) of interest, in terms of $\mathscr{S}(x,y,z,\omega_i)$ and $\mathscr{R}(x,y,z,\omega_i,\ t)$, as discussed above. In the next subsections, we have discussed the applicability, efficiency and limitations of this analysis in view of understanding the differences between collective plasmonic excitations and the excitations involving d-electrons, as well as the interplay between plasmon and d-electrons in the spatial behaviour of the modes corresponding to the respective excitations.

5.4.2 Modes in an Atomic Chain: Na$_{20}$

The left panel of the Fig. 5.6 shows the optical absorption spectrum for a linear atomic chain of 20 Na atoms, calculated in delta-kick RT-TDDFT method, using the PBE xc-functional [159, 160]. The time–dependent induced density of the delta-kick RT-TDDFT simulation is used to reconstruct the quantities $\mathscr{S}(x,y,z,\omega_i)$ and $\mathscr{R}(x,y,z,\omega_i,\ t)$, which are explained in the previous subsection. There are four distinct absorption peak in the PBE-spectra as can be seen in the figure at energies 0.53 eV, 1.31 eV, 1.87 eV, and 2.33 eV. $\mathscr{S}(x,y,z,\omega_i)$ has been calculated for each of these energies and is shown in different colors for the same isosurface value. The time–dependent oscillation of the modes, $\mathscr{R}(x,y,z,\omega_i,\ t)$, at the respective energies is also calculated using eq. 5.4.4. In the right panel of Fig. 5.6, snapshots of the modes at the maxima of their oscillations corresponding to respective energies are shown for the same isosurface value.

The transition densities for the first two peaks were previously calculated by Bernadotte et al. [197] using the LR-TDDFT approach. The transition density corresponds to the induced density that gives rise to the optical excitation at a certain energy. In

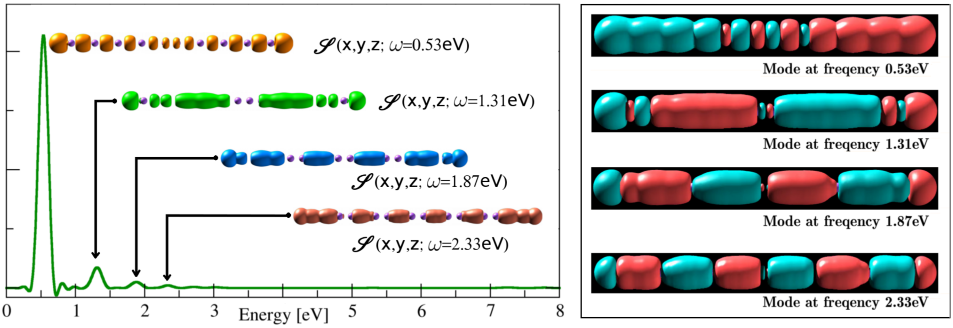

FIGURE 5.6: Absorption spectrum of Na_{20} and induced densities at some energies of interest corresponding to features in the spectrum. **Left**: the regions in space that contribute to the induced densities at different energies are reconstructed from the induced density of a delta-kick RT-TDDFT calculation and shown in different color representing different energies. **Right**: The reconstrued modes of the induced electron density oscillation at certain frequencies (ω_i), and at a maximum of the time–dependent oscillation ($\mathscr{R}(x, y, z,\ t = T/4, \omega_i)$, where T = time period of oscillation). The negative absorption apparent in the spectrum is due to numerical noise only.

Fig. 5.7, a comparison of the reconstructed modes for the first two peaks at 0.53 eV ($\mathscr{R}(x, y, z, t = T/4; \omega = 0.53\ \mathrm{eV})$) and 1.31 eV ($\mathscr{R}(x, y, z, t = T/4; \omega = 1.31\ \mathrm{eV})$), with the corresponding transition densities calculated in Ref. [197] is shown. This corroborates the fact that, in this simple model system, the optically excited even modes resembles to different harmonics in a stretched string.

5.4.3 Modes in Compact Icosahedral Na_{55}^{+}

Unlike in the quasi-one-dimensional atomic chain of 20 Na atoms, in a more compact icosahedral Na_{55} cluster, significant absorption features start to appear in the visible spectrum at about 2.5 eV. Fig. 5.8 shows absorption spectra for a Na_{55}^{+} cluster, calculated in different *ab initio* approaches. The brown curve belongs to the delta-kick RT-TDDFT simulation, while the red sticks show the oscillator strengths calculated in LR-TDDFT Casida approach by F. Rabilloud. The red curve is a convolution of the Casida spectrum with a Lorentzian. The '+' signifies the charge state, i.e., the fact that one electron is taken away from the cluster. The spectra are obtained using the PBE [159, 160] xc-functional. The RT-TDDFT spectrum is obtained in the code `octopus`, exciting the cluster with a delta-kick along the 5-fold symmetry axis of the cluster. The Casida spectrum is calculated using the code GAUSSIAN. The most

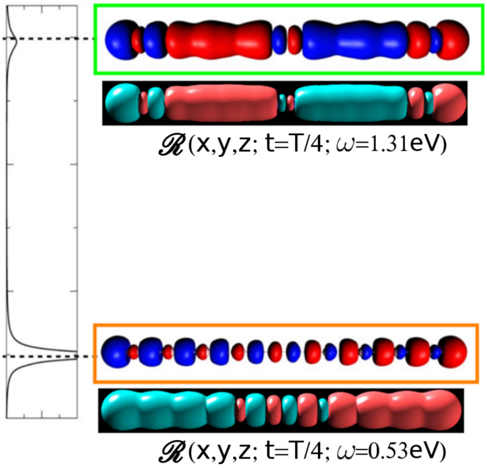

FIGURE 5.7: The reconstructed modes of the induced electron density oscillation at certain frequencies (ω_i), and at a maximum of the time–dependent oscillation ($\mathscr{R}(x, y, z,\ t = T/4, \omega_i)$, where T =time period of oscillation), is compared with the transition densities (in colored boxes) at the respective energies calculated in LR-TDDFT (Casida) method by Bernadotte et al. [197].

prominent peak in RT-TDDFT spectrum appears at 2.94 eV and in LR-TDDFT spectrum at 2.92 eV. The discrepancy in the spectral position of the most prominent peak is of the order of differences which we found between two GGA calculations done using octopus and GAUSSIAN, respectively. $\mathscr{S}(x, y, z, \omega_i)$, showing the spatial regions where the induced densities are large, are calculated at three different energies from the time–dependent induced density obtained from the delta-kick RT-TDDFT simulation. These are shown for the same isosurface value in three different colors in Fig. 5.8. Though all these three different spatial distributions of the induced densities at three different energies do not look exactly similar, they clearly show that the density response of the cluster is primarily from its surface. In all the three cases, the spatial distribution of the induced density corresponds to a largely rigid displacement of the density from its equilibrium position, leading to the appearance of the induced density mainly at the surface.

For the most prominent peak at about 2.9 eV, the mode is shown in Fig. 5.9. The upper panel of the figure shows different isosurface values for the transition density that correspond to the single excitation at exactly 2.92 eV as calculated in LR-TDDFT.

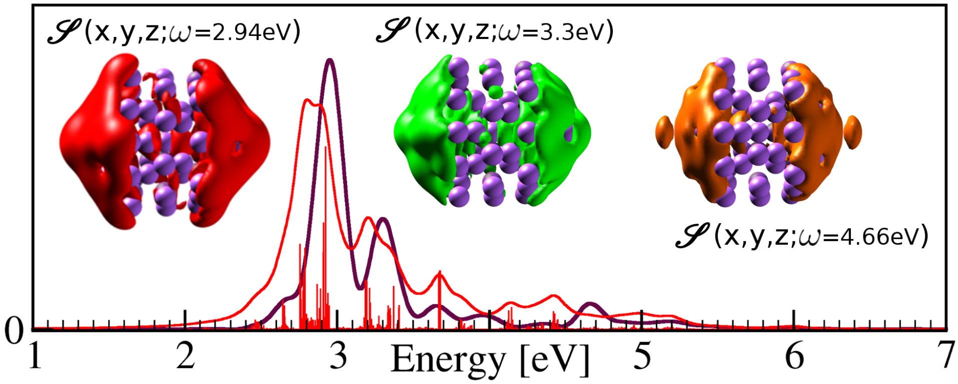

FIGURE 5.8: Absorption spectra of icosahedral Na_{55}^{+} calculated in RT-TDDFT (brown) and LR-TDDFT (red). The oscilator strengths are arbitrary. For the LR-TDDFT calculation, the oscillator strengths are shown both as sticks (red) and also as Lorentzian-convoluted curve (red). The spacial regions that contribute to the induced densities at some energies of interest are shown in different colors.

In the lower panel of the figure, the snapshots of the maximum of the density oscillation at 2.94 eV ($\mathscr{R}(x, y, z, t = T/4; \omega = 2.94 \text{ eV})$), for two different isosurface values are shown. This is obtained by reconstructing the mode at 2.94 eV from the Fourier transform of the time–dependent induced density obtained from a delta-kick RT-TDDFT simulation. The atomic structure of the system and the polarization of the delta-kick are shown at the middle of the lower panel. In both the *ab initio* approaches, the similarity in the appearances of the mode reconfirms the fact that the spatial profile of a mode at a certain energy is recovered simply by retrieving its contribution to the total density induced in the system due to the delta-kick.

5.4.3.a Resolution of The Mode

A careful comparison of the mode ($\mathscr{R}(x, y, z, t = T/4; \omega = 2.94eV)$) reconstructed from the induced density of the delta-kick simulation with the mode (transition density) obtained in LR-TDDFT shows that, although in general they look similar at the surface, they look different at the interior region. The explanation of this mismatch can be traced back to the resolution of the individual modes from RT-TDDFT. It depends on different parameters in the two different approaches. In LR-TDDFT approach, a mode is always resolved as long as the calculation is correctly performed

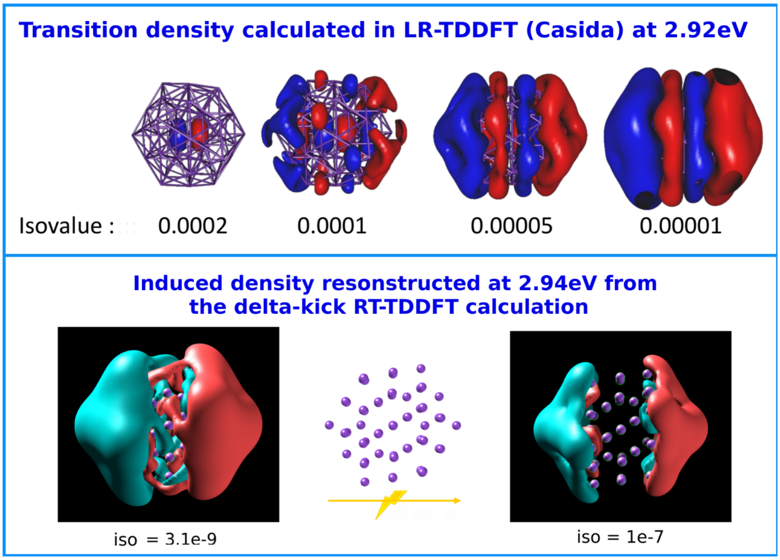

FIGURE 5.9: Modes of electron-density oscillation at 2.94 eV in icosahedral Na_{55}^{+}, reconstructed from the induced densities calculated in RT-TDDFT (lower panel), is compared to the transition density obtained from LR-TDDFT (upper panel), at 2.92 eV energy. The atomic structure and the polarization of the delta-kick excitation is shown in the middle of the lower panel. Diferrent isosurface values are shown in both the cases (RT-TDDFT & LR-TDDFT) to exhibit the distribution of the induced densities in different regions of the cluster.

by considering all the excited states that contribute to the mode. In RT-TDDFT, however, the resolution of a mode depends on the spectral resolution, which in turn depends on the total evolution time of the simulation. It can be seen in the LR-TDDFT spectrum in Fig. 5.8 that, there are many closely spaced spectral features around the most prominent one at 2.92 eV. As the resolution of a mode in the RT-TDDFT spectrum is always limited to the total evolution time, the mode at around at 2.94 eV has significant contribution from the modes excited at the neighbourhood. Therefore, all these neighbouring modes contributes to the electron-density response reflected in the mode reconstructed at 2.94 eV from the time–dependent induced density of the RT-TDDFT simulation. Due to all these significant contributions, though the mode at 2.94 eV resembles pretty much the transition density at 2.92 eV corresponding to the LR-TDDFT calculation (which corresponds to one individual transition), reflecting the main contribution from 2.94 eV, it gets superimposed with the neighbouring contributions and deviates from the exact nature of the mode. If the RT-TDDFT spectra would have been calculated from a “long-run” calculation where the evolution time is as large as infinite, one could recover the exact nature of the mode at 2.94 eV, which would look similar to the one obtained in LR-TDDFT calculation at 2.92 eV. Of course, "long-run" RT-TDDFT calculations are computationally expensive. An example of such a long-run calculation is shown in Fig. 6.5 in the next chapter. Although performing spatially resolved Fourier transform of the induced density corresponding to a "long-run" RT-TDDFT calculation numerically is not impossible, it requires more technical attention in treating large number of data efficiently.

5.4.4 Modes in Ag_{37} Rod

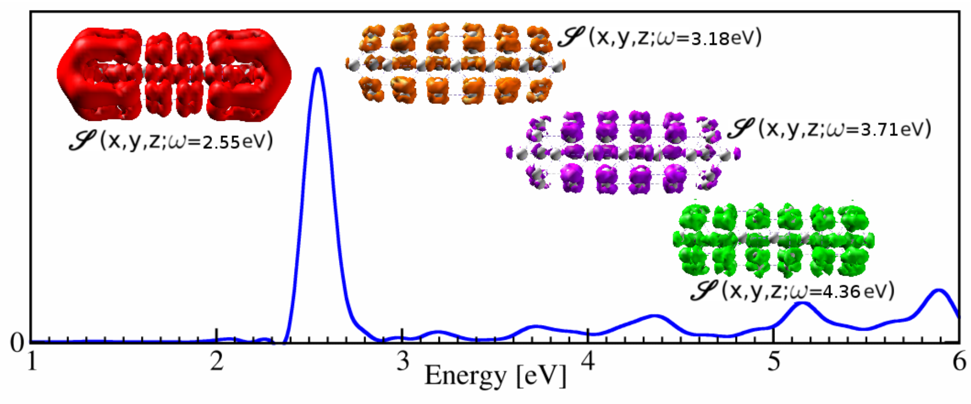

FIGURE 5.10: Absorption spectrum of Ag_{37} is shown in blue. The regions of space ($\mathscr{S}(x,y,z,\omega_i)$), where the induced densities corresponding to the modes at differrent energies of interest are large, are shown in different colors.

Following the reconstruction of modes of the induced density in a simple metal, we have performed the same analysis of the induced density obtained from a delta-kick RT-TDDFT simulation to explore the modes excited in noble metal clusters. In Fig. 5.10, the spectrum of Ag_{37} and the spatial regions ($\mathscr{S}(x,y,z,\omega_i)$) where the induced densities corresponding to the modes at differrent energies of interest are large, are shown. The spectrum is the same one that has been shown in the lowest left panel in Fig. 4.4 in red. The strongest peak at 2.55 eV corresponds to the LSPR, while the other spectral features at higher energies come from interband transitions. All the $\mathscr{S}(x,y,z,\omega_i)$ for different energies are shown for the same isosurface value. The distribution $\mathscr{S}(x,y,z,\omega = 2.55eV)$ reveals that the primary contribution in the formation of the mode comes from the surface of the rod, and in particular from its ends. Thus, this spatial distribution of the LSPR mode confirms the dipolar character of the mode. By contrast, the spatial distributions for the modes at higher energies, $\mathscr{S}(\omega = 3.18eV)$, $\mathscr{S}(\omega = 3.71eV)$, $\mathscr{S}(\omega = 4.36eV)$, reveal that the modes at those energies are primarily located around the silver atoms, suggesting strong contribution from the localized d-electrons. This observation becomes more apparent in Fig. 5.11, where the maximum of the electron density oscillation of the reconstructed modes are shown as isosurfaces of the same value for two (3.71eV, & 4.36eV) at higher energy excitations. These higher energy modes which lie in the region of interband transitions in the spectrum, primarily consist of many closely spaced excitations. As the spectrum is not sufficiently resolved, the spacial distribution of the modes shown in Fig. 5.11, rather represent superposition of more than one single excitation which are energetically very close.

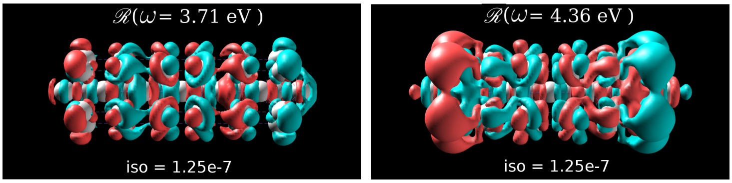

FIGURE 5.11: Mode of the induced density reconstructed at $\omega_i = 3.71$eV (left) and $\omega_i = 4.36$eV (right) from the induced density of the delta-kick simulation, shows contributions from localized d-electrons excited at higher energies.

5.4.4.a Modes at LSPR

In Fig. 5.12, we show the mode of the induced density that corresponds to the LSPR in Ag_{37} at 2.55 eV. As discussed earlier in chapter 4, the spatial profile of the induced density at a certain energy can be obtained from the amplitude of the self-sustained oscillation of the electron density, after exciting the system with a quasi-monochromatic laser of the particular energy (i.e., having a certain energetic width in the frequency domain). Thus, the middle panel of Fig. 5.12 shows the induced density obtained after a laser excitation with 2.55 eV energy. The right panel shows the mode of the induced density reconstructed at $\omega_i = 2.55$eV from the induced density of the delta-kick simulation. These two snapshots of the oscillating induced density are compared with the induced density obtained by the application of an *electrostatic* field, shown in the left panel of Fig. 5.12.

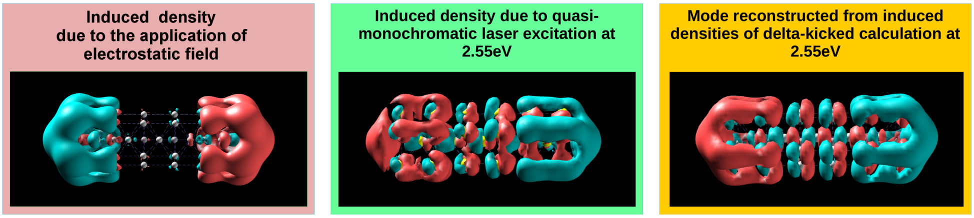

FIGURE 5.12: **Left**: Spatial distribution of the mode of the induced density of Ag_{37} due to the application of an electrostatic field polarized along the axis of the cluster. **Middle**: Induced density from the quasi-monochromatic laser excitation (QMLE) simulation, with laser of energy $\omega = 2.55\mathrm{eV}$ and polarized along the axis of the cluster. The induced density corresponds to a maximum of the self-sustained (i.e., free of perturbing force) oscillating dipole moment. **Right**: Spatial distribution of the mode of the induced density of Ag_{37} reconstructed at $\omega_i = 2.55\mathrm{eV}$ from the induced density of the delta-kick simulation.

The electrostatic field is polarized similarly as the delta-kick and the laser field, along the axis of the cluster. This comparison strongly corroborates the perception of the LSPR as a dipolar surface mode. Moreover, unlike in the electrostatic case, the dynamic screening by the d-electrons is evidenced in the dynamic response (either due to laser excitation or due to delta-kick perturbation) where significant contributions of the induced density from the regions around the atoms of the cluster are observed. These localized contributions, as mentioned earlier, belong to the oscillations of the localized d-electrons which oscillate in response to the induced field created by the dominating collective response of the s-electrons at resonance having a quarter of a period phase shift.

5.4.4.b Static response of the induced density

In the first section of this chapter, we have compared the *cross-section-integrated* induced density due to an electrostatic field and at LSPR energy for Ag_{145} rod in Fig. 5.2. For Ag_{37}, the spatial distribution of the induced density due to an external electrostatic field is shown in Fig. 5.12. In both this figures, we observe the absence of contribution to the overall induced density from the interior of the clusters. This confirms that there is no electric field inside these system and the whole electrostatic response is mainly at the surface regions, suggesting that the clusters preserve their metallic characters.

5.5 Absorption in Ligand-Protected $Ag_{29}P_4S_{24}C_{144}H_{108}$

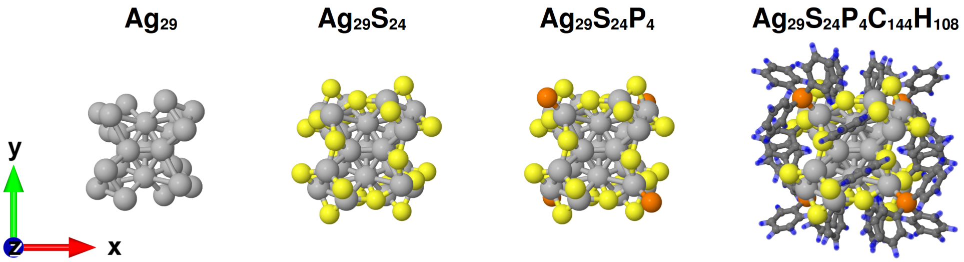

FIGURE 5.13: The arrangement of the different species in constructing the atomic structure of the $Ag_{29}P_4S_{24}C_{144}H_{108}$ cluster.

Finally, we have explored different modes of absorption in a ligand protected cluster of 29 Ag atoms. The atomic structure of the cluster and the arrangements of the different species are shown in Fig. 5.13. The core of the cluster consists of 16 Ag atoms around an interior core of 13-Ag-atom icosahedral structure. 24 sulfur atoms and four phosphorus atoms link the core of the cluster with the ligands consisting of benzene rings. The cluster falls in the group of atomically precise silver clusters with a self-assembled monolayer of ligands. This particular cluster has recently been synthesized and crystallized [205]. The structure features four unique tetrahedrally symmetrical binding surface sites and shows a chiral network of ligands around it. The absorption spectrum for this cluster is obtained in RT-TDDFT using a delta-kick along the x-direction. The PBE xc-functional [159, 160] is used. The spectrum is shown in orange in Fig. 5.14. The values of the absorption cross-section are shown in $Å^2$, in the left y-axis of the figure.

As expected, in ligand-protected silver clusters in this size range, there is no strong plasmon-like absorption in the visible [206]. However, there is a number of distinct spectral features. The first of these features appears at around 2.7 eV. The strongest peak in the absorption spectrum of the $Ag_{29}P_4S_{24}C_{144}H_{108}$ cluster appears in the far UV at 6.46 eV. In order to investigate the origin of this strong absorption, the absorption spectra of the isolated benzene molecule is also shown: The green curve corresponds to the absorption due to excitation parallel to the plane of the molecule, while the red one belongs to the excitation perpendicular to the plane of the molecule. The values of the absorption cross-section for this spectrum is shown

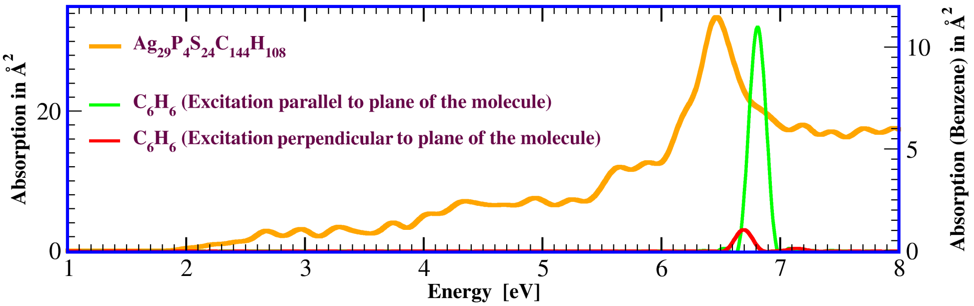

FIGURE 5.14: Absorption spectra for $Ag_{29}P_4S_{24}C_{144}H_{108}$ cluster and Benzene molecule. The scale for the oscillator strength of the benzene molecule is shown at the right side of the frame. Both the in plane (green) and perpendicular to the plane (red) modes for the benzene molecule is shown.

in Å^2, on the right y-axis of the figure.

The similarity of the strong peak at 6.46 eV in the spectra of the $Ag_{29}P_4S_{24}C_{144}H_{108}$ clusters and the spectrum of the isolated benzene molecule suggests a common physical origin. Indeed, the benzene rings in the ligands that stabilize the $Ag_{29}P_4S_{24}C_{144}H_{108}$ cluster could give rise to this absorption feature. The relatively small difference in energy (less then half an eV) is not surprising and reflects the fact that the rings are connected directly to the Ag_{29} core, which naturally modifies the response. In the next section, we investigate this hypothesis using the Fourier transform analysis developed in the present chapter.

5.5.1 Spatial Localization of Modes at Different Energies

In order to investigate the nature of the absorption at different energies, the spatial profiles of the modes of the induced density at certain energies of interest are reconstructed by spatially resolved Fourier transform of the time–dependent induced density belonging to delta-kick RT-TDDFT simulation. The results are shown below.

5.5.1.a Low-energy Mode Confined To The Core

Figure 5.15 shows the isosurface of the induced density that corresponds to the absorption at 2.69 eV energy in the $Ag_{29}P_4S_{24}C_{144}H_{108}$ cluster. An arrow (in yellow) indicates the direction of the delta-kick excitation. The left part in the figure shows the induced density of the mode, with the atomic structure of the whole cluster. In the middle of the figure the mode is shown with only the Ag atoms (in black). On the right, the structure is rotated 90° about the axis perpendicular to the direction of the excitation. The figure reveals that the mode excited at 2.69 eV is mainly located at the core of the whole cluster. The contribution from the ligands (containing the benzene rings) appears to be negligible as compared to the contribution of the Ag atoms in the core. This is in accordance with the optical behaviour of the benzene molecule which does not absorb in the visible. Moreover, in silver clusters having $\sim$30 atoms, spectral features start to appear around 2.5 eV.

5.5.1.b Mode Spread Around The Ligands

Following the analysis of the induced density of the reconstructed mode at 2.69 eV, the induced density corresponding to the mode at 6.46 eV is also shown in Fig. 5.16. In order to make a fair comparison, the same isosurface value as used for 2.69 eV mode is used to show the spatial profile of the mode at 6.46 eV. The 3D spread of the induced density profile is shown in the left part of the figure. A cut through the middle of the whole structure, and along a plane (z=0) perpendicular to the direction of the excitation, is shown with (in the middle of the figure) and without (at the right part of the figure) the atomic structure of the cluster. A comparison of this induced density with the one at 2.69 eV clearly reflects the higher oscillator strength at 6.46 eV than at 2.69 eV. More interestingly, it shows that this high-energy mode is mainly located around the benzene rings of the ligands, which all together forms a chiral ligand network around the surface of the cluster.

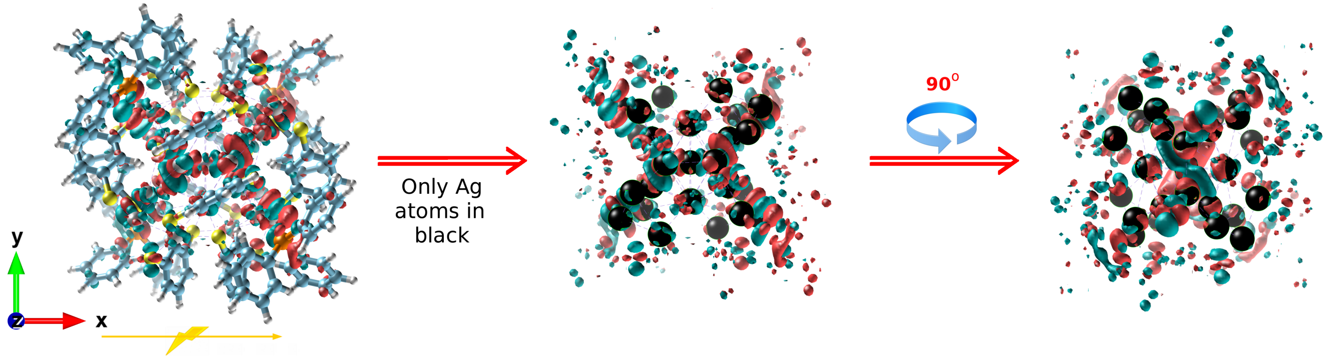

FIGURE 5.15: Mode of the induced density, shown as 3D isosurface (positive in blue, negative in red), that corresponds to the absorption in the $Ag_{29}P_4S_{24}C_{144}H_{108}$ cluster at 2.69 eV (the first prominent peak in the absorption spectrum). Presenting the mode with the core atomic structure consisting only of the Ag atoms shows that the mode is confined to the core of the whole cluster rather than to its surface area comrising the ligands.

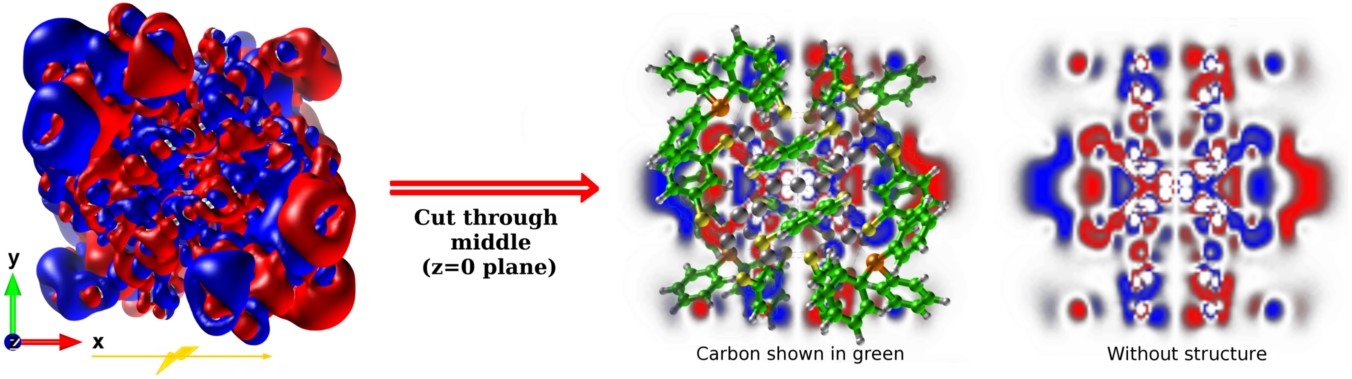

Carbon shown in green

Without structure

FIGURE 5.16: Mode of the induced density, shown at the left as 3D isosurface (positive in blue, negative in red), that corresponds to the absorption in the $Ag_{29}P_4S_{24}C_{144}H_{108}$ cluster at 6.46 eV. Presenting the mode as a cut through the middle plane (at z=0) of the whole system reveals that the principal contribution to the mode comes more from the ligands (which contains multiple benzene rings shown in green) of the whole cluster than from its core of Ag atoms.

Chapter 6

Absorption in Nano-Alloys of ≈1.8 nm Bimetallic Au-Cu Clusters

6.1 Nano-Alloys

Among the three coinage metals, silver is optically different from Au and Cu because the onset of interband transitions from the d band occurs at about 4 eV in silver, whereas in Au and Cu, it occurs at $\approx$ 2 eV. Therefore, silver behaves more like a free-electron metal and shows a clear LSPR down to very small sizes [207], although this depends also on the cluster surface; ligand-protected clusters of fewer than $\approx$ 150 silver atoms seem to loose the plasmonic character [206]. By contrast, as discussed for Au in the previous chapters, in Cu also interband transitions involving d electrons couple strongly with the LSPR, as much so as to make it disappear for small clusters, thereby creating the phenomenon of plasmon emergence/disappearance in dependence on cluster size [188, 208, 209]. In view of these differences, it is natural to look at nanoalloys of these materials. Mixing of gold with silver has been studied, both experimentally and theoretically, for both bare [103, 188] and ligand-covered [110, 111] clusters, showing in general a smooth change of the spectra with changing composition, whereby the outermost layer of bare clusters strongly influences the properties [103]. Insertion of a Cu core into a small silver cluster has been shown to strongly suppress the LSPR [210].

6.2 Thiolate Protected 144-atom Au Cluster Compound

The thiolate ligand-protected $Au_{144}(SR)_{60}$ cluster compound is an exceptionally well suited benchmark system for the investigation of optical properties in the 'intermediate size-range', and this for a number of reasons. First, its diameter ($D \approx 1.8\,\mathrm{nm}$) lies in the size range where the LSPR starts to develop in Au clusters, but also where the transition from molecular-cluster to metallic-nanoparticle behaviors occurs. It shows itself no strong resonance in the visible spectra [208, 209, 211]. Second, the cluster happens to be highly stable and has been studied by a number of different research groups [211–215]. Third, the cluster compound exhibits icosahedral symmetry [216, 217] which implies a high degree of degeneracy of its electronic levels and, consequently, strong individual structures in its optical spectra [211] although recent studies indicate polymorphism in certain samples [218, 219]. Finally, it has been shown experimentally that the precise nature of the ligand rest group (denoted R) bears little influence on the optical spectra. For a collection of results we refer the reader to Ref. [220].

6.2.1 Alloying $Au_{144}(SR)_{60}$ With Copper

Recent experiments have attempted to alloy gold and copper in the $Au_{144}(SR)_{60}$ class of cluster compounds, leading to the most extraordinary results: while both Au and Cu at this size do not show a plasmonic resonance, insertion of copper into the gold cluster samples leads to the development of a peak at 550 nm (2.25 eV), reminiscent of the LSPR [11, 12]. This outstanding result — the combination of two non-plasmonic metals (at this size) apparently leading to the development of a plasmon resonance – calls for explanation. The result is even more surprising in that it indicates that in some cases, a single copper atom might be sufficient to induce this effect [12], although this was not the case in the experiments performed in Ref. [11]. In order to understand this highly unexpected behavior, Malola *et al.* have carried out time-dependent density-functional theory (TDDFT) calculations and concluded that *"Copper Induces a Core Plasmon in Intermetallic* $Au_{(144,145)-x}Cu_x(SR)_{60}$ *Nanoclusters."* [221] Substituting copper for gold atoms in a number of different configurations and compositions, these authors obtain the development of a peak at about 550 nm compared to the spectrum of the pure $Au_{144}(SR)_{60}$, which is interpreted as a plasmonic resonance. Even the insertion of one copper atom in the center vacancy of the pure $Au_{144}(SR)_{60}$ has been interpreted to have this effect.

In this chapter, we show that this behavior is by no means general. The introduction of copper into the gold clusters leads essentially to the suppression of intensity at some wavelengths as well as to small red shifts in energy of some spectral features. The combination of these rather weak effects leads then in some cases to spectra that exhibit a weak hump at the wavelength in question, at around 550 nm ($\approx$ 2.2 eV). However, no indication is found of any increase of intensity in the spectra compared to those of the pure Au clusters, as it would correspond to a plasmonic resonance developing. We note that the energy range in question corresponds exactly to the onset of interband transitions from the d-electrons (2.0 ... 2.5 eV) *and* to the region where the LSPR in pure gold clusters should emerge [188]. In other words, in this energy range there is a strong coupling between d-electron excitations and the nascent surface plasmon. Therefore, any statement about the precise nature of spectral features has to be made with extreme care.

6.3 Absorption spectra

6.3.1 Different Technical Aspects

As sketched in Fig. 6.1, alloying is done by the inclusion of Cu into Au clusters by replacing individual gold atoms by copper atoms (and, in some cases, filling the central vacancy, which leads to numbers of atoms of 144 or 145 for the Au_{144}-derived liganded clusters, and an unchanged 147 for the bare clusters). The ionic ground-state relaxations have been done using the VASP code [222–224] with the projector-augmented wave method (PAW) [224]. The force tolerance has been set to 0.01 eV/Å. The absorption spectra are calculated in TDDFT using the real-space code `octopus` [186, 204]. Following a ground-state calculation, spectra are obtained with the time-evolution formalism [183, 184] and the PBE-GGA exchange-correlation functional [159, 160] *for all spectra* shown, including those where the structural relaxation was done using LDA. Norm-conserving Troullier-Martins pseudopotentials [176] have been used which include the d electrons in the valence (11 valence electrons for each Au or Cu atom, i.e., $\sim 2,500$ active electrons). The spacing of the real-space grid was set to 0.20 Å for the pure-Au clusters, and to 0.16 Å for the clusters containing copper. The radius of the spheres centered around each atom which make up the calculation domain was 5 Å. The clusters have been charged as

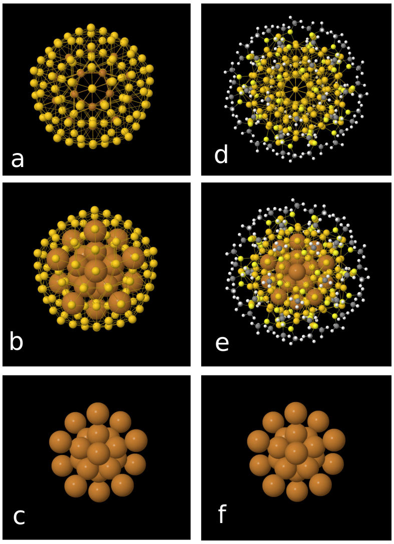

FIGURE 6.1: Structure of the bare 147-atom clusters (left-hand side, panels a-c) and the ligand-protected $Au_{144}(SR)_{60}$ clusters (right-hand side, d-f). Uppermost panels: complete pure-Au clusters; middle panels: alloying with 25 copper atoms, which leads to $Au_{122}Cu_{25}$ for the bare and to $Au_{120}Cu_{25}(SR)_{60}$ for the ligand-protected cluster. In the ligand-protected structure, the central vacancy of the pure-gold structure is filled with a copper atom. The copper atoms are represented with a larger radius for the sake of visibility. Lower panels (c,f): copper atoms only (25 in both cases). The distribution of the copper atoms is identical in the bare and the ligand-protected clusters and corresponds to "model 9" of Ref. [221].

indicated such that the degenerate HOMO states were fully occupied.

This approach simulating the absorption and the parameters mentioned in the previous paragraph have been employed to both the bare and the ligand-protected clusters following previous reports [210, 211, 220]. Apart from the customary 147-atom icosahedron that has been studied in many works, we have considered the following structural models of $Au_{144}(SR)_{60}$ and its alloys with copper. (For a detailed analysis of the differences between these structures, refer to Ref. [220].)

- The fully symmetric, GGA-relaxed $Au_{144}(SR)_{60}$ with $R=CH_3$ from the work of Bahena *et al.*, Ref. [217], is used as starting structure. For the respective comparison, this structure has also been re-relaxed using LDA .
- The $Au_{144}(SR)_{60}$ with R=H is obtained from the same structure by replacing the methyl group with H atoms and re-relaxing.

- For comparison, we have also used the “Malola *et al.* structure” as employed in the calculations of Ref. [208]. The structure is derived from the original, less symmetrical López-Acevedo *et al.* structure [225] by reducing the rest group to R=H, probably resulting in a partial symmetrization as discussed in Ref. [220].

- Copper (or, in one case, gold) is introduced into the center vacancy (resulting in $\mathrm{Au}_{144}\mathrm{Cu}_1(\mathrm{SR})_{60}$). For the higher copper content, $\mathrm{Au}_{120}\mathrm{Cu}_{25}(\mathrm{SR})_{60}$, we use the model structure that is called *model #9* in Malola *et al.* [13] which consists of a 13-atom Cu core (filled central vacancy) and 12 Cu atoms distributed symmetrically in the 42-atom shell around the 13-atom core so as to conserve the icosahedral symmetry [221]. This structure is shown in Fig. 6.4 in Appendix D, along with the other ones.

6.3.2 Bare icosahedral 147-atom clusters

Before analyzing absorption in the $\mathrm{Au}_{144}(\mathrm{SR})_{60}$ compound, we have studied the far simpler case of bare 147-atom icosahedral clusters. These clusters of ≈ 1.6 nm diameter have roughly the same number of gold atoms as the $\mathrm{Au}_{144}(\mathrm{SR})_{60}$ and exhibit likewise icosahedral symmetry. Unlike in the $\mathrm{Au}_{144}(\mathrm{SR})_{60}$ cluster, the central vacancy is filled. They show very clearly the difference between silver with a very strong LSPR visible in the spectra and gold without [210]. In fact, the 147-atom Au clusters appear to be just below the size where the LSPR emerges, which happens between $\approx$ 150 and 330 atoms. [208, 209] The calculated spectrum of Au_{147} is shown in Fig. 6.2 where the spectrum of the corresponding silver cluster with its strong resonance is shown in the inset for comparison.

Also in Fig. 6.2, we show the comparison of spectra following the incorporation of one, 25, and 55 Cu atoms in the cluster. The atomic structures of different configurations of the $\mathrm{Au}_{147-x}\mathrm{Cu}_x$ are shown in Fig. 6.4. The inclusion of one Cu atom replacing the central Au atom leads to minimal changes in the spectra. Adding more Cu, whereby we keep the cluster symmetric except in the case of random distributions where the symmetry is obviously broken, we obtain a clear and coherent picture: the changes upon adding copper are such that the structures between 2.0 and 3.5 eV (620 to 350 nm) are smoothened and that the spectral intensity is *reduced* at some energies. The shoulder at 2.2 eV is red-shifted to about 1.9 eV (650 nm). No indication of plasmon emergence is found. This is likewise true for clusters relaxed

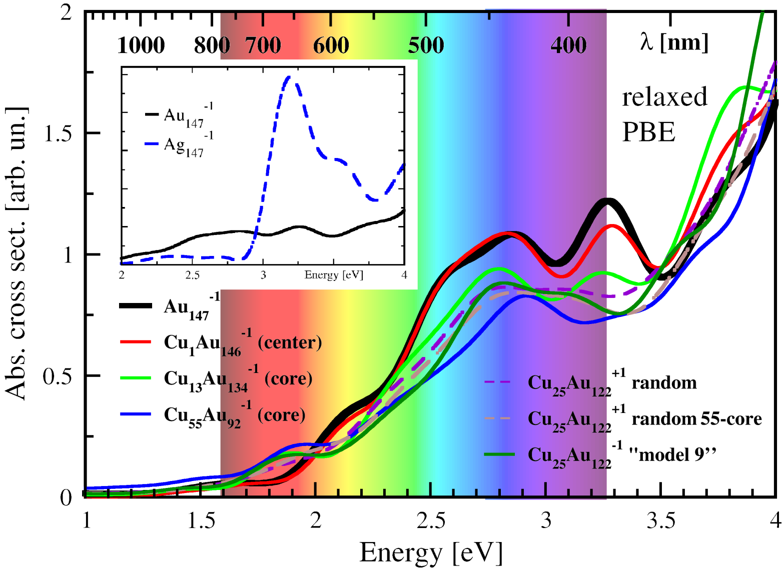

FIGURE 6.2: **Bare clusters:** Absorption spectrum of the bare 147-atom Au icosahedral cluster (thick black line) compared to different Au-Cu alloy clusters, all relaxed using the PBE GGA functional (spectra for LDA-relaxed clusters are shown in Fig. 6.3). We show the spectra corresponding to: insertion of one Cu atom in the center vacancy ($\mathrm{Cu_1Au_{146}}$, red), the replacement of the positions of the 13-atom core by Cu atoms ($\mathrm{Cu_{13}Au_{134}}$, green), the same for the 55-atom core ($\mathrm{Cu_{55}Au_{92}}$, blue), and $\mathrm{Cu_{25}Au_{122}}$ clusters with random configurations: 25 Cu atoms randomly distributed throughout the cluster (violet) and throughout the 55-atom core (brown). Finally, the dark green line corresponds to model # 9 of Reference [221]. In the inset, a comparison of the absorption spectra of icosahedral $\mathrm{Au_{147}}$ and the *plasmonic* $\mathrm{Ag_{147}}$ is shown. Clearly, no resonance emerges in any of the considered Au-Cu clusters, there is rather a suppression of intensity throughout the spectral range of interest ($\omega \sim 2.0 - 3.5$ eV, i.e., 620 to 350 nm), along with a small red-shift of the shoulder at 2.1 eV in pure gold to about 1.9 eV for the gold-copper alloy clusters. For the sake of visibility, we present here spectra from a time evolution of 15 fs, corresponding roughly to a broadening of 0.3 eV in the spectra.

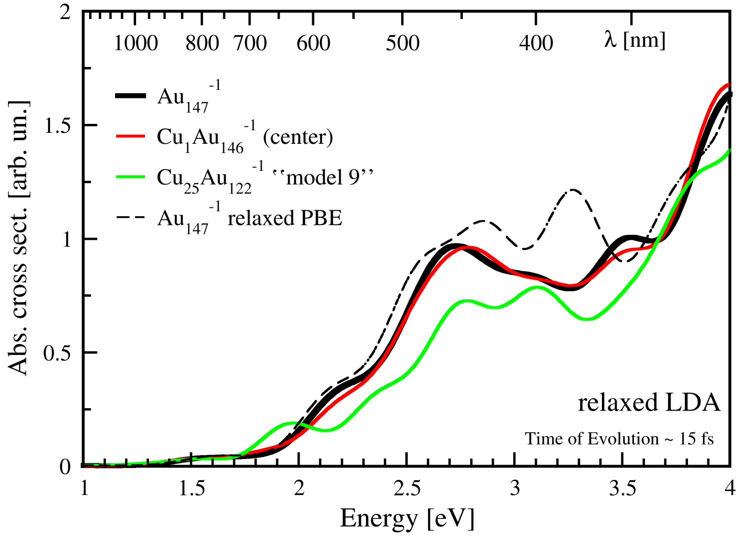

FIGURE 6.3: Absorption spectra of bare Au_{147} clusters, pure and alloyed with copper, relaxed using LDA to complement Fig. 6.2, where the results for clusters relaxed using a GGA functional are shown. The evolution time was 15 fs, corresponding to a broadening of the spectra of about 0.3 eV. The dashed line shows the GGA-relaxed Au_{147} cluster's spectrum for comparison. The conclusions differ in no way from those drawn for the GGA-relaxed clusters: there is no emergence of any resonance, the main effects are a suppression of intensity between 2 and 3.5 eV and a red-shift of the shoulder which in the pure Au cluster is located at 2.2 eV.

using the local density approximation (LDA) to the exchange-correlation functional instead of the generalized-gradient approximation (GGA). These spectra are shown in Fig. 6.3.

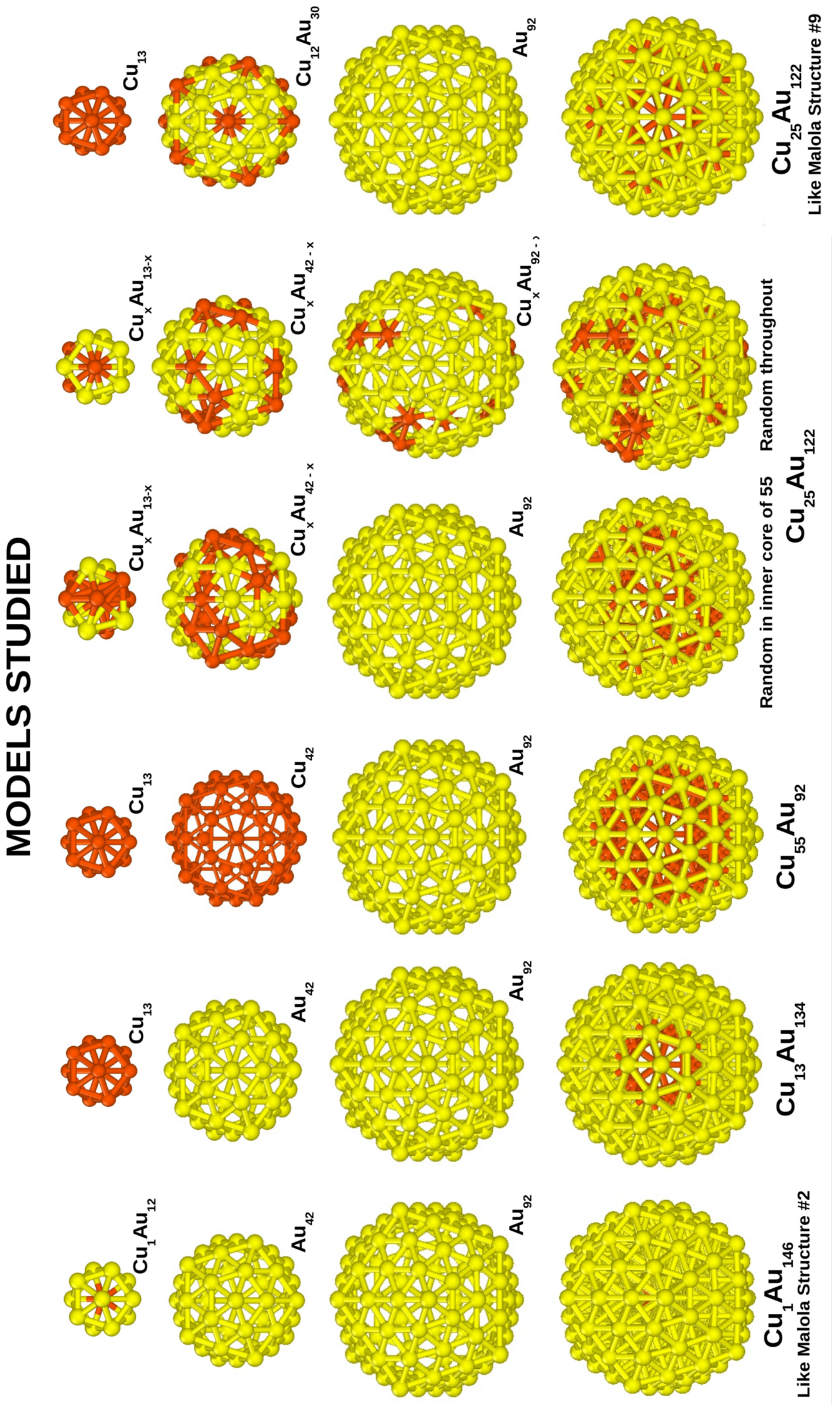

FIGURE 6.4: Different Configurations Of Bimetallic Icosahedral Au$_{147-x}$Cu$_x$ Studied

Furthermore, the spectra with an extremely small broadening (250 fs evolution time corresponding roughly to 0.018 eV broadening) in the Fig. 6.5, show that in the interesting range between 1.5 and 2.5 eV, there is some rearrangement of spectral intensity. However, no intensity increase is observed that would be characteristic of the emergence of a plasmonic resonance. This is particularly clear in view of the direct comparison, also in Fig. 6.5, with the strong resonance exhibited by the equivalent *silver* cluster Ag_{147} with it's clear plasmonic resonance.

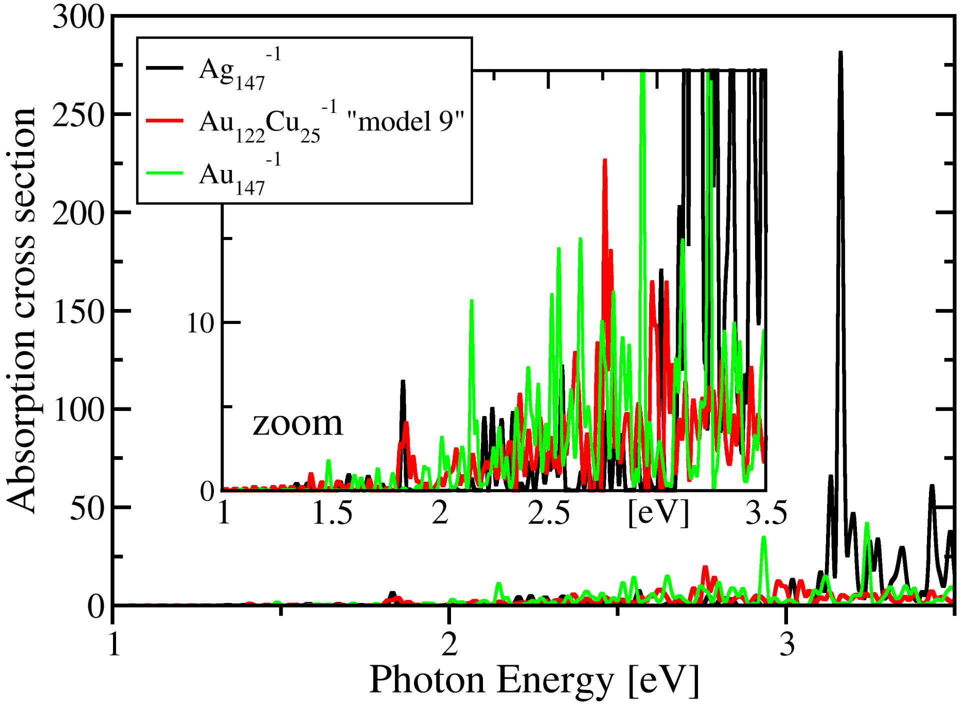

FIGURE 6.5: Spectra of the bare 147-atom icosahedral clusters, pure Au vs. Au with copper, for evolution time of 250 fs, resulting in a much lower broadening of 0.018 eV and, therefore, in finer spectral resolution. Clearly, this result demonstrates that while there are clearly rearrangements of oscillator strengths, there is no development of any strong resonance in the region of interest (around 2.2 eV, 550 nm) upon insertion of Cu. The spectra are compared with those of the bare Ag_{147} cluster with its strong plasmonic resonance. The inset shows a blow-up of the region of interest; the data are the same as in the main panel.

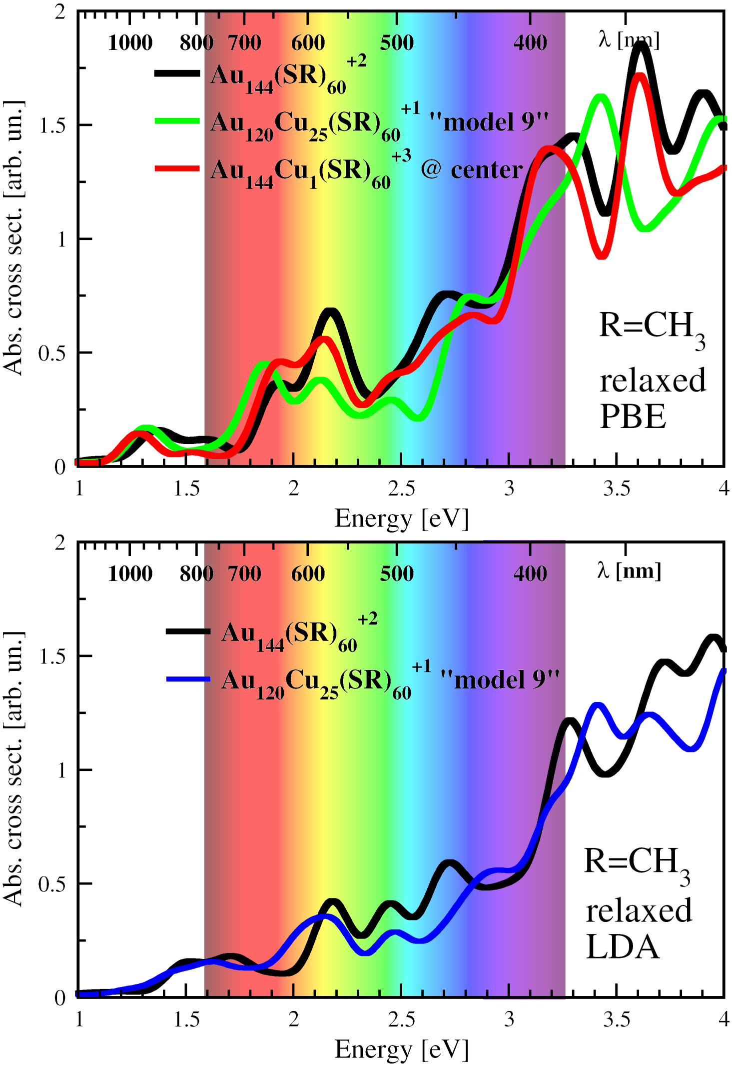

FIGURE 6.6: **Monolayer-protected $Au_{144}(SR)_{60}$ clusters:** Change of the absorption spectra of $Au_{144}(SR)_{60}$ upon alloying with copper. We compare the spectra of the pure-gold cluster (black) to those of the alloy clusters. "Model #9" corresponds to the configuration of the same denomination used in reference [221] and is shown in the present Figure 6.1. We use the rest group R=CH_3 and relaxation using the PBE (upper panel) and the LDA (lower panel) functionals. Spectra for R=H are shown in Fig. 6.7. The insertion of one copper atom into the central vacancy has a small but noticeable effect. Upon adding 25 copper atoms, a *suppression* of intensity in the range between 2 and 3 eV leads to a bump at around the desired energy, but there is clearly no increase of intensity that would be indicative of the emergence of a plasmonic resonance. These changes may modify the color of the samples, but they do not describe the emergence of a plasmonic resonance, i.e., the strong effects reported in the experimental studies [11, 12].

6.3.3 Ligand-covered 144-atom clusters

For the ligand-protected clusters, a number of additional parameters complicate the description of the system:
The rest group. Besides the structural relaxations in the available literature using either LDA or GGA [111,208,211], which leads to small but relevant changes [220], the description of the ligand rest groups plays an important role, although the optical measurements are rather insensitive to the precise nature of the rest group R of the thiolate ligands (see reference [220] for a direct comparison of measurements). The TDDFT calculations need to reduce the number of atoms as far as possible due to numerical limitations. It has been shown previously that the reduction of the ligand rest group to only R=H is too drastic [220] and, therefore, the methyl group is used in calculations, R=CH_3 [211, 220].
Symmetry. Another subtle but relevant factor is the symmetry of the system. The original model as published by López-Acevedo et al. [225] has the “staple motives” mutually oriented in a way that does not respect the overall icosahedral symmetry of the compound. Following the experimental work of Wong et al. [216] which indicated that all ligands are positioned in symmetry-equivalent positions, the model was refined so as to have the full icosahedral symmetry [217]. The resulting small differences in the spectra of the respective structures are discussed in detail in a previous work [220].

The study of Malola *et al.* [221] uses the original, slightly less symmetric geometry, the minimal ligand rest group R=H, and ground-state relaxation with the LDA functional. The latter is motivated by the fact that for gold, the interatomic distances are better reproduced by LDA than when a GGA is used. However, naturally the presence of the ligands as well as of the Cu reduces the plausibility of this choice somewhat. Other previous studies have used the GGA function PBE for relaxation [111, 211, 220]. It seems that the spectra using the fully symmetric structure, R=CH_3, and relaxation with PBE are the ones that are closest to experiment, compared to the spectra using different choices [111, 208, 211, 220].

In order to obtain generally valid results and to exclude the possibility that any of these parameters invalidate our conclusions, we studied all four different cases: ligand rest groups R=H and R=CH_3 for, in both cases, structural relaxations using

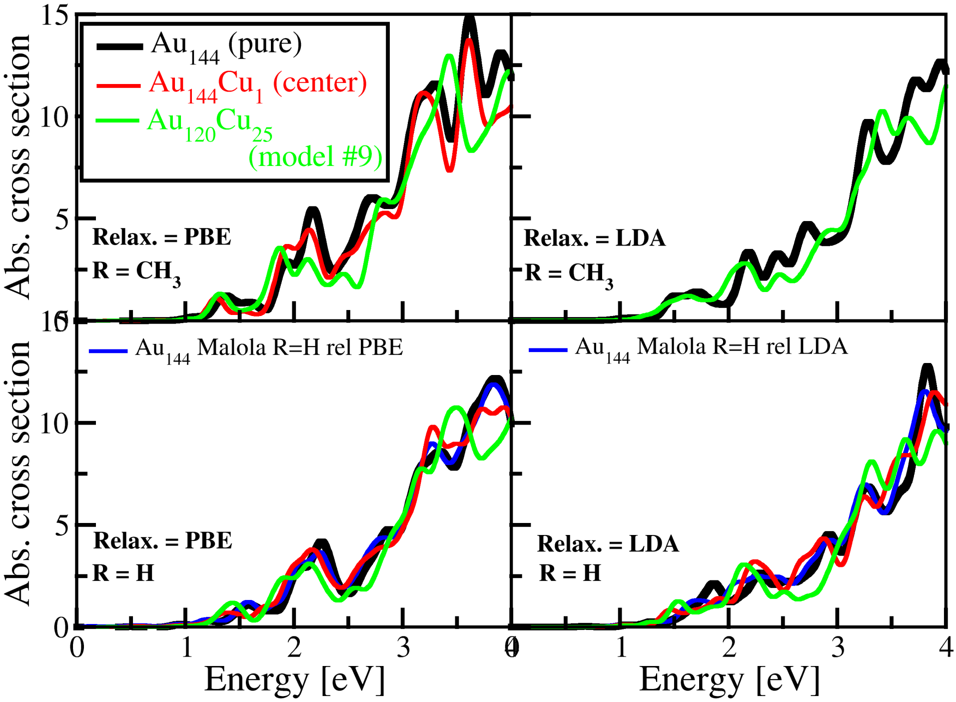

FIGURE 6.7: Comparison of all cases (R=H and R=CH_3) and relaxation in GGA and LDA. The upper panels repeat the figures from 6.6 for better comparison. The structure with R=H is obtained from the fully symmetric Bahena *et al.* structure [217] by replacement of each CH_3 group by an H atom and subsequent relaxation. In addition to the fully symmetric structure, we compare for the pure-Au clusters with the less symmetric R=H structure as used in Reference [221] (blue curve). Interestingly, the difference between the spectrum resulting from this calculation and that using the fully symmetrized starting point is rather large when LDA is used, resulting in a broad, rather featureless spectrum between 1.8 and 3.6 eV (lower right-hand panel). By contrast, upon re-relaxation of this structure using PBE, the difference with the symmetrized structure becomes marginal. Probably, some symmetrization effect is involved (for a deeper discussion, please refer to Ref. [220].) The Spectra are calculated with 25 fs evolution time, corresponding to a broadening of 0.18 eV.

either LDA or GGA. Our results are shown in Fig. 6.6 for R=CH_3. Clearly, the addition of copper does not induce any strong increase of spectral intensity in the region of interest around 2.2 eV. Apart from a very small red-shift of the shoulder at about 2 eV, the changes due to the insertion of copper occur by suppression of spectral intensity. The use of GGA and LDA in the relaxation leads to slightly different spectra, as shown before for the pure $Au_{144}(SR)_{60}$ [220], but the conclusions concerning the effect of alloying with copper do not differ between the two cases shown in Fig. 6.6.

Clearly, the choice of the methyl group CH_3 is physically better motivated than the reduction of the ligand rest group to just one hydrogen atom. However, in order to double-check for the possibility that the choice of the rest group influences the conclusions, we show the spectra for R=H, which we obtain by replacing each methyl group by an H atom and relaxing, in the lower panels of Fig. 6.7, and compared with the spectra of structures having R=CH_3, in the upper panels. The situation for the PBE-relaxed clusters is as clear as for the calculations using CH_3, there is again a small red-shift upon insertion of copper but no emergence of any resonance.

The case of the LDA-relaxed R=H calculation is slightly more intricate. It is interesting to note that in this case, for the pure $Au_{144}(SR)_{60}$, the LDA-relaxed less symmetric structure with R=H leads to a somehow more “flat”, rounded structure between 1.9 and 2.7 eV compared to the fully symmetric structure. Only in this case, insertion of copper produces indeed an – albeit very weak – increase of intensity in a very narrow range around the desired energy of 2.2 eV. Surprisingly, this is already the case when one single Cu atom is placed in the central vacancy. However, the change is small and the intensity of this peak does hereafter not change when the copper content is increased to 25 atoms. There is, instead, rather a *suppression* of intensity between 2.5 and 3.0 eV, which contributes to the impression of a peak developing at 2.2 eV. Nonetheless, comparing the respective spectra directly and to scale (comparing, in particular, the calculation using the physically preferable CH_3 rest group) it is clear that the interplay of the subtle structural changes leading to a fortuitous rearrangement of oscillator strength is at the origin of the development of the little peak; no emergence of any resonance is seen.

The erroneous conclusions by Malola *et al.* concerning the emergence of a plasmonic resonance can be traced back to the choice of the initial model of the pure $Au_{144}(SR)_{60}$. As it has been shown in earlier work [220], only the combination "lower-symmetry structure" & "R=H" & "structural relaxation using LDA" results in a particularly broad, "unpeaked" spectrum between 1.8 and 2.3 eV, while the other calculations show more structures there. Comparison with experiment in the Ref. [117] shows that there is no indication whatsoever that this geometry is closer to reality than the other structures used in the different simulations. In fact, it appears that the fully symmetric structure with R=CH_3 and GGA for relaxation is the closest to the optical experiment, even though there is plenty of room for improvement.

At this point it is worth to point out that the problem lies solely in the use of this structural model. As far as the optical calculations are concerned, the basic theory we use is the same that Malola *et al.* use, although the technical realization is very different. The results that we obtain are fully equivalent to those obtained by Malola *et al.* provided we use the same geometries. This corroborates our calculations (and those of Malola *et al.*, of course) and highlights the fact that only the comparison with a rather 'unluckily' chosen model structure of the pure Au_{144} has led to the erroneous conclusions of Ref. [221].

6.3.3.a One copper atom

It is interesting to note that even the addition of one copper atom in the central vacancy leads to noticeable changes in the spectrum, although in general, they remain small (where the case of the LDA-relaxed structures with R=H is somewhat an exception.) We have demonstrated in the previous paragraph that subtle changes in the geometry are responsible for the deceptive impression that a LSPR-like resonance might develop. In order to distinguish between the geometrical effect and the chemical effect of inserting a copper atom, we compare, in Fig. 6.8, the effect of adding a copper atom and that of adding a gold atom in the central vacancy. The addition of the gold atom allows for the consideration of only the effect of a geometric change, whereas the addition of Cu induces both a geometric and a chemical change. The finding in Fig. 6.8 is that the changes caused by the introduction of either a gold atom or a copper atom are similar to a very high degree. This allows for the important conclusion that the effect is almost entirely structural, with little influence of the chemical nature of the central atom. Again, this indicates that Cu does not induce a plasmonic resonance.

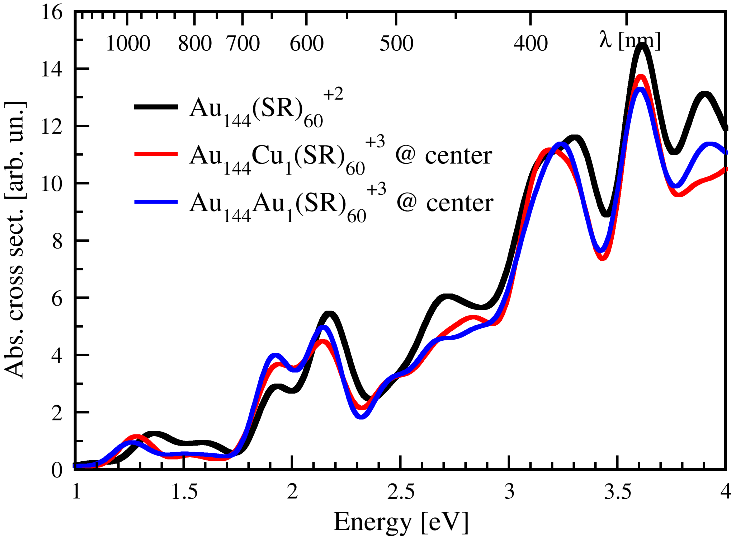

FIGURE 6.8: **One copper atom: chemical vs. geometrical effect:** Effect of the introduction of either a copper or a gold atom into the central vacancy of the pure $Au_{144}(SR)_{60}$ cluster compound in order to distinguish the purely geometric effect and the chemical effect. Ground state relaxation done using PBE, rest group $R=CH_3$. The two spectra deviate little but noticeably from the pure gold spectra but are almost identical; the entire effect is, consequently, geometric.

6.4 Dynamical polarizability and induced density

As discussed in chapter 3, the absorption cross-section ($\sigma_{\text{abs}}(\omega)$) in a system due to an external electromagnetic field can be calculated from the dynamical polarizability ($\alpha(\omega)$) using eq. 3.5.12. The dynamical polarizability ($\alpha(\omega)$) is obtained from the induced electron density ($n_1(\mathbf{r},\omega)$) as shown in eq. 3.5.11. According to the standard complex representation of harmonic functions, the time-dependent induced electron density is given by

$$n_1(\mathbf{r},t) = \cos(\omega t)\ \Re n_1(\mathbf{r},\omega) + \sin(\omega t)\ \Im n_1(\mathbf{r},\omega)\ , \tag{6.4.1}$$

and the real [imaginary] parts are then related to oscillations in phase [out of phase with a phase difference of a quarter of period] with the external E-field. Therefore, the absorption is proportional to the imaginary part of the polarizability $\alpha(\omega)$, which accounts for out-of-phase oscillations of the electron density with respect to the external E-field. However, further insights concerning the interaction between a

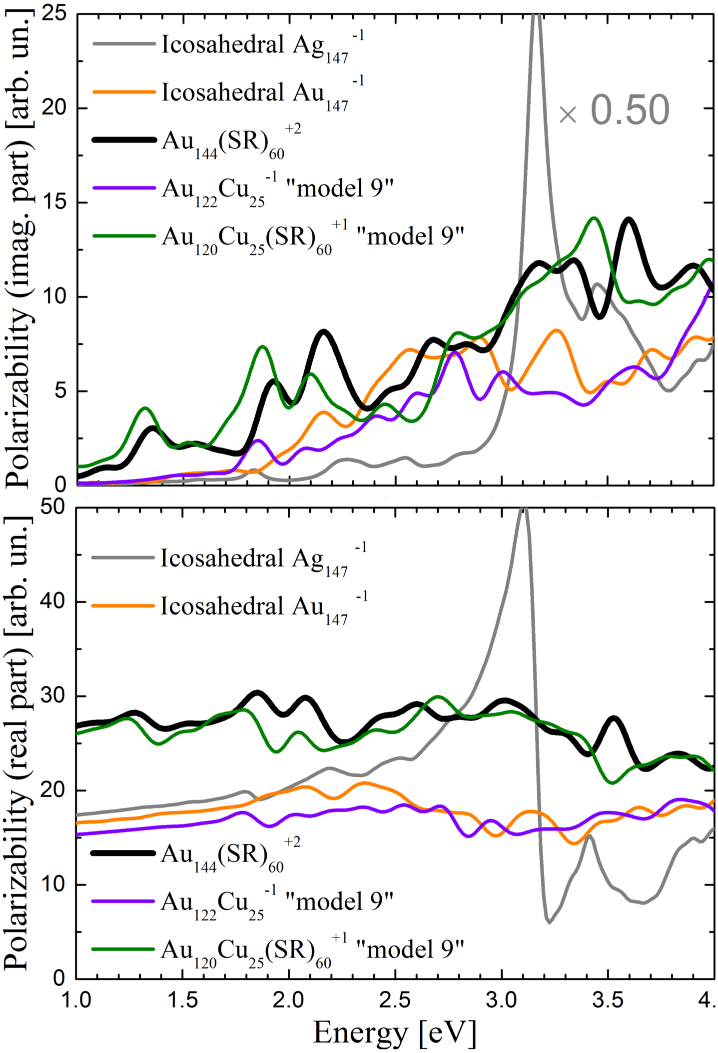

FIGURE 6.9: **Dynamical polarizability:** Real (bottom panel) and imaginary (top panel) parts of the dynamical polarizability, $\alpha(\omega)$, for selected bare and ligand-protected clusters. Thick gray line: bare Ag_{147}; thick black line: bare Au_{147}; green line: bare $Cu_{25}Au_{122}$ according to "model #9" of Reference [221] (cf., the present Figure 6.1); blue line: ligand-protected $Au_{144}(SR)_{60}$ cluster; red line: ligand-protected $Cu_{25}Au_{120}(SR)_{60}$ cluster (again "model #9"; rest group $R = CH_3$). While the real part of the polarizability for the plasmonic silver cluster Ag_{147} cluster exhibits a sharp variation at the LSPR frequency ($\omega_P \simeq 3.15$ eV), there is no noticeable structure for the Au-based nanoparticles, regardless of the inclusion of Cu atoms. A broadening of 0.05 eV has been used.

nanoparticle and an external EM field can be obtained by analyzing the real part of $\alpha(\omega)$, that is, the in-phase induced electric dipole.

In extended bulk systems, where electron-hole transitions form a continuum, the plasmon is a well-defined and distinct elementary excitation [226]. By contrast, for systems with a finite number of electrons, the concept of collective excitation and its corresponding distinction from electron-hole excitations is more vague as discussed in chapter 5. In fact, a LSPR might be seen as an electron-hole excitation that is highly renormalized by the electron-electron interaction [197]. This excitation can be coupled to surrounding electron-hole *intraband* transitions, in such a way that the LSPR acquires an effective width through a "Landau fragmentation" mechanism [227]. However, as we have mentioned before, the coupling of the LSPR with *interband* transitions leads to the practical disappearance of the plasmon resonance in the 'intermediate-size' noble-metal clusters. Such couplings prevent us from identifying a single spectral peak as "the" LSPR in many cases. Then, the signature of the existence of a LSPR is the concentration of spectral weight around a given frequency ω_{P} that, for sufficiently large systems, would be close to the classical-optics prediction. This is precisely the situation in bare and ligand-protected Au clusters and related nanoalloys: the region where the LSPR is expected to appear is already occupied by a multitude of electron-hole transitions.

The concentration of spectral weight around ω_{P} can not only be observed in the imaginary part of the dynamical polarizability; the real part of $\alpha(\omega)$ around the frequency of an isolated, well defined resonance must exhibit a change of sign (from positive to negative). The presence of less-intense nearby transitions can hamper this change of sign but, in any case, a sharp variation of $\Re\alpha(\omega)$ with negative slope is a clear indication of spectral-weight concentration and, therefore, of the existence of a LSPR. As we may see in Fig. 6.9, this is indeed the case for the icosahedral Ag_{147} cluster. However, there is not any distinctive behavior in both the real and imaginary parts of the polarizability of bare and ligand-protected Cu/Au alloys indicating a Cu-induced concentration of spectral weight in the region $2.0 - 2.5\ \mathrm{eV}$. Hence, the analysis of the real part of the dynamic polarizability confirms the findings based on the direct comparison of the different absorption spectra.

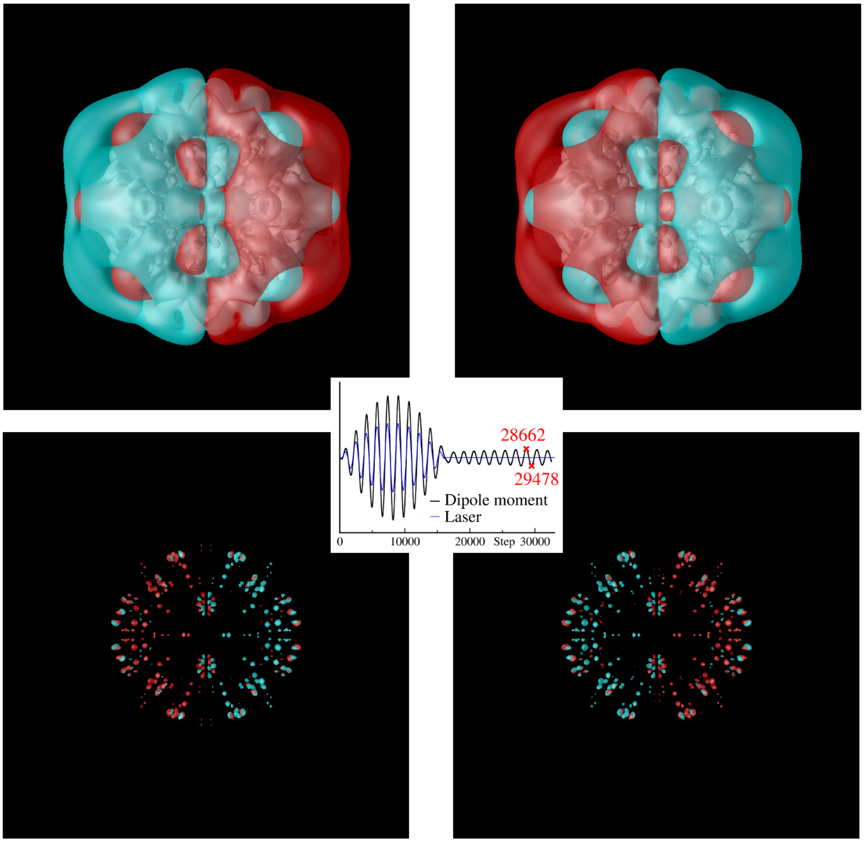

FIGURE 6.10: **Density dynamics:** Induced density following a monochromatic laser excitation at 2.17èV of the pure-Au 147-atom icosahedral cluster, well after the laser is switched off (see points at inset). In the upper panels, we chose a very low iso value, showing thus the movement of the strongly delocalized cloud of (mostly) s electrons. In the lower panels, we show the same for much higher iso-values, which demonstrates the screening of the overall excitation by the d electrons [228]. Even in this case, where the spectrum does not exhibit *any* strong plasmonic resonance, we see the sort of pattern that is reminiscent of a plasmonic excitation, including the out-of-phase movement of the d electrons that shows the screening of the LSPR. As this can be seen already for the pure Au without resonance, this behavior cannot be taken as an indication of the emergence of a plasmonic resonance in the copper-alloyed clusters, even though the dynamics is reminiscent of that in a plasmonic silver cluster. [228]

6.4.1 Density Dynamics:

A localized surface-plasmon resonance in 'intermediate' size noble-metal clusters can be considered as a dipolar collective oscillation of the quasi-free electrons, with modifications due to the atomistic inhomogeneity and the presence of the d electrons in the noble metals [228]. However, it is not enough to infer on the plasmonic character of a cluster by observing such a dipole mode in the dynamics of the density, as this can be present even in cases where no prominent resonance is present in the spectra. We show the induced density in the pure bare Au_{147} cluster after quasi-monochromatic laser excitation in Fig. 6.10. This induced density is obtained following excitation with a monochromatic laser excitation at 2.17 eV, of the pure-Au 147-atom icosahedral cluster, well after the laser is switched off. Even in this case, where the spectrum clearly does not exhibit any strong plasmonic resonance, we find the sort of dipole pattern that is reminiscent of a plasmonic excitation, including the out-of-phase movement of the d electrons that shows the screening of the oscillation. In Fig. 4.3 of chapter 4, the time-evolution of the dipole moments in Au_{147} at different energies compared to the same in Ag_{147} at LSPR energy, after being driven by the laser, confirms that the time–dependent oscillations of the dipole moments differ only in amplitudes. Therefore, the corresponding density dynamics would show the same behaviour: the oscillation of the induced density with different corresponding frequencies and amplitudes. Whether these oscillations represent resonant character or not is understood by comparing the phase of the oscillation of the corresponding dipole moment with the phase of the corresponding driving laser field. In other words, the presence of a dipole mode in the electron density dynamics, even if reminiscent of an LSPR dipole mode, is not sufficient to allow for clear conclusions about the plasmonic nature of spectral features.

6.5 Conclusions

Motivated by experimental findings and recently published calculations which concluded that *"Copper Induces a Core Plasmon in Intermetallic* $Au_{(144,145)-x}Cu_x(SR)_{60}$ *Nanoclusters."* [221], we have calculated the changes of the optical response of both the bare 147-atom icosahedron and of the $\mathrm{Au}_{144}(\mathrm{SR})_{60}$ cluster compound upon alloying with copper. Copper atoms are replacing gold atoms of the pure cluster (and, in addition, are inserted into the central vacancy of $\mathrm{Au}_{144}(\mathrm{SR})_{60}$). Considering a number of different situations as far as the ground-state relaxation of the structures is concerned (LDA vs. PBE), the choice of the rest group of the thiolate ligands (R=H vs. R=CH_3), and the subtle differences in symmetry/geometry discussed previously [220], we have shown that the addition of copper does not induce the development of any prominent resonance, plasmonic or other. The main changes are small and consist mostly in a) suppression of spectral intensity in the range between 2.0 and 3.5 eV (620 to 350 nm), and b) a red-shift of the lowest spectral features. Moreover, we demonstrate that the small but noticeable changes upon insertion of a single copper atom in the central vacancy of the pure $Au_{144}(SR)_{60}$ are almost entirely due to the geometric effect of the copper insertion.

The results allows for the strong general conclusion that alloying with copper does not create plasmonic resonances in gold clusters in this size range, i.e., around 1.8 nm, where the spectra do not yet show any clear LSPR. Regrettably, these findings mean that the experiments in which the development of an LSPR-like peak has been observed cannot be explained by the simple hypothesis that the insertion of copper changes the optical response be inducing a plasmonic resonance. Other hypotheses will need to be explored in order to obtain a fundamental understanding of the effects at play in these experiments.

Chapter 7

General Conclusions and Perspective

7.1 English Version

The fundamental research interest in nanometric pieces of noble metals is mainly due to the localized surface-plasmon resonance (LSPR) in the optical absorption. As discussed in detail in the preceding chapters, LSPRs appear in the absorption spectra of noble-metal nanoparticles as dominating broad and smooth spectral features in the visible and ultraviolet spectral regions. A number of emerging technologies in optics, electronics, diagnostic and therapeutic medicine [1–6], and in many other fields of basic research in chemistry and biology are based on LSPR.

As presented in the introductory chapter, theoretical research on LSPRs in nanoparticles is performed using different levels of theory depending on the size of the nanoparticles. In particular, the transition from larger metallic nanoparticles with smooth electronic bands and optical spectra to small molecule-like clusters with their discrete electronic states and spectra, reflects the quantum nature of the clusters [7–9]. In addition, in some noble metals, e.g. Au, we have the emergence phenomenon of LSPR in this size range which is referred as the intermediate-size range. The noble-metal clusters that fall in this size range are the systems that have been mainly studied in this thesis.

Different communities have been working on similar questions around the optical response of intermediate-size noble-metal particles, having different main interests and backgrounds. In particular, the enormously active plasmonics community has been using approaches based on classical electromagnetics. However, with the progressive miniaturization of objects that can be produced, handled, and applied, quantum-mechanical corrections to the purely classical description become increasingly important. However, precise studies of the limitations and problems of these methods are often not available.

On the other hand, the quantum description of the noble-metal clusters in the intermediate size rage interesting to us here has been developed mostly using density-functional theory, both static and time-dependent. However, practical TDDFT calculations contain necessarily approximations, notably the different exchange-correlation functionals or kernels. In addition, many effects are either fully neglected (like in many cases the finite temperature) or only approximately taken into account (e.g., surface/interface structure, etc.)

This thesis focuses on the LSPR and comprises several aspects of the present-day research into the interaction of electromagnetic waves with noble metal clusters at atomistic length scales. In order to gain a broader perspective of the usage of different methodologies to study the optical properties of 'intermediate-size' noble-metal clusters, both the *ab initio* and the classical electromagnetics approaches are employed. In particular, the *ab initio* calculations are performed using real-time TDDFT (RT-TDDFT) within the linear-response regime, whereas classical electromagnetics calculations are done for different descriptions of the metal permittivity.

7.1.1 Performance of Classical Electromagnetics for Quantum Systems

One of the objectives of this thesis is to explore the merits and limitations of the classical optics methods in explaining optical properties of intermediate-size noble-metal clusters. This is achieved by performing systematic comparisons with *ab initio* TDDFT approaches. To do so, the atomic structures need to be replaced by equivalent geometries in the classical optics calculations. In order to have equivalence between atomistic structures of sub-nanometric lateral dimensions on the one hand and corresponding geometries for the electromagnetics calculations on the other hand, we have developed in chapter 4 a simple and intuitive modelling (both shapes and dimensions). To mimic the soft single-atom termination of the atomistic rods, a “cigar”-shaped geometry is chosen for the metal regions in the electromagnetics calculations. The electron density in the cigars is taken to be the same as the average s-electron density in the bulk, and the volume of the cigar is set such that the number of electrons in it be the same as the number of s-electrons in the atomistic structures. Finally, the aspect ratio (AR) of the cigar is also made to be the same as that of the atomistic system.

7.1.1.a Aspect-ratio dependence of LSPR in sub-nanometric rods

Following this modelling of the geometries, the absorption spectra are calculated for different intermediate-size clusters of Au and Ag within the frameworks of *ab initio* TDDFT and electromagnetics. The electromagnetics calculations are performed using both the local and the nonlocal (hydrodynamic model) descriptions for the metal permittivity. The comparison of the absorption spectra calculated with different methods reveals the following interesting observations:

- As is well known, for systems with high AR, the behaviour of the absorption in Au and Ag is similar: appearance of a strong well-defined LSPR in the infrared. This is because in both Ag and Au, for high AR the LSPR appears well below the onset of interband transition. The systematic comparison shows that for rod structures of Ag with AR $>$ 5 and of Au with $\mathrm{AR} \gtrapprox 8$ (whose response is dominated by the LSPR), not only the spectral position of the LSPR, but also the strengths of the absorption calculated in TDDFT and electromagnetics approaches are in excellent agreement, even though the systems posses sub-nanometric lateral dimension, manifesting atomistic inhomogeneity.

- The comparison against *ab initio* predictions improves even further when the electromagnetics absorption cross-section is computed using the nonlocal hydrodynamic metal permittivity, except for the linear atomic chains, where the local optics calculations appear to be superior.

- As the AR of the systems is decreased, the agreement between TDDFT and electromagnetics calculations starts to degrade significantly. This degradation appears to be due to the blue-shift of the LSPR with the decrease in AR, which makes the LSPR couple with the interband transitions. This coupling is more apparent in Au than in Ag due to the lower energy onset of interband transitions in Au.

- In the rod systems, as the AR is decreased, the TDDFT calculations show the coupling between LSPR and the interband transitions as the LSPRs are fragmented. As the onset of the interband transitions does not depend on the size of the clusters [10], the coupling of LSPR and interband transitions is primarily governed by the AR-dependent spectral position of the LSPR. This coupling is not captured within nonlocal electromagnetics calculations. Therefore, in the Au and Ag rods, it is mainly the shape (i.e., AR) which determines the coupling of LSPR and interband transitions, and thus the agreement between nonlocal electromagnetics and TDDFT approaches.

In conclusion, we have compared local and nonlocal classical optics and quantum mechanical *ab initio* methods to calculate spectral positions and strengths of the LSPRs in elongated quantum-sized systems preserving the aspect ratio and number of Drude (or s) electrons. The comparison shows a remarkable agreement between the two approaches when the LSPR is largely decoupled from the interband transitions. This is the case for Ag rods of $\mathrm{AR} > 5$ and Au rods of $\mathrm{AR} \gtrapprox 8$. In addition, we can conclude that it is the shape, and not the overall size (i.e. the # atoms) that determines the quality of this agreement.

7.1.1.b Subtle effects of size on the aspect-ratio dependence of LSPR

Subsequently, in chapter 4 we perform a comparison of the dependence of LSPRs on the aspect ratio as calculated by classical approaches with the corresponding *ab initio* calculations in different atomistic structures of Ag and Au (rods, atomic chains, and icosahedral clusters). This comparison is of particular interest. When going from thin (chains) to thick (rods) for equal AR, the relative energy of the LSPR excited along the axis of the elongated systems increases. This trend of increase in the LSPR energy while the size is increased is only observed in the *ab initio* calculations for elongated systems, whereas the classical nonlocal optics calculations show the known opposite behaviour: increase in LSPR energy with decrease of absolute size. The conclusion inferred based on this observation is that, even though classical optics remarkably gives the same spectral positions and strengths of the LSPRs in elongated quantum-sized systems, there are subtle quantum mechanical effects which modify the classical size-dependent behaviour of the LSPRs.

7.1.1.c Interplay between plasmon and d-electrons in Au-chains

In monatomic chains of Ag, LSPRs are found to be free of d-transition contaminations, even for as short as 6-atom chains. By contrast, TDDFT spectra for the Au chains indicate that quasi-one-dimensional collective excitations are not well resolved for chains having numbers of atoms fewer than twelve. However, when the number of atoms in Au chains decreases, a transfer of the spectral weight from the lowest-frequency maximum to different plasmon-fragmented peaks manifests the emergence of a coupling of the LSPR with d-electron excitations; the classical optics predictions describe a rough spectral average of the fragmented peaks.

7.1.2 Near-field Characteristics of the Excitations

In chapter 5, we investigated induced charge densities at LSPR frequencies from classical and TDDFT calculations. This allowed to extend the comparative study of the two different theoretical approaches (electromagnetics and TDDFT) beyond far-field characteristics and verify the validity of the findings also in the near-field regime.

7.1.2.a Induced Charge Densities at LSPR

Comparing the cross-sectional integration of the induced charge densities of LSPRs along the rod length, we have demonstrated that, the classical and the fully quantum mechanical descriptions of the induced charges at LSPR energies are in remarkable agreement for elongated Ag systems. This allowed us to conclude that, as a consequence of the high plasmonic character of the elongated structures, they support well-defined collective LSPRs (both as surface modes in rods, and also as quasi-one-dimensional collective modes in chains,) free of the contamination from single electron-hole excitations.

For a less elongated (i.e., more compact) structure of Ag_{19}, where the high LSPR frequency is apparent in its absorption spectrum ($\sim$3 eV), the same comparison of the induced charge densities at LSPR from electromagnetics and TDDFT aprroaches reveals that d-electron transitions play a key role in the optical response. This conclusion can be traced back to the observation that in the compact noble-metal clusters, induced charges calculated in TDDFT spread significantly along the rod length toward its middle plane, completely disagreeing with the electromagnetics prediction, even though the spectra calculated in both the methods (TDDFT and nonlocal optics) show surprising resemblance.

7.1.2.b Need for the better exchange-correlation functional

Following the disagreement between the TDDFT and electromagnetics predictions of the induced charge densities at LSPR in compact Ag_{19} cluster, a verification of the quality of the *ab initio* calculations using the PBE AGGA functional is performed for rods of different lengths, by comparing with a long-range corrected hybrid exchange-correlation functional, LC-M06L. This functional is more suitable for the treatment of d-electron excitations and yields accurate spectra for small Ag clusters. Unfortunately, its use also requires a much larger numerical effort, compared to the simple GGA or LDA functionals. From this analysis, we concluded that the spectra obtained from TDDFT-PBE calculations are hardly different from the ones obtained using LC-M06L for elongated systems (like Ag_{67} rod). By contrast, for compact clusters like Ag_{19}, they are completely different. Thus, for compact clusters like Ag_{19}, TDDFT-PBE calculations are not reliable and the spectral agreement between classical and fully quantum results is partially coincidental. They fail to describe structures in which LSPRs and d-electrons couple strongly. Therefore, in the *ab initio* treatment of those systems, a description of exchange and correlation better than the AGGA functionals is required.

7.1.3 Modes of Induced Density at Different Energies

The spatial distribution of the induced electric field or the induced charge density provides a deeper insight into a given optical excitation. In the electromagnetics approaches, calculations are generally performed in the frequency domain, and the induced electric field (and, therefore, the induced density) at a given energy can be calculated. In RT-TDDFT, the optical response is calculated in the time-domain, and the induced charge density corresponding to an optical excitation at a given energy is not readily available. However, most RT-TDDFT simulations use a δ-kick perturbation which produces a time–dependent induced charge density which is the superposition of the induced densities that correspond to all the excitations that appear in the spectrum.

In chapter 5, by performing the spatially resolved Fourier transform of the time-dependent induced density obtained from a RT-TDDFT simulation, we have recovered the spatial profile of the induced density at any given energy of interest. We have discussed the differences between collective plasmonic excitations and the excitations involving d-electrons, as well as the interplay between plasmon and d-electrons in the spatial behaviour of the modes corresponding to the respective excitations.

- A comparison of the laser-driven induced density at the LSPR energy with the induced density due to an electrostatic field shows the dynamic screening by the d-electrons. We arrived at the general conclusion that, while for the dipolar LSPR the modes of the induced density have principal contributions from the surface region of the cluster, d-electrons respond to the field generated by this surface contribution with the same LSPR frequency and an out of phase oscillation.
- Using the Fourier-transformed densities, we are able to study the spatial contributions to individual features in the absorption spectrum. For example, in a more complex ligand-protected cluster, $Ag_{29}P_4S_{24}C_{144}H_{108}$, the spatially resolved Fourier transform of the time-dependent induced density reveals that the low-energy excitations are more confined to the Ag core of the compound than the strong high-energy excitation, which is found to have principal contributions from the benzene rings of the surrounding ligands.

7.1.4 Effects Of Alloying

Recent experiments on the $Au_{144}(SR)_{60}$ class of cluster compounds have demonstrated the emergence of an absorption peak at 550 nm (2.25 eV) upon adding copper to the pure Au samples; in some cases, as little as one Cu atom seems to have this effect [11, 12]. This finding is interesting because at this size, bare clusters of both Au and Cu (e.g., Au_{147}Ih) do not show strong absorption features in the spectra. As an attempt to explain these experiments, *ab initio* calculations on the $Au_{(144,145)-x}Cu_x(SR)_{60}$ class of nano–alloy compounds were also performed by Malola et al. [13], which claimed that "*Copper Induces a Core Plasmon in Intermetallic $Au_{(144,145)-x}Cu_x(SR)_{60}$ Nanoclusters*". In chapter 6 of this thesis, we have performed similar *ab initio* calculations on these clusters. These careful and detailed *ab initio* study presents subtle insights on the effects of alloying and the emergence of LSPRs in bare $\mathrm{Au}_{(147)-x}\mathrm{Cu}_x$ and the ligand covered $\mathrm{Au}_{(144,145)-x}\mathrm{Cu}_x(\mathrm{SR})_{60}$ clusters.

Considering a number of different situations as far as the ground-state relaxation of the structures is concerned (LDA & PBE), the choice of the truncated rest group of the thiolate ligands (R = H, & R = CH_3), and the subtle differences in symmetry/geometry of the $\mathrm{Au}_{144}(\mathrm{SR})_{60}$, we have shown that the addition of copper does not induce the development of any prominent resonance, plasmonic or other. The main changes are small and consist mostly in (a) suppression of spectral intensity in the range between 2.0 and 3.5 eV (620 to 350 nm), and (b) a red-shift of the lowest spectral features. Moreover, it is demonstrated that the small but noticeable changes upon the insertion of a single copper atom in the central vacancy of the pure $\mathrm{Au}_{144}(\mathrm{SR})_{60}$ are almost entirely due to the geometric effect of the copper insertion.

The results depend only very slightly on the details of the structural model, the kind of ligand rest group used in the calculations, and on the approximations used in the calculations. This allows for the strong general conclusion that alloying with copper does *not* create plasmonic resonances in gold clusters in this size range, i.e., around 1.8 nm, where the spectra do not yet show any clear LSPR. These findings mean that the experiments in which the development of an LSPR-like peak has been observed cannot be explained by the hypothesis that the insertion of copper changes the optical response by inducing a plasmonic resonance. Other hypotheses will need to be explored in order to obtain a fundamental understanding of the effects at play in the experiments.

7.1.5 Perspectives

The field of research involving optical properties of noble-metal nanoparticles and clusters is active with many aspects in applications as well as in understanding the origin of novel physical phenomena at sub-nanometric length scales. With the present-day advancements in technology, the engineering of subatomic systems has become possible. In the frontiers of plasmonics, this advancements have paved the way for novel devices based on the optical tunability at nanometric level, e.g., *dynamic plasmonic colour displays* [229] and *atomic scale plasmonic switches* [230].

Both the quantum-mechanical and the classical electromagnetics methods are employed in this thesis to provide theoretical understanding of recent experiments which explore the light-matter interaction at sub-nanometric length scales. In view of these different approaches, the work pursued in this thesis gives significant contributions: The systematic and detailed comparison of the *ab initio* and electromagnetics methods brings out the importance of being conscious of the limitations of the latter when applied to quantum-sized systems. For example, in the study of the field enhancement around an atomistic tip, which is exploited in surface-enhanced Raman spectroscopy (SERS) experiments, quantum mechanical effects are likely to modify purely classical results. On the other hand the limitations of the TDDFT calculation need to be kept in mind. In the *ab initio* calculations for quantum-sized noble-metal clusters, where the interband transitions can couple with the LSPR, the choice of approximations, in particular for the exchange-correlation functional, adopted to the system plays the key role. Thus, in order to capture properly the optical response in these systems within the density-functional theoretical framework, better approximations, for the exchange-correlation functional, which should also be computationally economic is solicited. Fascinating improvements have been made in cluster science through experimental studies using trailblazing techniques of synthesis and characterization of quantum-sized clusters. Intermediate-size noble-metal clusters protected by ligands are synthesized and crystallized [231–233]. Many of these experiments can give precise knowledge of the structures and compositions of the clusters. This knowledge of the structures provides the basis for an improvement of the *ab initio* calculations because these can now be carried out using definite atomic structures. Measurements (absorption spectra, etc.) on the structure-determined samples thus provide benchmarks that can be compared with the respective calculated quantities, which allows for definite conclusions about the quality of the employed approximations (in particular, the exchange-correlation functionals). This process is expected to greatly improve the quality of the *ab initio* description, finally achieving the goal of being predictive. This improvement of the *ab initio* description will bring out new aspects on understanding the way nature behaves at atomic length scales.

With the present-day knowledge and resources of quantum-mechanical calculations, efforts have been made to answer many interesting questions encountered while understanding recent experimental studies on the light-matter interactions in systems having sub-nanometric dimensions. In many cases, these efforts have succeeded to give the physically correct explanation, although not always. The reason is the following. In these experiments, several complex physical phenomena come into play.

In order to describe the light-matter interactions, the multiple effects need to be taken into account, and appropriate structural models must be employed. The *ab initio* calculations often neglect effects that are deemed unimportant for the questions at hand. For instance, most of the optical calculations neglect finite-temperature effects. In addition, the structural modelling tries to reduce the system for practical convenience. For instance, in the case of monolayer-protected clsuters, the ligand rest groups are mostly reduced to, e.g., a methyl group in order to reduce the numerical effort. These approximations reduce the quality of the calculations and, in many cases, make predictive quality impossible. A clear example of this fact is already demonstrated in this thesis: the *ab initio* study on the $\mathrm{Au}_{(144,145)-x}\mathrm{Cu}_x(\mathrm{SR})_{60}$ class of clusters shows that alloying Cu with Au at sub-nanometric size ($\approx$1.8 nm) does not give rise to any strong absorption, even though in experiments LSPR-like spectral features are observed to emerge, and the cause of this emergence is traced back to some form of alloying. A theoretical study had been published [13] that claimed to have evidenced the emergence of a LSPR upon alloying. Our systematic study showed that this is not the case, and that the conclusions of the other study [13] were erroneous due to an insufficient treatment of structural details. Clearly, in this case and also in many others, in order to discover the actual science at play care has to be taken to include the structural complexity and the main effects. In particular, better modelling is needed, e.g., the effect of the chemical environment surrounding the cluster, agglomeration, etc., which may contribute significantly on the absorption at sub-nanometric length scales.

In the optical experiments involving clusters, where photons give rise to electronic transitions, the eigen-modes of the excited systems correspond to dipole-active excitations. However, in electron energy-loss spectroscopy (EELS), different modes of electron-density oscillation can also be excited. Precise single-particle EELS measurements are now being carried out, demanding robust theoretical approaches to understand their outcomes. For example, a theoretical demonstration from an *ab initio* approach of the optically uncapturable modes that appear in single-particle EELS measurements has not yet been accomplished and is a challenging goal to achieve. Therefore, it is very likely that in coming years a good amount of research will be focused in this direction. In this context, the numerical tools developed and the experience gained in both the *ab initio* and classical electromagnetics theories during this thesis can be efficiently used. For example, if EELS excitation can be properly simulated within the *ab initio* theoretical framework of real-time TDDFT

(RT-TDDFT), the optically uncapturable modes can be identified using the spatially resolved Fourier decomposition of the corresponding time-dependent induced density, as it has been done for the optically active modes in this thesis.

Research interest in noble-metal nanoparticles are not limited only to exploring their optical properties. It also spans through their elegant applications in biology and medicine, e.g., for the development of drug delivery vectors in living cells. These application are in use since quite a long time. Many of these applications are based on empirical studies and require better understanding of the basic science at work. In this context, with the advent of the miniaturization of the noble-metal nanoparticles in recent experiments, understanding their impact on these applications is attracting research attention. To give an example, organic monolayer-protected Au clusters of $\sim 2-3$ nm size are being studied enormously in order to understand their interaction with lipids. Thus, it is very likely that research efforts are to be made in the near future in the overlapping frontiers of biology, physics and chemistry. A substantial amount of work has already started to understand simultaneously the role of the organic ligands in stabilizing Au clusters and their interactions with mesoscopic biological systems. The study of these ligand-protected clusters in order to understand their ability to control protein structures and dynamics, etc. are also a major subdomain of research that is taking shape.

On a broader perspective, in view of the progress of experimental methods, it is evident that there is plenty of room for improvement of the understanding of light-cluster interactions, and a long way to go to fulfill the demand of powerful theoretical techniques able to give complete insightful explanations, and, preferably reliable predictions.

7.2 Versión en Español

Desde la perspectiva de la ciencia fundamental, el interés en las estructuras de metal noble se ha debido, en gran medida, a la emergencia de las llamadas resonancias de plasmon de superficie localizadas (LSPR, por sus siglas en inglés) en su espectro de absorción óptico. Como se ha discutido en detalle en los capítulos anteriores, las LSPRs dominan el espectro de nanopartículas metálicas dando lugar a anchos picos de absorción tanto en el rango óptico como el ultravioleta. Un número creciente de nuevas tecnologías en el campo de la óptica, la electrónica y la medicina diagnóstica y terapéutica se basan en las LSPRs; y otras ciencias básicas como la química y la biología también las comienzan a utilizar en diferentes contextos.

Como se presentó en el capítulo introductorio, la investigación teórica sobre las LSPRs se ha realizado utilizando diferentes niveles de descripción dependiendo del tamaño de las nanopartículas. La transición entre partćulas grandes, con bandas electrónicas y espéctros ópticos suaves y bien definidos, a partículas microscópicas de tamaño molecular, con niveles elecrónicos y transiciones ópticas discretas, refleja la naturaleza cuántica de los clústeres metálicos. En algunos metales nobles, como el oro, el fenómeno de las LSPRs tiene lugar en un rango de tamaños intermedio. Los sistemas metálicos estudiados en esta tesis caen en este rango de tamaños intermedios.

En el pasado, diferentes comunidades científicas han trabajado en cuestiones similares relacionadas de la respuesta óptica de partículas metálicas de tamaño intermedio por distintos objetivos y motivaciones. En particular, el tremendamente activo campo de la plasmónica ha utilizado herramientas y enfoques basados en el electromagnetismo clásico. Sin embargo, con la constante miniaturización de estructuras que se ha producido en los últimos años, la introducción e implementación de correcciones cuánticas al tratamiento púramente clásico de estos sistemas se ha convertido en un tema cada vez de mayor importancia. Sin embargo, hasta el momento, pocos estudios se han dedicado a explorar las limitaciones y problemas de los diferentes métodos teóricos utilizados hasta la fecha.

Por otro lado, la descripción cuántica de los clústeres metálicos en el rango de tamaños intermedios se ha desarrollado principalmente dentro del marco de la teoría del funcional de la densidad, tanto estática como dependiente del tiempo (TD-DFT por sus siglas en inglés). Sin embargo, los cálculos TDDFT contienen necesariamente aproximaciones, principalmente en los funcionales de intercambio y correlación. Muchos fenómenos, tales como los efectos de temperatura, son completamente ignorados o tratados de una manera aproximada, como los efectos debidos a la estructura de la superficie del sistema.

Esta tesis se centra en las LSPRs y cubre varios aspectos de la investigación actual sobre la interacción entre ondas electromangnéticas y nanopartículas metálicas en la escala de longitudes atomística. Con el objetivo de conseguir una perspectiva más amplia sobre el uso de diferentes metodologías para el estudio de las propiedades ópticas de estructuras de tamaño intermedio, consideramos tanto técnicas *ab initio* como de electromagnetismo clásico. Concretamente, los cálculos de primeros principios se realizaron dentro del marco de TDDFT en el régimen de respuesta lineal, mientras que los cálculos electromagnéticos se realizaron utilizando diferentes modelos para la permitividad metálica.

7.2.1 Aplicación del Electromagnetismo Clásico en Sistemas Cuánticos

Uno de los objetivos de esta tesis es la exploración de los méritos y limitaciones de los métodos de la óptica clásica para la descripción de las propiedades ópticas de los clústeres de metales nobles. Esta tarea se ha llevado a cabo mediate comparaciones sistemáticas frente a técnicas de primeros principios. Para ello, las estructuras atomísticas han sido reemplazadas por geometrías equivalentes que pueden ser tratadas dentro del marco del electromagnetismo clásico. Para establecer esta equivalencia hemos desarrollado en el capítulo 4 un simple e intuitivo modelo para tratar tanto la forma como las dimensiones de la nanopartćula. Para imitar la suave terminación en un solo átomo de una barra metálica, hemos usado una geometría con forma de habano para las regiones metálicas en nuestros cálculos. La densidad electrónica de estas geometrías se ha tomado igual a la correspondiente a los electrones s en el volumen del metal, y el volumen del habano se ha fijado de forma que el número de electrones de conducción sea el mismo que en el sistema atomístico. Finalmente, la proporción de aspecto (AR, definida como el cociente entre longitud y grosor) de las geometrías electromagnéticas se ha tomado igual al de las estructuras atomísticas.

7.2.1.a Dependencia de las LSPRs en la AR de barras metálicas

Usando el modelado efectivo descrito arriba, los espectros de absorción de barras metálicas de tamaños intermedios de oro y plata han sido estudiados utilizando tanto TDDFT como la óptica clásica. Los cálculos electromagnéticos se han realizado tanto dentro de la descripción local como no-local (modelo hidrodinámico) de la permitividad metálica. La comparación entre los espectros obtenidos con diferentes métodos revela interesantes conclusiones:

- Como es bien sabido, la absorción de plata y oro en partículas elongadas es similar: en ambas se puede identificar fuertes LSPRs en el infrarrojo. Esto es debido a que estas resonancias aparecen a frecuencias mucho menores que las correspondientes a las transiciones interbanda en ambos metales. La comparación sistemática muestra que en barras de plata con $AR > 5$ y de oro con $AR \gtrapprox 8$ (cuya respuesta está dominada por LSPRs) no solo la posición de las resonancias sino también su intensidad calculadas con TDDFT y electromagnetismo clásico muestran un excelente acuerdo. Incluso en sistemas con dimensiones laterales subnanométricas y que manifiestan la inhomogeneidad atomísitca.

- La comparación frente a las predicciones de primeros principios mejora incluso cuando los espectros de absorción electromagnéticos se calculan usando un modelo hidrodinámico para la permitividad metálica, excepto en cadenas lineales de átomos, donde los cálculos locales parecen ser más precisos.

- Cuando la AR de las barras se reduce, el acuerdo entre TDDFT y los cálculos electromagnéticos se degrada significativamente. Esta degradación puede relacionarse con el corrimiento al azul que sufren las LSPRs, lo que las hace acoplarse con las transiciones interbanda. Esta interacción es más aparente en oro que en plata debido a la menor energía de las últimas.

- Al decrecer la AR de las barras, los cálculos TDDFT muestran el acoplo entre LSPRs y las transiciones interbanda, lo que da lugar a una fragmentación de los picos de absorción. Como la excitación de transiciones interbanda no depende del tamaño del clúster, el acoplo con las LSPRs está gobernado por la posición espectral, dependiente de la AR. Este acoplo no es capturado por el modelo electromangético no local. Así, en las barras de oro y plata, es la forma fundamentalmente (y por lo tanto la AR) la que determina la interacción entre

LSPRs y transciones interbanda, y también el acuerdo entre cálculos clásicos y cuánticos.

En conclusión, hemos comparado la óptica clásica local y no local frente a métodos *ab initio* cuánticos en el cálculo de las posiciones espectrales y las intensidades del las LSPRs en sistemas elongádos atomísticos preservando la AR y el número de electrones s (o Drude). La comparación muestra un acuerdo sorprendente entre ambos enfoques cuando las LSPRs están desacopladas de las transiciones interbanda. Éste es el caso para barras de plata de $\mathrm{AR} > 5$ y de oro de $\mathrm{AR} \gtrapprox 8$. Hemos concluido también que es la forma y no las dimensiones (es decir el número de átomos) lo que determina la calidad de este acuerdo.

7.2.1.b Efecto sutil del tamaño en la dependencia las LSPRs en la AR

En el capítulo 4, hemos realizado un análisis de cómo las LSPRs dependen de las proporciones de la partícula mediante cálculos clásicos y cuánticos para diferentes estructuras de plata y oro: barras, cadenas y clústeres icosaédricos. En la transición entre estructuras delgadas (cadenas) y gruesas (barras) de una misma AR, la energía relativa de las LSPRs excitadas a lo largo del eje longitudinal de estos sistemas aumenta. Esta tendencia creciente en la energía de las LSPRs solo se observa en los cálculos de primeros principios, mientras que los cálculos electromagnéticos no locales muestran el comportamiento opuesto. La conclusión a la que hemos llegado basada en esta observación es que aunque la óptica clásica da un acuerdo sorprendente en los atributos generales de las LSPRs, hay sutiles efectos cuánticos que alteran la dependencia en el tamaño de las LSPRs.

7.2.1.c Interrelación entre LSPRs y electrones d en cadenas de oro

En cadenas monoatómicas de plata, las LSPRs están libres de contaminación debida a los electrones d, involucrados en las transiciones interbanda, incluso en tamaños tan pequeños como 6 átomos. Por el contrario, los espectros TDDFT para cadenas de oro indican que el carácter quasi-unidimensional de las excitaciones colectivas no está bien descrito para cadenas menores que 12 átomos. Cuando el número de átomos se reduce más, tiene lugar una transferencia de peso espectral desde los picos de menor frecuencia a máximos plasmónicos fragmentados, que sólo puede ser descrito *ab initio*. En estos casos, los cálculos clásicos parecen reproducir un promedio espectral de todos estos picos fragmentados.

7.2.2 Características de las Excitaciones en el Campo Cercano

En el capítulo 5, hemos investigado las distribuciones de carga inducidas por la excitacion de LSPRs desde un punto de vista clásico y cuántico. Esto nos ha permitido extender el estudio comparativo entre los dos enfoques teóricos más allá de las magnitudes de campo lejano y verificar la validez de nuestros descubrimientos también en el régimen de campo cercano.

7.2.2.a Densidades de Carga Inducida por LSPRs

A través de la integración de las cargas inducidas dentro de la sección transversal de las partículas metálicas, hemos demostrado que las descripciones clásicas y cuánticas de las densidades de carga resonantes muestran, de nuevo, un acuerdo sorprendente para estructuras elongadas de plata. Esta observación nos ha permitido concluir que estos sistemas, como consecuencia de su alto carácter plasmónico, soportan LSPRs colectivas bien definidas, libres de la contaminación de excitaciones interbanda que involucran un único electrón-hueco.

Para el clúster Ag_{19}, que presenta una forma no tan elongada (más compacta) y en el que la energía de la LSPR aparece en el espectro alrededor de 3 eV, la comparación entre predicciones para la distribución de carga revelan que las transiciones de electrones d juegan un papel fundamental en sus propiedades ópticas. Este hallazgo es particularmente relevante en el caso de nanoestructuras compactas (quasi-esféricas), en las que la distribución de carga inducida en el plano de simetría obtenido por métodos clásicos y de primeros principios están en un total desacuerdo, a pesar de que los espectros de absorción obtenidos en ambos casos (TDDFT y óptica no local) son muy similares.

7.2.2.b Necesidad de un funcional de cambio y correlación mejorado

Tras el análisis de las predicciones TDDFT y electromagnéticas para las densidades de carga inducida correspondientes a LSPRs en Ag_{19}, hemos verificado la calidad de los cálculos *ab initio* usando el funcional PBE AGGA para barras de diferentes longitudes, comparándolos frente a los resultados obtenidos mediante el funcional híbrido y de largo alcance LC-M06L. Éste último es mas adecuado para el tratamiento de excitaciones de electrones d, y sus prediciones son más exactas para clústeres de plata pequeños. Desafortunadamente, su implementación requiere un esfuerzo de cálculo mucho mayor que los funcionales GGA o LDA. De nuestro estudio concluimos que los espectros obtenidos usando TDDFT-PBE son solo ligeramente diferentes de los resultados de LC-M06L para sistemas elongados (como Ag_{67}). Por el contrario, en clústeres compactos, como Ag_{19}, las predicciones son muy diferentes. Así, los cálculos TDDFT-PBE para sistemas compactos no son precisos y el acuerdo espectral entre cálculos clásicos y cuánticos es en parte fortuito. Ambos enfoques son incapaces de describir estructuras en las que LSPRs y electrones d estan acoplados fuertemente. En estos casos, el tratamiento *ab initio* requiere la introducción de funcionales de intercambio y correlación mejores que los sobresimplificados AGGA.

7.2.3 Densidades de Carga Inducida a Diferentes Energías

La distribución espacial del campo eléctrico inducido ofrece una visión profunda sobre la excitación óptica. En los métodos electromagnéticos clásicos, los cálculos son realizados normalmente en el dominio de frecuencia, y los campos eléctricos (y por tanto, también las distribuciones de carga) a una energía dada se obtiene de una forma natural. En TDDFT, la respuesta óptica se calcula en el dominio de tiempo, y las magnitudes anteriores han de calcularse a posteriori. Sin embargo, la mayoría de las simulaciones TDDFT usan una perturbación $/delta - kick$ que produce un una densidad de carga inducida que es la superposición de las distribuciones correspondientes a todas las excitaciones que se generan en el sistema (y que aparecen en el espectro).

En el capítulo 5, realizamos una transformada Fourier de las densidades inducidas dependientes del tiempo obtenidas mediante TDDFT. Así obtenemos las distribuciones a cualquier energía o frecuencia de interés. Hemos discutido las diferencias entre excitaciones plasmónicas y aquellas que involucran transiciones intrabanda, y también la interacción entre LSPRs y los electrones d en el comportamiento espacial de los modos ópticos para cada familia de excitaciones.

- La comparación para las densidades de carga inducida para una energía LSPR bajo excitación láser y mediante un campo puramente electrostático muestra el papel del apantallamiento debido a los electrones d. Hemos llegado a la conclusión general de que las LSPRs dipolares tienen una mayor contribución proveniente de la superficie del clúster. Por otro lado, los electrones d responden al campo electrico generado por esta contribución superficial con la misma frecuencia, pero con un desfase de 90 grados.

- Mediante las densidades de carga obtenidas mediante la transformación de Fourier, hemos sido capaces de estudiar las contribuciones espaciales debidas a cada elemento o rasgo identificable en el espectro de absorción. Por ejemplo, en un clúster complejo y protegido por ligandos, como $Ag_{29}P_4S_{24}C_{144}H_{108}$, la dependencia espacial de la transformada de Fourier de la densidad dependiente del tiempo revela que las excitaciones de baja energía están más confinadas en el núcleo de plata del compuesto que las intensas excitaciones de alta energía, que tienen una importante contribución proveniente de los anillos de benzeno en los ligandos.

7.2.4 Efectos debidos al aleado

Experimentos recientes realizados sobre la clase de agregados $Au_{144}(SR)_{60}$ han mostrado la emergencia de un pico de abosrción a 550 nm (2.25 eV) tras la la adición de cobre a las muestras de oro puro. En algunos casos parece incluso que la adición de un único átomo de Cu tiene este efecto [11, 12]. Este hallazgo es interesante porque, en el rango de tamaños considerados, los agregados simples de Au y Cu (e.g., Au_{147}Ih) no muestran ningún pico de absorción prominente en el espectro. Con el objeto de explicar estos experimentos, Malola et al. [13] realizaron cálculos *ab initio* sobre la clase de nanoaleaciones $Au_{(144,145)-x}Cu_x(SR)_{60}$. Su conclusión fue que "*Copper Induces a Core Plasmon in Intermetallic* $Au_{(144,145)-x}Cu_x(SR)_{60}$ *Nanoclusters*". En el capítulo 6 de esta tesis, presentamos cálculos *ab initio* para este tipo de agregados. Tras un análisis detallado de los resultados *ab initio* hemos obtenido una visión más clarificadora de cómo el aleado afecta a la emergencia de LSPRs en el caso de agregados "limpios" $Au_{(147)-x}Cu_x$ y recubiertos por ligandos $Au_{(144,145)-x}Cu_x(SR)_{60}$.

Tras considerar diferentes casos, en particular: la relajación de las estructuras en función del método empleado (LDA & PBE), el tipo de grupo R de los ligandos (R = H, & R = CH_3), y las mínimas diferencias en la simetría y la geometría de los diferentes compuestos $Au_{144}(SR)_{60}$, hemos mostrado que la adición de cobre no induce ninguna resonancia en el espectro, sea plasmónica o de otro tipo. Los cambios principales en el espectre son pequeños y consistent principalmente en: (a) la disiminución de peso espectral en el rango entre 2.0 y 3.5 eV (620 to 350 nm) y (b) el desplazamiento al rojo de los picos espectrales de frecuencia más baja. Mas aún, hemos mostrado que los pequeños pero apreciables cambios en el espectro de absorción tras la inserción de un átomo de cobre en la vacante central del agregado $Au_{144}(SR)_{60}$ son prácticamente debidas a la reconstrucción geométrica inducida por la propia inserción del átomo.

Como hemos indicado, los cambios en los resultados son pequeños y dependen únicamente de los detalles del modelo estructural y del tipo de grupo R del ligando. Además, son del mismo orden que los asociados a la utilización de diferentes aproximaciones funcionales. Esto nos lleva a la conclusión general de que el aleado con cobre *no* induce la aparición de resonancias plasmónicas en agregados de oro en este rango de tamaños (1.8 nm), en el que el espectro no muestra todavìa el desarrollo claro de una LSPR. En consecuencia, las diferencias en el espectro de absorción detectadas experimentalmente deben deberse a otro tipo de efectos que deben aún explorarse.

7.2.5 Perspectivas

El activo campo de investigación sobre propiedades ópticas de nanopartículas y agregados de metales nobles tiene numerosas aplicaciones y abre al puerta a la comprensión del origen de novedosos fenómenos físicos a escalas nanométrica y subnanométrica. Con los presentes avances en tecnología, la ingeniería de sistemas a escala atómica es posible. En las fronteras de la plasmónica, estos avances han allanado el camino para dispositivos novedosos basados en la capacidad de ajuste óptica a nivel nanométrico, por ejemplo, *pantallas de color plasmónicas dinámicas* [229] y *interruptores plasmónicos a escala atómica* [230].

En esta tesis se han empleado tanto métodos mecánico-cuánticos como electromagnéticos clásicos para proporcionar una comprensión teórica de experimentos recientes que exploran la interacción luz-materia a escalas de longitud sub-nanométricas. A la vista de estos diferentes enfoques, el trabajo realizado en esta tesis aporta contribuciones significativas: la comparación sistemática y detallada de los métodos ab-initio y de electromagnetismo clásico resalta la importancia de las limitaciones de este último cuando se aplica a sistemas de tamaño cuántico. Por ejemplo, en el estudio de la amplificación de campo alrededor de una punta atomística, que se explota en experimentos de espectroscopía Raman mejorada en superficie (SERS), los efectos mecánicos cuánticos pueden modificar resultados puramente clásicos.

Por otro lado, las limitaciones del cálculo TDDFT deben tenerse en cuenta. En los cálculos ab-initio para agregados de metales nobles de tamaño cuántico, donde las transiciones entre bandas pueden acoplarse con la LSPR, es clave la elección de las aproximaciones, en particular para el funcional de intercambio/correlación. Por lo tanto, para describir adecuadamente la respuesta óptica en estos sistemas dentro de la teoría del funcional de la densidad, se necesitan aproximaciones robustas (pero computacionalmente sencillas) para el funcional de intercambio/correlación. A su vez, se han producido muy intersantes avances en la ciencia de agregados a través de estudios experimentales que utilizan técnicas pioneras de síntesis y caracterización a escala atómica, siendo un ejemplo la síntesis y cristalización de agregados de metales nobles de tamaño intermedio protegidos por ligandos [231–233]. Muchos de estos experimentos pueden proporcionar un conocimiento preciso de la estructura y composición de los agregados, que proporcionan la base para una mejora de los cálculos ab-initio porque ahora pueden llevarse a cabo utilizando estructuras atómicas definidas. Las mediciones (espectros de absorción, etc.) en las muestras proporcionan puntos de referencia sobre los que se pueden comparar las cantidades calculadas teóricamente. Esto permite conclusiones definitivas sobre la calidad de las aproximaciones empleadas (en particular, los funcionales de correlación de intercambio). Se espera que este proceso mejore en gran medida la calidad de la descripción ab-initio, y finalmente logre el objetivo de ser predictivo. Esta mejora de la descripción ab-initio mostrará nuevos mecanismos para comprender la forma en que la naturaleza se comporta a escalas de longitud atómica.

Con el conocimiento actual y los recursos de los cálculos mecanocuánticos, se han realizado numerosos esfuerzos para entender estudios experimentales recientes en los que los fenómenos de interacción luz-materia se producen a escala subnanométrica. En muchos casos (no siempre), estos esfuerzos han logrado dar la explicación físicamente correcta. Los problemas surgen cuando varios fenómenos físicos complejos entran en juego a la vez, y para describir adecuadamente la interacción luz-materia se deben también considerar otros efectos como pequeños cambios estructurales que, en demasiadas ocasiones, se omitían al realizar cálculos ab-initio. Por ejemplo, la mayoría de los cálculos ópticos no tienen en cuenta los efectos de temperatura finita. Además, el modelado estructural se sobresimplifica en la práctica. Por ejemplo, en el caso de agregados recubiertos por monocapas, los grupos de los ligandos se reducen principalmente a, por ejemplo, un grupo metilo con el fin de reducir el esfuerzo computacional. Estas aproximaciones reducen la calidad de los cálculos y, en muchos casos, hacen que la calidad predictiva sea imposible. Un claro ejemplo de este hecho ya se demostró en esta tesis: el estudio *ab-initio* de los agregados $\mathrm{Au}_{(144,145)-x}\mathrm{Cu}_x(\mathrm{SR})_{60}$ muestra que la aleación de Cu con Au en agregados de tamaño nanométricos ($\approx$ 1.8 nm) no da lugar a ninguna efecto relevante de absorción óptica, aunque en los experimentos se observaba la emergencia de característica espectrales que sugieren la excitación de una resonancia plasmónica, excitación que también se sugería en un trabajo teórico previo [13]. Nuestro estudio sistemático mostró que este no es el caso, y que las conclusiones del otro estudio [13] fueron erróneas debido a un tratamiento insuficiente de los detalles estructurales.

En los experimentos de absorción óptica por agregados, en los que la absorción de fotones implica la aparición de transiciones electrónicas, los modos de excitación son dipolarmente activos. Por el contrario, en medidas de pérdida de energía electrónica (EELS, de sus siglas en inglés), otros modos no dipolares se pueden excitar. En la actualidad se pueden realizar experimentos EELS muy precisos sobre muestras individuales, lo que conlleva la necesidad de herramientas teóricas robustas para explicar los resultados. Por ejemplo, los cálculos *ab-initio* de espectros EELS para muestras aisladas de tamaño finito no están convenientemente desarrollados y suponen, por tanto, un reto inmediato. En este contexto, la experiencia adquirida en esta tesis tanto en cálculos ab-initio como de electromagnetismo clásico se podrán utilizar en esa dirección. Por ejemplo, si una excitación EELS se puede modelar adecuadamente en el formalismo RT-TDDFT, los nuevos modos (no dipolares) se pueden identificar de manera sencilla usando la decomposición de Fourier resuelta en espacio de la densidad de carga inducida, tal y como hemos mostrado para los modos ópticamente activos.

Obviamente, la investigación sobre agregados de metales nobles no se limita a la exploración de sus propiedades ópticas. También comprende, por ejemplo, aplicaciones en biología y medicina relacionadas con el desarrollo de vectores para la administración de medicamentos en células vivas. Estas aplicaciones ya están en uso desde hace tiempo, a pesar de estar basadas en estudios meramente empíricos, lo que hace deseable una mejor comprensión de los mecanismos básicos. En este contexto, la mencionada miniaturización en las técnicas de síntesis de nanopartículas de metales nobles abre la puerta a nuevos hallazgos. Como ilustración, agregados de oro de un tamaño de 2-3 nm recubiertos por una monocapa de material orgánico se estan estudiando con asiduidad para entender cómo interaccionan con lípidos. La investigación pluridisciplinar (biología, química, física) es así necesaria para abordar fenómenos en los que los ligandos, por una parte, sirven para estabilizar los agregados metálicos y, por otra, interaccionan con sistemas biológicos mesoscópicos. En esta línea, están empezando a tomar forma el desarrollo de este tipo de agregados mixtos como herramientas para controlar la estructura y la dinámica de proteinas.

Finalmente, y desde una perpectiva más amplia, a la vista de los progresos en técnicas experimentales resulta evidente que todavía hay un gran número de fenónemos relacionados con la óptica de agregados que todavía deben ser entendidos. Así, queda un largo camino para satisfacer la demanda de herramientas teóricas capaces de predecir y explicar completamente los hallazgos en este campo.

Appendix A

Proof of Runge–Gross Theorem

Theorem: *For every single–particle potential* $v(\mathbf{r},t)$ *which can be expanded into a Taylor series with respect to the time coordinate around* $t = t_0$*, a map* $G : v(\mathbf{r},t) \longleftrightarrow n(\mathbf{r},t)$ *is defined by merely solving the time–dependent Schrödinger equation with a fixed initial state* $\Psi_0 = \Psi(t_0)$ *and calculating the corresponding densities* $n(\mathbf{r},t)$*. This map can be inverted up to an additive merely time–dependent function in the potential.*

The first step of the proof is to show that infinitesimally after the initial time t_0, from which two potential $v(\mathbf{r},t)$ and $v'(\mathbf{r},t)$ start to have different time dependence, the corresponding current densities $\mathbf{j}(\mathbf{r},t)$ and $\mathbf{j}'(\mathbf{r},t)$ are different.

Considering,

$$\begin{aligned} \mathbf{j}(\mathbf{r},t) &= \langle\Psi(t)|\,\hat{\mathbf{j}}(\mathbf{r})\,|\Psi(t)\rangle\,; \quad \Psi(t) \textit{ belongs to } v(\mathbf{r},t) \\ \mathbf{j}'(\mathbf{r},t) &= \langle\Psi'(t)|\,\hat{\mathbf{j}}(\mathbf{r})\,|\Psi'(t)\rangle\,; \quad \Psi'(t) \textit{ belongs to } v'(\mathbf{r},t) \end{aligned} \tag{A.0.1}$$

we start with the equation of motion of the observable $\hat{\mathbf{j}}(\mathbf{r})$:

$$i\frac{\partial}{\partial t}\mathbf{j}(\mathbf{r},t) = \langle\Psi(t)|\,[\hat{\mathbf{j}}(\mathbf{r}),\hat{\mathcal{H}}(t)]\,|\Psi(t)\rangle \tag{A.0.2}$$

The commutator in A.0.2 is quite intricate and leads to an expression involving internal force densities of the many–body system due to kinetic and interaction effects that are present in the Hamiltonian. For working out the relation one can look into the references Ref. [181, 234]. Fortunately, for $t = t_0$ the complicate expression becomes tractable which when we use to get the difference of the partial time derivatives of $\mathbf{j}(\mathbf{r},t)$ and $\mathbf{j}'(\mathbf{r},t)$ at $t=t_0$, using A.0.1 & A.0.2, we get:

$$i\frac{\partial}{\partial t}\Big[\mathbf{j}(\mathbf{r},t)-\mathbf{j}'(\mathbf{r},t)\Big]_{t=t_0} = \langle\Psi(t_0)\ \Big[\hat{\mathbf{j}}(\mathbf{r}),\Big(\hat{\mathcal{H}}(t_0)-\hat{\mathcal{H}}'(t_0)\Big)\Big]\ |\Psi(t_0)\rangle \tag{A.0.3}$$

$$= \langle\Psi(t_0)\ \Big[\hat{\mathbf{j}}(\mathbf{r}),\Big(\hat{\mathcal{V}}(t_0)-\hat{\mathcal{V}}'(t_0)\Big)\Big]\ |\Psi(t_0)\rangle \tag{A.0.4}$$

$$\textit{because}\quad \hat{\mathcal{H}}(t_0)-\hat{\mathcal{H}}'(t_0)=\hat{\mathcal{V}}(t_0)-\hat{\mathcal{V}}'(t_0)$$

$$= i\ n(\mathbf{r},t_0)\ \nabla\Big[v(\mathbf{r},t_0)-v'(\mathbf{r},t_0)\Big] \tag{A.0.5}$$

So, if at $t=t_0$, $v(\mathbf{r},t_0)\neq v'(\mathbf{r},t_0)$, then the R.H.S. is non-vanishing, implying that $\mathbf{j}(\mathbf{r},t)$ and $\mathbf{j}'(\mathbf{r},t)$ will be different infinitesimally after $t=t_0$. But if that is not the case, then we first need to find the order k of the Taylor expansion at which $v'(\mathbf{r},t)$ differs from $v(\mathbf{r},t)$, such that the following equation holds:

$$\left(i\frac{\partial}{\partial t}\right)^{k+1}\Big[\mathbf{j}(\mathbf{r},t)-\mathbf{j}'(\mathbf{r},t)\Big]_{t=t_0} = i\ n(\mathbf{r},t_0)\ \nabla\left\{\left(i\frac{\partial}{\partial t}\right)^{k}\Big[v(\mathbf{r},t)-v'(\mathbf{r},t)\Big]_{t=t_0}\right\}$$
$$\neq 0 \tag{A.0.6}$$

assuring that, infinitesimally after $t=t_0$, $\mathbf{j}(\mathbf{r},t)\neq\mathbf{j}'(\mathbf{r},t)$, though at $(k+1)$-th order.

In next step of the proof, relating the density $n(\mathbf{r},t)$ with the current $\mathbf{j}(\mathbf{r},t)$ through the continuity equation:

$$\frac{\partial}{\partial t}n(\mathbf{r},t) = -\nabla\cdot\mathbf{j}(\mathbf{r},t), \tag{A.0.7}$$

one needs to show that, infinitesimally after $t=t_0$, $n(\mathbf{r},t)$ (corresponding to $v(\mathbf{r},t)$) and $n'(\mathbf{r},t)$ (corresponding to $v'(\mathbf{r},t)$) will be different, and thus the theorem is proved. Taking the difference of the continuity equations corresponding to $n(\mathbf{r},t)$ and $n'(\mathbf{r},t)$, we get:

$$\frac{\partial}{\partial t}[\ n(\mathbf{r},t)-n'(\mathbf{r},t)\ ] = -\nabla\cdot[\ \mathbf{j}(\mathbf{r},t)-\mathbf{j}'(\mathbf{r},t)\ ] \tag{A.0.8}$$

To relate to eq.A.0.6, we need to differentiate eq.A.0.8 more $(k+1)$ times at $t=t_0$, $n(\mathbf{r},t)$:

$$\frac{\partial^{k+2}}{\partial t^{k+2}}\Big[\, n(\mathbf{r},t) - n'(\mathbf{r},t)\,\Big]_{t=t_0} = -\nabla\cdot\left\{\frac{\partial^{k+1}}{\partial t^{k+1}}\Big[\,\mathbf{j}(\mathbf{r},t) - \mathbf{j}'(\mathbf{r},t)\,\Big]_{t=t_0}\right\}$$

$$= -\nabla\cdot\left\{\, n(\mathbf{r},t_0)\;\cdot\left[\nabla\left\{\left(\frac{\partial}{\partial t}\right)^{k}\Big[v(\mathbf{r},t) - v'(\mathbf{r},t)\Big]\right\}_{t=t_0}\right\}\qquad \text{(A.0.9)}$$

Here, we take,

$$u(\mathbf{r}) = \left(\frac{\partial}{\partial t}\right)^{k}\Big[v(\mathbf{r},t) - v'(\mathbf{r},t)\Big] \neq \ constant, \qquad \text{(A.0.10)}$$

i.e., the gradient of $u(\mathbf{r})$ exists.

So, now we need to show that R.H.S. of eq.A.0.9 is non-vanishing, i.e.

$$\nabla\cdot\Big[n(\mathbf{r},t_0)\ \nabla u(\mathbf{r})\Big] \neq 0, \text{provided, } u(\mathbf{r}) \neq \ constant, \qquad \text{(A.0.11)}$$

in order to prove that $n(\mathbf{r},t) \neq n'(\mathbf{r},t)$, as they are different immediately after $t = t_0$, for some value of k $(k \geq 0)$. This is shown by *reductio ad absurdum*.

Let's consider eq.A.0.11 is false, i.e.

$$\nabla\cdot\Big[n(\mathbf{r},t_0)\ \nabla u(\mathbf{r})\Big] = 0, \quad \text{while, } u(\mathbf{r}) \neq \ constant, \qquad \text{(A.0.12)}$$

$$\Longrightarrow \int d^3r\ u(\mathbf{r})\ \nabla\cdot\Big[n(\mathbf{r},t_0)\ \nabla u(\mathbf{r})\Big] = 0$$

$$or,\ \int d^3r\Big[u(\mathbf{r})\Big\{\nabla n(\mathbf{r},t_0)\cdot\nabla u(\mathbf{r})\Big\} \ +\ u(\mathbf{r})\ \Big\{\nabla\cdot\nabla u(\mathbf{r})\Big\}\Big] = 0 \qquad \text{(A.0.13)}$$

To get a tractable expression for eq.A.0.13, we make use of the divergence theorem, and deal with the following equation:

$$\int d^3r \; \nabla \cdot \Big[n(\mathbf{r}, t_0) \Big\{ \nabla u^2(\mathbf{r}) \Big\} \Big] = \oint n(\mathbf{r}, t_0) \Big\{ \nabla u^2(\mathbf{r}) \Big\} \cdot d\mathbf{S} \tag{A.0.14}$$

$$\begin{aligned}
or, \quad & \int d^3r \left[n(\mathbf{r}, t_0) \; \nabla \cdot \nabla u^2(\mathbf{r}) \; + \; \nabla n(\mathbf{r}, t_0) \cdot \nabla u^2(\mathbf{r}) \right] = \oint n(\mathbf{r}, t_0) \nabla u^2(\mathbf{r}) \cdot d\mathbf{S} \\
or, \quad & \int d^3r \left[n \; \nabla \cdot (2u\nabla u) \; + \; \nabla n \cdot (2u\nabla u) \right] = \oint n(\mathbf{r}, t_0) \nabla u^2(\mathbf{r}) \cdot d\mathbf{S} \\
or, \quad & 2 \int d^3r \left[\Big\{ n(\nabla u)^2 \; + \; n \; u \; \nabla^2 u \Big\} \; + \; u \; \nabla n \cdot \nabla u \right] = \oint n(\mathbf{r}, t_0) \nabla u^2(\mathbf{r}) \cdot d\mathbf{S} \\
or, \quad & \int d^3r \; n(\nabla u)^2 + \int d^3r \; n \; u \; \nabla^2 u + \int d^3r \; u \; \nabla n \cdot \nabla u = \frac{1}{2} \oint n(\mathbf{r}, t_0) \nabla u^2(\mathbf{r}) \cdot d\mathbf{S}
\end{aligned} \tag{A.0.15}$$

Now, recognizing the third and second term on the L.H.S. of eq.A.0.15, respectively as the first and second term on the L.H.S. of eq.A.0.13, we can re-write eq.A.0.13 as,

$$\begin{aligned}
& \int d^3r \Big[u(\mathbf{r}) \Big\{ \nabla n(\mathbf{r}, t_0) \cdot \nabla u(\mathbf{r}) \Big\} \; + \; u(\mathbf{r}) \; \Big\{ \nabla \cdot \nabla u(\mathbf{r}) \Big\} \Big] \\
& \qquad = - \int d^3r \; n(\mathbf{r}, t_0) \Big[\nabla u(\mathbf{r}) \Big]^2 + \frac{1}{2} \oint n(\mathbf{r}, t_0) \Big[\nabla u^2(\mathbf{r}) \Big] \cdot d\mathbf{S} = 0
\end{aligned} \tag{A.0.16}$$

At this point, to reach the proof we need to put an *extra* constraint on the density $n(\mathbf{r}, t_0)$: we consider that, *the density $n(\mathbf{r}, t_0)$ falls off so rapidly that at the surface,* **S***, it is negligible; therefore the* ***surface integral*** *at the L.H.S. of eq.A.0.16* ***vanishes****.* Thus eq.A.0.16 reads as,

$$\int d^3r \; n(\mathbf{r}, t_0) \Big[\nabla u(\mathbf{r}) \Big]^2 = 0 \tag{A.0.17}$$

Now, if the density $n(\mathbf{r}, t_0)$ is *reasonably well behaved,*

$$\Longrightarrow \qquad u(\mathbf{r}) = constant \tag{A.0.18}$$

which contradicts our starting assumption eq.A.0.12. This means, eq.A.0.11 holds.

$\Longrightarrow$ in eq.A.0.9,

$$\frac{\partial^{k+1}}{\partial t^{k+1}} \Big[\; \mathbf{j}(\mathbf{r}, t) - \mathbf{j}'(\mathbf{r}, t) \; \Big]_{t=t_0} \neq 0$$

$\Longrightarrow$ $n(\mathbf{r}, t)$ and $n'(\mathbf{r}, t)$ will be different infinitesimally after $t = t_0$, and hence, they are distinct. Thus the theorem is proved.

Appendix B

Surface Plasmon Polaritons (SPP): From Maxwell's Equations

The general expression for the Maxwell's equations are:

$$\nabla \cdot \mathbf{D} = \rho_{ext} \tag{B.0.1a}$$

$$\nabla \times \mathbf{E} = -\frac{\partial \mathbf{B}}{\partial t} \tag{B.0.1b}$$

$$\nabla \cdot \mathbf{B} = 0 \tag{B.0.1c}$$

$$\nabla \times \mathbf{H} = \mathbf{J}_{ext} + \frac{\partial \mathbf{D}}{\partial t} \tag{B.0.1d}$$

Considering our electric field as, $\mathbf{E}(\mathbf{r},t) = \mathbf{E}(\mathbf{r})\ e^{i\omega t}$, the Maxwell's equations becomes:

$$\nabla\cdot\epsilon\mathbf{E} = 0 \quad considering\ no\ presence\ of\ external\ charges \tag{B.0.2a}$$

$$\nabla\times\mathbf{E} = \begin{vmatrix} \hat{i} & \hat{j} & \hat{k} \\ \frac{\partial}{\partial x} & \frac{\partial}{\partial y} & \frac{\partial}{\partial z} \\ E_x & E_y & E_z \end{vmatrix} = -\frac{\partial\mathbf{B}}{\partial t} = -\mathbf{i}\omega\mu\mathbf{H} \tag{B.0.2b}$$

$$\nabla\cdot\mathbf{B} = 0 \quad \Longrightarrow \quad \nabla\cdot\mathbf{H} = 0 \quad considering\ material\ to\ be\ non-magnetic \tag{B.0.2c}$$

$$\nabla\times\mathbf{H} = \mathbf{J}_{ext} + \frac{\partial\mathbf{D}}{\partial t} = 0 + \frac{\partial\mathbf{D}}{\partial t} \quad considering\ absence\ of\ external\ current$$

$$i.e.,\ \nabla\times\mathbf{H} == \begin{vmatrix} \hat{i} & \hat{j} & \hat{k} \\ \frac{\partial}{\partial x} & \frac{\partial}{\partial y} & \frac{\partial}{\partial z} \\ E_x & E_y & E_z \end{vmatrix} = \mathbf{i}\omega\epsilon\mathbf{E} \tag{B.0.2d}$$

In order to obtain SPP as a solution of Maxwell's equation we need to solve the equation in the system which supports SSP. The system is schematically shown in Fig.B.1. It remains same along the y-direction. This means any derivative along the y-direction should vanish.

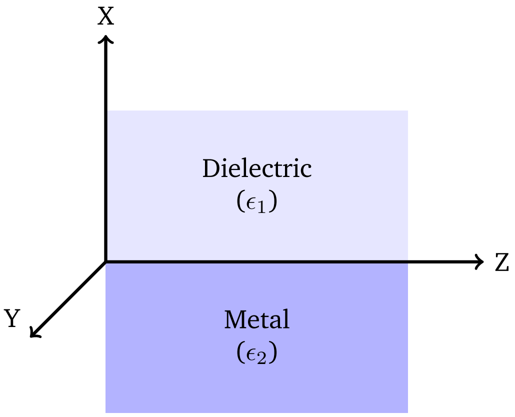

FIGURE B.1: Schematic representation of a metal dielectric interface (Y-Z plane), which supports SPP.

Then from equations B.0.2b & B.0.2d we get:

$$\frac{\partial E_y}{\partial z} = i\omega\mu H_x \tag{B.0.3a}$$

$$\frac{\partial E_x}{\partial z} - \frac{\partial E_z}{\partial x} = -i\omega\mu H_y \tag{B.0.3b}$$

$$\frac{\partial E_y}{\partial x} = -i\omega\mu H_z \tag{B.0.3c}$$

$$-\frac{\partial H_y}{\partial z} = i\omega\epsilon E_x \tag{B.0.3d}$$

$$\frac{\partial H_x}{\partial z} - \frac{\partial H_z}{\partial x} = i\omega\epsilon E_y \tag{B.0.3e}$$

$$\frac{\partial H_y}{\partial x} = i\omega\epsilon E_z \tag{B.0.3f}$$

From these equation one can get different solutions for electromagnetic field corresponding to different polarizations of electric field.

For the metal, having a dielectric function ϵ_2 as shown in Fig.B.1, there is no electric field inside. And, the boundary condition, the parallel component of the electric field at the boundary of two media has to be continuous, implying, parallel components of the electric field to be zero at the interface.

$\Longrightarrow$ E_y and E_z has to be zero.

Now, if both E_y and E_z are zero then there will be no surface mode.

$\Longrightarrow$ The solution can't be such that the electric field is solely perpendicular to the interface, i.e., *the solution can not be a transverse electric* (**TE**) mode.

But if the solution is *a transverse magnetic* (**TM**) wave, (i.e. there is not component of magnetic field along the direction of propagation of the wave) there can be some component of electric field along the direction of propagation (which in our problem lie on the interface), and we can have electric field at the interface.

Considering z-direction to be the direction of propagation of the surface waves (SPPs) for **TM** waves, we must have, $H_z = 0$. Having H_z,E_y and E_z disappear from the eqs.B.0.3, we get only the following set of equations to solve in order to describe SPP:

$$\frac{\partial E_x}{\partial z} - \frac{\partial E_z}{\partial x} = -i\omega\mu H_y \tag{B.0.4}$$

$$-\frac{\partial H_y}{\partial z} = i\omega\epsilon E_x \tag{B.0.5}$$

$$\frac{\partial H_y}{\partial x} = i\omega\epsilon E_z \tag{B.0.6}$$

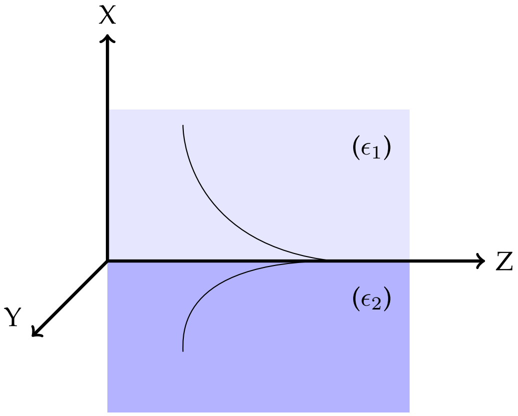

FIGURE B.2: Schematic representation of evanescent electric fields describing SPP.

As the SPPs are surface waves they must be confined at the surface (here interface) only. This can only happen if the field be evanescent , i.e. it decays exponentially away from the interface, as shown Fig.2. This means we should look for solutions having following forms:

$$E_i(z) = \begin{bmatrix} E_{x,i} \\ E_{z,i} \end{bmatrix} e^{-\kappa_i |x|} \, e^{ikz} \tag{B.0.7}$$

$$H_i(z) = H_{y,i} e^{-\kappa_i |x|} \, e^{ikz} \tag{B.0.8}$$

here, κ is the evanescent decay factor; the index "i" refers to the media, i=1 for the insulator, i=2 for the metal; and k is the wave vector for the SPPs.

Substituting these wave forms in equations of TM modes we get,

$$from\ B.0.4, \qquad \frac{\partial}{\partial z}\left(E_{x,i} e^{-\kappa_i |x|} \, e^{ikz}\right) - \frac{\partial}{\partial x}\left(E_{z,i} e^{-\kappa_i |x|} \, e^{ikz}\right) = -i\omega\mu \, H_{y,i} e^{-\kappa_i |x|} \, e^{ikz} \tag{B.0.9}$$

$$from\ B.0.5, \qquad -\frac{\partial}{\partial z}\left(H_{y,i} e^{-\kappa_i |x|} \, e^{ikz}\right) = i\omega\epsilon \, E_{x,i} e^{-\kappa_i |x|} \, e^{ikz} \tag{B.0.10}$$

$$from\ B.0.6, \qquad \frac{\partial}{\partial x}\left(H_{y,i} e^{-\kappa_i |x|} \, e^{ikz}\right) = i\omega\epsilon \, E_{z,i} e^{-\kappa_i |x|} \, e^{ikz} \tag{B.0.11}$$

Solving these in both the regions and then canceling the exponentials from both sides of equality we get,

In region 1 :

$$ikE_{x,1} + \kappa_1 E_{z,1} = -i\omega\mu_0\mu_{r,1}H_{y,1} \tag{B.0.12}$$

$$-ikH_{y,1} = i\omega\epsilon_0\varepsilon_1 E_{x,1} \tag{B.0.13}$$

$$-\kappa_1 H_{y,1} = i\omega\epsilon_0\varepsilon_1 E_{z,1} \tag{B.0.14}$$

From B.0.13, $E_{x,1} = \dfrac{kH_{y,1}}{\omega\epsilon_0\varepsilon_1}$. Putting this in B.0.12 we get,

$$\frac{ik^2\ H_{y,1}}{\omega\epsilon_0\varepsilon_1} + \kappa_1 E_{z,1} = -i\omega\mu_0\mu_{r,1}H_{y,1}$$

$$= \frac{-i\omega\mu_0\mu_{r,1}H_{y,1}}{\omega\epsilon_0\varepsilon_1}\omega\epsilon_0\varepsilon_1 = \frac{-i\dfrac{\omega^2}{c^2}\varepsilon_1\mu_{r,1}H_{y,1}}{\omega\epsilon_0\varepsilon_1} = \frac{-ik_0^2\varepsilon_1\mu_{r,1}H_{y,1}}{\omega\epsilon_0\varepsilon_1}$$

$$\kappa_1 E_{z,1} = -\frac{i}{\omega\epsilon_0\varepsilon_1}\left(k_0^2\varepsilon_1\mu_{r,1} - k^2\right)H_{y,1} \tag{B.0.15}$$

And now eliminating $E_{z,1}$ from B.0.14 & B.0.15, we get the dispersion relation in region 1 as,

$$\boldsymbol{k_0^2\varepsilon_1\mu_{r,1} = k^2 - \kappa_1^2} \tag{B.0.16}$$

In region 2 :

$$ikE_{x,2} - \kappa_2 E_{z,2} = -i\omega\mu_0\mu_{r,2}H_{y,2} \tag{B.0.17}$$

$$-ikH_{y,2} = i\omega\epsilon_0\varepsilon_2 E_{x,2} \tag{B.0.18}$$

$$\kappa_2 H_{y,2} = i\omega\epsilon_0\varepsilon_2 E_{z,2} \tag{B.0.19}$$

(as this medium is extended over the region where x has -ve values, signs have been changed accordingly).
Following the same analysis in region we also get ,

$$\kappa_2 E_{z,2} = \frac{i}{\omega\epsilon_0\varepsilon_2}\left(k_0^2\varepsilon_2\mu_{r,2} - k^2\right)H_{y,2} \tag{B.0.20}$$

and the dispersion relation in this region also looks same,

$$\boldsymbol{k_0^2\varepsilon_2\mu_{r,2} = k^2 - \kappa_2^2} \tag{B.0.21}$$

BOUNDARY CONDITIONs. The electric field boundary condition is $\mathbf{E_{z,1} = E_{z,2}}$, and the magnetic field boundary condition is $\mathbf{H_{y,1}} = \mathbf{H_{y,2}}$. So, using them and either starting by equating B.0.14 & B.0.19 or starting from equating B.0.15 & B.0.20 we get,

$$\boxed{\boldsymbol{\frac{\varepsilon_1}{\kappa_1} + \frac{\varepsilon_2}{\kappa_2} = 0}} \tag{B.0.22}$$

This equation is known as **EXISTENCE CONDITION** for SPPs.

If we divide B.0.16 by B.0.21, after doing a bit of side changing of terms we get,

$$\begin{aligned}
\frac{k^2 - k_0^2\varepsilon_1\mu_{r,1}}{k^2 - k_0^2\varepsilon_2\mu_{r,2}} &= \frac{\kappa_1^2}{\kappa_2^2} \\
or, \quad \frac{k^2 - k_0^2\varepsilon_1\mu_{r,1}}{k^2 - k_0^2\varepsilon_2\mu_{r,2}} &= \frac{\varepsilon_1^2}{\varepsilon_2^2} \quad [from\ eq. B.0.22] \\
or, \quad k^2\varepsilon_2^2 - k_0^2\varepsilon_1\mu_{r,1}\varepsilon_2^2 &= k^2\varepsilon_1^2 - k_0^2\varepsilon_2\mu_{r,2}\varepsilon_1^2 \\
or, \quad k^2\Big(\varepsilon_2^2 - \varepsilon_1^2\Big) &= k_0^2\varepsilon_1\varepsilon_2\Big(\varepsilon_2\mu_{r,1} - \varepsilon_1\mu_{r,2}\Big) \\
or, \quad k^2\Big(\varepsilon_1 + \varepsilon_2\Big)\Big(\varepsilon_2 - \varepsilon_1\Big) &= k_0^2\varepsilon_1\varepsilon_2\Big(\varepsilon_2\mu_{r,1} - \varepsilon_1\mu_{r,2}\Big)
\end{aligned}$$

So, for interfaces where the materials that constitutes the interface are magnetic the dispersion relation becomes,

$$\boldsymbol{k = k_0\sqrt{\frac{\varepsilon_1\varepsilon_2\Big(\varepsilon_2\mu_{r,1} - \varepsilon_1\mu_{r,2}\Big)}{\varepsilon_2^2 - \varepsilon_1^2}}} \tag{B.0.23}$$

And, for interface where the materials that constitutes the interface are non-magnetic the DISPERSION RELATION is simply,

$$\boxed{\boldsymbol{k = k_0\sqrt{\frac{\varepsilon_1\varepsilon_2}{\varepsilon_1 + \varepsilon_2}}}} \tag{B.0.24}$$

Appendix C

Hydrodynamic Equation of Motion

In order to describe the collective motion of the nearly-free conduction band electrons in a conducting medium, the hydrodynamic variables are, the charge density n_e, the velocity of electron fluid $\mathbf{v}(\mathbf{r}, t)$, and electron pressure $p(\mathbf{r}, t)$. Under the influence of electromagnetic field the equation of motion for the electrons is given by,

$$m_e \frac{d\mathbf{v}}{dt} + \gamma m_e \mathbf{v} = -\Big(e\mathbf{E} + e\mathbf{v} \times \mathbf{B} \Big) - \frac{\nabla p}{n_e}. \tag{C.0.1}$$

The total time derivative of velocity is given by,

$$\frac{d\mathbf{v}}{dt} = \frac{\partial \mathbf{v}}{\partial t} + (\mathbf{v} \cdot \nabla)\mathbf{v} \tag{C.0.2}$$

Having eq.C.0.2 in eq.C.0.1 we get,

$$m_e \frac{\partial \mathbf{v}}{\partial t} + m_e(\mathbf{v} \cdot \nabla)\mathbf{v} + \gamma m_e \mathbf{v} = -\Big(e\mathbf{E} + e\mathbf{v} \times \mathbf{B} \Big) - \frac{\nabla p}{n_e}. \tag{C.0.3}$$

Dividing eq.C.0.3 by m_e, and multiplying it by $-en_e$, we get

$$-en_e \frac{\partial \mathbf{v}}{\partial t} - en_e(\mathbf{v} \cdot \nabla)\mathbf{v} - e\gamma n_e \mathbf{v} = \frac{n_e e^2}{m_e}\Big(\mathbf{E} + \mathbf{v} \times \mathbf{B} \Big) + e\frac{\nabla p}{m_e}. \tag{C.0.4}$$

Now, the current density is defined as,

$$\mathbf{J} = -en_e \mathbf{v} \tag{C.0.5}$$

and it follows the continuity equation relating the density n_e as,

$$\nabla \cdot \mathbf{J} = e\frac{\partial n_e}{\partial t} = e\dot{n}_e. \tag{C.0.6}$$

From eq.C.0.5 we get the partial derivative of $\mathbf{J}$ as,

$$\frac{\partial \mathbf{J}}{\partial t} = -e\dot{n}_e\mathbf{v} - en_e\frac{\partial \mathbf{v}}{\partial t} \tag{C.0.7}$$

Using, eqs.C.0.7 and C.0.6 in the first and second terms on the L.H.S of eq.C.0.4, we respectively get,

$$-en_e\frac{\partial \mathbf{v}}{\partial t} = \frac{\partial \mathbf{J}}{\partial t} - (\nabla \cdot \mathbf{J})\frac{\mathbf{J}}{en_e} \tag{C.0.8}$$

$$-en_e(\mathbf{v} \cdot \nabla)\mathbf{v} = -(\mathbf{J} \cdot \nabla)\frac{\mathbf{J}}{en_e} \tag{C.0.9}$$

Clubbing eqs. C.0.8 & C.0.9, and using eq.C.0.5 in the equation of motion (C.0.4), we get,

$$\frac{\partial \mathbf{J}}{\partial t} - (\nabla \cdot \mathbf{J})\frac{\mathbf{J}}{en_e} - (\mathbf{J} \cdot \nabla)\frac{\mathbf{J}}{en_e} + \gamma\mathbf{J} = \frac{n_e e^2}{m_e}\mathbf{E} - \frac{e}{m_e}(\mathbf{J} \times \mathbf{B}) + e\frac{\nabla p}{m_e} \tag{C.0.10}$$

The second and third term in the eq.C.0.10 involves higher order of $\mathbf{J}$, and can be approximated to contribute insignificantly, to give:

$$\frac{\partial \mathbf{J}}{\partial t} + \gamma\mathbf{J} = \frac{n_e e^2}{m_e}\mathbf{E} - \frac{e}{m_e}(\mathbf{J} \times \mathbf{B}) + \frac{e}{m_e}\nabla p. \tag{C.0.11}$$

Recognizing the electrical polarization vector ($\mathbf{P}$) corresponding to the polarization of conduction band electrons, in terms of the current density as,

$$\dot{\mathbf{P}} = \mathbf{J}, \tag{C.0.12}$$

the equation of motion (C.0.11) takes the form as,

$$\ddot{\mathbf{P}} + \gamma\dot{\mathbf{P}} = \frac{n_e e^2}{m_e}\mathbf{E} + \frac{e}{m_e}\nabla p \tag{C.0.13}$$

Thomas–Fermi pressure: In order to have a tractable expression for the pressure term, the quantum mechanical description of the electron pressure within Thomas–Fermi model can be considered:

$$p(\mathbf{r},t) = \zeta\left[n(\mathbf{r},t)\right]^{5/3}, \quad where, \zeta = \frac{h^2(3\pi)^{2/3}}{5m_e}. \tag{C.0.14}$$

Thus, the electron pressure term becomes:

$$\frac{e}{m_e}\nabla p = \frac{e}{m_e}\zeta\frac{5}{3}n^{2/3}\nabla n_e \simeq \frac{5}{3}n_0^{2/3}\frac{e}{m_e}\nabla n_e, \tag{C.0.15}$$

where, $n_e(\mathbf{r},t)$ is approximated to $n_0(\mathbf{r})$, the equilibrium electron density corresponding to the system unperturbed by the electromagnetic field. The expression for the gradient of $n_e(\mathbf{r},t)$ can be found through the continuity equation for density:

$$n(\mathbf{r},t) = n_0\mathbf{r} + \frac{1}{e}\nabla\cdot\mathbf{P} \tag{C.0.16}$$

. Using eq.C.0.16, $\nabla n_e(\mathbf{r},t)$ is,

$$\nabla n_e = \frac{1}{e}\nabla(\nabla\cdot\mathbf{P}); \tag{C.0.17}$$

and thus, the pressure term (C.0.15) can be expressed in terms of polarization as,

$$\frac{e}{m_e}\nabla p = \zeta\frac{5}{3}\frac{n_0^{2/3}}{m_e}\nabla(\nabla\cdot\mathbf{P}). \tag{C.0.18}$$

Having this expression for pressure term in eq.C.0.13, we get,

$$\ddot{\mathbf{P}} + \gamma\dot{\mathbf{P}} = \frac{n_e e^2}{m_e}\mathbf{E} + \left(\zeta\frac{5}{3}\frac{n_0^{2/3}}{m_e}\right)\nabla(\nabla\cdot\mathbf{P}). \tag{C.0.19}$$

Having defined,

$$\text{the plasma frequency,} \quad \omega_p = \sqrt{\frac{n_e e^2}{\epsilon_0 m_e}}, and, \tag{C.0.20}$$

$$\text{the nonlocal parameter,} \quad \beta = \sqrt{\frac{5}{3}\,\zeta\,\frac{n_0^{2/3}}{m_e}} \tag{C.0.21}$$

we get,

$$\boxed{-\beta^2\nabla(\nabla\cdot\mathbf{P})+\ddot{\mathbf{P}}+\gamma\dot{\mathbf{P}}=\epsilon_0\omega_p^2\mathbf{E}} \tag{C.0.22}$$

the usual form of the hydrodynamic equation of motion for the conduction band electrons.

Appendix D

Working Principle Of Local Analogue Model (LAM)

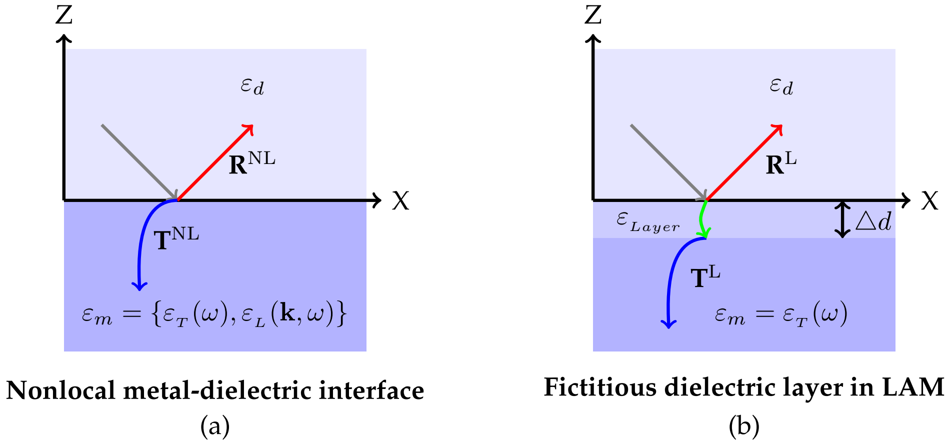

FIGURE D.1: In (a), the geometry represnting the nonlocal metal-dielctric interface, where the dielectric function for the metallic region is described by both the transverse and longitudinal components. The structure represented in (b) shows the local analogue model (LAM), where a fictitious dielectric layer is introduced in between the metal and the dielectric background.

In order to demonstrate the working principle of local analogue model (LAM), we shall take the example of a *nonlocal metal-dielectric interface*, as shown in Fig. D.1(a). The idea of LAM implementation to produce the same results as in the full three-dimensional implementation of the hydrodynamic model is based on the following philosophy. Mimicking the spatial nonlocality only through the transverse modes, and by playing with the width ($\triangle d$), and the dielectric function ($\varepsilon_{_{Layer}}$) of an intermediate layer, as shown in Fig. D.1(b), between the metal and the surrounding dielectric, one obtains the same reflection an transmission coefficients as from the three-dimensional implementation of the hydrodynamical model, irrespective of the parallel component of the wave vector (k) at the interface. This description of the working principle of LAM is explained in details in the supplementary information of Ref. [146].

Nonlocal metal-dielectric interface

Following the Fig. D.1(a), at the metal-dielectric interface, where the metal dielectric function (ε_m) accounts for the spatial nonlocality as described by the hydrodynamic model (i.e., $\varepsilon_m = \{\varepsilon_{_T}, \varepsilon_{_L}\}$), the electric field associated with the surface plasmon polariton (SPP) in the metallic region can be given as,

$$H_y^m = T^{^{NL}} e^{zk_z}\, e^{ikx}, \tag{D.0.1}$$

$$E_x^m = \left[\frac{-ik_z}{\varepsilon_m k_0}\, T^{^{NL}} e^{zk_z} + \frac{-ik_0}{q_{_L}}\, T^{^{LG}} e^{zq_{_L}}\right] e^{ikx}, \tag{D.0.2}$$

$$E_z^m = \left[\frac{-k}{\varepsilon_m k_0}\, T^{^{NL}} e^{zk_z} + \frac{-k_0}{k}\, T^{^{LG}} e^{zq_{_L}}\right] e^{ikx}; \tag{D.0.3}$$

where, $\mathbf{k} = k\hat{\mathbf{x}}$, i.e. k is the wave vector of SPP;
$T^{^{NL}}$ and $T^{^{LG}}$ stands for the amplitudes (transmission coefficients) associated with the transverse and longitudinal electric waves;
it is approximated that, $\sqrt{k^2 + q_{_L}^2} = q_{_L}$, as $q_{_L} \gg k$;
$k_0 = \omega/c$, $k_z = \sqrt{k^2 - \varepsilon_m k_0^2}$ is the normal component of wave vector in the metal which is inversely proportional to the penetration depth of the transverse component of the SPP into the metal; and
$q_{_L}$ is the wave vector of the longitudinal bulk plasmon, normal to the metal-dielectric interface, as defined in eq. 2.3.22.

Now, if we consider a plane electromagnetic wave of unit magnetic field amplitude to be incident upon the metal surface, in the background dielectric medium the total (incident + reflected) magnetic and electric fields can be written as,

$$H_y^b = \left[e^{-zk_z^b} \; + \; R^{^{NL}} \; e^{+zk_z^b}\right] e^{ikx}, \tag{D.0.4}$$

$$E_x^b = \frac{-ik_z^b}{\varepsilon_b k_0}\left[e^{-zk_z^b} \; - \; R^{^{NL}} \; e^{+zk_z^b}\right] e^{ikx}, \tag{D.0.5}$$

$$E_z^b = \frac{-k}{\varepsilon_b k_0}\left[e^{-zk_z^b} \; + \; R^{^{NL}} \; e^{+zk_z^b}\right] e^{ikx}; \tag{D.0.6}$$

where,
$R^{^{NL}}$ is the reflection coefficient associated with the transverse electric waves, and $k_z^b = \sqrt{k^2 - \varepsilon_b k_0^2}$ is the normal component of wave vector in the dielectric medium, ε_b being the dielectric constant.

Applying electromagnetic boundary conditions: continuity of H_y, E_x, and E_z, at the interface $z = 0$, we get expressions for the reflection and transmission coefficients as follows.

$$R^{^{NL}} = \frac{1 - \dfrac{\varepsilon_b k_z}{\varepsilon_m k_z^b} - \dfrac{k^2}{q_{_L} k_z^b}\left(1 - \dfrac{\varepsilon_b}{\varepsilon_m}\right)}{1 + \dfrac{\varepsilon_b k_z}{\varepsilon_m k_z^b} + \dfrac{k^2}{q_{_L} k_z^b}\left(1 - \dfrac{\varepsilon_b}{\varepsilon_m}\right)}, \quad \text{and} \tag{D.0.7}$$

$$T^{^{NL}} = \frac{2}{1 + \dfrac{\varepsilon_b k_z}{\varepsilon_m k_z^b} + \dfrac{k^2}{q_{_L} k_z^b}\left(1 - \dfrac{\varepsilon_b}{\varepsilon_m}\right)} \tag{D.0.8}$$

Metal-dielectric interface with a fictitious dielectric layer in between

The structure in Fig. D.1(b) represent the LAM. In this structure only transverse component of the electric field (which comes as the usual solution of Maxwell's equations) are considered and consequently $\varepsilon_m = \varepsilon_{_T}$. The fictitious dielectric material in between the metal and dielectric background is considered to have an anisotropic permittivity of a parallel component ϵ_{xx}, and a normal component ϵ_{zz}. The components of electromagnetic field in each of the three region in the Fig. D.1(b) can be written as,

Metal region:

$$H_y^m = T^{L} e^{(z+\triangle d)k_z}\ e^{ikx}, \tag{D.0.9}$$

$$E_x^m = \frac{-ik_z}{\varepsilon_m k_0}\ T^{L} e^{(z+\triangle d)k_z}\ e^{ikx}, \tag{D.0.10}$$

$$E_z^m = \frac{-k}{\varepsilon_m k_0}\ T^{L} e^{(z+\triangle d)k_z}\ e^{ikx}; \tag{D.0.11}$$

where, T^{L} is the transmission coefficients associated with the electric wave. As the metal is described in local optics, no longitudinal component appears in the field equations.

In fictitious dielectric layer:

$$H_y^{Layer} = \left[C^{-} e^{zk_z^{Layer}}\ +\ C^{+}\ e^{-(z+\triangle d)k_z^{Layer}}\right] e^{ikx} \tag{D.0.12}$$

$$E_x^{Layer} = \frac{-ik_z^{Layer}}{\varepsilon_{xx} k_0}\left[C^{-} e^{zk_z^{Layer}}\ -\ C^{+}\ e^{-(z+\triangle d)k_z^{b}}\right] e^{ikx}, \quad \text{for } -\triangle d < z < 0 \tag{D.0.13}$$

$$E_z^{Layer} = \frac{-k}{\varepsilon_{zz} k_0}\left[C^{-} e^{zk_z^{Layer}}\ +\ C^{+}\ e^{-(z+\triangle d)k_z^{Layer}}\right] e^{ikx}; \tag{D.0.14}$$

where,

$$k_z^{Layer} = \sqrt{\varepsilon_{xx}\left(\frac{k^2}{\varepsilon_{zz}} - k_0^2\right)}. \tag{D.0.15}$$

In the background dielectric:

$$H_y^b = \left[e^{-zk_z^b}\ +\ R^{L}\ e^{+zk_z^b}\right] e^{ikx}, \tag{D.0.16}$$

$$E_x^b = \frac{-ik_z^b}{\varepsilon_b k_0}\left[e^{-zk_z^b}\ -\ R^{L}\ e^{+zk_z^b}\right] e^{ikx}, \tag{D.0.17}$$

$$E_z^b = \frac{-k}{\varepsilon_b k_0}\left[e^{-zk_z^b}\ +\ R^{L}\ e^{+zk_z^b}\right] e^{ikx}; \tag{D.0.18}$$

where, R^{L} is the reflection coefficients associated with the electric wave reflected back into the dielectric.

Applying the boundary conditions at the two boundaries at $z = 0$ and $z = -d$, we get the expressions for the reflection and transmission coefficients as,

$$R^{L} = \frac{\left(1 - \dfrac{\varepsilon_b k_z}{\varepsilon_m k_z^b}\right) cosh(k_z^{Layer} \triangle d) \; - \; \left(\dfrac{\varepsilon_b k_z^{Layer}}{\varepsilon_{xx} k_z^b} - \dfrac{\varepsilon_{xx} k_z}{\varepsilon_m k_z^{Layer}}\right) sinh(k_z^{Layer} \triangle d)}{\left(1 + \dfrac{\varepsilon_b k_z}{\varepsilon_m k_z^b}\right) cosh(k_z^{Layer} \triangle d) \; + \; \left(\dfrac{\varepsilon_b k_z^{Layer}}{\varepsilon_{xx} k_z^b} + \dfrac{\varepsilon_{xx} k_z}{\varepsilon_m k_z^{Layer}}\right) sinh(k_z^{Layer} \triangle d)} \tag{D.0.19}$$

$$T^{L} = \frac{2}{\left(1 + \dfrac{\varepsilon_b k_z}{\varepsilon_m k_z^b}\right) cosh(k_z^{Layer} \triangle d) \; + \; \left(\dfrac{\varepsilon_b k_z^{Layer}}{\varepsilon_{xx} k_z^b} + \dfrac{\varepsilon_{xx} k_z}{\varepsilon_m k_z^{Layer}}\right) sinh(k_z^{Layer} \triangle d)} \tag{D.0.20}$$

Two different solution for LAM

Anisotropic solution: In the limit of $k_z^{Layer} \triangle d \to 0$, the second terms in the numerator and the denominator of eq. D.0.19 become,

$$\begin{aligned}
\lim_{(k_z^{Layer} \triangle d) \to 0} \left(\frac{\varepsilon_b k_z^{Layer}}{\varepsilon_{xx} k_z^b} \mp \frac{\varepsilon_{xx} k_z}{\varepsilon_m k_z^{Layer}}\right) sinh(k_z^{Layer} \triangle d) &= \left(\frac{\varepsilon_b k_z^{Layer}}{\varepsilon_{xx} k_z^b} \mp \frac{\varepsilon_{xx} k_z}{\varepsilon_m k_z^{Layer}}\right) k_z^{Layer} \triangle d \\
&= \frac{\varepsilon_b (k_z^{Layer})^2 \triangle d}{\varepsilon_{xx} k_z^b} \mp \frac{\varepsilon_{xx} k_z \triangle d}{\varepsilon_m} \\
&= \frac{\varepsilon_b \triangle d}{k_z^b} \left(\frac{k^2}{\varepsilon_{zz}} - k_0^2\right) \mp \frac{\varepsilon_{xx} k_z \triangle d}{\varepsilon_m} \qquad (from\ eq.\ D.0.15) \\
&\approx \frac{\varepsilon_b \ \triangle d \ k^2}{k_z^b \ \varepsilon_{zz}} \mp \frac{\varepsilon_{xx} k_z \triangle d}{\varepsilon_m}
\end{aligned} \tag{D.0.21}$$

For $\varepsilon_{xx} = 0$, which also means $k_z^{Layer} = 0$, eq. D.0.21 reduces to,

$$\lim_{(k_z^{Layer} \triangle d) \to 0} \left(\frac{\varepsilon_b k_z^{Layer}}{\varepsilon_{xx} k_z^b} \mp \frac{\varepsilon_{xx} k_z}{\varepsilon_m k_z^{Layer}}\right) sinh(k_z^{Layer} \triangle d) \approx \frac{\varepsilon_b \ \triangle d \ k^2}{k_z^b \ \varepsilon_{zz}} \tag{D.0.22}$$

Thus, in the limit of $k_z^{Layer} \triangle d \to 0$, by having $\varepsilon_{xx} = 0$, eqs. D.0.19 and D.0.20 become,

$$R^{L} \approx \frac{1 - \dfrac{\varepsilon_b k_z}{\varepsilon_m k_z^b} - \dfrac{\varepsilon_b \triangle d\, k^2}{k_z^b\, \varepsilon_{zz}}}{1 + \dfrac{\varepsilon_b k_z}{\varepsilon_m k_z^b} + \dfrac{\varepsilon_b \triangle d\, k^2}{k_z^b\, \varepsilon_{zz}}} \tag{D.0.23}$$

$$T^{L} \approx \frac{2}{1 + \dfrac{\varepsilon_b k_z}{\varepsilon_m k_z^b} + \dfrac{\varepsilon_b \triangle d\, k^2}{k_z^b\, \varepsilon_{zz}}} \tag{D.0.24}$$

Comparing these coefficients of reflectance and transmittance with R^{NL} and T^{NL} we get,

$$\varepsilon_{zz} = \frac{\varepsilon_b\, \varepsilon_m\, q_{L}\, \triangle d}{\varepsilon_m - \varepsilon_b} \tag{D.0.25}$$

Thus a local analogue model to give the same optical properties (reflectance and transmittance) as can be found in a nonlocal metal-dielectric interface is given by the structure represented in Fig. D.1(b), where the dielectric function of the fictitious layer of arbitrary thickness $\triangle d$ is given by ε_{zz} (eq. D.0.25) and $\varepsilon_{xx} = 0$.

Thin layer solution: Though the formulation of LAM using anisotropic dielectric layer is exact, for numerical implementation it preferable to have a layer with isotropic dielectric function as,

$$\varepsilon_{Layer} = \varepsilon_t = \frac{\varepsilon_b\, \varepsilon_m\, q_{L}\, \triangle d}{\varepsilon_m - \varepsilon_b}. \tag{D.0.26}$$

Having this dielectric function, in equation D.0.19 and D.0.20, ε_{zz} and ε_{xx} modifies to ε_t; and the normal wave vector component in the fictitious dielectric layer is given as,

$$k_z^{Layer} = \sqrt{k^2 - \varepsilon_t k_0^2}. \tag{D.0.27}$$

Using equations D.0.26 and D.0.27, in equations D.0.19 and D.0.20, and expanding the hyperbolic functions in Taylor series, R^{L} and T^{L} become,

$$R^{L} = \frac{\left(1 - \dfrac{\varepsilon_b k_z}{\varepsilon_m k_z^b}\right) - \dfrac{k^2}{q_{L} k_z^b}\left(1 - \dfrac{\varepsilon_b}{\varepsilon_m}\right) + \left[\dfrac{\varepsilon_b q_{L} k_z}{\varepsilon_m - \varepsilon_b} + \dfrac{k^2}{2}\left(1 - \dfrac{\varepsilon_b k_z}{\varepsilon_m k_z^b}\right)\right](\triangle d)^2 + \cdots}{\left(1 + \dfrac{\varepsilon_b k_z}{\varepsilon_m k_z^b}\right) + \dfrac{k^2}{q_{L} k_z^b}\left(1 - \dfrac{\varepsilon_b}{\varepsilon_m}\right) + \left[\dfrac{\varepsilon_b q_{L} k_z}{\varepsilon_m - \varepsilon_b} + \dfrac{k^2}{2}\left(1 + \dfrac{\varepsilon_b k_z}{\varepsilon_m k_z^b}\right)\right](\triangle d)^2 + \cdots} \tag{D.0.28}$$

$$T^{L} = \frac{2}{\left(1+\frac{\varepsilon_b k_z}{\varepsilon_m k_z^b}\right) + \frac{k^2}{q_L k_z^b}\left(1-\frac{\varepsilon_b}{\varepsilon_m}\right) + \left[\frac{\varepsilon_b q_L k_z}{\varepsilon_m - \varepsilon_b} + \frac{k^2}{2}\left(1+\frac{\varepsilon_b k_z}{\varepsilon_m k_z^b}\right)\right](\triangle d)^2 + \cdots} \tag{D.0.29}$$

where, '$\cdots$' represents the existence of terms in higher orders of $\triangle d$, and $\triangle d \ll k_z$ is implied.

So, considering the fictitious dielectric layer to have an isotropic dielectric function given by eq. D.0.26, introduces corrective terms having higher orders of $\triangle d$. All these higher order terms can be neglected by making $\triangle d$ relatively smaller than the penetration depth of SPP, to give

$$R^{L} \approx \frac{1-\frac{\varepsilon_b k_z}{\varepsilon_m k_z^b} - \frac{k^2}{q_L k_z^b}\left(1-\frac{\varepsilon_b}{\varepsilon_m}\right)}{1+\frac{\varepsilon_b k_z}{\varepsilon_m k_z^b} + \frac{k^2}{q_L k_z^b}\left(1-\frac{\varepsilon_b}{\varepsilon_m}\right)}, \quad \text{and} \tag{D.0.30}$$

$$T^{L} \approx \frac{2}{1+\frac{\varepsilon_b k_z}{\varepsilon_m k_z^b} + \frac{k^2}{q_L k_z^b}\left(1-\frac{\varepsilon_b}{\varepsilon_m}\right)} \tag{D.0.31}$$

which is same as R^{NL} and T^{NL} in equations D.0.7 and D.0.8 for the nonlocal metal-dielectric interface. Thus, the local analogue model for having the same optical properties as the nonlocal metal-dielectric interface is given by introducing a very thin fictitious dielectric layer in between the metal and the dielectric background. The thickness of the layer is much smaller than the penetration length of the SPP and the isotropic dielectric function is given by eq. D.0.26.

In this thesis, we have used the thin-layer solution of LAM using an istropic dielectric function for the thin fictitious dielectric layer. It is worth mentioning here, that the consideration of the intermediate layer has nothing to do with accounting for the quantum mechanical *spill-out* of the ground-state electron density. The sole motive of LAM implementation is to get rid of the cumbersome three-dimensional implementation of the hydrodynamic model. Thus, the electromagnetic fields, in the LAM implementation, are purely transverse, and the dielectric function of the bulk metal is given by $\varepsilon(\omega) = \varepsilon_{T}(\omega)$.

Implementation of LAM for nanoparticles:

The LAM implementation using a thin layer (with isotropic dielectric function) to nanoparticles with radius of curvature comparable to (or smaller than) the Thomas-Fermi wavelength is shown in Fig.D.2. As we are interested for particles within the quasi-static size limit, the polarizability of the nanosphere of radius R, within the hydrodynamic description [235], can be obtained as,

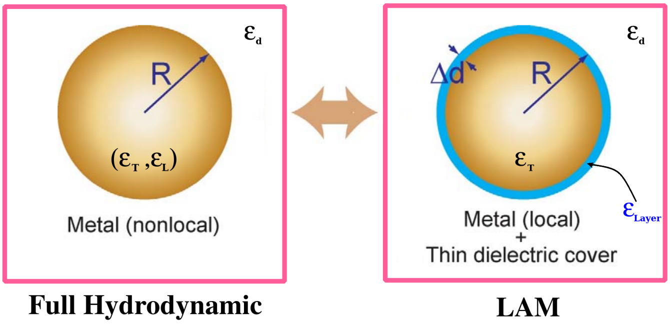

FIGURE D.2: Schematic representation of the local analogue model (LAM, while implemented to a spherical metal cluster, having a radius of curvature comparable to (or smaller than) the Thomas-Fermi wavelength). Courtesy: Ref. [146] PRL 111, 093901 (2013)

$$\alpha_{nl} = 4\pi R^3 \frac{\dfrac{\varepsilon(\omega)}{\varepsilon_d} - \left[1 + \dfrac{\varepsilon(\omega) - \varepsilon_d}{\varepsilon_d q_{_L} R} \dfrac{i_1(q_{_L} R)}{i_1'(q_{_L} R)}\right]}{\dfrac{\varepsilon(\omega)}{\varepsilon_d} + \left[2 + \dfrac{\varepsilon(\omega) - \varepsilon_d}{\varepsilon_d q_{_L} R} \dfrac{i_1(q_{_L} R)}{i_1'(q_{_L} R)}\right]} \tag{D.0.32}$$

where i_1 and i_1' denote the modified spherical Bessel function of the first kind and its derivative, respectively. The expression reduces to its local optics counterpart, eq. 2.1.7, as $q_{_L} \longrightarrow \infty$. Within LAM, the polarizability of the whole system (nanosphere + fictitious layer) can be derived as,

$$\alpha_{\text{LAM}} = 4\pi R^3 \frac{\dfrac{\varepsilon(\omega)}{\varepsilon_d} - \dfrac{R}{R - \triangle d}\left\{1 + \dfrac{\varepsilon(\omega)}{\varepsilon_{Layer}} \dfrac{\triangle d}{R}\right\}}{\dfrac{\varepsilon(\omega)}{\varepsilon_d} + \dfrac{2R}{R - \triangle d}\left\{1 + \dfrac{\varepsilon(\omega)}{\varepsilon_{Layer}} \dfrac{\triangle d}{R}\right\}} \tag{D.0.33}$$

The expression for the $\varepsilon_{_{Layer}}$, can then be obtained by comparing eqs. D.0.32 & D.0.33, as,

$$\varepsilon_{_{Layer}}^{sphere} = \frac{\varepsilon(\omega)}{\dfrac{R}{R-\triangle d}\left(\dfrac{\varepsilon(\omega)-\varepsilon_d}{\varepsilon_d q_{_L} R}\right)\left(\dfrac{i_1(q_{_L}R)}{i_1'(q_{_L}R)}\right)-1} \tag{D.0.34}$$

This expression for the dielectric function of the fictitious shell used in LAM is exact, irrespective of the thickness of the dielectric shell, $\triangle d$. For, a dielectric shell of very small thickness ($\triangle d \ll R$), the expression D.0.34 can be expressed as,

$$\varepsilon_{_{Layer}}^{sphere} \approx \frac{\varepsilon_d\ (\triangle d)\ \varepsilon(\omega)\ q_{_L}}{\varepsilon(\omega)-\varepsilon_d}\frac{i_1'(q_{_L}R)}{i_1(q_{_L}R)} \tag{D.0.35}$$

Appendix E

Jellium Description

A jellium system is a system of interacting electrons bound by a positive background called jellium. Thus, within a jellium description there is no notion of atomic lattice. The charge density and the spatial extension of the homogeneous positive background defines the jellium. For the “simple" metals, like the alkalies, the optical properties (,in other words, the linear response to the density) in the infrared–visible are primarily governed by the loosely bound outermost electrons. Therefore, in order to describe them, it is a good approximation to put all the ions into the jellium with a density ρ_+. In order to make the jellium description numerically more tractable, spherical symmetry is often imposed for the shape of the jellium, and is defined by the radius, $r_{jellium}$, of the jellium sphere. The $r_{jellium}$ is simply defined using the Wigner-Seitz radius, r_s of the species and the number of electrons, N_e, to be considered in the jellium system:

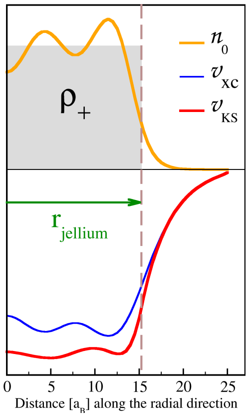

FIGURE E.1: A spherical jellium system. The shaded area shows the positive jellium background. In red the Kohn–Sham potential; in blue te xc potential (LDA). The profile of the ground state electron density is shown in orange.

$$r_{jellium} = N_e^{1/3}\, r_s \tag{E.0.1}$$

The Hamiltonian of the jellium system is thus:

$$\begin{aligned}\hat{\mathcal{H}}_{jell-sys} &= \hat{\mathcal{T}} + \hat{\mathcal{V}}_{e-jell} + \hat{\mathcal{W}}_{e-e} + \hat{\mathcal{H}}_{jell-back} \\ &= -\frac{1}{2}\sum_{j}^{N_e} \nabla_j^2 \, + \, \sum_{j=1}^{N_e} v_{j,e-jell}(\mathbf{r_j}) \, + \, \frac{1}{2}\sum_{\substack{j,k=1\\ j\neq k}}^{N_e} \frac{1}{|\mathbf{r_j}-\mathbf{r_k}|} \, + \, \hat{\mathcal{H}}_{jell-back}\end{aligned} \tag{E.0.2}$$

where, the $\mathbf{R}$ is used as a continuous variable for the jellium; and the external potential, $v_{j,e-jell}(\mathbf{r_j})$, is given by,

$$v_{j,e-jell}(\mathbf{r_j}) = \rho_+^2(\mathbf{R}) \int d^3\mathrm{R} \, \frac{-1}{|\mathbf{r_j}-\mathbf{R}|} \tag{E.0.3}$$

Starting from this Hamiltonian one can follow the standard prescription for a RT-TDDFT in order to get the linear response optical spectrum. An example of the jellium description for 58-atom sodium cluster is shown in Fig.E.1. For the cases of noble metals, there are strongly bound d-electrons which are not far away from the Fermi level and therefore have a screening effect on the nearly–free valence electron. The effect of this screening is incorporated in jellium description by using an effective permittivity for an effective region inside the jellium.

Bibliography

[1] J. Christopher Love, Lara A. Estroff, Jennah K. Kriebel, Ralph G. Nuzzo, and George M. Whitesides. Self-assembled monolayers of thiolates on metals as a form of nanotechnology. *Chemical Reviews*, 105(4):1103–1170, 2005.

[2] Ivan H. El-Sayed Prashant K. Jain, Xiaohua Huang and Mostafa A. El-Sayed. Noble metals on the nanoscale: Optical and photothermal properties and some applications in imaging, sensing, biology, and medicine. *Accounts of Chemical Research*, 41(12):1578–1586, 2008.

[3] James F. Hainfeld, Wenqiu Liu, Carol M.R. Halsey, Paul Freimuth, and Richard D. Powell. Ni–nta–gold clusters target his-tagged proteins. *Journal of Structural Biology*, 127(2):185 – 198, 1999.

[4] Christopher J. Ackerson, Richard D. Powell, and James F. Hainfeld. Chapter nine - site-specific biomolecule labeling with gold clusters. In Grant J. Jensen, editor, *Cryo-EM Part A Sample Preparation and Data Collection*, volume 481 of *Methods in Enzymology*, pages 195 – 230. Academic Press, 2010.

[5] Mary-Catherine Bowman, T. Eric Ballard, Christopher J. Ackerson, Daniel L. Feldheim, David M. Margolis, and Christian Melander. Inhibition of hiv fusion with multivalent gold nanoparticles. *Journal of the American Chemical Society*, 130(22):6896–6897, 2008.

[6] Jamee Bresee, Keith E. Maier, Amy E. Boncella, Christian Melander, and Daniel L. Feldheim. Growth inhibition of staphylococcus aureus by mixed monolayer gold nanoparticles. *Small*, 7(14):2027–2031, 2011.

[7] F. Javier Garcia de Abajo. Microscopy: Plasmons go quantum. *Nature*, 483:417–418, 2012.

[8] Jonathan A. Scholl, Ai Leen Koh, and Jennifer A. Dionne. Quantum plasmon resonances of individual metallic nanoparticles. *Nature*, 483(7390):421–427, Mar 2012.

[9] Hellmut Haberland. Looking from both sides. *Nature*, 494(7435):E1–E2, Feb 2013.

[10] K. J. Taylor, C. L. Pettiette-Hall, O. Cheshnovsky, and R. E. Smalley. Ultraviolet photoelectron spectra of coinage metal clusters. *The Journal of Chemical Physics*, 96(4):3319–3329, 1992.

[11] Asantha C. Dharmaratne and Amala Dass. $\mathrm{Au}_{144-x}\mathrm{cu}_x(\mathrm{sc}_6\mathrm{h}_{13})_{60}$ nanomolecules: effect of cu incorporation on composition and plasmon-like peak emergence in optical spectra. *Chem. Commun.*, 50:1722–1724, 2014.

[12] Nabraj Bhattarai, David M. Black, Snigdha Boppidi, Subarna Khanal, Daniel Bahena, Alfredo Tlahuice-Flores, S. B. H. Bach, Robert L. Whetten, and Miguel Jose-Yacaman. Esi-ms identification of abundant copper-gold clusters exhibiting high plasmonic character. *The Journal of Physical Chemistry C*, 119(20):10935–10942, 2015.

[13] Sami Malola, Michael J. Hartmann, and Hannu Häkkinen. Copper induces a core plasmon in intermetallic au(144,145)–xcux(sr)60 nanoclusters. *The Journal of Physical Chemistry Letters*, 6(3):515–520, 2015. PMID: 26261973.

[14] Ian Freestone, Nigel Meeks, Margaret Sax, and Catherine Higgitt. The lycurgus cup — a roman nanotechnology. *Gold Bulletin*, 40(4):270–277, Dec 2007.

[15] Collection blue gold. `http://www.ludwigmuller.ch/collection.html`. Joaillier créator Ludwig Muller.

[16] M. Faraday. The bakerian lecture: Experimental relations of gold (and other metals) to light. *Phil. Trans. R. Soc. Lond.*, 147:129–143, 1857.

[17] R. M. Zsigmondy. Properties of colloids. *Nobel Lecture*, 1926.

[18] Gustav Mie. Beiträge zur optik trüber medien, speziell kolloidaler metallösungen. *Annalen der Physik*, 330(3):377–445, 1908.

[19] Jin Zhong Zhang. Biomedical applications of shape-controlled plasmonic nanostructures: A case study of hollow gold nanospheres for photothermal ablation therapy of cancer. *The Journal of Physical Chemistry Letters*, 1(4):686–695, 2010.

[20] Christopher J. Ackerson, Pablo D. Jadzinsky, Jonathan Z. Sexton, David A. Bushnell, and Roger D. Kornberg. Synthesis and bioconjugation of 2 and 3 nm-diameter gold nanoparticles. *Bioconjugate Chemistry*, 21(2):214–218, 2010. PMID: 20099843.

[21] James F. Hainfeld, Wenqiu Liu, Carol M.R. Halsey, Paul Freimuth, and Richard D. Powell. Ni–nta–gold clusters target his-tagged proteins. *Journal of Structural Biology*, 127(2):185 – 198, 1999.

[22] Christopher J. Ackerson, Richard D. Powell, and James F. Hainfeld. Site-specific biomolecule labeling with gold clusters. *Methods in Enzymology*, 481:195 – 230, 2010. Cryo-EM Part A Sample Preparation and Data Collection.

[23] Mary-Catherine Bowman, T. Eric Ballard, Christopher J. Ackerson, Daniel L. Feldheim, David M. Margolis, and Christian Melander. Inhibition of hiv fusion with multivalent gold nanoparticles. *Journal of the American Chemical Society*, 130(22):6896–6897, 2008. PMID: 18473457.

[24] Jamee Bresee, Keith E. Maier, Amy E. Boncella, Christian Melander, and Daniel L. Feldheim. Growth inhibition of staphylococcus aureus by mixed monolayer gold nanoparticles. *Small*, 7(14):2027–2031, 2011.

[25] S. A. Maier, M. L. Brongersma, P. G. Kik, S. Meltzer, A. A. G. Requicha, and H. A. Atwater. Plasmonics—a route to nanoscale optical devices. *Advanced Materials*, 13(19):1501–1505, 2001.

[26] Stefan A. Maier, Pieter G. Kik, Harry A. Atwater, Sheffer Meltzer, Elad Harel, Bruce E. Koel, and Ari A. G. Requicha. Local detection of electromagnetic energy transport below the diffraction limit in metal nanoparticle plasmon waveguides. *Nat Mater*, 2(4):229–232, Apr 2003.

[27] Rashid Zia, Jon A. Schuller, Anu Chandran, and Mark L. Brongersma. Plasmonics: the next chip-scale technology. *Materials Today*, 9(7):20 – 27, 2006.

[28] Harry A. Atwater and Albert Polman. Plasmonics for improved photovoltaic devices. *Nat Mater*, 9(3):205–213, Mar 2010.

[29] Marco Notarianni, Kristy Vernon, Alison Chou, Muhsen Aljada, Jinzhang Liu, and Nunzio Motta. Plasmonic effect of gold nanoparticles in organic solar cells. *Solar Energy*, 106:23 – 37, 2014. Third and Fourth Generation Solar Cells.

[30] Inho Kim, Kyu-Sung Lee, Taek-Sung Lee, Doo Seok Jung, Wook-Seong Lee, Won Mok Kim, and Kyeong-Seok Lee. Size dependence of spherical metal nanoparticles on absorption enhancements of plasmonic organic solar cells. *Synthetic Metals*, 199:174 – 178, 2015.

[31] Vladimir M. Shalaev. Optical negative-index metamaterials. *Nat Photon*, 1(1):41–48, Jan 2007.

[32] Glauco R. Souza, Carly S. Levin, Amin Hajitou, Renata Pasqualini, Wadih Arap, and J. Houston Miller. In vivo detection of gold-imidazole self-assembly complexes: Nir-sers signal reporters. *Analytical Chemistry*, 78(17):6232–6237, 2006. PMID: 16944906.

[33] David L. Jeanmaire and Richard P. Van Duyne. Surface raman spectroelectrochemistry. *Journal of Electroanalytical Chemistry and Interfacial Electrochemistry*, 84(1):1 – 20, 1977.

[34] Martin Moskovits and Dae Hong Jeong. Engineering nanostructures for giant optical fields. *Chemical Physics Letters*, 397(1):91 – 95, 2004.

[35] Amanda J. Haes and Richard P. Van Duyne. A unified view of propagating and localized surface plasmon resonance biosensors. *Analytical and Bioanalytical Chemistry*, 379(7):920–930, Aug 2004.

[36] J.H. Liao, C. L. Nehl, and J. H. Hafner. Biomedical applications of plasmon resonant metal nanoparticles. *Nanomedicine*, 1(2):201–208, 2006. PMID: 17716109.

[37] Yue Bing Zheng, Linlin Jensen, Wei Yan, Thomas R. Walker, Bala Krishna Juluri, Lasse Jensen, and Tony Jun Huang. Chemically tuning the localized surface plasmon resonances of gold nanostructure arrays. *The Journal of Physical Chemistry C*, 113(17):7019–7024, 2009.

[38] M. Haruta, N. Yamada, T. Kobayashi, and S. Iijima. Gold catalysts prepared by coprecipitation for low-temperature oxidation of hydrogen and of carbon monoxide. *Journal of Catalysis*, 115(2):301 – 309, 1989.

[39] Masatake Haruta and Masakazu Daté. Advances in the catalysis of au nanoparticles. *Applied Catalysis A: General*, 222(1):427 – 437, 2001. Celebration Issue.

[40] Richard M. Crooks, Mingqi Zhao, Li Sun, Victor Chechik, and Lee K. Yeung. Dendrimer-encapsulated metal nanoparticles: synthesis, characterization, and applications to catalysis. *Accounts of Chemical Research*, 34(3):181–190, 2001. PMID: 11263876.

[41] Masatake Haruta. When gold is not noble: Catalysis by nanoparticles. *The Chemical Record*, 3(2):75–87, 2003.

[42] M. Valden, X. Lai, and D. W. Goodman. Onset of catalytic activity of gold clusters on titania with the appearance of nonmetallic properties. *Science*, 281(5383):1647–1650, 1998.

[43] M. S. Chen and D. W. Goodman. The structure of catalytically active gold on titania. *Science*, 306(5694):252–255, 2004.

[44] I. Langmuir. Oscillations in ionized gases. *Proceedings of the National Academy of Science*, 14:627–637, August 1928.

[45] Lewi Tonks and Irving Langmuir. Oscillations in ionized gases. *Phys. Rev.*, 33:195–210, Feb 1929.

[46] L. Tonks. Plasma-electron resonance, plasma resonance and plasma shape. *Phys. Rev.*, 38:1219–1223, Sep 1931.

[47] P. Drude. Zur elektronentheorie der metalle. *Annalen der Physik*, 306(3):566–613, 1900.

[48] Gerhard Ruthemann. Elektronenbremsung an röntgenniveaus. *Die Naturwissenschaften*, 30(9):145–145, Feb 1942.

[49] Erik Rudberg. Inelastic scattering of electrons from solids. *Phys. Rev.*, 50:138–150, Jul 1936.

[50] W. Lang. *Optik*, 3:233, 1948.

[51] David Pines and David Bohm. A collective description of electron interactions: Ii. collective vs individual particle aspects of the interactions. *Phys. Rev.*, 85:338–353, Jan 1952.

[52] David Bohm and David Pines. A collective description of electron interactions: Iii. coulomb interactions in a degenerate electron gas. *Phys. Rev.*, 92:609–625, Nov 1953.

[53] David Pines. A collective description of electron interactions: Iv. electron interaction in metals. *Phys. Rev.*, 92:626–636, Nov 1953.

[54] D. Pines. Collective energy losses in solids. *Rev. Mod. Phys.*, 28:184–198, Jul 1956.

[55] R. H. Ritchie. Plasma losses by fast electrons in thin films. *Phys. Rev.*, 106:874–881, Jun 1957.

[56] C. J. Powell and J. B. Swan. Origin of the characteristic electron energy losses in aluminum. *Phys. Rev.*, 115:869–875, Aug 1959.

[57] E. A. Stern and R. A. Ferrell. Surface plasma oscillations of a degenerate electron gas. *Phys. Rev.*, 120:130–136, Oct 1960.

[58] Richard A. Ferrell. Predicted radiation of plasma oscillations in metal films. *Phys. Rev.*, 111:1214–1222, Sep 1958.

[59] R. W. Brown, P. Wessel, and E. P. Trounson. Plasmon reradiation from silver films. *Phys. Rev. Lett.*, 5:472–473, Nov 1960.

[60] E. T. Arakawa, R. J. Herickhoff, and R. D. Birkhoff. Detection of plasma radiation from electron-bombarded al and mg foils. *Phys. Rev. Lett.*, 12:319–320, Mar 1964.

[61] J. F. Donohue and E. Y. Wang. Observation of radiative surface plasmons in metal-oxide-metal tunnel junctions. *Journal of Applied Physics*, 59(9):3137–3143, 1986.

[62] Ye-Yung Teng and Edward A. Stern. Plasma radiation from metal grating surfaces. *Phys. Rev. Lett.*, 19:511–514, Aug 1967.

[63] H. Kanazawa. On the plasma oscillations in metal foils. *Progress of Theoretical Physics*, 26(6):851, 1961.

[64] R. H. Ritchie. On surface plasma oscillations in metal foils. *Progress of Theoretical Physics*, 29(4):607, 1963.

[65] F. Bloch. Bremsvermögen von atomen mit mehreren elektronen. *Zeitschrift für Physik*, 81(5):363–376, 1933.

[66] D. E. Beck. Quantum-mechanical random-phase-approximation calculation of the surface-plasmon dispersion relation for a semi-infinite electron gas. *Phys. Rev. B*, 4:1555–1560, Sep 1971.

[67] U. Kreibig and M. Voller. *Optical Properties of Metal Clusters*. Springer-Verlag Berlin Heidelberg, 1995.

[68] L. P. Gor'kov and G. M. Éliashberg. Minute metallic particles in an electromagnetic field. *Zh. Eksp. Teor. Fiz.*, 48:1407, Dec 1964.

[69] F Fujimoto and K-ich. Komaki. Plasma oscillations excited by a fast electron in a metallic particle. *Journal of the Physical Society of Japan*, 25(6):1679–1687, 1968.

[70] U. Kreibig and Peter Zacharias. Surface plasma resonances in small spherical silver and gold particles. *Zeitschrift für Physik A Hadrons and nuclei*, 231(2):128–143, Apr 1970.

[71] John T. Foley and D.N. Pattanayak. Electromagnetic scattering from a spatially dispersive sphere. *Optics Communications*, 12(2):113 – 117, 1974.

[72] G. S. Agarwal, D. N. Pattanayak, and E. Wolf. Structure of electromagnetic fields in spatially dispersive media of arbitrary geometry. *Phys. Rev. B*, 11:1342–1351, Feb 1975.

[73] R. Ruppin. Optical properties of small metal spheres. *Phys. Rev. B*, 11:2871–2876, Apr 1975.

[74] R. Ruppin. Plasmon frequencies of small metal spheres. *Journal of Physics and Chemistry of Solids*, 39(3):233 – 237, 1978.

[75] Basab B. Dasgupta and Ronald Fuchs. Polarizability of a small sphere including nonlocal effects. *Phys. Rev. B*, 24:554–561, Jul 1981.

[76] Francisco Claro and Ronald Fuchs. Optical absorption by clusters of small metallic spheres. *Phys. Rev. B*, 33:7956–7960, Jun 1986.

[77] E J Austin and M Wilkinson. Electric dipole absorption by ballistic electrons in small metal spheres. *Journal of Physics: Condensed Matter*, 5(44):8461, 1993.

[78] S. Olszewski. Long-wavelength absorption in small metallic spheres. *physica status solidi (b)*, 178(1):247–256, 1993.

[79] W. D. Knight, Keith Clemenger, Walt A. de Heer, Winston A. Saunders, M. Y. Chou, and Marvin L. Cohen. Electronic shell structure and abundances of sodium clusters. *Phys. Rev. Lett.*, 52:2141–2143, Jun 1984.

[80] W. Ekardt. Dynamical polarizability of small metal particles: Self-consistent spherical jellium background model. *Phys. Rev. Lett.*, 52:1925–1928, May 1984.

[81] C. Yannouleas, E. Vigezzi, and R. A. Broglia. Evolution of the optical properties of alkali-metal microclusters towards the bulk: The matrix random-phase-approximation description. *Phys. Rev. B*, 47:9849–9861, Apr 1993.

[82] Matthias Brack. The physics of simple metal clusters: self-consistent jellium model and semiclassical approaches. *Rev. Mod. Phys.*, 65:677–732, Jul 1993.

[83] M. Madjet, C. Guet, and W. R. Johnson. Comparative study of exchange-correlation effects on the electronic and optical properties of alkali-metal clusters. *Phys. Rev. A*, 51:1327–1339, Feb 1995.

[84] J. Lermé, B. Palpant, E. Cottancin, M. Pellarin, B. Prével, J. L. Vialle, and M. Broyer. Quantum extension of mie's theory in the dipolar approximation. *Phys. Rev. B*, 60:16151–16156, Dec 1999.

[85] J. Lermé. Introduction of quantum finite-size effects in the mie's theory for a multilayered metal sphere in the dipolar approximation: Application to free and matrix-embedded noble metal clusters. *The European Physical Journal D - Atomic, Molecular, Optical and Plasma Physics*, 10(2):265–277, Apr 2000.

[86] John L. Persson, Robert L. Whetten, Hai-Ping Cheng, and R.Stephen Berry. Evidence for quantized electronic level structure for 100–1300 electrons in metal-atomic clusters. *Chemical Physics Letters*, 186(2):215 – 222, 1991.

[87] S. Link, M. B. Mohamed, and M. A. El-Sayed. Simulation of the optical absorption spectra of gold nanorods as a function of their aspect ratio and the effect of the medium dielectric constant. *The Journal of Physical Chemistry B*, 103(16):3073–3077, 1999.

[88] Stefan A. Maier and Harry A. Atwater. Plasmonics: Localization and guiding of electromagnetic energy in metal/dielectric structures. *Journal of Applied Physics*, 98(1):011101, 2005.

[89] Prashant K. Jain, Xiaohua Huang, Ivan H. El-Sayed, and Mostafa A. El-Sayed. Review of some interesting surface plasmon resonance-enhanced properties of noble metal nanoparticles and their applications to biosystems. *Plasmonics*, 2(3):107–118, Sep 2007.

[90] P. K. Jain, S. Eustis, and M. A. El-Sayed. Plasmon coupling in nanorod assemblies: Optical absorption, discrete dipole approximation simulation, and exciton-coupling model. *The Journal of Physical Chemistry B*, 110(37):18243–18253, 2006. PMID: 16970442.

[91] K.-S. Lee and M. A. El-Sayed. Gold and silver nanoparticles in sensing and imaging: Sensitivity of plasmon response to size, shape, and metal composition. *The Journal of Physical Chemistry B*, 110(39):19220–19225, 2006. PMID: 17004772.

[92] M. Harb, F. Rabilloud, D. Simon, A. Rydlo, S. Lecoultre, F. Conus, V. Rodrigues, and C. Félix. Optical absorption of small silver clusters: Agn, (n=4–22). *The Journal of Chemical Physics*, 129(19):194108, 2008.

[93] V. Bonačić-Koutecky, J Pittner, M. Boiron, and P. Fantucci. An accurate relativistic effective core potential for excited states of ag atom: An application for studying the absorption spectra of agn and agn+ clusters. *The Journal of Chemical Physics*, 110(8):3876–3886, 1999.

[94] V. Bonačić-Koutecky, V Veyret, and R Mitrić. Ab initio study of the absorption spectra of agn (n=5–8) clusters. *The Journal of Chemical Physics*, 115(22):10450–10460, 2001.

[95] U. Kreibig and L. Genzel. Optical absorption of small metallic particles. *Surface Science*, 156:678 – 700, 1985.

[96] Y. Borensztein, P. De Andrès, R. Monreal, T. Lopez-Rios, and F. Flores. Blue shift of the dipolar plasma resonance in small silver particles on an alumina surface. *Phys. Rev. B*, 33:2828–2830, Feb 1986.

[97] W. Harbich, S. Fedrigo, and J. Buttet. The optical absorption spectra of small silver clusters (n=5–11) embedded in argon matrices. *Chemical Physics Letters*, 195(5):613 – 617, 1992.

[98] Josef Tiggesbäumker, Lars Köller, Karl-Heinz Meiwes-Broer, and Ansgar Liebsch. Blue shift of the mie plasma frequency in ag clusters and particles. *Phys. Rev. A*, 48:R1749–R1752, Sep 1993.

[99] Walt A. de Heer, Kathy Selby, Vitaly Kresin, Jun Masui, Michael Vollmer, A. Chatelain, and W. D. Knight. Collective dipole oscillations in small sodium clusters. *Phys. Rev. Lett.*, 59:1805–1808, Oct 1987.

[100] C. Bréchignac, Ph. Cahuzac, F. Carlier, and J. Leygnier. Collective excitation in closed-shell potassium cluster ions. *Chemical Physics Letters*, 164(4):433 – 437, 1989.

[101] A. Liebsch. Surface-plasmon dispersion and size dependence of mie resonance: Silver versus simple metals. *Phys. Rev. B*, 48:11317–11328, Oct 1993.

[102] H.-Ch. Weissker and C. Mottet. Optical properties of pure and core-shell noble-metal nanoclusters from tddft: The influence of the atomic structure. *Phys. Rev. B*, 84:165443, Oct 2011.

[103] Xochitl López-Lozano, C. Mottet, and H.-Ch. Weissker. Effect of alloying on the optical properties of ag/au nanoparticles. *The Journal of Physical Chemistry C*, 117(6):3062–3068, 2013.

[104] Xóchitl López-Lózano, Hector Barron, Christine Mottet, and Hans-Christian Weissker. Aspect-ratio- and size-dependent emergence of the surface-plasmon resonance in gold nanorods - an ab initio tddft study. *Phys. Chem. Chem. Phys.*, 16:1820–1823, 2014.

[105] B.G. de Boer and G.D. Stein. Production and electron diffraction studies of silver metal clusters in the gas phase. *Surface Science*, 106(1):84 – 94, 1981.

[106] Tobias Lunskens, Philipp Heister, Martin Thamer, Constantin A. Walenta, Aras Kartouzian, and Ulrich Heiz. Plasmons in supported size-selected silver nanoclusters. *Phys. Chem. Chem. Phys.*, 17:17541–17544, 2015.

[107] Liana D. Socaciu, Jan Hagen, Ueli Heiz, Thorsten M. Bernhardt, Thomas Leisner, and Ludger Wöste. Reaction mechanism for the oxidation of free silver dimers. *Chemical Physics Letters*, 340(3):282 – 288, 2001.

[108] S. Fedrigo, W. Harbich, and J. Buttet. Collective dipole oscillations in small silver clusters embedded in rare-gas matrices. *Phys. Rev. B*, 47:10706–10715, Apr 1993.

[109] Rongchao Jin, Chenjie Zeng, Meng Zhou, and Yuxiang Chen. Atomically precise colloidal metal nanoclusters and nanoparticles: Fundamentals and opportunities. *Chemical Reviews*, 116(18):10346–10413, 2016. PMID: 27585252.

[110] Chanaka Kumara and Amala Dass. (auag)144(sr)60 alloy nanomolecules. *Nanoscale*, 3:3064–3067, 2011.

[111] Giovanni Barcaro, Luca Sementa, Alessandro Fortunelli, and Mauro Stener. Comment on "(au-ag)144(sr)60 alloy nanomolecules" by c. kumara and a. dass, nanoscale, 2011, 3, 3064. *Nanoscale*, pages –, 2014.

[112] Ryo Takahata, Seiji Yamazoe, Kiichirou Koyasu, and Tatsuya Tsukuda. Surface plasmon resonance in gold ultrathin nanorods and nanowires. *Journal of the American Chemical Society*, 136(24):8489–8491, 2014. PMID: 24901286.

[113] Ryo Takahata, Seiji Yamazoe, Chompunuch Warakulwit, Jumras Limtrakul, and Tatsuya Tsukuda. Rayleigh instability and surfactant-mediated stabilization of ultrathin gold nanorods. *The Journal of Physical Chemistry C*, 120(30):17006–17010, 2016.

[114] H.-Ch. Weissker, O. Lopez-Acevedo, R. L. Whetten, and X. López-Lozano. Optical spectra of the special au144 gold-cluster compounds: Sensitivity to structure and symmetry. *The Journal of Physical Chemistry C*, 119(20):11250–11259, 2015.

[115] Rongchao Jin. Quantum sized, thiolate-protected gold nanoclusters. *Nanoscale*, 2:343–362, 2010.

[116] Walt A. de Heer. The physics of simple metal clusters: experimental aspects and simple models. *Rev. Mod. Phys.*, 65:611–676, Jul 1993.

[117] H. Ch Weissker, H. Barron Escobar, V. D. Thanthirige, K. Kwak, D. Lee, G. Ramakrishna, R. L. Whetten, and X. López-Lozano. Information on quantum states pervades the visible spectrum of the ubiquitous au144(sr)60 gold nanocluster. 5:3785 EP –, Apr 2014. Article.

[118] D.C. Marinica, A.K. Kazansky, P. Nordlander, J. Aizpurua, and A. G. Borisov. Quantum plasmonics: Nonlinear effects in the field enhancement of a plasmonic nanoparticle dimer. *Nano Letters*, 12(3):1333–1339, 2012. PMID: 22320125.

[119] Lorenzo Stella, Pu Zhang, F. J. García-Vidal, Angel Rubio, and P. García-González. Performance of nonlocal optics when applied to plasmonic nanostructures. *The Journal of Physical Chemistry C*, 117(17):8941–8949, 2013.

[120] M. Barbry, P. Koval, F. Marchesin, R. Esteban, A. G. Borisov, J. Aizpurua, and D. Sánchez-Portal. Atomistic near-field nanoplasmonics: Reaching atomic-scale resolution in nanooptics. *Nano Letters*, 15(5):3410–3419, 2015. PMID: 25915173.

[121] Hans-Christian Weissker and Xochitl Lopez-Lozano. Surface plasmons in quantum-sized noble-metal clusters: Tddft quantum calculations and the classical picture of charge oscillations. *Phys. Chem. Chem. Phys.*, 17:28379–28386, 2015.

[122] Varas Alejandro, García-González Pablo, Feist Johannes, García-Vidal F.J., and Rubio Angel. *nanoph*, volume 5, chapter Quantum plasmonics: from jellium models to ab initio calculations, page 409. 2017 2016. 3.

[123] P. E. Blöchl. Projector augmented-wave method. *Phys. Rev. B*, 50:17953–17979, Dec 1994.

[124] Arto Sakko, Tuomas P. Rossi, Jussi Enkovaara, and Risto M. Nieminen. Atomistic approach for simulating plasmons in nanostructures. *Applied Physics A*, 115(2):427–431, May 2014.

[125] M. Kuisma, A. Sakko, T. P. Rossi, A. H. Larsen, J. Enkovaara, L. Lehtovaara, and T. T. Rantala. Localized surface plasmon resonance in silver nanoparticles: Atomistic first-principles time-dependent density-functional theory calculations. *Phys. Rev. B*, 91:115431, Mar 2015.

[126] Yuichi Negishi, Tafu Nakazaki, Sami Malola, Shinjiro Takano, Yoshiki Niihori, Wataru Kurashige, Seiji Yamazoe, Tatsuya Tsukuda, and Hannu Häkkinen. A critical size for emergence of nonbulk electronic and geometric structures in dodecanethiolate-protected au clusters. *Journal of the American Chemical Society*, 137(3):1206–1212, 2015. PMID: 25549276.

[127] Ruben Esteban, Andrei G. Borisov, Peter Nordlander, and Javier Aizpurua. Bridging quantum and classical plasmonics with a quantum-corrected model. 3:825 EP –, May 2012. Article.

[128] Tianyu Dong, Xikui Ma, and Raj Mittra. Optical response in subnanometer gaps due to nonlocal response and quantum tunneling. *Applied Physics Letters*, 101(23):233111, 2012.

[129] Thomas Christensen, Wei Yan, Antti-Pekka Jauho, Marin Soljačić, and N. Asger Mortensen. Quantum corrections in nanoplasmonics: Shape, scale, and material. *Phys. Rev. Lett.*, 118:157402, Apr 2017.

[130] Giuseppe Toscano, Jakob Straubel, Alexander Kwiatkowski, Carsten Rockstuhl, Ferdinand Evers, Hongxing Xu, N. Asger Mortensen, and Martijn Wubs. Resonance shifts and spill-out effects in self-consistent hydrodynamic nanoplasmonics. 6:7132 EP –, May 2015. Article.

[131] Wei Yan. Hydrodynamic theory for quantum plasmonics: Linear-response dynamics of the inhomogeneous electron gas. *Phys. Rev. B*, 91:115416, Mar 2015.

[132] Richard A. Davison, Luca V. Delacrétaz, Blaise Goutéraux, and Sean A. Hartnoll. Erratum: Hydrodynamic theory of quantum fluctuating superconductivity [phys. rev. b 94, 054502 (2016)]. *Phys. Rev. B*, 96:059902, Aug 2017.

[133] Shu Fen Tan, Lin Wu, Joel K.W. Yang, Ping Bai, Michel Bosman, and Christian A. Nijhuis. Quantum plasmon resonances controlled by molecular tunnel junctions. *Science*, 343(6178):1496–1499, 2014.

[134] Peter Nordlander. Molecular tuning of quantum plasmon resonances. *Science*, 343(6178):1444–1445, 2014.

[135] E. Prodan, C. Radloff, N. J. Halas, and P. Nordlander. A hybridization model for the plasmon response of complex nanostructures. *Science*, 302(5644):419–422, 2003.

[136] Stefan A. Maier. *Plasmonic: Fundamentals and Applications*. Springer US, 2007.

[137] John D. Jackson. *Classical Electrodynamics*. John Wiley & Sons, Inc., New York, NY, 3 edition, 1999.

[138] Craig F. Bohren and Donald R. Huffman. *Absorption and scattering of light by small particles*. John Wiley & Sons, Inc., New York, NY, 1 edition, 1983.

[139] P. B. Johnson and R. W. Christy. Optical constants of the noble metals. *Phys. Rev. B*, 6:4370–4379, Dec 1972.

[140] Aleksandar D. Rakić, Aleksandra B. Djurišić, Jovan M. Elazar, and Marian L. Majewski. Optical properties of metallic films for vertical-cavity optoelectronic devices. *Appl. Opt.*, 37(22):5271–5283, Aug 1998.

[141] R. Brendel and D. Bormann. An infrared dielectric function model for amorphous solids. *Journal of Applied Physics*, 71(1):1–6, 1992.

[142] S. C. Ying. Hydrodynamic response of inhomogeneous metallic systems. *Il Nuovo Cimento B (1971-1996)*, 23(1):270–281, Sep 1974.

[143] Adolfo Eguiluz and J. J. Quinn. Hydrodynamic model for surface plasmons in metals and degenerate semiconductors. *Phys. Rev. B*, 14:1347–1361, Aug 1976.

[144] Cristian Ciracì, John B. Pendry, and David R. Smith. Hydrodynamic model for plasmonics: A macroscopic approach to a microscopic problem. *ChemPhysChem*, 14(6):1109–1116, 2013.

[145] A. Moreau, C. Ciracì, and D. R. Smith. Impact of nonlocal response on metallodielectric multilayers and optical patch antennas. *Phys. Rev. B*, 87:045401, Jan 2013.

[146] Y. Luo, A. I. Fernandez-Dominguez, A. Wiener, Stefan A. Maier, and J. B. Pendry. Surface plasmons and nonlocality: A simple model. *Phys. Rev. Lett.*, 111:093901, Aug 2013.

[147] P. Halevi and R. Fuchs. Generalised additional boundary condition for non-local dielectrics. i. reflectivity. *Journal of Physics C: Solid State Physics*, 17(21):3869, 1984.

[148] P. Halevi and R. Fuchs. Generalised additional boundary condition for non-local dielectrics. ii. surface polaritons. *Journal of Physics C: Solid State Physics*, 17(21):3889, 1984.

[149] Søren Raza, Giuseppe Toscano, Antti-Pekka Jauho, Martijn Wubs, and N. Asger Mortensen. Unusual resonances in nanoplasmonic structures due to nonlocal response. *Phys. Rev. B*, 84:121412, Sep 2011.

[150] Søren Raza, Sergey I Bozhevolnyi, Martijn Wubs, and N Asger Mortensen. Nonlocal optical response in metallic nanostructures. *Journal of Physics: Condensed Matter*, 27(18):183204, 2015.

[151] Andreas Trügler, Ulrich Hohenester, and F. Javier García de Abajo. Plasmonics simulations including nonlocal effects using a boundary element method approach. *International Journal of Modern Physics B*, 31(24):1740007, 2017.

[152] Cristian Ciracì. Current-dependent potential for nonlocal absorption in quantum hydrodynamic theory. *Phys. Rev. B*, 95:245434, Jun 2017.

[153] P. Hohenberg and W. Kohn. Inhomogeneous electron gas. *Phys. Rev.*, 136:B864–B871, Nov 1964.

[154] W. Kohn and L. J. Sham. Self-consistent equations including exchange and correlation effects. *Phys. Rev.*, 140:A1133–A1138, Nov 1965.

[155] C.-O. Almbladh and U. von Barth. Exact results for the charge and spin densities, exchange-correlation potentials, and density-functional eigenvalues. *Phys. Rev. B*, 31:3231–3244, Mar 1985.

[156] R. M. Dreizler and E. K. U. Gross. *Quantum Theory of The Electron Liquid*. Cambridge university Press, 2005.

[157] R. O. Jones and O. Gunnarsson. The density functional formalism, its applications and prospects. *Rev. Mod. Phys.*, 61:689–746, Jul 1989.

[158] R. M. Dreizler and E. K. U. Gross. *Density Functional Theory*. Springer Berlin Heidelberg, 1990.

[159] John P. Perdew, Kieron Burke, and Matthias Ernzerhof. Generalized gradient approximation made simple. *Phys. Rev. Lett.*, 77:3865–3868, Oct 1996.

[160] J. P. Perdew, K. Burke, and M. Ernzerhof. Erratum: Generalized gradient approximation made simple [phys. rev. lett. 77, 3865 (1996)]. *Phys. Rev. Lett.*, 78:1396–1396, Feb 1997.

[161] A. D. Becke. Density-functional exchange-energy approximation with correct asymptotic behavior. *Phys. Rev. A*, 38:3098–3100, Sep 1988.

[162] C. Lee, W. Yang, and R. G. Parr. Development of the colle-salvetti correlation-energy formula into a functional of the electron density. *Phys. Rev. B*, 37:785–789, Jan 1988.

[163] R. van Leeuwen and E. J. Baerends. Exchange-correlation potential with correct asymptotic behavior. *Phys. Rev. A*, 49:2421–2431, Apr 1994.

[164] John P. Perdew, Stefan Kurth, Ale š Zupan, and Peter Blaha. Accurate density functional with correct formal properties: A step beyond the generalized gradient approximation. *Phys. Rev. Lett.*, 82:2544–2547, Mar 1999.

[165] P. J. Stephens, F. J. Devlin, C. F. Chabalowski, and M. J. Frisch. Ab initio calculation of vibrational absorption and circular dichroism spectra using density functional force fields. *The Journal of Physical Chemistry*, 98(45):11623–11627, 1994.

[166] Joachim Paier, Martijn Marsman, and Georg Kresse. Why does the b3lyp hybrid functional fail for metals? *The Journal of Chemical Physics*, 127(2):024103, 2007.

[167] Roi Baer, Ester Livshits, and Ulrike Salzner. Tuned range-separated hybrids in density functional theory. *Annual Review of Physical Chemistry*, 61(1):85–109, 2010. PMID: 20055678.

[168] H. Ikura, T. Tsuneda, T. Yanai, and K. Hirao. A long-range correction scheme for generalized-gradient-approximation exchange functionals. *J. Chem. Phys.*, 115:3540–3544, 2001.

[169] Yan Zhao and Donald G. Truhlar. A new local density functional for main-group thermochemistry, transition metal bonding, thermochemical kinetics, and noncovalent interactions. *J. Chem. Phys.*, 125(19):194101, 2006.

[170] J. P. Perdew and Alex Zunger. Self-interaction correction to density-functional approximations for many-electron systems. *Phys. Rev. B*, 23:5048–5079, May 1981.

[171] David Vanderbilt. Soft self-consistent pseudopotentials in a generalized eigenvalue formalism. *Phys. Rev. B*, 41:7892–7895, Apr 1990.

[172] P. E. Blöchl. Projector augmented-wave method. *Phys. Rev. B*, 50:17953–17979, Dec 1994.

[173] G. Kresse and D. Joubert. From ultrasoft pseudopotentials to the projector augmented-wave method. *Phys. Rev. B*, 59:1758–1775, Jan 1999.

[174] Walter A. Harrison. *Pseudopotentials in the theory of metals*. 1966.

[175] Marvin L. Cohen. Predicting new solids and superconductors. *Science*, 234(4776):549–553, 1986.

[176] N. Troullier and José Luís Martins. Efficient pseudopotentials for plane-wave calculations. *Phys. Rev. B*, 43:1993–2006, Jan 1991.

[177] Erich Runge and E. K. U. Gross. Density-functional theory for time-dependent systems. *Phys. Rev. Lett.*, 52:997–1000, Mar 1984.

[178] Bu-Xing Xu and A. K. Rajagopal. Current-density-functional theory for time-dependent systems. *Phys. Rev. A*, 31:2682–2684, Apr 1985.

[179] Asish K. Dhara and Swapan K. Ghosh. Density-functional theory for time-dependent systems. *Phys. Rev. A*, 35:442–444, Jan 1987.

[180] Robert van Leeuwen. Mapping from densities to potentials in time-dependent density-functional theory. *Phys. Rev. Lett.*, 82:3863–3866, May 1999.

[181] C. A. Ullrich. *Time–dependent Density–Functional Theory*. Oxford University Press, 2012.

[182] Mark E. Casida. *In Recent Developments and Applications of Modern Density Functional Theory (ed. J. M. Seminario)*, volume 4. Elsevier, Amsterdam, 1996.

[183] K. Yabana and G. F. Bertsch. Time-dependent local-density approximation in real time. *Phys. Rev. B*, 54:4484–4487, Aug 1996.

[184] K. Yabana, T. Nakatsukasa, J.-I. Iwata, and G. F. Bertsch. Real-time, real-space implementation of the linear response time-dependent density-functional theory. *physica status solidi (b)*, 243(5):1121–1138, 2006.

[185] Emily Townsend and Garnett W. Bryant. Plasmonic properties of metallic nanoparticles: The effects of size quantization. *Nano Letters*, 12(1):429–434, 2012. PMID: 22181554.

[186] Miguel A.L. Marques, Alberto Castro, George F. Bertsch, and Angel Rubio. octopus a first-principles tool for excited electron–ion dynamics. *Computer Physics Communications*, 151(1):60 – 78, 2003.

[187] Alberto Castro, Miguel A. L. Marques, and Angel Rubio. Propagators for the time-dependent kohn–sham equations. *The Journal of Chemical Physics*, 121(8):3425–3433, 2004.

[188] E. Cottancin, G. Celep, J. Lermé, M. Pellarin, J. Huntzinger, J. Vialle, and M. Broyer. Optical properties of noble metal clusters as a function of the size: Comparison between experiments and a semi-quantal theory. *Theoretical Chemistry Accounts: Theory, Computation, and Modeling (Theoretica Chimica Acta)*, 116:514, 2006.

[189] C. Ciracì, R. T. Hill, J. J. Mock, Y. Urzhumov, A. I. Fernández-Domínguez, S. A. Maier, J. B. Pendry, A. Chilkoti, and D. R. Smith. Probing the ultimate limits of plasmonic enhancement. *Science*, 337(6098):1072–1074, 2012.

[190] Peter J. Feibelman. Surface electromagnetic fields. *Progress in Surface Science*, 12(4):287 – 407, 1982.

[191] Xochitl López-Lozano, Hector Barron, Christine Mottet, and Hans-Christian Weissker. Aspect-ratio and size-dependent emergence of the surface-plasmon resonance in gold nanorods - an ab initio tddft study. *Phys. Chem. Chem. Phys.*, 16:1820–1823, 2014.

[192] Emilie B. Guidez and Christine M. Aikens. Diameter dependence of the excitation spectra of silver and gold nanorods. *The Journal of Physical Chemistry C*, 117(23):12325–12336, 2013.

[193] A. E DePrince III, M. Pelton, J. R. Guest, and S. K. Gray. Emergence of Excited-State Plasmon Modes in Linear Hydrogen Chains from Time-Dependent Quantum Mechanical Methods. *Phys. Rev. Lett.*, 107:196806, 2011.

[194] R. Zhang, Y. Zhang, Z. C. Dong, S. Jiang, C. Zhang, L. G. Chen, L. Zhang, Y. Liao, J. Aizpurua, Y. Luo, J. L. Yang, and J. G. Hou. Chemical mapping of a single molecule by plasmon-enhanced raman scattering. *Nature*, 498:82–86, 2013.

[195] S Gao and Z Yuan. Emergence of collective plasmon excitation in a confined one-dimensional electron gas. *Phys. Rev. B*, 72:121406, 2005.

[196] J. Yan and S. Gao. Plasmon resonances in linear atomic chains: Free-electron behavior and anisotropic screening of d electrons. *Physical Review B*, 78:235413, 2008.

[197] S Bernadotte, F Evers, and C R Jacob. Plasmons in molecules. *J. Phys. Chem. C*, 117:1863–1878, 2013.

[198] R. Wu, Y Yu, H. Xue, H. Hu, and Q. Liu. Dipole and quadrupole plasmon in confined quasi-one dimensional electron gas systems. *Physics Letters A*, 378:2995–3000, 2014.

[199] S. D. Sarma and W. Lai. Screening and elementary excitations in narrow-channel semiconductor microstructures. *Phys. Rev. B*, 32:1401–1404, 1985.

[200] G. Onida, L. Reining, and A. Rubio. Electronic excitations: Density-functional versus many-body green's-function approaches. *Rev. Mod. Phys.*, 74:601, 2002.

[201] M. A. L. Marques, N. T. Maitra, F. M. S. Nogueira, E. K. U. Gross, and A. Rubio, editors. *Fundamentals of Time-Dependent Density Functional Theory*. Springer, Berlin, 2012.

[202] A. Varas, P. García-González, J. Feist, F. J. García-Vidal, and A. Rubio. Quantum plasmonics: from jellium models to ab initio calculations. *Nanophotonics*, 5:409, 2016.

[203] F. Rabilloud. Description of plasmon-like band in silver clusters: The importance of the long-range hartree-fock exchange in time-dependent density-functional theory simulations. *J. Chem. Phys.*, 141:144302, 2014.

[204] Alberto Castro, Heiko Appel, Micael Oliveira, Carlo A. Rozzi, Xavier Andrade, Florian Lorenzen, M. A. L. Marques, E. K. U. Gross, and Angel Rubio. octopus: a tool for the application of time-dependent density functional theory. *physica status solidi (b)*, 243(11):2465–2488, 2006.

[205] Lina G. AbdulHalim, Megalamane S. Bootharaju, Qing Tang, Silvano Del Gobbo, Rasha G. AbdulHalim, Mohamed Eddaoudi, De-en Jiang, and Osman M. Bakr. Ag29(bdt)12(tpp)4: A tetravalent nanocluster. *Journal of the American Chemical Society*, 137(37):11970–11975, 2015. PMID: 26104755.

[206] Indranath Chakraborty, Jayanthi Erusappan, Anuradha Govindarajan, K. S. Sugi, Thumu Udayabhaskararao, Atanu Ghosh, and Thalappil Pradeep. Emergence of metallicity in silver clusters in the 150 atom regime: a study of differently sized silver clusters. *Nanoscale*, 6:8024–8031, 2014.

[207] S. Fedrigo, W. Harbich, and J. Buttet. Collective dipole oscillations in small silver clusters embedded in rare-gas matrices. *Phys. Rev. B*, 47:10706–10715, 1993.

[208] Sami Malola, Lauri Lehtovaara, Jussi Enkovaara, and Hannu Häkkinen. Birth of the localized surface plasmon resonance in monolayer-protected gold nanoclusters. *ACS Nano*, 7(11):10263–10270, 2013.

[209] Huifeng Qian, Yan Zhu, and Rongchao Jin. Atomically precise gold nanocrystal molecules with surface plasmon resonance. *Proceedings of the National Academy of Sciences*, 109(3):696–700, 2012.

[210] H.-Ch. Weissker and C. Mottet. Optical properties of pure and core-shell noble-metal nanoclusters from tddft: The influence of the atomic structure. *Phys. Rev. B*, 84:165443, Oct 2011.

[211] H.-Ch. Weissker, H. Barron Escobar, V. D. Thanthirige, K. Kwak, D. Lee, G. Ramakrishna, R.L. Whetten, , and X. López-Lozano. Information on quantum states pervades the visible spectrum of the ubiquitous au144 gold nanocluster. *Nature Communications*, 5:3785, 2014.

[212] Marcos M. Alvarez, Joseph T. Khoury, T. Gregory Schaaff, Marat N. Shafigullin, Igor Vezmar, and Robert L. Whetten. Optical absorption spectra of nanocrystal gold molecules. *The Journal of Physical Chemistry B*, 101(19):3706–3712, 1997.

[213] Shaowei Chen, Roychelle S. Ingram, Michael J. Hostetler, Jeremy J. Pietron, Royce W. Murray, T. Gregory Schaaff, Joseph T. Khoury, Marcos M. Alvarez, and Robert L. Whetten. Gold nanoelectrodes of varied size: Transition to molecule-like charging. *Science*, 280(5372):2098–2101, 1998.

[214] T. Gregory Schaaff, Marat N. Shafigullin, Joseph T. Khoury, Igor Vezmar, and Robert L. Whetten. Properties of a ubiquitous 29 kda au:sr cluster compound. *The Journal of Physical Chemistry B*, 105(37):8785–8796, 2001.

[215] Nirmalya K. Chaki, Yuichi Negishi, Hironori Tsunoyama, Yukatsu Shichibu, and Tatsuya Tsukuda. Ubiquitous 8 and 29 kda gold:alkanethiolate cluster compounds: Mass-spectrometric determination of molecular formulas and structural implications. *Journal of the American Chemical Society*, 130(27):8608–8610, 2008. PMID: 18547044.

[216] O. Andrea Wong, Christine L. Heinecke, Ashli R. Simone, Robert L. Whetten, and Christopher J. Ackerson. Ligand symmetry-equivalence on thiolate protected gold nanoclusters determined by nmr spectroscopy. *Nanoscale*, 4:4099–4102, 2012.

[217] Daniel Bahena, Nabraj Bhattarai, Ulises Santiago, Alfredo Tlahuice, Arturo Ponce, Stephan B. H. Bach, Bokwon Yoon, Robert L. Whetten, Uzi Landman, and Miguel Jose-Yacaman. Stem electron diffraction and high-resolution images used in the determination of the crystal structure of the au144(sr)60 cluster. *The Journal of Physical Chemistry Letters*, 4(6):975–981, 2013.

[218] Seiji Yamazoe, Shinjiro Takano, Wataru Kurashige, Toshihiko Yokoyama, Kiyofumi Nitta, Yuichi Negishi, and Tatsuya Tsukuda. Hierarchy of bond stiffnesses within icosahedral-based gold clusters protected by thiolates. *Nat. Commun.*, 7:10414, 2016.

[219] Polymorphism in magic-sized Au144(SR)60 clusters. *Nat. Commun.*, 7:11859, 2016.

[220] H.-Ch. Weissker, O. Lopez-Acevedo, R. L. Whetten, and X. López-Lozano. Optical spectra of the special au144 gold-cluster compounds: Sensitivity to structure and symmetry. *The Journal of Physical Chemistry C*, 119(20):11250–11259, 2015.

[221] Sami Malola, Michael J. Hartmann, and Hannu Häkkinen. Copper induces a core plasmon in intermetallic Au(144,145)-xCux(sr)60 nanoclusters. *The Journal of Physical Chemistry Letters*, 6(3):515–520, 2015.

[222] G. Kresse and J. Hafner. Ab initio molecular dynamics for liquid metals. *Phys. Rev. B*, 47:558, 1993.

[223] G. Kresse and J. Furthmüller. Efficiency of ab-initio total energy calculations for metals and semiconductors using a plane-wave basis set. *Comput. Mat. Sci.*, 6:15, 1996.

[224] G. Kresse and D. Joubert. From ultrasoft pseudopotentials to the projector augmented-wave method. *Phys. Rev. B*, 59:1758, 1999.

[225] Olga Lopez-Acevedo, Jaakko Akola, Robert L. Whetten, Henrik Grönbeck, and Hannu Häkkinen. Structure and bonding in the ubiquitous icosahedral metallic gold cluster au144(sr)60. *The Journal of Physical Chemistry C*, 113(13):5035–5038, 2009.

[226] David Pines. *Elementary excitations in solids*. Benjamin, New-York, 1963.

[227] C. Yannouleas, E. Vigezzi, and R. A. Broglia. Evolution of the optical properties of alkali-metal microclusters towards the bulk: The matrix random-phase-approximation description. *Phys. Rev. B*, 47:9849–9861, Apr 1993.

[228] Hans-Christian Weissker and Xochitl Lopez-Lozano. Surface plasmons in quantum-sized noble-metal clusters: Tddft quantum calculations and the classical picture of charge oscillations. *Phys. Chem. Chem. Phys.*, 17:28379–28386, 2015.

[229] Xiaoyang Duan, Simon Kamin, and Na Liu. Dynamic plasmonic colour display. 8:14606 EP –, Feb 2017. Article.

[230] Alexandros Emboras, Jens Niegemann, Ping Ma, Christian Haffner, Andreas Pedersen, Mathieu Luisier, Christian Hafner, Thomas Schimmel, and Juerg Leuthold. Atomic scale plasmonic switch. *Nano Letters*, 16(1):709–714, 2016. PMID: 26670551.

[231] Manzhou Zhu, Christine M. Aikens, Frederick J. Hollander, George C. Schatz, and Rongchao Jin. Correlating the crystal structure of a thiol-protected au25 cluster and optical properties. *Journal of the American Chemical Society*, 130(18):5883–5885, 2008. PMID: 18407639.

[232] Michael W. Heaven, Amala Dass, Peter S. White, Kennedy M. Holt, and Royce W. Murray. Crystal structure of the gold nanoparticle [n(c8h17)4][au25(sch2ch2ph)18]. *Journal of the American Chemical Society*, 130(12):3754–3755, 2008. PMID: 18321116.

[233] Huifeng Qian, William T. Eckenhoff, Yan Zhu, Tomislav Pintauer, and Rongchao Jin. Total structure determination of thiolate-protected au38 nanoparticles. *Journal of the American Chemical Society*, 132(24):8280–8281, 2010. PMID: 20515047.

[234] Paul C. Martin and Julian Schwinger. Theory of many-particle systems. i. *Phys. Rev.*, 115:1342–1373, Sep 1959.

[235] R Ruppin. Extinction properties of thin metallic nanowires. *Optics Communications*, 190(1):205 – 209, 2001.

List of Figures

2.1 Plane-wave illumination on sphere 15
2.2 Ellipsoid 16
2.3 $\varepsilon_{Drude}(\omega)$ vs. Johnson-Christy for gold 18
2.4 SPP schematic representation 20
2.5 Dispersion relation for SPP 21
2.6 SPP as confined dipolar SPP 22
2.7 Dispersion relation for SPP and bulk plasmons 24
2.8 Dispersion relation for spatially dispersive modes 31
2.9 SPP in a metal-dielectric interface 34

3.1 Self-consistent solution of Kohn–sham equation 47
3.2 Pseudopotential and pseudowavefunction 53
3.3 Context of van-Leeuwen theorem 58
3.4 Effect of the Hartree-xc kernel 69
3.5 Time evolution scheme 75

4.1 Optimal geometry corresponding to model pentagonal sub-nanometric rod 82
4.2 Absorption cross section for Ag/Au_{147}Ih 85
4.3 Time dependence of the electric fields of laser excitations at different energies and the corresponding dipole moments for Ag/Au_{147}Ih . . . 88
4.4 Absorption cross section for rods 92
4.5 Dependence of nonlocal blue-shift on aspect ratio and absolute size in classical optics 94
4.6 Absorption cross section for atomic chains 95

4.7 TDDFT absorption cross section per atom (in $\AA^2$) versus frequency and the number of atoms in Au chains. The solid line plots the LSPR frequency under local optics descriptions. The various *ab initio* spectral maxima are given by solid circles (connected to guide the eye): collective plasmon modes in blue and single d-electron excitations in black and red. 98
4.8 LSPR vs AR for elongated systems of Au 100
4.9 LSPR vs AR for different systems of Ag 101
4.10 Spectra for different other systems of Ag 101
4.11 Comparison of spectra calculated in PBE and LC-M06L 103

5.1 Comparison of the cross-section integrated induced charge densities obtained in *ab initio* and electromagnetics approaches for Ag_{145}, Ag_{19}, Ag_{18}, and a $N = 18$ purely one-dimensional system. 109
5.2 Comparison of the cross-section integrated induced charge densities obtained in *ab initio* approaches for Ag_{145}, from a delta-kick simulation (i.e. dynamic) and a electrostatic calculation. 110
5.3 Induced density of Ag_{37} at LSPR: Delta-kick vs QMLE 112
5.4 Different iso-surfaces of induced density of Ag_{37} at LSPR from QMLE simulation 113
5.5 Different iso-surfaces of induced density of Na_{216} from δ-kick RTTDDFT simulation at a maximum of the oscillating dipole moment. 114
5.6 Absorption spectrum of Na_{20} and induced densities at some energies of interest. 117
5.7 Modes of the induced density in Na_{20} at some energies of interest comaped to the results of Bernadotte et. al. [197]. 118
5.8 Absorption spectra of icosahedral Na_{55}^+ calculated in RT-TDDFT and LR-TDDFT, and the spacial regions that contribute to the induced densities at some energies of interest. 119
5.9 Modes of electron-density oscillation in icosahedral Na_{55}^+, reconstructed from the induced densities calculated in RT-TDDFT (lower panel), compared to the transition density obtained from LR-TDDFT, at corresponding energy. 120
5.10 Absorption spectrum of Ag_{37} and regions of space that contribute to the modes of the induced densities at some energies of interest. . . . 121

5.11 Induced density modes of Ag_{37} showing contributions from localized d-electrons. 122
5.12 Induced density of Ag_{37} at LSPR as the mode reconstructed from delta-kick, the induced density from QMLE simulation, and the induced density due to the application of an electrostatic field. 123
5.13 Atomic structure of the $Ag_{29}P_4S_{24}C_{144}H_{108}$ cluster. 124
5.14 Absorption spectra for $Ag_{29}P_4S_{24}C_{144}H_{108}$ cluster and Benzene molecule.125
5.15 Mode of the induced electron density that correspond to the absorption in $Ag_{29}P_4S_{24}C_{144}H_{108}$ cluster at 2.69 eV. 127
5.16 Mode of the induced electron density that correspond to the absorption in $Ag_{29}P_4S_{24}C_{144}H_{108}$ cluster at 6.46 eV. 128

6.1 Structure of the bare 147-atom clusters and the ligand-protected $Au_{144}(SR)_{60}$ clusters. 132
6.2 Absorption spectrum of the bare 147-atom Au icosahedral cluster (thick black line) compared to different Au-Cu alloy clusters, all relaxed using the PBE GGA functional. 134
6.3 Spectra of LDA relaxed bare clusters of $Au_{147-x}Cu_x$ 135
6.4 Different Configurations Of Bimetallic Icosahedral $Au_{147-x}Cu_x$ Studied 136
6.5 Spectra for bare Au_{147} clusters, pure and alloyed with copper, for 250fs evolution time 137
6.6 Change of the absorption spectra of monolayer-protected $Au_{144}(SR)_{60}$ upon alloying with copper. 138
6.7 Spectra of monolayer-protected clusters, with R=CH_3 & R=H, and also for the cases when the structures are relaxed and the spectra are calculated using LDA and PBE. 140
6.8 Effect of the introduction of either a copper or a gold atom into the central vacancy of the pure $Au_{144}(SR)_{60}$ cluster compound 143
6.9 Real and imaginary parts of the dynamical polarizability, $\alpha(\omega)$, for selected bare and ligand-protected clusters. 144
6.10 Induced density following a monochromatic laser excitation at 2.17ėV of the pure-Au 147-atom icosahedral cluster, well after the laser is switched off. 146

B.1 Metal-Dielectric interface 178
B.2 Evanescent SPP 180

D.1 LAM 187
D.2 Schematic representation of the LAM 194

E.1 Jellium description 197

List of Tables

4.1 Geometrical parameters of equivalent compact structures for nanorods 82
4.2 Geometrical parameters of equivalent compact structures for nanorods 83
4.3 Geometrical parameters of equivalent compact structures for atomic chains . . . 84
4.4 Radii of equivalent spheres for icosaderoa . . . 84

Symbols, Physical Constants, and Abbreviations

$\mathbf{a}$	vector $\vec{a}$	
$\hat{\mathbf{a}}$	the unit vector in the direction of vector $\vec{a}$	
$\mathbf{r_j}$	the position vector of the jth particle	
∇_j	The gradiant operator with respect to $\mathbf{r_j}$	
$\hat{\mathbf{a}}$	the unit vector in the direction of vector $\mathbf{a}$	
ω	angular frequency	rad
c	Speed of Light	$2.997\,924\,58 \times 10^{8}\,\mathrm{m\,s^{-1}}$
R.H.S.	right hand side (of the equation)	
L.H.S.	left hand side (of the equation)	
LSPR	Localized Surface Plasmon Rersonance	
QMLE	Quasi-Monochromatic Laser Excitations	
AR	Aspect Ratio	
FWHM	Full Width at Half Maximum (of a spectral feature)	

Publications

- In Search of the Quantum-Electronic Origin of Color Change: Elucidation of the Subtle Effects of Alloying with Copper on ∼1.8 nm Gold Nanoclusters.
  R. Sinha-Roy, Xóchitl López Lozano, R.L. Whetten, P. García González, H.-Ch. Weissker
  J. Phys. Chem. C, **2017**, 121 (10), pp 5753–5760

- Classical and ab Initio Plasmonics Meet at Sub-nanometric Noble Metal Rods.
  R. Sinha Roy, P. García González, H.-Ch. Weissker, F. Rabilloud, A. I. Fernández-Domínguez
  ACS Photonics ***2017**, 4, 1484–1493*

- Realization Of Different Spatial Modes of Electron-Density Oscillation Corresponding to Absorption In Noble-Metal Clusters
  R. Sinha-Roy, P. García González, H.-Ch. Weissker
  To be submitted soon

ACS Photonics

Article

pubs.acs.org/journal/apchd5

Classical and *ab Initio* Plasmonics Meet at Sub-nanometric Noble Metal Rods

Rajarshi Sinha-Roy,*[†,‡,§] Pablo García-González,[‡,§] Hans-Christian Weissker,[†,§] Frank Rabilloud,[¶] and Antonio I. Fernández-Domínguez*[‡]

[†] Aix Marseille University, CNRS, CINaM UMR 7325, 13288, Marseille, France

[‡] Departamento de Física Teórica de la Materia Condensada and Condensed Matter Physics Center (IFIMAC), Universidad Autónoma de Madrid, E-28049 Madrid, Spain

[¶] Université Lyon, Université Claude Bernard Lyon 1, CNRS, Institut Lumière Matière, F-69622, Villeurbanne, France

[§] European Theoretical Spectroscopy Facility (ETSF)

Supporting Information

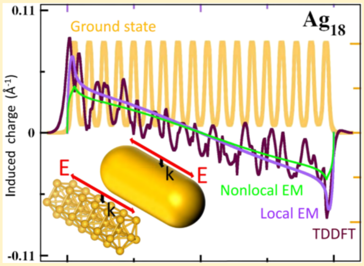

ABSTRACT: Applications of noble metal clusters and nanoparticles in different size ranges abound, from a couple of atoms through mesoscopic sizes. Classical electromagnetics calculations are now employed on smaller and smaller sizes, creating an effervescent dynamic in fields such as plasmonics and approaching the tiny sizes where quantum effects and the atomistic structure of matter play predominant roles. Nonetheless, explicit demonstrations of their merits and limitations are rare. Here we study the optical absorption of subnanometric elongated coinage-metal particles using *ab initio* and classical electromagnetics methods. The comparison between both approaches reveals that the classical plasmonic frequencies are in astonishing agreement with those predicted by *ab initio* theory for atomistic *three-dimensional* rods and *quasi-one-dimensional* chains, as long as collective surface-plasmon resonances lie far below the onset of d-electron excitations. The physical origin of this striking agreement is clarified through the analysis of the resonant induced electron densities and with the aid of model calculations for a purely one-dimensional system of electrons. Furthermore, we show that even when plasmonic/collective and electron−hole excitations are strongly coupled, the classical description accounts rather well for the spectral average of the corresponding quantum hybrid excitations. Our theoretical findings demonstrate that classical optics is surprisingly accurate in describing localized surface plasmon resonances even for angstrom-sized systems, provided the geometrical modeling of the atomistic structures is properly defined.

KEYWORDS: *localized plasmon resonance, d-electron excitations, time-dependent density−functional theory, ab initio methods, classical optics, nanorod, atomic chain*

Localized surface-plasmon resonances (LSPRs) in noble metal nanoparticles are receiving enormous research attention due to their numerous applications in biological sensing,[1] surface-enhanced Raman spectroscopy (SERS),[2] cancer therapy,[3] detection technologies,[4] and also as efficient light-harvesting agents.[5] The main properties that make LSPRs essential for these applications are their ability to confine and enhance light down to the nanoscale, their design flexibility through size and geometry, and their highly sensitive dependence on the environment.[6,7]

Over the years, classical optics has been customarily used to investigate LSPRs in large (sizes greater than 10 nm) noble-metal nanoparticles. Among the broad range of structures explored, special attention has been focused on elongated particles, or nanorods,[8−10] in which LSPR frequencies can be tuned through the geometrical aspect ratio (AR, defined as the ratio between the longitudinal and lateral dimensions of the system). However, small clusters of noble metals[11−13] and ultrathin rods with diameters smaller than 2 nm[14] can be synthesized as well. Also, a number of stable thiolate-protected Au clusters[15−17] can be formed, among which $Au_{144}(SR)_{60}$ has appeared to be of utmost interest due to its size (≃1.8 nm), stability, and coherent reproducibility of optical spectra.[18,19] These advances open up a different length scale for plasmonics, where genuine quantum effects such as quantization of electron energy levels, electron-density spill-out, and reduced surface d-electron screening become important. An example of the peculiar LSPR phenomenology emerging in this regime is the suppression of transverse plasmonic modes due to the quantization of electron energy levels in ultrathin Au rods.[14] As anticipated above, apart from their robustness against purely quantum physical effects, LSPRs in nanostructures present another very interesting optical characteristic: their spectral

Received: March 16, 2017
Published: May 12, 2017

DOI: 10.1021/acsphotonics.7b00254

tunability through the nanostructure AR.[8,20] In particular, as recently reported for Au rods,[21,22] this paves the way to controlling the coupling between LSPRs and d-electron excitations through geometry. Moreover, when the width of the elongated nanostructure reaches a critical value, the electron motion is practically confined along the rod axis. In this regime, the system cannot be considered as a three-dimensional one and, as a consequence, collective electron excitations can no longer be considered as surface modes.[23]

Lately, there has been an increasing interest in the modeling of the LSPR response of tiny noble metal structures by electromagnetics tools. Thus, it has been recently shown that sub-nanometric inhomogeneities in field-enhancement patterns in plasmonic gaps[24−26] can be described, at least qualitatively, through classical optics calculations. On the other hand, the physical mechanisms behind the failure of classical predictions for the LSPR frequencies in compact nanoparticles (with sizes in the ∼1−3 nm range) are well understood.[11,12,27−29] Nonetheless, a careful exploration of the actual capabilities and limitations of electromagnetics methods when applied to elongated noble-metal subnanometric structures is, to the best of our knowledge, still lacking. In order to fill this gap, we present a comparative study of *ab initio* and classical optics (local and nonlocal) descriptions of the optical properties of noble-metal (Ag and Au) rods and chains of different sizes and ARs.

We develop a simple and intuitive link between quantum and classical descriptions of LSPRs, which allows us to define geometries (both shapes and dimensions) for the electromagnetics calculations in correspondence with atomistic structures having sub-nanometric lateral dimensions. Subsequently, we demonstrate the astonishing quality of the AR dependence of LSPRs as calculated by classical means in these quantum-sized systems, even in the quasi-one-dimensional limit. A direct comparison of LSPR frequencies and spectral strengths by both classical and *ab initio* descriptions reveals the influence of d-electron transitions in the plasmonic response of low-AR (quasi-spherical) structures. Finally, we investigate induced LSPR charge densities from classical and TDDFT calculations. This allows us to extend our comparative study beyond far-field characteristics and verify the validity of our findings also in the near-field regime. Apart from their evident methodological implications, our theoretical findings shed light on the interplay between collective and single-electron excitations in metallic nanostructures, a topic that is attracting much attention currently in various fields, including plasmon-enhanced hot electron generation,[30] photocatalysis,[31] and nanoscale heat sources.[32]

■ THEORETICAL BACKGROUND

There is a wide range of tools for the theoretical description of LSPRs. The most suitable approach varies from case to case, depending on the geometry and size of the metallic structure and its environment. From an *ab initio* perspective, time-dependent density-functional theory (TDDFT)[33] is the method of choice to study collective excitations in metallic nanostructures.[21,29,34−38] In TDDFT, the time evolution of the density of the many-electron system is obtained from a fictitious noninteracting one, the time-dependent Kohn−Sham system, under the action of an effective time-dependent potential. This potential is a functional of the electron density $n(\mathbf{r}, t)$ and accounts for the nonlocal spatial and temporal response of the correlated many-body system.[39,40] As long as collective excitations dominate the optical spectra, adiabatic generalized-gradient approximations (AGGAs) suffice.[35] However, AGGA exhibits problems in the description of the d states, leading, in particular, to d-band energies too close to the Fermi energy, in part due to the incomplete cancellation of the electron self-interaction. The precise description of the delicate interplay between d-electron and collective excitations in coinage metals requires more sophisticated functionals such as the long-range-corrected hybrid functional LC-M06L.[41,42] The problem has likewise been treated successfully using DFT +U calculations of the generation of hot carriers from surface plasmon decay.[43]

Application of TDDFT is limited to rather small systems having a number of electrons below ∼5000. Therefore, above this size limit we need a more tractable yet robust theoretical framework. Since LSPRs appear naturally as self-sustained solutions of Maxwell's equations, classical local optics provides the required accuracy in many cases. Within this framework, the existence of abrupt metal−dielectric boundaries is assumed, and the electromagnetic response of metallic regions is described in terms of their macroscopic dielectric function, $\epsilon_{\text{bulk}}(\omega)$. In the limit of small sizes and/or sub-nanometric radii of curvature, the nonlocal nature of the electromagnetic response becomes crucial.[13,44] As a consequence, the use of spatially dispersive dielectric functions is required for a practical description of the smearing of induced charges across metal−dielectric boundaries.[45] This can be done through simplified, yet numerically efficient implementations[46,47] of the hydrodynamical model for electron motion[34,48] or by defining a suitable space-dependent dielectric function in the metal−dielectric interface.[49] These nonlocal corrections lead to blue-shifts of LSPR frequencies with respect to local optics predictions,[50,51] a trend that can be traced back to the fact that nonlocal corrections spread the induced density inward from the abrupt bulk surface.[52]

While providing relevant corrections to local predictions, nonlocal optics still lacks important ingredients in the elucidation of LSPR behavior. First, the spill-out of the electron density at metal−dielectric interfaces, which in general leads to LSPR frequency red-shifts,[53,54] is missing. Second, quantum finite size effects that are manifest in the discretization of electron energy levels[28] are absent. Finally, surface corrugation at the sub-nanometric scale is essentially missing, although it can be partially accounted for through phenomenological modeling of metal/vacuum interfaces in an effective manner.[24,26] By contrast the quantum mechanical TDDFT calculations are exact in principle and would provide all the quantum many-body corrections if it were not for the fact that we need to rely on approximate functionals/kernels for practical calculations. Beyond these approximations, TDDFT can provide all the necessary corrections to local optics results, not only those due to bulk spatial nonlocality in the metal permittivity.

■ SYSTEMS AND METHODS

Following previous studies on the absorption spectra of noble-metal nanorods,[21,22,55] we consider model pentagonal rods of Au and Ag derived from the 13-atom decahedral cluster by stacking rings of five atoms each plus a central atom along the rotational axis (see Figure 1). The longest rod (with highest AR) is made up of $N = 145$ atoms, while the shortest one (with lowest AR) has $N = 19$. The structures in our study are the same for both Au and Ag, and, to allow for a proper discussion of the dependence of the optical absorption on AR, they are not

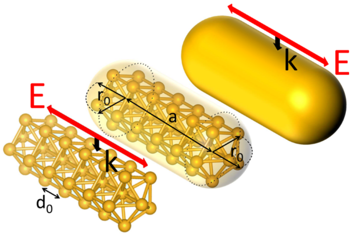

Figure 1. Sketch of the modeling of Ag and Au rods: ionic lattice (left) for TDDFT calculations and cigar-shaped volume geometry (right) for classical optics. In between, the definition of the boundaries of the rod geometry establishing the mapping between both levels of description is illustrated. The geometrical parameters are indicated: atom−atom distance, d_0, and the cigar-geometry curvature radius and bulk length, r_0 and a, respectively.

relaxed. The atom−atom distance along the rod axis is set to $d_0 = 2.88$ Å. The other class of systems here considered are single atom chains of Au and Ag having a number of atoms between 6 and 24, with the same interatomic distance d_0 as in the rods. We focus our investigation on excitations by electric fields polarized along the rod axis (x-direction), and the corresponding absorption spectra are calculated using the time-propagation formalism[56] of TDDFT. The rods are excited by a delta-impulse perturbing electric field $\delta\mathbf{E}(\mathbf{r}, t) = E_0\tau_0\delta(t)\mathbf{e}_x$ (see Figure 1), and the frequency-dependent absorption cross section is obtained from the Fourier transform of the induced time-dependent dipole moment

$$\sigma_{\mathrm{abs}}(\omega) = -\frac{4\pi\omega}{cE_0\tau_0}\Im\int_0^\infty \mathrm{d}t e^{\mathrm{i}\omega t}\int \mathrm{d}\mathbf{r}x\ \delta n(\mathbf{r}, t) \tag{1}$$

Here, c is the speed of light and $\delta n(\mathbf{r}, t)$ is the time-dependent induced density after the "kick". This induced density is computed through the solution of the time-dependent Kohn−Sham equations as implemented in the real-space code Octopus.[57] Valence s- and d-electrons are treated explicitly, whereas core electrons are described through norm-conserving Troullier−Martins pseudopotentials.[58] The Perdew−Burke−Ernzerhof[59] (PBE) AGGA exchange−correlation functional is used. However, as anticipated, the performance of this particular functional has to be carefully assessed. Figure S2 in the Supporting Information (SI) shows a comparison of PBE results for selected rods with those obtained using the more sophisticated LC-M06L hybrid functional, obtained by applying a long-range correction[60] to the meta-GGA functional of ref 41. This functional has demonstrated high accuracy for small silver clusters[42] and is therefore considered as a benchmark here. Our comparison indicates that the PBE spectra are valid as long as the dominant LSPR is well decoupled from interband transitions, which is the case for the high-AR rods treated here. By contrast, their accuracy degrades strongly when LSPRs couple with d-electron excitations, as in the case of Ag_{19}, the shortest silver rod considered here. Thus, special care needs to be taken when comparing TDDFT and electromagnetics predictions for such cases.

A consistent comparison of LSPRs from *ab initio* and electromagnetics calculations requires a proper correspondence between atomistic structures and geometric regions having well-defined boundaries. In order to mimic the soft single-atom termination of our atomistic rods, we choose "cigar"-shaped geometries for our classical optics metal regions. These sub-nanometric cigars are defined as cylinders of length a and radius r_0 decorated by two hemispherical ends of the same radius; see Figure 1. The electron density in the cigars is the same as the average s-electron density in the bulk, given by $n_{\mathrm{av}} = 3/(4\pi r_s^3)$, where, $r_s = 3.02\ a_B$ (a_B Bohr radius) is the Wigner radius for Au and Ag. As mentioned above, from the electromagnetics perspective, the optical response of noble-metal nanostructures is described through their dispersive bulk permittivity, $\epsilon_{\mathrm{bulk}}(\omega)$. For coinage metals, this consists of a Drude term accounting for the contributions of loosely bound (nearly free) conduction band electrons (s-electrons) and a series of Lorentzian terms describing the effect of strongly bound core electrons. In our calculations, we use experimental fittings of this form, tested at visible frequencies (up to 5 eV).[61] The proper modeling of the atomistic quantum-sized systems is achieved by defining the geometries for the electromagnetics calculations through two parameters. First, the AR = $(a + 2r_0)/2r_0$ for the classical optics cigar is chosen to be the same as for the atomistic structures. Second, their volume, V, is set so that the number, N, of Drude electrons (expressed in terms of the fitted parameter for the plasma frequency) is equal to the number of s-electrons in the TDDFT calculations. More details on the cigar geometry definition and optimization can be found in the SI.

Both local and nonlocal optics calculations for the rods' absorption spectra were performed using COMSOL Multiphysics, a commercial solver of Maxwell's equations that implements the finite element method. The nonlocal spatial dispersion in the metal permittivity is modeled through the so-called hydrodynamic model, with a β parameter (~Fermi Velocity) equal to 10^6 m/s.[44] Within the hydrodynamic model (see ref 51 for details of the method and its implementation), bulk longitudinal plasmon modes can be optically excited inside the metal. This leads to an induced surface charge thickening that cannot be described within the realm of local optics. The implementation of the hydrodynamic model is simplified here by using the so-called local analogous model,[49] which accounts for the smearing of metal boundaries through a fictive dielectric layer of vanishing thickness, d, covering the metal surface. The dielectric function within this layer is $\epsilon_{\mathrm{layer}}(\omega) = \frac{\epsilon_{\mathrm{bulk}}(\omega)}{\epsilon_{\mathrm{bulk}}(\omega) - 1}q_L d$, where

$$q_L = \sqrt{-\epsilon_{\mathrm{bulk}}(\omega)}\,\frac{\omega}{\beta} \tag{2}$$

is the longitudinal plasmon evanescent wave-vector expressed in terms of the bulk permittivity. Equation 2 gives the dispersion relation of the longitudinal plasmon modes within the bulk metal. In all our nonlocal hydrodynamic calculations, the convergence of results in the limit $d \to 0$ was checked.

■ ABSORPTION SPECTRA

Figure 2 shows a direct comparison between *ab initio* and local and nonlocal optics absorption spectra for Ag and Au sub-nanometric rods. There is an excellent agreement between TDDFT (reported already in ref 22 and in general agreement with refs 21 and 55) and local optics calculations for structures with AR > 5 (whose response is dominated by the LSPR). Let us remark that there is no fitting between *ab initio* and electromagnetics models; only the *a priori* definition of classical geometries introduced above was followed. The comparison against *ab initio* predictions improves even further when the

DOI: 10.1021/acsphotonics.7b00254

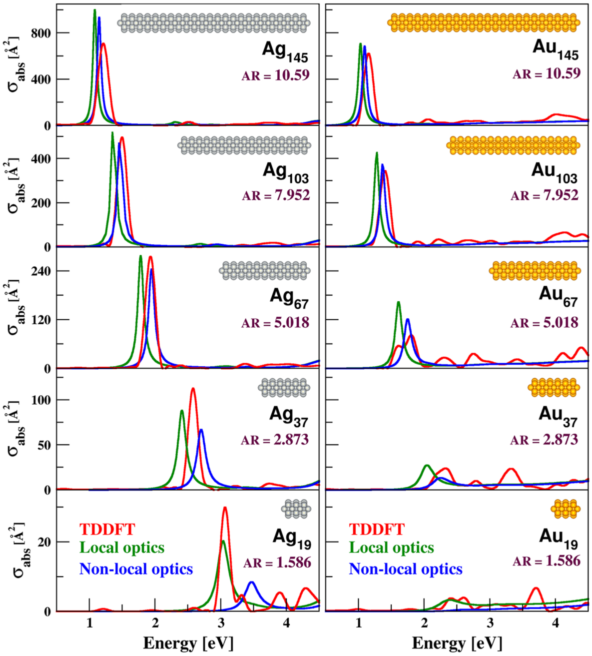

Figure 2. Optical absorption cross section for silver (left column) and gold (right column) three-dimensional rods of different aspect ratio (AR) and number of atoms.

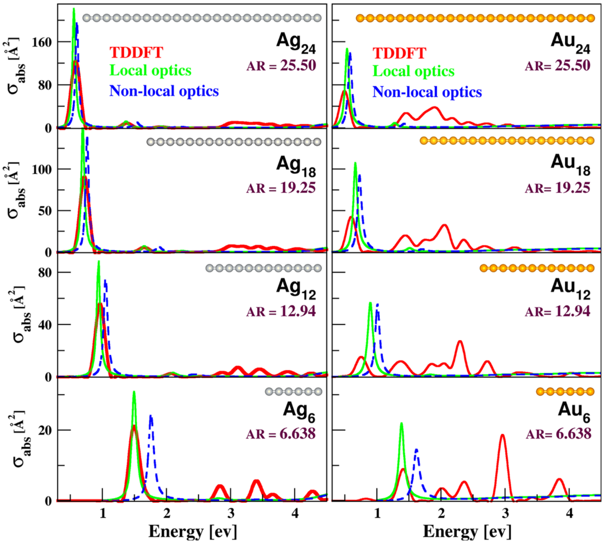

Figure 3. Optical absorption cross section for quasi-one-dimensional silver (left column) and gold (right column) atomic chains of different aspect ratio (AR) and number of atoms.

absorption cross section is computed using a nonlocal hydrodynamic metal permittivity. This gives rise to the aforementioned nonlocal resonance blue-shift, a signature of the different LSPR energy dependence on absolute size in local and nonlocal optics. See Figure S3 of the SI for a comprehensive analysis of the dependence of this nonlocal blue-shift on absolute size and AR.

Classical optics fails to accurately describe the *ab initio* spectra for compact low-AR structures in Figure 2 ($N \leq 37$ atoms, AR < 2.9). This is expected, since genuine quantum effects, such as electron-density spill-out and energy level discretization due to size confinement, become more significant as the rod's length (and thus AR) decreases. However, in the case of Ag, despite relatively small spectral deviations, TDDFT and classical calculations are still in qualitative agreement even for low AR. By contrast, for Au rods having AR ≤ 5 (i.e., $N \leq 67$ atoms), classical predictions are already qualitatively different from the TDDFT spectra. In these Au systems, the classical LSPR frequencies lie at or above the onset of interband transitions (~2 eV) due to d-electrons. This fact prevents the formation of purely collective surface plasmon resonances in the TDDFT spectrum, which in turn is dominated by a set of multiple maxima (of similar height) originated by d-electron excitations. Identifying the lowest−frequency absorption features in the TDDFT spectra for short Au rods as LSPRs (having noticed that these are located at roughly the same position as the classical optics peaks), we can conclude that the spectral overlap with the d-excitations gives rise to the partial damping, splitting, and fragmentation of LSPRs. It is worth mentioning here that the inclusion of nonlocality in the electromagnetics calculations does not reproduce any of these purely quantum physical features. It only improves the comparison against *ab initio* results at higher AR by correcting local classical optics LSPR frequencies, which are otherwise too red-shifted due to the abrupt character of induced local charges.

Figure 3 plots the absorption spectra for Ag and Au atomic chains of different AR. We find a strikingly good agreement between TDDFT and local optics results for Ag chains, an observation similar to previous studies on linear hydrogen atomic chains.[62,63] As in the case of the rods in Figure 2, for Ag atomic chains the weak spectral deviations above ~3 eV can be attributed to single electron−hole excitations owing to interband transitions. These spectral features are more apparent in Au chains, where the spectral weight of transitions involving d-electrons is comparable to those attributed to LSPRs. As discussed below, the predictive value of local electromagnetics calculations for high AR chains (for both Ag and Au) originates from their quasi-one-dimensional nature: electron motion in these systems is confined along the longitudinal axis. Therefore, the collective LSPR that dominates their absorption spectra cannot be regarded as a surface mode.[64−67] We note that our hydrodynamic model was constructed to account for the impact of spatial nonlocality due to the optical excitation of three-dimensional (bulk) longitudinal plasmons, described by eq 2, instead of one-dimensional ones. This explains the offset of nonlocal predictions in Figure 3, significantly blue-shifted with respect to local optics and *ab initio* spectra.

The striking agreement between the absorption spectra for quasi-one-dimensional quantum systems and their three-dimensional local optics counterparts can be easily understood in terms of simple geometrical considerations. To a first approximation, we can take the analytical expression[68] for the lowest LSPR in ellipsoidal nanoparticles for our cigar geometries. In the limit of large AR, we obtain

$$\omega_{\mathrm{LSPR}}^2 = \frac{4}{\pi}\frac{\rho_{\mathrm{av}}e^2}{m_{\mathrm{e}}\epsilon_0(a+2r_0)^2}\ln(2\mathrm{AR}) = \frac{n_{\mathrm{av}}e^2}{m_{\mathrm{e}}\epsilon_0(AR)^2}\ln(2\mathrm{AR}) \tag{3}$$

where $\rho_{\mathrm{av}} = \pi r_0^2 n_{\mathrm{av}}$ is the number of Drude electrons per unit length, ϵ_0 is the vacuum permittivity, and m_{e} and e the electron mass and charge, respectively. It is worth noticing that the absence of the Lorentzian component of $\epsilon_{\mathrm{bulk}}(\omega)$ in eq 3 indicates that the dynamical screening by d-electrons is ineffective for rods with large AR. On the other hand, the plasmon dispersion relation in a homogeneous one-dimensional electron system in the long-wavelength limit reads[23] $\omega_{\mathrm{1D}}^2(q) = \frac{-\rho_{\mathrm{av}}e^2}{2\pi\epsilon_0 m_{\mathrm{e}}}q^2\ln(\xi_0 q/\pi)$, where ξ_0 is the length parameter measuring the electron confinement in the transverse direction. Evaluating this expression at $q = \pi/(a + 2r_0)$ and making $\xi_0 = r_0$, we obtain the resonant frequency for the dipole collective mode sustained by the system, the *ab initio* equivalent for the classical LSPR,

$$\omega_{\mathrm{1D\text{-}dipole}}^2 = \frac{\pi}{2}\frac{\rho_{\mathrm{av}}e^2}{m_{\mathrm{e}}\epsilon_0(a+2r_0)^2}\ln(2\mathrm{AR}) = \frac{\pi^2}{8}\frac{n_{\mathrm{av}}e^2}{m_{\mathrm{e}}\epsilon_0(AR)^2}\ln(2\mathrm{AR}) \tag{4}$$

Equations 3 and 4 describe collective excitations of different nature, but their remarkable similarity allows us to identify both of them. This also clarifies the unexpected agreement between TDDFT and local optics spectra in Figure 3. Note that the equations above yield $\omega_{\mathrm{LSPR}} < \omega_{\mathrm{1D\text{-}dipole}}$, which is also in agreement with the numerical spectra. Classical optics slightly underestimates the LSPR frequencies in the limit of very long chains (where the analytical expressions are valid), a deviation that, in principle, could be corrected through the appropriate one-dimensional nonlocal corrections.

As mentioned above, the TDDFT spectra for Au chains in Figure 3 indicate that quasi-one-dimensional collective excitations are not well resolved for $N \leq 12$. In fair correspondence with the three-dimensional case, this effect can be directly attributed to the coupling of the collective mode with single electron−hole excitations. This coupling can be observed in detail in Figure 4, where we show the variation of the absorption cross section normalized to N for different Au chains. For $N = 18$, the quasi-one-dimensional LSPR is well separated from the spectral region where single-electron transitions occur. As a consequence, it appears as a well-defined absorption peak whose position is in good agreement with the one predicted classically. When decreasing the number of atoms, the lowest−frequency maxima lose spectral weight. For $N = 10$, this resonance is fragmented and none of the local maxima can be interpreted as the collective LSPR excitation. However, Figure 4 demonstrates that classical optics describes a rough spectral average of the fragmented peaks. Finally, for the six-atom chain, the lowest frequency *ab initio* maximum is very weak, and the transfer of spectral weight to the region of electron−hole excitations is almost complete. Interestingly, a new spectral feature emerges very close to the frequency corresponding to the classical plasmon by taking spectral

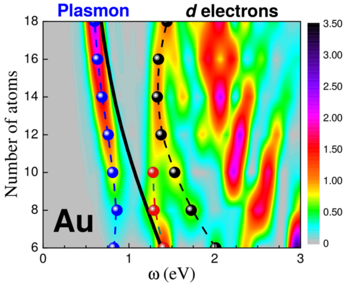

Figure 4. TDDFT absorption cross section per atom (in Å^2) versus frequency and the number of atoms in Au chains. The solid line plots the LSPR frequency under local optics prescription. The various *ab initio* spectral maxima are rendered by solid circles (connected as a guide to the eye): collective plasmon modes in blue and single d-electron excitations in black and red.

weight from the original one-dimensional LSPR and the lowest–energy electron–hole excitation. Although plasmon formation in gold chains is clearly beyond the scope of any classical optics treatment, it is worth emphasizing that it seems to account rather accurately for the spectral average of the split quantum excitations in the *ab initio* calculations.

LSPR FREQUENCY VERSUS ASPECT RATIO

As shown above, our combined *ab initio* and electromagnetics modeling of Ag and Au rods indicates that, through a careful mapping between atomistic structures and classical geometries containing a bulk permittivity, LSPRs can be quantitatively described by classical optics methods as long as they are free of interband contamination. In order to further check this conclusion and provide a more general perspective, we plot in Figure 5 the spectral position of all the absorption maxima in Figures 2, 3, and 4 versus AR for Ag (top) and Au (bottom) systems (note the log–log scale). TDDFT results for collective LSPR-like modes are shown in solid red circles (rods) and rhombuses (chains). In all cases, the number of atoms is indicated. Significant absorption features in Au structures originating from single electron–hole excitations are represented by empty circles (rods) and rhombuses (chains). Local (nonlocal) optics predictions for the corresponding cigar geometries are rendered in green (blue) lines. We observe that while the LSPR frequencies within the local approximation depend only on AR, they depend on absolute size once nonlocal corrections are included. Thus, solid and dashed blue lines correspond to nonlocal resonances for rods and chains, respectively.

Figure 5 shows that while the AR dependence of LSPR frequencies obtained from local optics calculations is already in good agreement with TDDFT results, the nonlocal blue-shift slightly improves it for long Au and Ag rods. This suggests that these systems, despite having lateral sub-nanometric dimensions, preserve a quasi-bulk optical response. By contrast, in the Ag chains, the TDDFT resonant frequencies are better described within the local optics framework. In the top panel of Figure 5, circles lie above rhombuses, which indicates that the rod LSPRs are blue-shifted with respect to the atomic chain ones. This trend is exactly the opposite of that predicted by nonlocal optics (see solid and dashed blue lines). As discussed above, not only this failure of the nonlocal hydrodynamic model but also the good agreement between local optics and *ab initio* predictions in Ag chains can be linked to the inherent one-dimensional nature of these systems. In the case of short Au rods and chains, the occurrence of d-electron transitions above ~2 eV causes qualitative differences in the spectral behavior between TDDFT and electromagnetics approaches. The discrepancy in the AR dependence between both methods is most apparent in chains with $N = 6-12$, where multiple *ab initio* single-electron peaks occur far apart from the LSPR band. In order to verify the validity of local optics descriptions, we evaluate the ellipsoidal LSPR dispersion in ref 68 for the full Drude–Lorentz permittivity as well as for a simplified Drude-only fitting. The results, plotted in magenta (full $\epsilon_{\text{bulk}}(\omega)$, i.e., Drude and Lorentz parts) and black (simplified $\epsilon_{\text{bulk}}(\omega)$, i.e., Drude part only), reveal that agreement with TDDFT predictions occurs if the dielectric function is mainly governed by the Drude contribution, as expected.

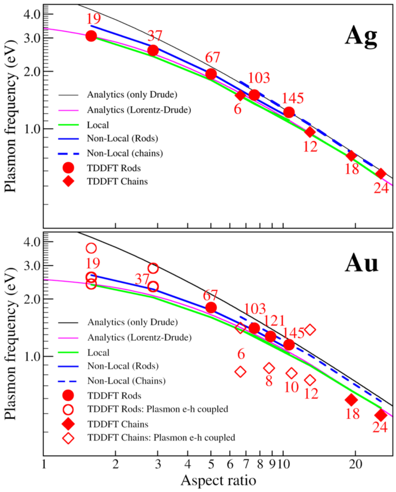

Figure 5. LSPR frequencies in Ag (upper panel) and Au (lower panel) sub-nanometric rods and atomic chains versus aspect ratio. Black (magenta) line renders analytical local optics calculations in ellipsoidal geometries with fitted Drude (Drude–Lorentz) permittivity, where analytics refers to eqs 5.13b and 5.15 of ref 6. Green and blue (solid and dashed) lines plot local and nonlocal classical simulations for Drude–Lorentz cigars, respectively. TDDFT LSPR frequencies for N-atom systems are shown in solid red circles (rods) and rhombuses (chains). Empty circles (rods) and rhombuses (chains) correspond to single electron–hole excitations apparent in the absorption spectra.

INDUCED DENSITY

To gain further insight into our results, we compare now the near-field characteristics of LSPRs, interpreted as collective dipolar surface modes, within the *ab initio* and classical optics frameworks. Specifically, we consider the cross-sectional integration of the resonant induced charge densities along the rod length (for 3D visualization of the TDDFT densities cf. ref 69). This magnitude can be evaluated using TDDFT by exciting the atomistic systems with a weak quasi-monochromatic laser field polarized along the rod axis (x-direction). The

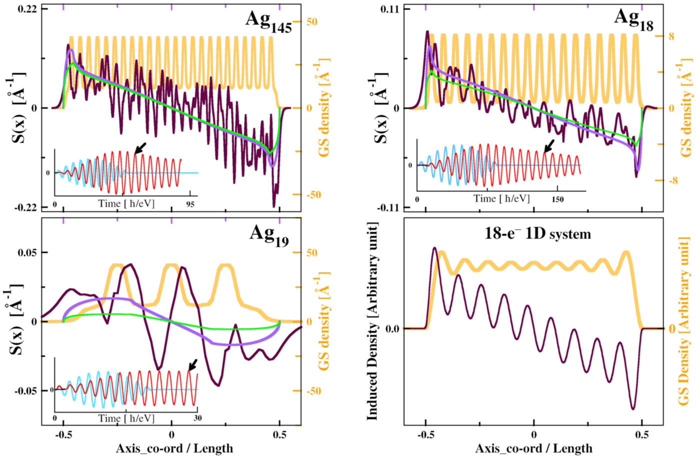

Figure 6. Induced charge density for Ag_{145} (top left), Ag_{19} (bottom left), Ag_{18} (top right), and an $N = 18$ purely one-dimensional system (bottom right). In all panels, the brown curve plots a snapshot of the TDDFT induced charge density along the normalized rod/chain length in units of electrons/Å. The orange curve displays the ground-state density profile, shown for reference. The violet and green curves in the first three panels show the induced surface charge distribution (in electrons/Å) obtained from local and nonlocal optics calculations, respectively. The insets show the time dependence of the driving laser (blue) and of the TDDFT induced dipole moment (red).

laser pulse has a sinusoidal envelope of finite duration, T, and its bandwidth is centered at the LSPR frequency: $\mathbf{E}(t) = E_0 e^{i\omega_{\mathrm{LSPR}} t} \sin(\omega_{\mathrm{LSPR}} t/T)\mathbf{e}_x$. In our calculations the envelope duration was set to 10 plasmon oscillations ($T = 20\pi/\omega_{\mathrm{LSPR}}$). The system is left evolving freely for a sufficient amount of time after the external driving laser is switched off. The cross-section-integrated charge density can then be evaluated from

$$S(x) = \int\int [\rho(x, y, z; \tau) - \rho_{\mathrm{GS}}(x, y, z)]\, \mathrm{d}y\, \mathrm{d}z \qquad (5)$$

where $\rho_{\mathrm{GS}}(x, y, z)$ is the ground-state density and $\rho(x, y, z; \tau)$ is the time-dependent density at a time τ, longer than T, when the oscillation of the electron density is self-sustained. Within the *ab initio* description, the induced charges spread across the rod's volume. By contrast, in the electromagnetics picture, they are confined at the metal surface: surface charges are located exactly at the geometric boundaries in the local optics treatment, whereas nonlocal corrections provide the charge distribution with a nonvanishing thickness. Taking this into account, we can estimate the induced charges using classical electromagnetics through the discontinuity in the normal component of the electric field. Explicitly, we can write

$$S(x) = 2\pi\epsilon_0 r(x)[\mathbf{E}_{\mathrm{out}}(x) - \mathbf{E}_{\mathrm{in}}(x)]\cdot\mathbf{e}(x) \qquad (6)$$

where $r(x) = \sqrt{y(x)^2 + z(x)^2}$ is the radial coordinate along the metal boundary, $\mathbf{e}(x)$ is the unit vector along the surface normal, and $\mathbf{E}_{\mathrm{out}}(x)$ and $\mathbf{E}_{\mathrm{in}}(x)$ are the electric fields outside and inside the cigar boundaries. Note that, taking into account the confined (extended) character of induced surface charges, $\mathbf{E}_{\mathrm{in}}(x)$ is evaluated exactly at (at a distance $1/q_{\mathrm{L}}$ from) the metal−dielectric interface in the local (nonlocal) calculations.

Figure 6 plots $S(x)$ against the length-normalized axis coordinate for three distinct Ag systems whose spectra (both in TDDFT-PBE and in classical optics) present a well-defined LSPR: 145-atom rod (top left panel), 19-atom rod (bottom left panel), and $N = 18$ atomic chain (top right panel). In all cases, the induced density profiles obtained from TDDFT (brown) and local (violet) and nonlocal (green) classical optics are shown. The TDDFT ground-state density is shown as an orange line (note the different scales of the left and right axes in all panels). To allow for a quantitative comparison between *ab initio* and electromagnetics treatments of $S(x)$, the amplitude of the driving laser in all simulations was set to 10^8 V/m (within the linear response). The insets show the laser field (blue) and the TDDFT time evolution of the induced dipole moment (red). The black arrows indicate the time τ at which the induced charges were computed. The bottom right panel displays the *ab initio* induced (brown) and ground-state (orange) density profiles for an 18-electron purely one-dimensional jellium system modeling Ag_{18}.

Figure 6 shows that the excellent quantitative agreement between *ab initio* and classical predictions for the absorption spectra of Ag_{145} (see Figure 2) and Ag_{18} (Figure 3) also holds in the near-field regime. Remarkably, the peaks of the induced charge distribution from TDDFT and electromagnetics are not only located at the same position but present very similar heights. This can be interpreted as a consequence of the high plasmonic character of both structures, which supports well-defined collective LSPRs free of the contamination from single electron−hole excitations. There are two relevant aspects in the *ab initio* density profiles that deserve attention. First, there is the inhomogeneity of $S(x)$ across the length of the structure. These regular modulations of the density are caused by the highly localized nature of the d-electrons and their contribution to the overall response of the system. Second, there are weak, somewhat irregular fluctuations overlaid onto those modulations. These arise from the fact that the quasi-monochromatic laser excitation has a finite energetic width and hence can excite several energetically close modes. The superposition of the

DOI: 10.1021/acsphotonics.7b00254
ACS Photonics 2017, 4, 1484−1493

different modes leads to the irregular fluctuations that modify the overall behavior of the induced density and lead to a certain asymmetry in the density profile. By comparison, a static external field would lead to a profile reflecting the perfectly symmetric geometry along the rod axis. Both the modulations due to the atomistic density inhomogeneity and the fluctuations due to the superposition of different modes are naturally absent in the classical induced-density profiles. The right bottom panel of Figure 6 confirms our interpretation of these TDDFT induced density features missing in the classical optics results. It renders a perfectly symmetric and smoothly oscillating $S(x)$ (free from sharp fluctuations) for the purely one-dimensional jellium system.

Despite the correspondence in the LSPR spectral position (see lowest left panel in Figure 2), the comparison between classical and *ab initio* induced densities for Ag_{19} (shown in the left bottom panel of Figure 6) is rather poor. Unlike Ag_{145} and Ag_{18}, electromagnetic calculations for Ag_{19} yield an $S(x)$ profile that is not peaked at the rod ends. On the contrary, induced charges spread significantly along the nanorod length toward its middle plane. The TDDFT distribution develops several maxima along the length of the system. These are reminiscent of the sharp fluctuations in the *ab initio* $S(x)$ for Ag_{145} and Ag_{18}. This indicates that, as expected from the high LSPR frequency apparent in its absorption spectrum (∼3 eV), d-electron transitions play a key role in the optical response of Ag_{19}. Thus, we can conclude that this rod configuration presents a rather low plasmonic character, despite the fact that its TDDFT-PBE absorption spectrum is dominated by a single peak reproduced by classical optics. In fact, as mentioned before, our TDDFT calculations use the PBE AGGA functional, whose validity for the description of Ag_{19} is questionable. This appears in a refined *ab initio* study on Ag_{19}, comparing PBE with the range-separated hybrid functional LC-M06L,[41,60] which we have included in the SI (Figure S2). The LC-M06L functional is more suitable for the treatment of d-electron excitations and yields accurate spectra for small Ag clusters.[42] From our analysis, we conclude that TDDFT-PBE calculations for Ag_{19} are not reliable, and hence, the spectral agreement between classical and fully quantum results on Ag_{19} is partially coincidental. In fact, the comparison of *ab initio* and classical LSPR-induced densities for Ag_{19} (see Figure 6) establishes the limitations of the electromagnetics predictions. They fail to describe structures in which LSPRs and d-electrons couple strongly. Even in the TDDFT treatment of those systems, a description of exchange and correlation better than the AGGA functionals is required. In contrast, if the LSPR is largely free of d-electron excitations (as it is for Ag_{145} and other long rods and atomic chains), the *ab initio* spectra obtained using PBE AGGA functionals are accurate (see Figure S2 of the SI). In this situation, classical optics predicts remarkably well the TDDFT spectral position, strength, and character of the induced LSPR density.

■ CONCLUSIONS

In conclusion, we have presented a comprehensive theoretical study on the plasmonic properties of sub-nanometric elongated coinage-metal systems. Our investigation compares local and nonlocal classical optics and quantum *ab initio* methods. By preserving the aspect ratio and number of Drude (or s) electrons, we have established simple model geometries, which can be treated within the electromagnetics framework, in correspondence with atomistic structures having sub-nanometric dimensions. We find a remarkable agreement between the *ab initio* and classical descriptions of the absorption spectral characteristics of Ag rods and chains. The agreement for the equivalent Au systems is significantly worse due to the low-energy onset of d-electron excitations. In addition, we have shown that it is the shape, not the overall size, that determines the degree of d-electron contamination suffered by the localized plasmon resonances sustained by these structures. Finally, we have transferred our comparative analysis from the far-field to the near-field regime. We have demonstrated that, despite its higher sensitivity to atomistic features, the classical and the fully quantum mechanical descriptions of localized plasmon-induced charges are in remarkable agreement for elongated Ag systems.

■ ASSOCIATED CONTENT

Ⓢ Supporting Information

The Supporting Information is available free of charge on the ACS Publications website at DOI: 10.1021/acsphotonics.7b00254.

> Detailed description of the mapping between atomistic structures and classical electromagnetics geometries; comparison between TDDFT absorption spectra obtained using GGA (PBE) and LC-M06L functionals for three different Ag rods; study of the dependence of the nonlocal optics blue-shift on aspect ratio and absolute size of Ag rods (PDF)

■ AUTHOR INFORMATION

Corresponding Authors

*E-mail: sinharoy@cinam.univ-mrs.fr.
*E-mail: a.fernandez-dominguez@uam.es.

ORCID

Rajarshi Sinha-Roy: 0000-0002-1324-9820
Frank Rabilloud: 0000-0002-5011-3949
Antonio I. Fernández-Domínguez: 0000-0002-8082-395X

Notes

The authors declare no competing financial interest.

■ ACKNOWLEDGMENTS

The project leading to this publication has received funding from Excellence Initiative of Aix-Marseille University - A*MIDEX, a French "Investissements d'Avenir" programme". We acknowledge support from the French National Research Agency (Agence Nationale de Recherche, ANR) in the frame of the project "FIT SPRINGS", ANR-14-CE08-0009. This work has used HPC resources from GENCI-IDRIS (Grant 2016-096829). P.G.G. and A.I.F.D. acknowledge funding from the Spanish MINECO through the "María de Maeztu" Programme for Units of Excellence in R&D (MDM-2014-0377) and through research grants MAT2014-53432-C5-5-R (P.G.G.) and FIS2015-64951-R (A.I.F.D.). A.I.F.D. also acknowledges funding from the EU Seventh Framework Programme under contract FP7-PEOPLE-2013-CIG-630996.

■ REFERENCES

(1) Anker, J. N.; Paige-Hall, W.; Lyandres, O.; Shah, N. C.; Zhao, J.; Van-Duyne, R. P. Biosensing with plasmonic nanosensors. *Nat. Mater.* **2008**, *7*, 442−453.

(2) Seney, C. S.; Gutzman, B. M.; Goddard, R. H. Correlation of Size and Surface-Enhanced Raman Scattering Activity of Optical and Spectroscopic Properties for Silver Nanoparticles. *J. Phys. Chem. C* **2009**, *113*, 74−80.

different modes leads to the irregular fluctuations that modify the overall behavior of the induced density and lead to a certain asymmetry in the density profile. By comparison, a static external field would lead to a profile reflecting the perfectly symmetric geometry along the rod axis. Both the modulations due to the atomistic density inhomogeneity and the fluctuations due to the superposition of different modes are naturally absent in the classical induced-density profiles. The right bottom panel of Figure 6 confirms our interpretation of these TDDFT induced density features missing in the classical optics results. It renders a perfectly symmetric and smoothly oscillating $S(x)$ (free from sharp fluctuations) for the purely one-dimensional jellium system.

Despite the correspondence in the LSPR spectral position (see lowest left panel in Figure 2), the comparison between classical and *ab initio* induced densities for Ag_{19} (shown in the left bottom panel of Figure 6) is rather poor. Unlike Ag_{145} and Ag_{18}, electromagnetic calculations for Ag_{19} yield an $S(x)$ profile that is not peaked at the rod ends. On the contrary, induced charges spread significantly along the nanorod length toward its middle plane. The TDDFT distribution develops several maxima along the length of the system. These are reminiscent of the sharp fluctuations in the *ab initio* $S(x)$ for Ag_{145} and Ag_{18}. This indicates that, as expected from the high LSPR frequency apparent in its absorption spectrum (∼3 eV), d-electron transitions play a key role in the optical response of Ag_{19}. Thus, we can conclude that this rod configuration presents a rather low plasmonic character, despite the fact that its TDDFT-PBE absorption spectrum is dominated by a single peak reproduced by classical optics. In fact, as mentioned before, our TDDFT calculations use the PBE AGGA functional, whose validity for the description of Ag_{19} is questionable. This appears in a refined *ab initio* study on Ag_{19}, comparing PBE with the range-separated hybrid functional LC-M06L,[41,60] which we have included in the SI (Figure S2). The LC-M06L functional is more suitable for the treatment of d-electron excitations and yields accurate spectra for small Ag clusters.[42] From our analysis, we conclude that TDDFT-PBE calculations for Ag_{19} are not reliable, and hence, the spectral agreement between classical and fully quantum results on Ag_{19} is partially coincidental. In fact, the comparison of *ab initio* and classical LSPR-induced densities for Ag_{19} (see Figure 6) establishes the limitations of the electromagnetics predictions. They fail to describe structures in which LSPRs and d-electrons couple strongly. Even in the TDDFT treatment of those systems, a description of exchange and correlation better than the AGGA functionals is required. In contrast, if the LSPR is largely free of d-electron excitations (as it is for Ag_{145} and other long rods and atomic chains), the *ab initio* spectra obtained using PBE AGGA functionals are accurate (see Figure S2 of the SI). In this situation, classical optics predicts remarkably well the TDDFT spectral position, strength, and character of the induced LSPR density.

■ CONCLUSIONS

In conclusion, we have presented a comprehensive theoretical study on the plasmonic properties of sub-nanometric elongated coinage-metal systems. Our investigation compares local and nonlocal classical optics and quantum *ab initio* methods. By preserving the aspect ratio and number of Drude (or s) electrons, we have established simple model geometries, which can be treated within the electromagnetics framework, in correspondence with atomistic structures having sub-nanometric dimensions. We find a remarkable agreement between the *ab initio* and classical descriptions of the absorption spectral characteristics of Ag rods and chains. The agreement for the equivalent Au systems is significantly worse due to the low-energy onset of d-electron excitations. In addition, we have shown that it is the shape, not the overall size, that determines the degree of d-electron contamination suffered by the localized plasmon resonances sustained by these structures. Finally, we have transferred our comparative analysis from the far-field to the near-field regime. We have demonstrated that, despite its higher sensitivity to atomistic features, the classical and the fully quantum mechanical descriptions of localized plasmon-induced charges are in remarkable agreement for elongated Ag systems.

■ ASSOCIATED CONTENT

Supporting Information

The Supporting Information is available free of charge on the ACS Publications website at DOI: 10.1021/acsphotonics.7b00254.

> Detailed description of the mapping between atomistic structures and classical electromagnetics geometries; comparison between TDDFT absorption spectra obtained using GGA (PBE) and LC-M06L functionals for three different Ag rods; study of the dependence of the nonlocal optics blue-shift on aspect ratio and absolute size of Ag rods (PDF)

■ AUTHOR INFORMATION

Corresponding Authors

*E-mail: sinharoy@cinam.univ-mrs.fr.
*E-mail: a.fernandez-dominguez@uam.es.

ORCID

Rajarshi Sinha-Roy: 0000-0002-1324-9820
Frank Rabilloud: 0000-0002-5011-3949
Antonio I. Fernández-Domínguez: 0000-0002-8082-395X

Notes

The authors declare no competing financial interest.

■ ACKNOWLEDGMENTS

The project leading to this publication has received funding from Excellence Initiative of Aix-Marseille University - A*MIDEX, a French "Investissements d'Avenir" programme". We acknowledge support from the French National Research Agency (Agence Nationale de Recherche, ANR) in the frame of the project "FIT SPRINGS", ANR-14-CE08-0009. This work has used HPC resources from GENCI-IDRIS (Grant 2016-096829). P.G.G. and A.I.F.D. acknowledge funding from the Spanish MINECO through the "María de Maeztu" Programme for Units of Excellence in R&D (MDM-2014-0377) and through research grants MAT2014-53432-C5-5-R (P.G.G.) and FIS2015-64951-R (A.I.F.D.). A.I.F.D. also acknowledges funding from the EU Seventh Framework Programme under contract FP7-PEOPLE-2013-CIG-630996.

■ REFERENCES

(1) Anker, J. N.; Paige-Hall, W.; Lyandres, O.; Shah, N. C.; Zhao, J.; Van-Duyne, R. P. Biosensing with plasmonic nanosensors. *Nat. Mater.* **2008**, *7*, 442−453.

(2) Seney, C. S.; Gutzman, B. M.; Goddard, R. H. Correlation of Size and Surface-Enhanced Raman Scattering Activity of Optical and Spectroscopic Properties for Silver Nanoparticles. *J. Phys. Chem. C* **2009**, *113*, 74−80.

(43) Sundararaman, R.; Narang, P.; Jermyn, A. S.; Goddard, W. A., III; Atwater, H. A. Theoretical predictions for hot-carrier generation from surface plasmon decay. *Nat. Commun.* **2014**, *5*, 5788.

(44) Ciraci, C.; Hill, R. T.; Mock, J. J.; Urzhumov, Y.; Fernández-Domínguez, A. I.; Maier, S. A.; Pendry, J. B.; Chilkoti, A.; Smith, D. R. Probing the Ultimate Limits of Plasmonic Enhancement. *Science* **2012**, *337*, 1072−1074.

(45) Boardman, A. *Electromagnetic Surface Modes. Hydrodynamic Theory of Plasmon-Polaritons on Plane Surfaces*; John Wiley and Sons: Chichester, 1982.

(46) García de Abajo, F. J. Nonlocal Effects in the Plasmons of Strongly Interacting Nanoparticles, Dimers, and Waveguides. *J. Phys. Chem. C* **2011**, *112*, 17983−17987.

(47) Raza, S.; Toscano, G.; Jauho, A.-P.; Wubs, M.; Mortensen, N. A. Unusual Resonances in Nanoplasmonic Structures due to Nonlocal Response. *Phys. Rev. B: Condens. Matter Mater. Phys.* **2011**, *84*, 121412.

(48) Eguiluz, A.; Quinn, J. Hydrodynamic model for surface plasmons in metals and degenerate semiconductors. *Phys. Rev. B* **1976**, *14*, 1347.

(49) Luo, Y.; Fernández-Domínguez, A. I.; Wiener, A.; Maier, S. A.; Pendry, J. B. Surface Plasmons and Nonlocality: A Simple Model. *Phys. Rev. Lett.* **2013**, *111*, 093901.

(50) Stella, L.; Zhang, P.; García-Vidal, F. J.; Rubio, A.; García-González, P. Performance of Nonlocal Optics When Applied to Plasmonic Nanostructures. *J. Phys. Chem. C* **2013**, *117*, 8941−8949.

(51) Ciraci, C.; Pendry, J. B.; Smith, D. R. Hydrodynamic Model for Plasmonics: A Macroscopic Approach to a Microscopic Problem. *ChemPhysChem* **2013**, *14*, 1109−1116.

(52) Feibelman, P. J. Surface electromagnetic fields. *Prog. Surf. Sci.* **1982**, *12*, 287−407.

(53) Toscano, G.; Straubel, J.; Kwiatkowski, A.; Rockstuhl, C.; Evers, F.; Xu, H.; Mortensen, N. A.; Wubs, M. Resonance shifts and spill-out effects in self-consistent hydrodynamic nanoplasmonics. *Nat. Commun.* **2010**, *4*, 5269−5276.

(54) Ciraci, C.; Della Sala, F. Quantum hydrodynamic theory for plasmonics: Impact of the electron density tail. *Phys. Rev. B: Condens. Matter Mater. Phys.* **2016**, *93*, 205405.

(55) Johnson, H. E.; Aikens, C. M. Electronic Structure and TDDFT Optical Absorption Spectra of Silver Nanorods. *J. Phys. Chem. A* **2009**, *113*, 4445−4450.

(56) Yabana, K.; Bertsch, G. F. Time-dependent local-density approximation in real time. *Phys. Rev. B: Condens. Matter Mater. Phys.* **1996**, *54*, 4484−4487.

(57) Marques, M. A.; Castro, A.; Bertsch, G. F.; Rubio, A. Octopus: a first-principles tool for excited electronion dynamics. *Comput. Phys. Commun.* **2003**, *151*, 60−78.

(58) Troullier, N.; Martins, J. L. Efficient pseudopotentials for plane-wave calculations. *Phys. Rev. B: Condens. Matter Mater. Phys.* **1991**, *43*, 1993−2006.

(59) Perdew, J. P.; Burke, K.; Ernzerhof, M. Generalized Gradient Approximation Made Simple. *Phys. Rev. Lett.* **1996**, *77*, 3865−3868.

(60) Ikura, H.; Tsuneda, T.; Yanai, T.; Hirao, K. A long-range correction scheme for generalized-gradient-approximation exchange functionals. *J. Chem. Phys.* **2001**, *115*, 3540−3544.

(61) Rakić, A. D.; Djurišić, A. B.; Elazar, J. M.; Majewski, M. L. Optical properties of metallic films for vertical-cavity optoelectronic devices. *Appl. Opt.* **1998**, *37*, 5271−5283.

(62) DePrince, A. E., III; Pelton, M.; Guest, J. R.; Gray, S. K. Emergence of Excited-State Plasmon Modes in Linear Hydrogen Chains from Time-Dependent Quantum Mechanical Methods. *Phys. Rev. Lett.* **2011**, *107*, 196806.

(63) Zhang, R.; Zhang, Y.; Dong, Z. C.; Jiang, S.; Zhang, C.; Chen, L. G.; Zhang, L.; Liao, Y.; Aizpurua, J.; Luo, Y.; Yang, J. L.; Hou, J. G. Chemical mapping of a single molecule by plasmon-enhanced Raman scattering. *Nature* **2013**, *498*, 82−86.

(64) Gao, S.; Yuan, Z. Emergence of collective plasmon excitation in a confined one-dimensional electron gas. *Phys. Rev. B: Condens. Matter Mater. Phys.* **2005**, *72*, 121406.

(65) Yan, J.; Gao, S. Plasmon resonances in linear atomic chains: Free-electron behavior and anisotropic screening of d electrons. *Phys. Rev. B* **2008**, *78*, 235413.

(66) Bernadotte, S.; Evers, F.; Jacob, C. R. Plasmons in molecules. *J. Phys. Chem. C* **2013**, *117*, 1863−1878.

(67) Wu, R.; Yu, Y.; Xue, H.; Hu, H.; Liu, Q. Dipole and quadrupole plasmon in confined quasi-one dimensional electron gas systems. *Phys. Lett. A* **2014**, *378*, 2995−3000.

(68) Bohren, C. F.; Huffman, D. R. *Absorption and Scattering of Light by Small Particles*; Wiley-VCH: New York, 1998.

(69) Weissker, H.-C.; López-Lozano, X. Surface plasmons in quantum-sized noble-metal clusters: TDDFT quantum calculations and the classical picture of charge oscillations. *Phys. Chem. Chem. Phys.* **2015**, *17*, 28379−28386.

THE JOURNAL OF
PHYSICAL CHEMISTRY C

Article

pubs.acs.org/JPCC

In Search of the Quantum-Electronic Origin of Color Change: Elucidation of the Subtle Effects of Alloying with Copper on ≈1.8 nm Gold Nanoclusters

Rajarshi Sinha-Roy,[†,‡,§] Xóchitl López-Lozano,[¶] R. L. Whetten,[*,¶] Pablo García-González,[§,‡] and H.-Ch. Weissker[*,†,‡]

[†]Aix Marseille University, CNRS, CINaM UMR 7325, 13288, Marseille, France

[¶]Department of Physics & Astronomy, The University of Texas at San Antonio, One UTSA Circle, San Antonio, Texas 78249-0697, United States

[§]Departamento de Física Teórica de la Materia Condensada and Condensed Matter Physics Center (IFIMAC), Universidad Autónoma de Madrid, E-28049 Cantoblanco, Madrid, Spain

Ⓢ *Supporting Information*

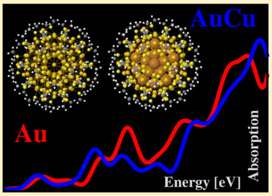

ABSTRACT: Experiments on the $\mathrm{Au}_{144}(\mathrm{SR})_{60}$ class of cluster compounds have demonstrated the emergence of an absorption peak at 550 nm (2.25 eV) upon adding copper to the pure Au samples; in some cases, as little as one Cu atom seems to have this effect [*Chem. Commun.* **2014**, *50*, 1722 and *J. Phys. Chem. C* **2015**, *119*, 10935]. These results are highly surprising as they appear to indicate that the combination of two metals that are not plasmonic in this size range produces a plasmon-like resonance. On the basis of calculations using time-dependent density-functional theory (TDDFT), it has recently been reported that "Copper Induces a Core Plasmon in Intermetallic $\mathrm{Au}_{(144,145)-x}\mathrm{Cu}_x(\mathrm{SR})_{60}$ Nanoclusters" [*J. Phys. Chem. Lett.* **2015**, *6*, 515]. In the present study we show that this effect is by no means general; systematic TDDFT calculations on both bare and ligand-covered clusters do not show the emergence of any clear resonance, plasmonic or other. Instead, suppression of intensity in the range of interest between 2.0 and 3.5 eV (620 to 350 nm) and small red shifts of weak spectral features may indeed change the color of the samples and may be seen as inducing a broad bump in the spectra. However, no clear increase in intensity if observed at the energy of interest (2.25 eV ≈ 550 nm) that would indicate the emergence of a plasmonic resonance. Other hypotheses will have to be explored to explain the experimental results, which show a strong resonance developing.

■ INTRODUCTION

Noble-metal nanoclusters play an immensely important role as critical agents in a number of emerging technologies—in optics; in electronics; in diagnostic and therapeutic medicine.[1−6] They can act as intense pigments of high durability in spectral ranges uniquely adapted to human color vision. The localized surface−plasmon resonance (LSPR), which for many clusters dominates the visible (VIS) spectral region with a broad and smooth peak,[7,8] is the physical mechanism exploited in most of the aforementioned applications. Nonetheless, while the general aspects of the clusters' optical response are well understood, a full understanding of the precise mechanisms governing the emergence of plasmon resonances and their coupling to other elementary excitations is still missing. In particular, the transition from small molecule-like clusters, with their discrete electronic states and spectra, to larger metallic and plasmonic nanoparticles reflects the quantum nature of the clusters.[9−11] A large number of studies have focused on different aspects of this transition: On the one hand, the emergence of the LSPR has been investigated for gold clusters, where it seems to take place between 150 and 330 atoms,[12,13] with smaller Au clusters not showing the resonances. The presence of the plasmon depends on the underlying electron−hole transition spectrum which could lead either to fragmentation (if the e−h transitions are of s−p character) or suppression (if they are of d character). The exact conditions (geometry, chemical composition and configuration, and environment including presence and nature of ligand layers) are not entirely understood. On the other hand, the information content of the optical spectra provides precious information concerning the discrete electronic levels in the small clusters and on the way they develop into bands for bigger particles.[14] In addition to the large number of gold clusters, ligand-stabilized silver clusters have likewise been synthesized.[15,16]

The thiolate ligand-protected $\mathrm{Au}_{144}(\mathrm{SR})_{60}$ cluster compound is an exceptionally well suited benchmark system for the investigation of optical properties in this transition size-range, and this for a number of reasons. First, its diameter ($D \approx 1.8$ nm) lies in the size range where the LSPR starts to develop in Au clusters, but also where the transition from molecular-

Received: January 18, 2017
Published: March 7, 2017

DOI: 10.1021/acs.jpcc.7b00581
J. Phys. Chem. C 2017, 121, 5753−5760

cluster to metallic-nanoparticle behaviors occurs. It shows itself no strong resonance in the visible spectra.[12−14] Second, the cluster happens to be highly stable and has been studied by a number of different research groups.[14,17−20] Third, the cluster compound exhibits icosahedral symmetry[21,22] which implies a high degree of degeneracy of its electronic levels and, consequently, strong individual structures in its optical spectra[14] although recent studies indicate polymorphism in certain samples.[23,24] Finally, it has been shown experimentally that the precise nature of the ligand rest group (denoted R) bears little influence on the optical spectra. For a collection of results, see ref 25.

Among the three coinage metals, silver is optically different from Au and Cu because the onset of interband transitions from the d band occurs at about 4 eV in silver, whereas in Au and Cu, it occurs at ≈2 eV. Therefore, silver behaves more like a free-electron metal and shows a clear LSPR down to very small sizes,[26] although this depends also on the cluster surface; ligand-protected clusters of fewer than ≈150 silver atoms seem to lose the plasmonic character.[16] By contrast, in Au and Cu, interband transitions involving d electrons couple strongly with the LSPR, as much so as to make it disappear for small clusters, thereby creating the above-mentioned phenomenon of plasmon emergence/disappearance in dependence on cluster size.[12,13,27] In view of these differences, it is natural to look at nanoalloys of these materials. Mixing of gold with silver has been studied, both experimentally and theoretically, for both bare[27,28] and ligand-covered[29,30] clusters, showing in general a smooth change of the spectra with changing composition, whereby the outermost layer of bare clusters strongly influences the properties.[28] Insertion of a Cu core into a small silver cluster has been shown to strongly suppress the LSPR.[31]

Recent experiments have attempted to alloy gold and copper in the $Au_{144}(SR)_{60}$ class of cluster compounds, leading to the most extraordinary results: while both Au and Cu at this size do not show a plasmonic resonance, insertion of copper into the gold cluster samples leads to the development of a peak at 550 nm (2.25 eV), reminiscent of the LSPR.[32,33] This outstanding result—the combination of two nonplasmonic metals (at this size) apparently leading to the development of a plasmon resonance—calls out for explanation. The result is even more surprising in that it indicated that in some cases, a single copper atom might be sufficient to induce this effect,[33] although this was not the case in the experiments performed by the Dass group.[32] In order to understand this highly unexpected behavior, Malola et al. have carried out time-dependent density-functional theory (TDDFT) calculations and concluded that "Copper Induces a Core Plasmon in Intermetallic $Au_{(144,145)-x}Cu_x(SR)_{60}$ Nanoclusters."[34] Substituting copper for gold atoms in a number of different configurations and compositions, these authors obtain the development of a peak at about 550 nm compared to the spectrum of the pure $Au_{144}(SR)_{60}$, which is interpreted as a plasmonic resonance. Even the insertion of one copper atom in the center vacancy of the pure $Au_{144}(SR)_{60}$ has been interpreted to have this effect.

In the present work, we show that this behavior is by no means general. The introduction of copper into the gold clusters leads essentially to the suppression of intensity at some wavelengths as well as to small red shifts in energy of some spectral features. The combination of these rather weak effects leads then in some case to spectra that exhibit a weak hump at the wavelength in question, at around 550 nm (≈ 2.2 eV). However, no indication is found of any increase of intensity in the spectra compared to those of the pure Au clusters, as it would correspond to a plasmonic resonance developing. We note that the energy range in question corresponds exactly to the onset of interband transitions from the d electrons (2.0−2.5 eV) *and* to the region where the LSPR in pure gold clusters should emerge.[27] In other words, in this energy range there is a strong coupling between d-electron excitations and the nascent surface plasmon. Therefore, any statement about the precise nature of spectral features has to be made with extreme care.

The results depend only very slightly on the details of the structural model, the kind of ligand rest group used in the calculations, and on the approximations used in the calculations. This allows for the strong general conclusion that alloying with copper does not create plasmonic resonances in gold clusters in this size range, i.e., around 1.8 nm, where the spectra do not yet show any clear LSPR. Regrettably, this means that the exciting experiments cannot be explained in this way; different mechanisms will have to be considered for their explanation.

■ ABSORPTION SPECTRA

As sketched in Figure 1, we study the inclusion of Cu into Au clusters by replacing individual gold atoms by copper atoms (and, in some cases, filling the central vacancy, which leads to numbers of atoms of 144 or 145 for the Au_{144}-derived liganded clusters, and an unchanged 147 for the bare clusters). We use the time-evolution formalism[35] of time-dependent density-

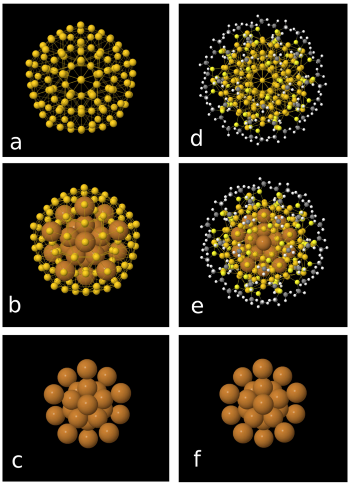

Figure 1. Structure of the bare 147-atom clusters (left-hand side, panels a−c) and the ligand-protected $Au_{144}(SR)_{60}$ clusters (right-hand side, panels d−f). Uppermost panels: complete pure-Au clusters; middle panels: alloying with 25 copper atoms, which leads to $Au_{122}Cu_{25}$ for the bare and to $Au_{120}Cu_{25}(SR)_{60}$ for the ligand-protected cluster. In the ligand-protected structure, the central vacancy of the pure-gold structure is filled with a copper atom. The copper atoms are represented with a larger radius for the sake of visibility. Lower panels (c, f): copper atoms only (25 in both cases). The distribution of the copper atoms is identical in the bare and the ligand-protected clusters and corresponds to "model 9" of ref 34.

functional theory and employ the real-space pseudopotential code octopus.[36] The technical details are described in the Technical Details section. We have demonstrated the applicability of this approach to bare[31] and ligand-protected clusters[14,25] as well as to nanoalloys.[28] The results are in agreement with those obtained using the Casida approach (LR-TDDFT),[37,38] which is illustrated in the Supporting Information of ref 14 for the thiolate-ligand covered Au_{38} cluster and, for a bare Au cluster, in the Supporting Information of ref 39.

Bare Icosahedral 147-Atom Clusters. Before we discuss the $Au_{144}(SR)_{60}$ compound, we study the far simpler case of bare 147-atom icosahedral clusters. These clusters of ≈1.6 nm diameter have roughly the same number of gold atoms as the $Au_{144}(SR)_{60}$ and exhibit likewise icosahedral symmetry. Unlike in the $Au_{144}(SR)_{60}$ cluster, the central vacancy is filled. They show very clearly the difference between silver with a very strong LSPR visible in the spectra and gold without.[31] In fact, the 147-atom Au clusters appear to be just below the size where the LSPR emerges, which happens between ≈150 and 330 atoms.[12,13] The calculated spectrum of Au_{147} is shown in Figure 2 where the spectrum of the corresponding silver cluster with its strong resonance is shown in the inset for comparison.

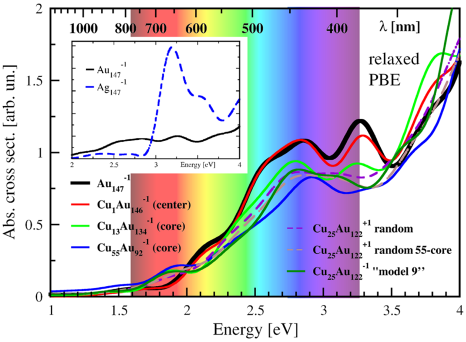

Figure 2. Bare clusters: Absorption spectrum of the bare 147-atom Au icosahedral cluster (thick black line) compared to different Au−Cu alloy clusters, all relaxed using the PBE GGA functional (spectra for LDA-relaxed clusters are shown in Figure S1 of the Supporting Information). We show the spectra corresponding to insertion of one Cu atom in the center vacancy (Cu_1Au_{146}, red), the replacement of the positions of the 13-atom core by Cu atoms ($Cu_{13}Au_{134}$, green), the same for the 55-atom core ($Cu_{55}Au_{92}$, blue), and $Cu_{25}Au_{122}$ clusters with random configurations: 25 Cu atoms randomly distributed throughout the cluster (violet) and throughout the 55-atom core (brown). Finally, the dark green line corresponds to model no. 9 of ref 34 (see section "Technical Details"). In the inset, a comparison of the absorption spectra of icosahedral Au_{147} and the *plasmonic* Ag_{147} is shown. Clearly, no resonance emerges in any of the considered Au−Cu clusters, there is rather a suppression of intensity throughout the spectral range of interest ($\omega \sim 2.0$−3.5 eV, i.e., 620 to 350 nm), along with a small red-shift of the shoulder at 2.1 eV in pure gold to about 1.9 eV for the gold−copper alloy clusters. For the sake of visibility, we present here spectra from a time evolution of 15 fs, corresponding roughly to a broadening of 0.3 eV in the spectra. To highlight the rich details in the spectral features, we show spectra with much higher spectral resolution (0.18 and 0.018 eV) in the Supporting Information, Figures S2 and S3.

Also in Figure 2, we show the comparison of spectra following the incorporation of one, 25, and 55 Cu atoms in the cluster. The inclusion of one Cu atom replacing the central Au atom leads to minimal changes in the spectra. Adding more Cu, whereby we keep the cluster symmetric except in the case of random distributions where the symmetry is obviously broken, we obtain a clear and coherent picture: the changes upon adding copper are such that the structures between 2.0 and 3.5 eV (620 to 350 nm) are smoothened and that the spectral intensity is *reduced* at some energies. The shoulder at 2.2 eV is red-shifted to about 1.9 eV (650 nm). No indication of plasmon emergence is found. This is likewise true for clusters relaxed using the local density approximation (LDA) to the exchange-correlation functional instead of the generalized-gradient approximation (GGA). These spectra are shown in Figure S1.

The present spectra are calculated with an evolution time of 15 fs, corresponding to a broadening of about 0.3 eV in the spectra. For more finely resolved spectra, and in order to check for the development of narrow, weaker resonances that might go unnoticed in the calculation with this broadening, we show in Figure S2 of the Supporting Information spectra calculated for longer evolution time, viz., 25 fs corresponding to 0.18 eV. In these more finely resolved spectra, the general findings are naturally the same. Comparing the copper-alloyed clusters with the pure-Au cluster, there is the clear suppression of intensity between 2.0 and 3.5 eV as well as a red shift of the small peak at 2.15 to 1.9 eV, which corresponds to the shoulders in Figure 2. The findings are similar for all chemical configurations of the copper alloying.

Finally, the spectra with an extremely small broadening (250 fs evolution time corresponding roughly to 0.018 eV broadening) in the supplementary figure S3 show that in the interesting range between 1.5 and 2.5 eV, there is some rearrangement of spectral intensity. However, no intensity increase is observed that would be characteristic of the emergence of a plasmonic resonance. This is particularly clear in view of the direct comparison, also in Figure S3, with the strong resonance exhibited by the equivalent *silver* cluster Ag_{147} with its clear plasmonic resonance.

Ligand-Covered 144-Atom Clusters. For the ligand-protected clusters, a number of additional parameters complicate the description of the system. Besides the structural relaxations in the available literature using either LDA or GGA,[12,14,30] which leads to small but relevant changes,[25] the description of the ligand rest groups plays an important role, although the optical measurements are rather insensitive to the precise nature of the rest group R of the thiolate ligands (see ref 25 for a direct comparison of measurements). The TDDFT calculations need to reduce the number of atoms as far as possible due to numerical limitations. We have shown previously that the reduction of the ligand rest group to only R = H is too drastic[25] and kept the methyl group in our calculations, R = CH_3.[14,25] Another subtle but relevant factor is the symmetry of the system. The original model as published by López-Acevedo et al.[40] has the "staple motives" mutually oriented in a way that does not respect the overall icosahedral symmetry of the compound. Following the experimental work of Wong et al.[21] which indicated that all ligands are positioned in symmetry-equivalent positions, the model was refined so as to have the full icosahedral symmetry.[22] The resulting small differences in the spectra of the respective structures are discussed in detail in a previous work.[25] The study of Malola et al.[34] uses the original, slightly less symmetric geometry, the minimal ligand rest group R = H, and ground-state relaxation with the LDA functional. The latter is motivated by the fact that for gold, the interatomic distances are better reproduced by LDA than when a GGA is used. However, naturally the presence of the ligands as well as of the Cu reduces the plausibility of this choice somewhat. Other previous studies have used the GGA function PBE for relaxation.[14,25,30] It seems that the spectra using the fully symmetric structure, R = CH_3, and relaxation with PBE are the ones that are closest to experiment, compared to the spectra using different choices.[12,14,25,30]

In order to obtain generally valid results and to exclude the possibility that any of these parameters invalidate our conclusions, we treat all four different cases: ligand rest groups R = H and R = CH_3 for, in both cases, structural relaxations using either LDA or GGA. Our results are shown in Figure 3 for R = CH_3. Clearly, the addition of copper does not induce any strong increase of spectral intensity in the region of interest around 2.2 eV. Apart from a very small red-shift of the shoulder at about 2 eV, the changes due to the insertion of copper occur by suppression of spectral intensity. The use of GGA and LDA in the relaxation leads to slightly different spectra, as shown before for the pure $Au_{144}(SR)_{60}$,[25] but the conclusions concerning the effect of alloying with copper do not differ between the two cases shown in Figure 3.

Clearly, the choice of the methyl group CH_3 is physically better motivated than the reduction of the ligand rest group to just one hydrogen atom. However, in order to double-check for the possibility that the choice of the rest group influences the conclusions, we show in the Supporting Information the spectra for R = H, which we obtain by replacing each methyl group by an H atom and relaxing, in the lower panels of Figure S4. The situation for the PBE-relaxed clusters is as clear as for the calculations using CH_3, there is again a small red-shift upon insertion of copper but no emergence of any resonance.

The case of the LDA-relaxed R = H calculation is slightly more intricate. It is interesting to note that in this case, for the pure $Au_{144}(SR)_{60}$, the LDA-relaxed less symmetric structure with R = H leads to a somehow more "flat", rounded structure between 1.9 and 2.7 eV compared to the fully symmetric structure. Only, in this case, insertion of copper produces indeed an—albeit very weak—increase of intensity in a very narrow range around the desired energy of 2.2 eV. Surprisingly, this is already the case when one single Cu atom is placed in the central vacancy. However, the change is small and the intensity of this peak does hereafter not change when the copper content is increased to 25 atoms. There is, instead, rather a *suppression* of intensity between 2.5 and 3.0 eV, which contributes to the impression of a peak developing at 2.2 eV. Nonetheless, comparing the respective spectra directly and to scale (comparing, in particular, the calculation using the physically preferable CH_3 rest group) it is clear that the interplay of the subtle structural changes leading to a fortuitous rearrangement of oscillator strength is at the origin of the development of the little peak; no emergence of any resonance is seen.

One Copper Atom. It is interesting to note that even the addition of one copper atom in the central vacancy leads to noticeable changes in the spectrum, although in general, they remain small (where the case of the LDA-relaxed structures with R = H is somewhat an exception.) We have demonstrated in the previous paragraph that subtle changes in the geometry are responsible for the deceptive impression that a LSPR-like resonance might develop. In order to distinguish between the geometrical effect and the chemical effect of inserting a copper atom, we compare, in Figure 4, the effect of adding a copper atom and that of adding a gold atom in the central vacancy. The addition of the gold atom allows for the consideration of only the effect of a geometric change, whereas the addition of Cu induces both a geometric and a chemical change. The finding in Figure 4 is that the changes caused by the introduction of either a gold atom or a copper atom are similar to a very high degree. This allows for the important conclusion that the effect is almost entirely structural, with little influence of the chemical nature of the central atom. Again, this indicates that Cu does not induce a plasmonic resonance.

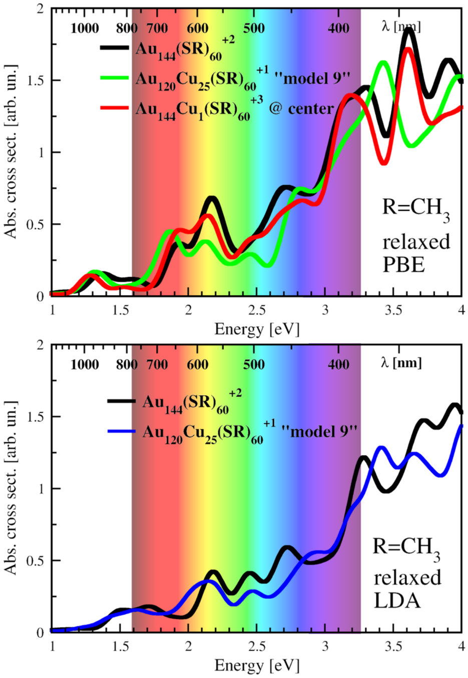

Figure 3. Monolayer-protected $Au_{144}(SR)_{60}$ clusters: Change of the absorption spectra of $Au_{144}(SR)_{60}$ upon alloying with copper. We compare the spectra of the pure-gold cluster (black) to those of the alloy clusters. "Model #9" corresponds to the configuration of the same denomination used in ref 34 and is shown in the present Figure 1. We use the rest group R = CH_3 and relaxation using the PBE (upper panel) and the LDA (lower panel) functionals. Spectra for R = H are shown in the Supporting Information, Figure S4. The insertion of one copper atom into the central vacancy has a small but noticeable effect. Upon adding 25 copper atoms, a *suppression* of intensity in the range between 2 and 3 eV leads to a bump at around the desired energy, but there is clearly no increase of intensity that would be indicative of the emergence of a plasmonic resonance. These changes may modify the color of the samples, but they do not describe the emergence of a plasmonic resonance, i.e., the strong effects reported in the experimental studies.[32,33]

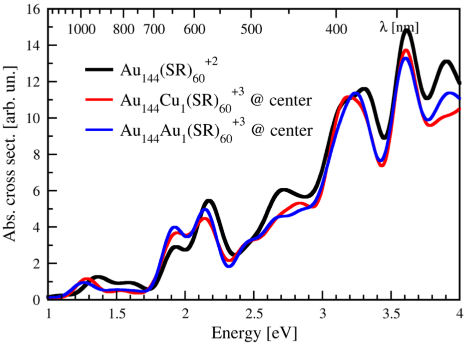

Figure 4. One copper atom: chemical vs geometrical effect: Effect of the introduction of either a copper or a gold atom into the central vacancy of the pure $Au_{144}(SR)_{60}$ cluster compound in order to distinguish the purely geometric effect and the chemical effect. Ground state relaxation done using PBE, rest group R = CH_3. The two spectra deviate little but noticeably from the pure gold spectra but are almost identical; the entire effect is, consequently, geometric.

DYNAMICAL POLARIZABILITY AND INDUCED DENSITY

As it is well-known, in the dipole approximation the absorption cross section corresponding to an external electromagnetic (EM) plane wave of frequency ω whose E-field is polarized along the z direction [that is, $\mathbf{E}_{\text{ext}}(t) = E_0 \cos(\omega t)\mathbf{e}_z$] is given by

$$\sigma_{\text{abs}}(\omega) = \frac{4\pi\omega}{c}\Im\alpha(\omega) \tag{1}$$

where c is the speed of light and $\alpha(\omega)$ is the dynamical polarizability. The latter is defined as the induced electric dipole divided by the amplitude E_0 of the incident electric field:

$$\alpha(\omega) = -\frac{1}{E_0}\int z\delta n(\mathbf{r}, \omega)\,\mathrm{d}\mathbf{r} \tag{2}$$

$\delta n(\mathbf{r}, \omega)$ being the induced electron density. Note that according to the standard complex representation of harmonic functions, the time-dependent induced electron density is given by

$$\delta n(\mathbf{r}, t) = \cos(\omega t)\mathcal{R}\delta n(\mathbf{r}, \omega) + \sin(\omega t)\Im\delta n(\mathbf{r}, \omega) \tag{3}$$

and the real [imaginary] parts are then related to oscillations in phase [out of phase with a phase difference of a quarter of a period] with the external E-field. Therefore, the absorption is proportional to the imaginary part of the polarizability $\alpha(\omega)$, which accounts for out-of-phase oscillations of the electron density with respect to the external E-field. However, further insights concerning the interaction between a nanoparticle and an external EM field can be obtained by analyzing the real part of $\alpha(\omega)$, that is, the in-phase induced electric dipole.

In extended bulk systems, where electron−hole transitions form a continuum, the plasmon is a well-defined and distinct elementary excitation.[41] By contrast, for systems with a finite number of electrons the concept of collective excitation and its corresponding distinction from electron−hole excitations is more vague. In fact, a LSPR might be seen as an electron−hole excitation that is highly renormalized by the electron−electron interaction.[42] This excitation can be coupled to surrounding electron−hole *intraband* transitions, in such a way that the LSPR acquires an effective width through a "Landau fragmentation" mechanism.[43] However, as we have mentioned before, the coupling of the LSPR with *interband* transitions leads practically to the disappearance of the plasmon resonance. Such couplings prevent us from identifying a single spectral peak as "the" LSPR in many cases. Then, the signature of the existence of a LSPR is the concentration of spectral weight around a given frequency ω_P that, for sufficiently large systems, would be close to the classical-optics prediction. This is precisely the situation in bare and ligand-protected Au clusters and related nanoalloys: the region where the LSPR is expected to appear is already occupied by a multitude of electron−hole transitions.

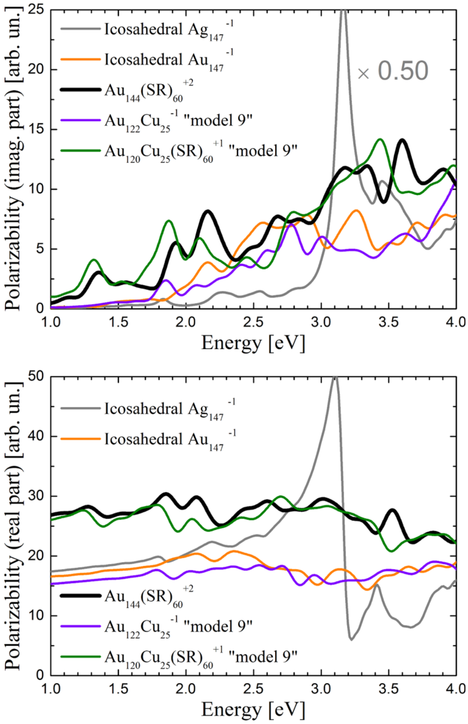

Figure 5. Dynamical polarizability: Real (bottom panel) and imaginary (top panel) parts of the dynamical polarizability, $\alpha(\omega)$, for selected bare and ligand-protected clusters. Key: thick gray line, bare Ag_{147}; thick black line, bare Au_{147}; green line, bare $Cu_{25}Au_{122}$ according to "model no. 9" of ref 34 (cf., the present Figure 1); blue line, ligand-protected $Au_{144}(SR)_{60}$ cluster; red line, ligand-protected $Cu_{25}Au_{120}(SR)_{60}$ cluster (again "model no. 9"; rest group R = CH_3). While the real part of the polarizability for the plasmonic silver cluster Ag_{147} cluster exhibits a sharp variation at the LSPR frequency ($\omega_P \simeq$ 3.15 eV), there is no noticeable structure for the Au-based nanoparticles, regardless of the inclusion of Cu atoms. A broadening of 0.05 eV has been used.

The concentration of spectral weight around ω_P can not only be observed in the imaginary part of the dynamical polarizability; the real part of $\alpha(\omega)$ around the frequency of an isolated, well-defined resonance must exhibit a change of sign (from positive to negative). The presence of less-intense nearby transitions can hamper this change of sign but, in any case, a sharp variation of $\mathcal{R}\alpha(\omega)$ with negative slope is a clear indication of spectral-weight concentration and, therefore, of the existence of a LSPR. As we may see in Figure 5, this is indeed the case for the icosahedral Ag_{147} cluster (a more detailed presentation including the use of a lower broadening is shown in the Supporting Information, Figure S5). However, there is not any distinctive behavior in both the real and imaginary parts of the polarizability of bare and ligand-protected Cu/Au alloys indicating a Cu-induced concentration of spectral weight in the region 2.0−2.5 eV. Hence, the analysis of the real part of the dynamic polarizability confirms the findings based on the direct comparison of the different absorption spectra.

Density Dynamics. We need to point out one more issue. The time-dependent polarization of the system is connected to the movement of the electrons and, therefore, the dynamics of the electron density. A localized surface-plasmon resonance can be considered a collective oscillation of the quasi-free electrons, with modifications due to the atomistic inhomogeneity and the presence of the *d* electrons in the noble metals.[44] However, it is not enough to find such a dipole mode in the dynamics of the density, as this can be present even in cases where no prominent resonance appears in the spectra. We show the induced density in the pure bare Au_{147} cluster after quasi-monochromatic laser excitation in Figure S6 of the Supporting Information. Even in this case, where the spectrum clearly does not exhibit any strong plasmonic resonance, we find the sort of dipole pattern that is reminiscent of a plasmonic excitation, including the out-of-phase movement of the d electrons that shows the screening of the oscillation. In other words, the presence of a dipole mode in the electron density dynamics, even if reminiscent of an LSPR dipole mode, does not allow for clear conclusions about the plasmonic nature of spectral features.

■ SUMMARY AND CONCLUSIONS

Motivated by experimental findings and recently published calculations which concluded that "Copper Induces a Core Plasmon in Intermetallic $Au_{(144,145)-x}Cu_x(SR)_{60}$ Nanoclusters",[34] we have calculated the changes of the optical response of both the bare 147-atom icosahedron and of the $Au_{144}(SR)_{60}$ cluster compound upon alloying with copper. Copper atoms are replacing gold atoms of the pure cluster (and, in addition, are inserted into the central vacancy of $Au_{144}(SR)_{60}$). Considering a number of different situations as far as the ground-state relaxation of the structures is concerned (LDA vs PBE), the choice of the rest group of the thiolate ligands ($R = H$ vs $R = CH_3$), and the subtle differences in symmetry/geometry discussed previously,[25] we show that the addition of copper does not induce the development of any prominent resonance, plasmonic or other. The main changes are small and consist mostly in (a) suppression of spectral intensity in the range between 2.0 and 3.5 eV (620 to 350 nm), and (b) a red-shift of the lowest spectral features. Moreover, we demonstrate that the small but noticeable changes upon insertion of a single copper atom in the central vacancy of the pure $Au_{144}(SR)_{60}$ are almost entirely due to the geometric effect of the copper insertion.

These findings mean that the experiments in which the development of an LSPR-like peak has been observed cannot be explained by the simple hypothesis that the insertion of copper changes the optical response be inducing a plasmonic resonance. Other hypotheses will need to be explored in order to obtain a fundamental understanding of the effects at play in these experiments.

■ TECHNICAL DETAILS

The ionic ground-state relaxations have been done using the VASP code[45−47] with the projector-augmented wave method (PAW).[47] The force tolerance has been set to 0.01 eV/Å.

The absorption spectra are calculated in TDDFT using the real-space code "octopus".[36,48] Following a ground-state calculation, spectra are obtained with the time-evolution formalism[35] and the PBE-GGA exchange-correlation functional[49] *for all spectra* shown, including those where the structural relaxation was done using LDA. Norm-conserving Troullier-Martins pseudopotentials[50] have been used which, similarly as in our previous work,[14,25] include the d electrons in the valence (11 valence electrons for each Au or Cu atom, i.e., ∼2500 active electrons). The spacing of the real-space grid was set to 0.20 Å for the pure-Au clusters, and to 0.16 Å for the clusters containing copper. The radius of the spheres centered around each atom which make up the calculation domain was 5 Å. The clusters have been charged as indicated such that the degenerate HOMO states were fully occupied.

The time-evolution formalism is equivalent to the transition-based Casida formalism (LR-TDDFT).[37,38] A comparison of the time-evolution results with a transition-based calculation is shown in the Supporting Information of ref 14 for the thiolate-ligand covered Au_{38} cluster. For a bare Au cluster, a similar comparison is shown in the Supporting Information of ref 39. The good agreement shows likewise that the technical parameters of our calculations are well controlled.

Apart from the customary 147-atom icosahedron that has been studied in many works, we consider the following structural models of $Au_{144}(SR)_{60}$ and its alloys with copper. (For a detailed analysis of the differences between these structures, refer to ref 25.)

- The fully symmetric, GGA-relaxed $Au_{144}(SR)_{60}$ with $R = CH_3$ from the work of Bahena et al.[22] is used as the starting structure. For the respective comparison, this structure has also been rerelaxed using LDA.
- The $Au_{144}(SR)_{60}$ with $R = CH_3$ is obtained from the same structure by replacing the methyl group with H atoms and rerelaxing.
- For comparison (only shown in the Supporting Information) we have also used the "Malola et al. structure" as employed in the calculations of ref 12. The structure is derived from the original, less symmetrical "López-Acevedo et al. structure"[40] by reducing the rest group to $R = H$, probably resulting in a partial symmetrization as discussed in ref 25.
- Copper (or, in one case, gold) is introduced into the center vacancy (resulting in $Au_{144}Cu_1(SR)_{60}$). For the higher copper content, $Au_{120}Cu_{25}(SR)_{60}$, we use the model structure that is called model no. 9 in ref 34, which consists of a 13-atom Cu core (filled central vacancy) and 12 Cu atoms distributed symmetrically in the 42-atom shell around the 13-atom core so as to conserve the icosahedral symmetry.[34]

DOI: 10.1021/acs.jpcc.7b00581
J. Phys. Chem. C 2017, 121, 5753−5760

■ ASSOCIATED CONTENT

Ⓢ Supporting Information

The Supporting Information is available free of charge on the ACS Publications website at DOI: 10.1021/acs.jpcc.7b00581.

Figures showing absorption spectra of bare and monolayer-protected clusters, Dynamical polarizability, and density dynamics (PDF)

■ AUTHOR INFORMATION

Corresponding Authors

*E-mail: weissker@cinam.univ-mrs.fr.
*E-mail: Robert.Whetten@utsa.edu.

Notes

The authors declare no competing financial interest.

‡Member of the European Theoretical Spectroscopy Facility.

■ ACKNOWLEDGMENTS

Useful discussions with Antonio Fernández-Domínguez are gratefully acknowleded. This work has been carried out thanks to the support of the A*MIDEX Grant (No. ANR-11-IDEX-0001-02) funded by the French Government "Investissements d'Avenir" program. We acknowledge support from the French National Research Agency (Agence Nationale de Recherche, ANR) in the frame of the project "FIT SPRINGS," ANR-14-CE08-0009. X.L.L. acknowledges the support of the Department of Physics & Astronomy. R.L.W. acknowledges the support of the Welch Foundation under Grant AX-1857. P.G.G. acknowledges financial support from the Spanish Ministry of Economy and Competitiveness through the "María de Maeztu" Programme for Units of Excellence in R&D (MDM-2014-0377) and through Research Grant MAT2014-53432-C5-5-R. The work received computational support from Computational System Biology Core, funded by the National Institute on Minority Health and Health Disparities (G12MD007591) from the National Institutes of Health, as well as the Texas Advanced Computing Center (TACC) at The University of Texas at Austin and HPC resources from GENCI-IDRIS (Grant 2016-096829).

■ REFERENCES

(1) Love, J. C.; Estroff, L. A.; Kriebel, J. K.; Nuzzo, R. G.; Whitesides, G. M. Self-Assembled Monolayers of Thiolates on Metals as a Form of Nanotechnology. *Chem. Rev.* **2005**, *105*, 1103−1170.

(2) Jain, P. K.; Huang, X.; El-Sayed, I. H.; El-Sayed, M. A. Noble Metals on the Nanoscale: Optical and Photothermal Properties and Some Applications in Imaging, Sensing, Biology, and Medicine. *Acc. Chem. Res.* **2008**, *41*, 1578−1586.

(3) Hainfeld, J. F.; Liu, W.; Halsey, C. M.; Freimuth, P.; Powell, R. D. Ni−NTA−Gold Clusters Target His-Tagged Proteins. *J. Struct. Biol.* **1999**, *127*, 185−198.

(4) Ackerson, C. J.; Powell, R. D.; Hainfeld, J. F. Cryo-EM Part A Sample Preparation and Data Collection. *Methods Enzymol.* **2010**, *481*, 195−230.

(5) Bowman, M.-C.; Ballard, T. E.; Ackerson, C. J.; Feldheim, D. L.; Margolis, D. M.; Melander, C. Inhibition of HIV Fusion with Multivalent Gold Nanoparticles. *J. Am. Chem. Soc.* **2008**, *130*, 6896−6897.

(6) Bresee, J.; Maier, K. E.; Boncella, A. E.; Melander, C.; Feldheim, D. L. Growth Inhibition of Staphylococcus aureus by Mixed Monolayer Gold Nanoparticles. *Small* **2011**, *7*, 2027−2031.

(7) Faraday, M. Noble Metals on the Nanoscale: Optical and Photothermal Properties and Some Applications in Imaging, Sensing, Biology, and Medicine. *Philosophical Transactions: Royal Society London* **1857**, *147*, 145−181.

(8) Craig, F., Bohren, D. R. H. *Absorption and Scattering of Light by Small Particles*; Wiley-VCH: 1983; Chapter 9-12.

(9) de Abajo, F. J. G. Microscopy: Plasmons go quantum. *Nature* **2012**, *483*, 417−418.

(10) Scholl, J. A.; Koh, A. L.; Dionne, J. A. Quantum plasmon resonances of individual metallic nanoparticles. *Nature* **2012**, *483*, 421−427.

(11) Haberland, H. Looking from both sides. *Nature* **2013**, *494*, E1−E2.

(12) Malola, S.; Lehtovaara, L.; Enkovaara, J.; Häkkinen, H. Birth of the Localized Surface Plasmon Resonance in Monolayer-Protected Gold Nanoclusters. *ACS Nano* **2013**, *7*, 10263−10270.

(13) Qian, H.; Zhu, Y.; Jin, R. Atomically precise gold nanocrystal molecules with surface plasmon resonance. *Proc. Natl. Acad. Sci. U. S. A.* **2012**, *109*, 696−700.

(14) Weissker, H.-C.; Escobar, H. B.; Thanthirige, V. D.; Kwak, K.; Lee, D.; Ramakrishna, G.; Whetten, R.; López-Lozano, X. Information on quantum states pervades the visible spectrum of the ubiquitous Au144 gold nanocluster. *Nat. Commun.* **2014**, *5*, 3785.

(15) Desireddy, A.; Conn, B. E.; Guo, J.; Yoon, B.; Barnett, R. N.; Monahan, B. M.; Kirschbaum, K.; Griffith, W. P.; Whetten, R. L.; Landman, U.; et al. Ultrastable silver nanoparticles. *Nature* **2013**, *501*, 399−402.

(16) Chakraborty, I.; Erusappan, J.; Govindarajan, A.; Sugi, K. S.; Udayabhaskararao, T.; Ghosh, A.; Pradeep, T. Emergence of metallicity in silver clusters in the 150 atom regime: a study of differently sized silver clusters. *Nanoscale* **2014**, *6*, 8024−8031.

(17) Alvarez, M. M.; Khoury, J. T.; Schaaff, T. G.; Shafigullin, M. N.; Vezmar, I.; Whetten, R. L. Optical Absorption Spectra of Nanocrystal Gold Molecules. *J. Phys. Chem. B* **1997**, *101*, 3706−3712.

(18) Chen, S.; Ingram, R. S.; Hostetler, M. J.; Pietron, J. J.; Murray, R. W.; Schaaff, T. G.; Khoury, J. T.; Alvarez, M. M.; Whetten, R. L. Gold Nanoelectrodes of Varied Size: Transition to Molecule-Like Charging. *Science* **1998**, *280*, 2098−2101.

(19) Schaaff, T. G.; Shafigullin, M. N.; Khoury, J. T.; Vezmar, I.; Whetten, R. L. Properties of a Ubiquitous 29 kDa Au:SR Cluster Compound. *J. Phys. Chem. B* **2001**, *105*, 8785−8796.

(20) Chaki, N. K.; Negishi, Y.; Tsunoyama, H.; Shichibu, Y.; Tsukuda, T. Ubiquitous 8 and 29 kDa Gold:Alkanethiolate Cluster Compounds: Mass-Spectrometric Determination of Molecular Formulas and Structural Implications. *J. Am. Chem. Soc.* **2008**, *130*, 8608−8610.

(21) Wong, O. A.; Heinecke, C. L.; Simone, A. R.; Whetten, R. L.; Ackerson, C. J. Ligand symmetry-equivalence on thiolate protected gold nanoclusters determined by NMR spectroscopy. *Nanoscale* **2012**, *4*, 4099−4102.

(22) Bahena, D.; Bhattarai, N.; Santiago, U.; Tlahuice, A.; Ponce, A.; Bach, S. B. H.; Yoon, B.; Whetten, R. L.; Landman, U.; Jose-Yacaman, M. STEM Electron Diffraction and High-Resolution Images Used in the Determination of the Crystal Structure of the $Au_{144}(SR)_{60}$ Cluster. *J. Phys. Chem. Lett.* **2013**, *4*, 975−981.

(23) Yamazoe, S.; Takano, S.; Kurashige, W.; Yokoyama, T.; Nitta, K.; Negishi, Y.; Tsukuda, T. Hierarchy of bond stiffnesses within icosahedral-based gold clusters protected by thiolates. *Nat. Commun.* **2016**, *7*, 10414.

(24) Jensen, K. M. O.; et al. Polymorphism in magic-sized $Au_{144}(SR)_{60}$ clusters. *Nat. Commun.* **2016**, *7*, 11859.

(25) Weissker, H.-C.; Lopez-Acevedo, O.; Whetten, R. L.; López-Lozano, X. Optical Spectra of the Special Au144 Gold-Cluster Compounds: Sensitivity to Structure and Symmetry. *J. Phys. Chem. C* **2015**, *119*, 11250−11259.

(26) Fedrigo, S.; Harbich, W.; Buttet, J. Collective dipole oscillations in small silver clusters embedded in rare-gas matrices. *Phys. Rev. B: Condens. Matter Mater. Phys.* **1993**, *47*, 10706−10715.

(27) Cottancin, E.; Celep, G.; Lermé, J.; Pellarin, M.; Huntzinger, J.; Vialle, J.; Broyer, M. Optical Properties of Noble Metal Clusters as a Function of the Size: Comparison between Experiments and a Semi-Quantal Theory. *Theor. Chem. Acc.* **2006**, *116*, 514.

(28) López-Lozano, X.; Mottet, C.; Weissker, H.-C. Effect of Alloying on the Optical Properties of Ag/Au Nanoparticles. *J. Phys. Chem. C* **2013**, *117*, 3062−3068.

(29) Kumara, C.; Dass, A. $(AuAg)_{144}(SR)_{60}$ alloy nanomolecules. *Nanoscale* **2011**, *3*, 3064−3067.

(30) Barcaro, G.; Sementa, L.; Fortunelli, A.; Stener, M. Comment on "$(Au-Ag)_{144}(SR)_{60}$ alloy nanomolecules" by C. Kumara and A. Dass, *Nanoscale*, 2011, 3, 3064. *Nanoscale* **2015**, *7*, 8166−8167.

(31) Weissker, H.-C.; Mottet, C. Optical properties of pure and core-shell noble-metal nanoclusters from TDDFT: The influence of the atomic structure. *Phys. Rev. B: Condens. Matter Mater. Phys.* **2011**, *84*, 165443.

(32) Dharmaratne, A. C.; Dass, A. $Au_{144-x}Cu_x(SC_6H_{13})_{60}$ nanomolecules: effect of Cu incorporation on composition and plasmon-like peak emergence in optical spectra. *Chem. Commun.* **2014**, *50*, 1722−1724.

(33) Bhattarai, N.; Black, D. M.; Boppidi, S.; Khanal, S.; Bahena, D.; Tlahuice-Flores, A.; Bach, S. B. H.; Whetten, R. L.; Jose-Yacaman, M. ESI-MS Identification of Abundant Copper-Gold Clusters Exhibiting High Plasmonic Character. *J. Phys. Chem. C* **2015**, *119*, 10935−10942.

(34) Malola, S.; Hartmann, M. J.; Häkkinen, H. Copper Induces a Core Plasmon in Intermetallic Au(144,145)-xCux(SR)60 Nanoclusters. *J. Phys. Chem. Lett.* **2015**, *6*, 515−520.

(35) Yabana, K.; Bertsch, G. F. Time-dependent local-density approximation in real time. *Phys. Rev. B: Condens. Matter Mater. Phys.* **1996**, *54*, 4484−4487.

(36) Marques, M. A. L.; Castro, A.; Bertsch, G. F.; Rubio, A. *Comput. Phys. Commun.* **2003**, *151*, 60.

(37) Casida, M. E. *Recent Advances in Density Functional, Methods, Part I* **1995**, *1*, 155.

(38) Casida, M. E. *Theor. Comput. Chem.* **1996**, *4*, 391.

(39) Lopez-Lozano, X.; Barron, H.; Mottet, C.; Weissker, H.-C. Aspect-ratio- and size-dependent emergence of the surface-plasmon resonance in gold nanorods - an ab initio TDDFT study. *Phys. Chem. Chem. Phys.* **2014**, *16*, 1820−1823.

(40) Lopez-Acevedo, O.; Akola, J.; Whetten, R. L.; Grönbeck, H.; Häkkinen, H. Structure and Bonding in the Ubiquitous Icosahedral Metallic Gold Cluster $Au_{144}(SR)_{60}$. *J. Phys. Chem. C* **2009**, *113*, 5035−5038.

(41) Pines, D. *Elementary excitations in solids*; Benjamin: New York, 1963.

(42) Bernadotte, S.; Evers, F.; Jacob, C. R. Plasmons in molecules. *J. Phys. Chem. C* **2013**, *117*, 1863−1878.

(43) Yannouleas, C.; Vigezzi, E.; Broglia, R. A. Evolution of the optical properties of alkali-metal microclusters towards the bulk: The matrix random-phase-approximation description. *Phys. Rev. B: Condens. Matter Mater. Phys.* **1993**, *47*, 9849−9861.

(44) Weissker, H.-C.; Lopez-Lozano, X. Surface plasmons in quantum-sized noble-metal clusters: TDDFT quantum calculations and the classical picture of charge oscillations. *Phys. Chem. Chem. Phys.* **2015**, *17*, 28379−28386.

(45) Kresse, G.; Hafner, J. Ab initio molecular dynamics for liquid metals. *Phys. Rev. B: Condens. Matter Mater. Phys.* **1993**, *47*, 558.

(46) Kresse, G.; Furthmüller, J. Efficiency of ab-initio total energy calculations for metals and semiconductors using a plane-wave basis set. *Comput. Mater. Sci.* **1996**, *6*, 15.

(47) Kresse, G.; Joubert, D. From ultrasoft pseudopotentials to the projector augmented-wave method. *Phys. Rev. B: Condens. Matter Mater. Phys.* **1999**, *59*, 1758.

(48) Castro, A.; Marques, M. A. L.; Appel, H.; Oliveira, M.; Rozzi, C.; Andrade, X.; Lorenzen, F.; Gross, E. K. U.; Rubio, A. *Phys. Status Solidi B* **2006**, *243*, 2465.

(49) Perdew, J. P.; Burke, K.; Ernzerhof, M. Generalized Gradient Approximation made simple. *Phys. Rev. Lett.* **1996**, *77*, 3865.

(50) Troullier, N.; Martins, J. L. Efficient pseudopotentials for plane-wave calculations. *Phys. Rev. B: Condens. Matter Mater. Phys.* **1991**, *43*, 1993−2006.

Résumé

L'intérêt de la recherche fondamentale pour les morceaux nanométriques de métaux nobles est principalement dû à la résonance localisée des plasmons de surface (LSPR) dans l'absorption optique. Différents aspects, liés à la compréhension théorique de la LSPR dans le cas de clusters de métaux nobles de taille dite intermédiaire, sont étudiés dans ce manuscrit. Afin d'avoir une vision plus large nous utilisons deux approches : l'approche électromagnétique classique et le formalisme ab initio en temps réel de la théorie de la fonctionnelle de la densité dépendant du temps (RT-TDDFT). Une comparaison systématique et détaillée de ces deux approches souligne et quantifie les limitations de l'approche électromagnétique lorsqu'elle est appliquée à des systèmes de taille quantique. Les différences entre les excitations plasmoniques collectives et celles impliquant les électrons d, ainsi que leurs interactions, sont étudiées grâce au comportement spatial des densités correspondantes. Ces densités sont obtenues en appliquant une transformée de Fourier dans l'espace à la densité obtenue par les simulations DFT utilisant une perturbation delta-kick. Dans ce manuscrit, des clusters de métaux nobles nus et protégés par des ligands sont étudiés. En particulier, motivé par de récents travaux sur les phénomènes d'émergence de plasmon, l'étude par TD-DFT de nano-alliages Au-Cu de taille tout juste inférieure à 2nm à fourni de subtiles connaissances sur les effets d'alliages sur la réponse optique de tels systèmes.

Abstract

The fundamental research interest in nanometric pieces of noble metals is mainly due to the localized surface-plasmon resonance (LSPR) in the optical absorption. Different aspects related to the theoretical understanding of LSPRs in 'intermediate-size' noble-metal clusters are studied in this thesis. To gain a broader perspective both the real-time *ab initio* formalism of time–dependent density-functional theory (RT-TDDFT) and the classical electromagnetics approach are employed. A systematic and detailed comparison of these two approaches highlights and quantifies the limitations of the electromagnetics approach when applied to quantum-sized systems. The differences between collective plasmonic excitations and the excitations involving d-electrons, as well as the interplay between them are explored in the spatial behaviour of the corresponding induced densities by performing the spatially resolved Fourier transform of the time-dependent induced density obtained from a RT-TDDFT simulation using a δ-kick perturbation. In this thesis, both bare and ligand-protected noble-metal clusters were studied. In particular, motivated by recent experiments on plasmon emergence phenomena, the TDDFT study of Au-Cu nanoalloys in the size range just below 2 nm produced subtle insights into the general effects of alloying on the optical response of these systems.